Analysis of P-wave Seismic Reflection Data for Azimuthal Anisotropy

by

Yan-Qiang (Yi-Jie) Liu

Thesis submitted for the degree of Doctor of Philosophy

University of Edinburgh

February 2003

Declaration

This thesis contains no material that has been submitted, either in whole or in part, for a degree at this or any other university, and to the best of my knowledge and belief, all work is original except where reference is made in the text to the work of other authors.

Analysis of P-wave Seismic Reflection Data for Azimuthal Anisotropy

by

Yan-Qiang (Yi-Jie) Liu

Thesis submitted for the degree of Doctor of Philosophy

University of Edinburgh

February 2003

Declaration

This thesis contains no material that has been submitted, either in whole or in part, for a degree at this or any other university, and to the best of my knowledge and belief, all work is original except where reference is made in the text to the work of other authors.

Yan-Qiang Liu, known as Yi-Jie Liu

February, 2003

Abstract

A vast quantity of hydrocarbons exist in naturally fractured reservoirs of otherwise low permeability, where fracturing is critical to economic production of oil and gas. During the late 1990s, use of P-wave seismic data to study azimuthal anisotropy for fracture estimation in land seismic surveys became increasingly popular. However, there was a general lack of understanding on several issues. These include: (1) the problem of extending the methodology to the marine environment, where the azimuthal coverage in conventional towed streamer data is poor;(2) the robustness of the four principal P-wave attributes: amplitude, traveltime, velocities, and AVO (amplitude versus offset) gradient; (3) the effects of an anisotropic overburden and thin-layering on the estimation of anisotropy.

The primary focus of this thesis is to address above issues. The relationship between the computed anisotropy and the inferred fracture orientation and intensity is not part of my thesis. I use Hudson's well-known equivalent anisotropic medium model for this step in the calculations. I derive equations for the estimation of azimuthal anisotropy parameters using the four P-wave attributes, and develop specific techniques for utilizing repeated marine streamer surveys of different vintages.

In the case of a special orthogonal configuration, the attributes difference between two orthogonal lines is simply a function of $\cos 2(\varphi - \Phi)$, with respect to the survey-line azimuth φ and the fracture-strike azimuth Φ. Thus, the fracture-strike azimuth may be determined from two pairs of orthogonal lines by cross-plotting the attribute difference of one pair against the difference pertaining to the other pair. This cross-plotting technique using two pairs of orthogonal lines is robust for azimuthal anisotropy estimation and is particularly suitable for repeated 2D ma-

rine surveys. However, this configuration yields information only at the point of intersection.

Joint 2D and 3D marine surveys may be employed to investigate more intersecting points for improved lateral spatial coverage. However application of the technique to real data requires careful analysis of geometry, data matching and conditioning, and especially quality control. For 3D data acquired with wide azimuthal coverage, one may use different attributes and processing schemes to utilise azimuthal anisotropy for fracture detection. Real 2D and 3D datasets from three different areas were analysed: two marine data sets from the North Sea and one 3D land dataset from the Yellow-River Delta in China. It is found that amplitude and velocity attributes in the 3D data are not very reliable indicators of azimuthal anisotropy. The most reliable results are given by surface fitting of interval travel times. It is also noted that the commonly-used narrow-azimuth stacking method may enhance the acquisition footprint, and the surface fitting method is generally preferred.

I have studied the effects of overburden anisotropy and thin-layering using synthetic seismic data. The effect of the overburden may be removed by a layer-stripping method that is achieved by normal moveout correction performed separately for each individual line. For the case of a thin anisotropic layer embedded in a sequence of isotropic layers, it is possible to create an effective target layer by combining the thin layer with overlying and underlying isotropic layers. Analysis of synthetic data shows that this procedure can be used to provide reliable information about azimuthal anisotropy even if the thickness of the anisotropic layer is as small as one eighth of a wavelength.

Acknowledgments

After studying and working in The University of Petroleum and service companies in respectively, Shandong, Zhuozhou, Singapore, Beijing and Houston for more than 10 years, I moved to Edinburgh to begin my PhD study. I am fortunate to have Dr Xiang-Yang Li and Professor Anton Ziolkowski as my supervisors. Their unique insight into the needs of the Oil & Gas industry has provided me numerous guidances. I hope that this thesis can be used as a reflection of the elegance of their scientific work: a combination of complicated maths and simple, especially practical methods for application.

I particularly thank Dr Xiang-Yang Li for his extensive review and corrections for this thesis. I also thank Professor Anton Ziolkowski for his emphasis on the practical problems of the industry. Without their strict administrating of my thesis and thorough consideration, supervision and support of my work, it would have been impossible to complete this thesis, especially after I began my career in the oil industry.

I would cordially thank Dr Enru Liu for his supervision, particularly the modelling work. I benefit a lot from his supervision of my thesis writing. His in-depth review and correction forms a part of the thesis. I especially appreciate his readiness to share his 20 years professional experiences with me. I also thank Colin MacBeth for discussion and organization of the field data for my marine data analysis at the early stage of my study. Thanks to David Kerridge and Chris Browitt of the British

Geological Survey, and Roger Scrutton in the department, for their administrative work.

Many thanks to the helps from the following people: Hengcheng Dai for programming and processing on ProMAX and so many other things not only in academic but also in personal life, Peter Hanssen for web authoring and PC utilities, Jianxin Yuan for LaTex and LyX, Anna Droujinina for Matlab, Frank Ohlsen and Thomas Kühnel for sharing their programs; I should thank those people in the Edinburgh Anisotropy Project for sharing so many wonderful seminars and good times: Mark Chapman, Jun Yan, Alexander Druzhinin, Hejie Wang, Fabien Borocin, Simon Tod, Bärbel Traub, Andrew Dobson, Sonja Maultzsch, Xiucheng Wei and Brian Bainbridge. We enjoyed so many evenings in BGS.

I would like to thank FINA (TotalFinaElf) for providing the marine 2D & 3D data and SINOPEC for providing the 3D full-azimuthal data, and for their permission to publish the work at the international conferences. My Ph.D study was supported by the sponsors of the Edinburgh Anisotropy Project: Agip, BP, BGS, Chevron, Conoco, ExxonMobil, FINA (TotalFinaElf), PGS, Phillips, Norsk Hydro, Trade Partners UK (DTI), Schlumberger, Shell, SINOPEC, Texaco, and Veritas DGC.

Lastly, I would like to thank my family and friends for all their support. Especially, my wife and I would also sincerely thank Taohua Li, our close friend, for all the helps she has ever given to my family throughout the years.

P.S. I would like to thank my examiners Professor Ian Main and Dr. Tim Pointer for their detailed analysis of this thesis. I appreciate their comments to correct and improve this thesis.

Bibliography (1998-2002)

Sections of the work presented in this thesis that have been published or presented at conferences or journals, as follow:

1. **Fracture detection using land 3D seismic from the Yellow-River delta, China**: Li, X.-Y., Liu, Y., Liu, E. and Feng, Shen and Qi, Li and Shouli, Qu, 2003, The Leading Edge, Volume 22: 680-683

2. **Fracture detection using land 3D seismic from the Yellow-River delta, China**: Li, X.-Y., Liu, Y., Liu, E. and Feng, Shen and Qi, Li and Shouli, Qu, 2002, 72nd Ann. Internat. SEG Mtg., Expanded Abstracts.

3. **Fracture detection using land 3D seismic data from the Yellow-River Basin**: Liu, Y., Li, X.-Y., Liu, E. and Feng, Shen, 2001, Ann. EAP Sponsors Mtg., Research Report, Volume 8: 231-261.

4. **The effects of thin layers on azimuthal anisotropy**: Liu, Y., Ziolkowski, A., Li, X.-Y. and Liu, E., 2001, Ann. EAP Sponsors Mtg., Research Report, Volume 8: 193-230.

5. **Characterization of azimuthal anisotropy in the presence of thin layers using P-waves**: Liu, Y., Ziolkowski, A., Liu, E. and Li, X.-Y., 2001, 71st Ann. Internat. SEG Mtg., Expanded Abstracts.

6. **Effects of thin layers on the detection of azimuthal anisotropy using P-waves**: Liu, Y., Ziolkowski, A., Liu, E. and Li, X.-Y., 2001, 63rd Ann. EAGE Mtg., Expanded Abstracts.

7. **Can we extract fracture information from 3D marine streamer data?** Liu, Y., Li, X.-Y., 2000, 70th Ann. Internat. SEG Mtg., Expanded Abstracts.

8. **Fracture detection using 3D marine streamer data: a case study**: Liu, Y., Li, X.-Y., 2000, Ann. EAP Sponsors Mtg., Research Report, Volume 7: 245-288.

9. **Can we extract fracture information from 3D marine streamer data?** Li, X.-Y., Liu, Y. and Liu, E., 2000, Proceedings of 9IWSA.

10. **Fracture-related azimuthal variation in P-wave signatures from orthogonal streamer data**: Liu, Y., Li, X.-Y., MacBeth, C. and Anderton, P., 1999, Ann. EAP Sponsors Mtg., Research Report, Volume 6: 213-241.

11. **Analysis of azimuthal variation in P-wave signature from orthogonal streamer lines**: Liu, Y., Li, X.-Y., MacBeth, C. and Anderton, P., 1999, 69th Ann. Internat. SEG Mtg., Expanded Abstracts, 1959-1962

Mathematical convention and notations

All the mathematical variables and other abbreviations used in the thesis are explained here. They are arranged in the order of their appearance.

Abbreviations

Symbol	Meaning
3A	azimuthal attribute analysis
AAA	azimuthal attribute analysis
AMR	azimuthal moveout response
AVO	amplitude vary with offset
AVOA	amplitude vary with offset and azimuth
AVOZ	amplitude vary with offset and azimuth
AVAZ	amplitude versus azimuth
TVAZ	time versus azimuth
VVAZ	velocity versus azimuth
GVAZ	gradient versus azimuth
AVD	attribute vary with direction
CRP	common reflection point

CMP	common middle point
CDP	common depth point
C-wave	*P-SV* converted waves at the reflection point
DMO	dip moveout
EAP	Edinburgh Anisotropy Project
HTI	transverse isotropy with a horizontal axis of symmetry
NMO	normal moveout
OBC	ocean-bottom cable
P-wave	compressional wave
PP	reflected P-wave due to P-wave incident
PSV	reflected SV-wave due to P-wave incident
PSH	reflected SH-wave due to P-wave incident
QC	quality control
qP	quasi-P wave
qSV (qS1)	quasi-SV wave
qSH (qS2)	quasi-SH wave
RMS	root-mean-square
SVP	reflected P-wave due to SV-wave incident
SVSV	reflected SV-wave due to SV-wave incident
SVSH	reflected SH-wave due to SV-wave incident
SHP	reflected P-wave due to SH-wave incident
SHSV	reflected SV-wave due to SH-wave incident
SHSH	reflected SH-wave due to SH-wave incident
S-R	source-receiver
SL-RL	source line - receiver line

TIH	transverse isotropy with a horizontal axis of symmetry
TIV	transverse isotropy with a vertical axis of symmetry
VSP	vertical seismic profile
VTI	transverse isotropy with a vertical axis of symmetry

Mathematical symbols

Symbol	Meaning	Unit
λ	lamé parameter	Pa
μ	lamé parameter	Pa
P	pressure	Pa
K	bulk modulus	Pa
σ_{ij}	stress tensor	Pa
ϵ_{ij}	strain tensor	Pa
C_{ij}	elastic constant	Pa
C_{ijkl}	elastic constant	Pa
ρ	density	kgm^{-3}
u_i	i'th displacement in i^{th}direction	
U_i	i'th displacement amplitude in i^{th}direction	
k_i	wave number	
ω	angular frequency	s^{-1}
x	coordinate in x direction	m
y	coordinate in y direction	m
z	coordinate in z direction	m
f	frequency	Hz
α_i	i'th component of unit vector in the direction of displacement	
L_{nk}	ray segment	
β_i	i'th component of unit vector in wave normal direction	
Γ	Kelvin-Christoffel matrix	
V	velocity	ms^{-1}
g_i	i'th group velocity	ms^{-1}
b	displacement-stress matrix	

Symbol	Meaning	Unit
τ	vertical component vector of stress tensor	
p_i	i'th slowness	sm^{-1}
R	reflection coefficient matrix	
T	transmission coefficient matrix	
$S(t)$	time series of seismic amplitude	
$R(t)$	time series of reflection coefficient	
Ω_R	ratio of reflection coefficient between two pairs of orthogonal lines	
Ω_S	ratio of seismic amplitude between two pairs of orthogonal lines	
V_p	P-wave velocity	ms^{-1}
V_{p0}	P-wave velocity in vertical direction	ms^{-1}
V_s	S-wave velocity	ms^{-1}
V_{s0}	S-wave velocity in vertical direction	ms^{-1}
$V_{s\|\|}$	shear wave velocity polarized parallel to the symmetry plane	ms^{-1}
V_{rms}	RMS velocity	ms^{-1}
V_{nmo}	NMO velocity	ms^{-1}
η	slowness	sm^{-1}
ε	Thomsen parameter $(C_{11}-C_{33})/2C_{33}$	
γ	Thomsen parameter $(C_{66}-C_{44})/2C_{44}$	
δ	Thomsen parameter $\frac{(C_{13}+C_{44})^2-(C_{33}-C_{44})^2}{2C_{33}(C_{33}-C_{44})}$	
ζ	the velocity ratio of V_P and V_S	
θ	incident angle	
θ_p	incident angle of P-wave	
θ_s	incident angle of S-wave	

Symbol	Meaning	Unit
t	travel time	s
t_0	two-way zero-offset travel time	s
$t_{\parallel}$	traveltime in the direction parallel to the fracture strike	s
$t_{\perp}$	traveltime in the direction perpendicular to the fracture strike	s
φ_0	the angle between line1 and line 2 in the four-line system	
ϕ (Φ)	azimuth of fracture strike	
I	AVO intercept	
G	AVO gradient	
$W(t)$	wavelet function	

Contents

Chapter 1

Introduction

1.1 Seismic exploration and fractures

Oil and gas reservoir traps can be classified into three types: stratigraphic, structural and a combination of both. In fractured reservoirs the interior fracture direction and fracture density are the two most important parameters. Field and laboratory observations have shown that fractured media are anisotropic to seismic waves (e.g. Crampin, 1977; Crampin et al., 1980; Crampin, 1984a). This fact must be taken into account during fractured reservoir characterization using seismic methods. Before we discuss further, we should first indicate the fundamental differences between wave propagation in isotropic and anisotropic structure. The are three body waves propagating in every direction in anisotropic media other than two like in isotropic media. They are a quasi-compressional wave, qP, and two quasi-shear waves, $qS1$ and $qS2$, with velocities which vary with direction, and with particle-motion which also varies with direction, but has fixed orthogonal polarizations for any particular direction of phase propagation (Crampin, Crampin, 1977). This feature of shear waves in anisotropic media is the so-called shear-wave splitting and is used in three ways when the anisotropic media is induced by fractured media. Their travel time

difference can be used to calculate the layer thickness. Their orthogonal directions of the particle-motion can be understood as the fracture normal and strike. The fractional difference of their velocities can be used to indicate the degree or strength of anisotropy.

One of the common forms of anisotropy is known as Transverse Isotropy with a Vertical axis of symmetry (Vertical Transverse Isotropy, VTI or TIV). Another common form of anisotropy is known as Transverse Isotropy with a Horizontal axis of symmetry (Horizontal Transverse Isotropy, HTI or TIH).

Geophysical results arise after application of a serial of processing steps such as filtering, deconvolution, amplitude recovery, velocity analysis, NMO, DMO, migration and so on. Some of the conventional processing steps such as NMO, velocity analysis, DMO and migration fit well with the basic assumption of an isotropic medium. Of course, if this basic assumption is violated, i.e. the medium is anisotropic, we have to be careful when we process seismic data.

Two main applications of anisotropy become apparent. On the one hand, anisotropy is used to correct the isotropic NMO or to develop anisotropic NMO, and thereby to increase the accuracy of the seismic processing. On the other hand, new applications have been developed in recent years whose results are impossible to obtain by conventional means. One of these new applications is the detection and estimation of fracture parameters that are below the seismic resolution of P- or S-wave in the characterisation of naturally fractured reservoirs.

Fractures play an important part in reservoir development and enhanced oil recovery. Shear-waves have been shown to be much more effective than P-waves in detecting fractures. Crampin and Booth (1985; 1987) suggested that the observation of shear-wave splitting in field data is a significant advance in the application of anisotropy to exploration. The use of shear-wave splitting to detect fractures has been gradually accepted as an exploration tool over the last fifteen years (e.g. Willis

et al., 1986; Winterstein and Meadows, 1991; MacBeth et al., 1992; Li and Crampin, 1993). Owing to the high cost of acquisition and processing of shear-wave seismic data, and the difficulties of obtaining S-wave data with reasonably good quality, P-waves have attracted a growing interest since the middle 1990s. Tsvankin(1995) and Alkhalifah (1996) showed that the anisotropic P-wave velocity can be used to locate anisotropic zones. Rüger (1996a) and Teng and Mavko (1996) suggested that seismic amplitude can be also used to inverse anisotropic parameters. Later on, Li (1997) presented another technology to use seismic travel time to detect azimuthal anisotropy.

Theoretical study and field data show that P-waves are also sensitive to fractures and, in particular, azimuthal P-wave AVO (Amplitude Versus Offset) analysis (Chen, 1995; Rüger, 1996b; Teng and Mavko, 1996; Krasovec et al., 1998; Li et al., 1996), azimuthal travel time or azimuthal moveout analysis (Schoenberg et al., 1991; Kendall et al., 1998; Li, 1997; Li, 1999), and velocity analysis (Sena, 1991; Sayers and Ebrom, 1997) can be used to extract fracture information. We refer to these techniques as P-wave AVD (attributes versus direction) analysis. In this thesis, I will focus on the use of the P-wave AVD techniques for evaluating fracture parameters.

1.2 Gaps in fracture estimation

The development and application of AVD technology for the estimation of azimuthal anisotropy has evolved through its three generations. The first generation is by using shear-wave splitting or converted waves. Historically, azimuthal anisotropy and fractures have been almost synonymous with shear waves, and anisotropy from fractures has oftern been inappropriately called shear wave anisotropy. This overemphasis is principally due to the noticeable feature of shear waves: shear-wave

splitting, which is greatest at vertical incidence, and hence the method is suited to near-offset VSP and posts-tack surface seismic. The method in this stage relied upon direct excitation and recording of shear waves in land multicomponent acquisitions. Many successful application examples of this approach have been published. For example, Mueller (1991) and Li (1998) have succeed in locating fracture swarms in the Austin Chalk, Texas by using 2-D lines, and guiding horizontal drilling into productive zone. Despite the many successes, multicomponent surveys are not shot on a routine basis. A full 9C 3-D acquisition is thought to be too costly. In addition, there are many processing and interpretation issues not yet fully resolved. Therefore, AVD technology evolved into its second generation by using the P-wave signature in conventional land data. This is due to a combination of theoretical development, culminating in a number of analytical approximations for practical use (Thomsen, 1986; Rüger, 1996a; Teng and Mavko, 1996; Li et al., 1996; Li, 1999; Tsvankin, 1995; Alkhalifah et al., 1996). The approach shifts the emphasis from acquisition effort onto additional processing, relying upon the detection of amplitude and moveout variations in individual pre-stack gathers. The evolution of field practice for this generation method started with a discussion of using onshore 3D data from the Paris Basin (Lefeuvre, 1994) and followed by many successful examples in using different seismic attributes (Corrigan et al., 1997; Pérez et al., 1999; Lynn and Beckham, 1998). From a land acquisition prospective, this new technique heralds an era of less inexpensive acquisition for fracture detection using traditional P-wave seismic. In regard to the data quality, the seismic data in offshore environment are quite suited to the approach developed in the previous two stages because the large available volumes covering most of the North Sea and the Gulf of Mexico have good signal-to-noise ratio compared to land data. Thus the AVD technique opens a whole area of interest and potential application. For the offshore environment, there are a number of different seismic data acquisition systems such as vertical

cable data, seabed data, VSP data and streamer data. Here I will focus on the application of P-wave AVD technique to marine streamer 3D P-wave data. The early streamer 3D data normally have about 2 to 8 streamers which is oftern very limited in azimuth coverage and are not suited to AVD technique application that requires good azimuth coverage. To overcome this problem, datasets of different vantages are required.

In recent years, various technologies have been developed in the use of P-waves AVD for studying azimuthal anisotropy and a lot of them have been commonly used in the industry. However, all of these studies assumes either an azimuthally isotropic overburden, or a depth-invariant principal direction of azimuthal anisotropy. But practically, it has been found that depth dependence of the principal direction of azimuthal anisotropy is common in the Earth's crust (Crampin 1985), and a layer-stripping process is thus necessary to obtain the interval measurements of azimuthal anisotropy. The first generation of layer-stripping is performed for shear-wave data analysis, for which various processing techniques have been developed (Winterstein and Meadows 1991, MacBeth et al. 1992, Thomsen and Tsvankin 1995, and Dai and Li 1998). The second generation of layer-stripping is for P-wave AVD application, it started by Grechka and Tsvankin (1998b) who extend the NMO approach of Tsvankin (1995) to vertically inhomogeneous anisotropic media. In practice, the NMO approach requires careful data processing to minimise the error propagation and magnification through various processing steps (Al-Dajani and Alkhalifah, 1997), and this limits the application of the technique to some extent. In this thesis, I have presented an alternative approach based on the P-wave azimuthal moveout response to achieve layer stripping of azimuthal anisotropy.

In the above, I have referenced to many authors who have developed numerous P-wave AVD technologies by using different seismic attributes, such as amplitude, NMO velocity, AVO gradient and travel time, on different field data. In regarding

to fracture detection, I realize that different attribute has its own features. For example, amplitude is sensitive to noise and wavelet variations and is very expensive to recovery the true amplitude. Travel time can be directly picked up from traces with much less cost in processing. NMO velocity can be derived from travel time. In regarding to estimating azimuthal anisotropy, a simple question is for which case which seismic attribute may be more suitable than others, or what are the advantages and disadvantages for these attributes. Thus I felt that there is a gap in the integration of these attributes for application. In this thesis, to reveal the merits of these attributes for fracture detection, I present a case study on a full-azimuth and full-offset field data by applying a range of different seismic attributes.

1.3 Aims of this thesis

At the start of my PhD research in 1998, the use of P-wave AVD for fracture detection became increasingly popular in land seismic exploration. However, the application of P-wave AVD analysis to marine 3D streamer data was still a problem owing to the lack of good azimuthal coverage. Marine 3D streamer data are usually recorded in a different way from land 3D data, with shot and receiver lines parallel to each other, giving rise to narrow azimuthal coverage. This limits the application of P-wave AVD analysis for fracture detection in the marine environment in which it is frequent to see that more than one survey were shot. Can we use those surveys of different vintages shot in different directions to compensate for this lack of azimuthal coverage? What can we obtain from such datasets and how reliable will the results be? These are important issues that need to be addressed.

One of the primary aims is to address the above issues and thereby extend the P-wave AVD technology to the marine environment. In order to achieve this, I have developed specific techniques to handle repeated surveys and have carried out a

series of case studies to understand the merits and limitations of these techniques.

Furthermore, assuming an ideal 3D dataset with full azimuthal and offset coverage, a range of different attributes and different processing methods may be used for estimating fracture information. Two important questions are: (a) Which processing methods and attributes give the most reliable fracture information? (b) How should the processing scheme and attribute selection be approached for such a reliable estimation? I address these questions by using a 3D dataset with good azimuthal and offset coverages.

Finally, most existing processing techniques assume an isotropic overburden and a sufficiently thick fractured reservoir. However thin layering and anisotropic overburden cause problems in fracture detection. How can one achieve a reliable fracture prediction in these conditions? In order to answer this question, it is necessary to understand the seismic responses in fractured media, and develop processing techniques and analysis procedures to extract fracture orientation and density.

To summarise, my goals are to (1) extend the P-wave AVD technology to the marine environment, (2) develop practical algorithms, using different seismic attributes, for estimating fracture parameters reliably from P-wave seismic data. Theoretically, the fracture information estimated using different attributes should be the same for a single seismic data volume. In practice, the estimated fracture parameters are often different. Therefore an integrated interpretation of the predicted results may provide a more reliable understanding about the subsurface fracturing. Above all, we must bear in mind that whatever method is employed for fracture estimation, improving the reliability of predicted information is always critical to its applications.

1.4 Outline of the thesis

This thesis is divided into nine chapters. Following this introductory chapter, the basic anisotropic theories and methods for fracture detection using azimuthal anisotropy are discussed in Chapters 2 and 3. Chapters 4 and 5 treat the effects of overburden and thin-layering, respectively. Chapters 6, 7 and 8 present three case studies using 2D crossed lines, joint 2D and 3D repeated surveys, and a wide azimuthal 3D survey, respectively. Chapter 9 summarizes the results and findings. A more detailed description of each chapter is presented below.

Chapter 2 reviews the theory of anisotropy, and the link between azimuthal anisotropy and fractures. Synthetic seismic data are generated in media with respectively, strong anisotropy, weak anisotropy and isotropy, to demonstrate the reasons why fracture-induced anisotropy may be estimated from seismic records. An error analysis shows that the analytic approximate equations are accurate only in the case of weak anisotropy.

My contributions to the methodology of fracture estimation using P-wave data are presented in Chapter 3. Equations for fracture orientation and intensity calculation using azimuthal AVO, AVO gradient, slowness and traveltime are given. I also propose a general formula which can be used to describe the azimuthal variation of four seismic attributes: amplitude, traveltime, AVO gradient and velocity. Based on this formula, I propose the use of orthogonal-line configurations for fracture detection through a cross-plotting procedure. Synthetic data examples are used to illustrate these ideas. The general application procedures are also demonstrated using noise-free and noisy synthetic data.

Chapter 4 details a layer-stripping procedure to determine interval measurements of fracture parameters in multi-layered media with vertically-varying strike directions. The procedure is based on the P-wave traveltime difference between

two orthogonal seismic survey lines. This difference is referred to as the P-wave azimuthal moveout response (AMR). In the case of a weakly fractured overburden (less than 3% azimuthal anisotropy) underlain by a heavily fractured target, layer stripping can be achieved through the alignment of the top-target event by performing NMO-correction separately for all survey lines. The interval AMR of the target layer may then be calculated from the residual moveout of the bottom-target event. In the general case, a ray tracing procedure, similar to that used in AVO analysis, is required to perform effective layer-stripping. Full-wave modelling is used to verify and illustrate these procedures.

Thin layering entails another common and difficult problem that is addressed and tackled in Chapter 5. I use modelling to study the effects of thin layers on the AVD response. After applying azimuthal AVO analysis to the synthetic seismograms, I find that fracture orientation and intensity can be estimated accurately if the thickness of the thin layers is larger than a quarter of the dominant wavelength. However, there are large discrepancies in the orientation and intensity estimates when the thickness is less than this limit. Subsequently I present a new procedure to compensate for the effects of thin layering.

The applications of the methods proposed in Chapter 3 to real data are documented in Chapters 6 and 7. In Chapter 6, I present the case study of fracture detection using offshore 2D orthogonal lines. The dataset comprises four 2D lines forming two orthogonal pairs which intersect each other at a well location. Four azimuthal observations with near and far offset information are contained in such a seismic dataset. Therefore it is possible to apply the azimuthal analysis techniques to obtain the subsurface fracture orientation and intensity. My analysis shows that the fracture orientation is consistent with the major fault system in the area. This configuration, however, only yields information at a single point, and no lateral information can be inferred.

In Chapter 7, I present a case study from the North Sea to demonstrate that fracture parameters can be estimated from by combining 2D and 3D marine streamer data. The data include a 3D survey shot ten years ago using a two-streamer boat. The approach requires careful data processing to match acquisition geometries, and phase and amplitude characteristics of the 2D and 3D surveys. Azimuthal AVO analysis is performed for each CMP point along the crossed line. Fracture orientations along the ten 2D lines are estimated and plotted on rose diagrams. In this way, the lateral variations in fracture orientations can be determined. This case study reveals a great potential for further application of P-wave AVD to modern 3D surveys with much wider azimuthal coverage.

In Chapter 8, I present a case study from China. This dataset has full azimuthal and offset coverage. I use it not only to demonstrate the application of the techniques described in Chapters 3, 4 and 5 for evaluating overburden anisotropy and estimating fracture information, but also to assess the merits and limitations of different attributes and processing techniques for fracture estimation. A major aspect of this study is the comparison of the different techniques on a common dataset. The aim is to develop a robust and reliable azimuthal attribute analysis technique for fracture detection. The results from this study have an important implication for the design and implementation of multi-azimuth, multi-offset data acquisition on land, and for marine surveys where multi-component ocean bottom cable surveys are carried out.

Finally in Chapter 9, I summarise the major conclusions of this thesis, and speculate on possible future work to further fracture characterisation using seismic data. Parts of the contents of Chapters 2, 3, 4, 5, 6, 7 and 8 were published in various international conferences or journal as listed in the Bibliography.

1.5 Datasets used in this thesis

Here I give an overview on the datasets used in this thesis.

1.5.1 Synthetic datasets

A total of more than 360 isotropic and anisotropic seismograms corresponding to a three-layer geological model were generated using ANRAY (Gajewski and Psencik, 1995) for the purposes of Chapter 2 and 3. A further 180 or more azimuthally anisotropic CMP gathers were generated using ANISEIS (Taylor, 1990), and correspond to the multi-layer geological models employed in Chapters 4 and 5.

1.5.2 Marine 2D and 3D datasets

A total of more than $1000km$ 2D lines and $250km^2$ 3D data from the Central North Sea were processed on the ProMAX system, which have been analysed in Chapters 6 and 7 for illustrating P-wave AVD technology in the marine environment. The data constitute three block 1, 2 and 3. Block 1 consists of four 2D lines, forming two orthogonal pairs, recorded in 1986, which are used in both Chapter 6 and Chapter 7. Block 2 consists of six 2D lines acquired in August 1989. Block 3 is composed of 90 swaths of marine 3D data collected in December 1989. Eighty-eight swath 3D datasets and all the ten 2D lines are used in Chapter 7.

1.5.3 Land 3D wide-azimuth dataset

$60km^2$ of land seismic 3D data from the second largest oilfield of China, ShengLi Oilfield, have been processed. The central super-binned $10km^2$ data have been used in Chapter 8 for evaluating the different seismic attributes for fracture estimation and improving accuracy and reliability of the predicted results. The data were shot

in mid-2000 using a wide azimuthal acquisition system that has 10 parallel receiver lines. The shot lines are perpendicular to the receiver lines.

Chapter 2

Seismic Responses In Fracture-induced Anisotropic Media

Abstract

This chapter reviews the theory of azimuthal anisotropy and the link between azimuthal anisotropy and fractures. Synthetic seismic responses are generated in media with strong VTI anisotropy, HTI anisotropy, and isotropy, respectively, to demonstrate, qualitatively, why fracture-induced anisotropy may be estimated from seismic records. Error analysis shows that the analytical approximate equations are accurate in the case of weak anisotropy for fracture detection.

2.1 Basic anisotropy theory

The widely used method of seismic exploration is based upon the theory of acoustic and elastic waves propagation. We usually make the following assumptions (Helbig, 1998):

- the medium is isotropic

- the medium is homogeneous, and
- stresses are linearly related to strains

Real media usually violate at least some, and often all of these assumptions. A valid theoretical description of wave propagation in real media thus depends on the qualitative and quantitative description of the relevant anisotropy inhomogeneity, and non-linearity: one either has to assume that the deviation from the assumption can be neglected for the problem in hand, or develop a theoretical description that is valid under the deviation. While the effect of a single deviation from the ideal state is rather well understood, difficulties arise with the combination of several such deviations. Attempts to treat and understand such departures lead to the development of anisotropy theory whose basic concepts are reviewed in this section.

2.1.1 Definitions

What is anisotropy? I restate one of the definitions of anisotropy and homogeneity, following Helbig, (1994). Imagine that the following measurement of a material property (e.g., thermal conductivity) is carried out in the following way: cut an elementary cube with a side length determined by the resolution attainable with the experiment, and measure the property of this cube. Repeat this measurement in different directions with differently located and differently oriented cubes. If the result of the measurement is invariant against any rotation of the cube, the medium is said to be isotropic. If the result of the measurement is the same for all the locations in a region of space, this region is said to be homogeneous. Conversely, if the measurement result varies with the rotation of the cube, the cube is said to be anisotropic. If the measurements change with locations, the medium is called inhomogeneous. Simply, anisotropy is the variation of properties with direction. Inhomogeneity is the variation of properties with location.

What causes anisotropy of wave propagation? Anisotropy can manifest itself in many different physical properties (e.g., magnetic fields); and be affected by the relative motion of the reference system of the observer with respect to the medium in which the wave is traveling. Anisotropy can be, of course, caused by the structure of the medium. Common cases of anisotropy observed in seismic data may include the following (Helbig, 1987):

- Fracturing: both horizontal and vertical fracturing;
- Fine layering;
- Tectonic grain;
- Formation of oriented cracks under tensile stress;
- Preferential opening or closing of compliant cracks and pores by unequal principal stresses;
- Flow in igneous rocks that produces orientation of elongated crystals;
- Stress

In summary, anisotropy is often caused by structural alignment on a scale smaller than the resolution of the seismic waves. Therefore, by observing anisotropy and tracing it back to its cause we have the possibility of gathering gross or statistical information at a scale finer than the insurmountable limit of resolution.

2.1.2 Seismic wave equations in anisotropic media

For an infinitesimal deformation of a general elastic body Hooke's law holds. The stress tensor σ_{ij}, strain tensor ϵ_{kl} and elastic modulus tensor C_{ijkl} satisfy the following equation:

$$\sigma_{ij} = C_{ijkl}\epsilon_{kl}, \quad i,j,k,l = 1,2,3 \tag{2.1}$$

C_{ijkl} is a 3x3x3x3 matrix. In general C has **81** components. However, both the stress and strain tensors are symmetric, i.e.,

$$C_{ijkl} = C_{jikl} = C_{ijlk} = C_{jilk} \tag{2.2}$$

This reduces the number of components number to **36**. We can use the following mapping rules:

$$\begin{array}{cccccccc} ij & = & ji = & 11 & 22 & 33 & 23 & 13 & 12 \\ & & & \downarrow & \downarrow & \downarrow & \downarrow & \downarrow & \downarrow \\ & & m & 1 & 2 & 3 & 4 & 5 & 6 \end{array}$$

to convert C_{ijkl} (equation 2.2) to C_{mn}:

$$C_{mn} = \begin{bmatrix} C_{11} & C_{12} & C_{13} & C_{14} & C_{15} & C_{16} \\ C_{21} & C_{22} & C_{23} & C_{24} & C_{25} & C_{26} \\ C_{31} & C_{32} & C_{33} & C_{34} & C_{35} & C_{36} \\ C_{41} & C_{42} & C_{43} & C_{44} & C_{45} & C46 \\ C_{51} & C_{52} & C_{53} & C_{54} & C_{55} & C_{56} \\ C_{61} & C_{62} & C_{63} & C_{64} & C_{65} & C_{66} \end{bmatrix} \tag{2.3}$$

Equation (2.1) is simplified as:

$$\begin{bmatrix} \sigma_{xx} \\ \sigma_{yy} \\ \sigma_{zz} \\ \sigma_{yz} \\ \sigma_{zx} \\ \sigma_{xy} \end{bmatrix} = \begin{bmatrix} C_{11} & C_{12} & C_{13} & C_{14} & C_{15} & C_{16} \\ C_{21} & C_{22} & C_{23} & C_{24} & C_{25} & C_{26} \\ C_{31} & C_{32} & C_{33} & C_{34} & C_{35} & C_{36} \\ C_{41} & C_{42} & C_{43} & C_{44} & C_{45} & C46 \\ C_{51} & C_{52} & C_{53} & C_{54} & C_{55} & C_{56} \\ C_{61} & C_{62} & C_{63} & C_{64} & C_{65} & C_{66} \end{bmatrix} \begin{bmatrix} \epsilon_{xx} \\ \epsilon_{yy} \\ \epsilon_{zz} \\ \epsilon_{yz} \\ \epsilon_{zx} \\ \epsilon_{xy} \end{bmatrix} \tag{2.4}$$

Furthermore, from strain energy considerations: $C_{ijkl} = C_{klij}$ which leads to:

$C_{12} = C_{21}$, $C_{13} = C_{31}$, $C_{14} = C_{41}$, $C_{15} = C_{51}$, $C_{16} = C_{61}$, $C_{23} = C_{32}$, $C_{24} = C_{42}$, $C_{25} = C_{52}$, $C_{26} = C_{62}$, $C_{34} = C_{43}$, $C_{35} = C_{53}$, $C_{36} = C_{63}$, $C_{45} = C_{54}$, $C_{46} = C_{64}$ and $C_{56} = C_{65}$.

Thus, if the coordinate system is selected so that the coordinate axes coincide with the principal axes of the elasticity tensor, then there should be at most **21** elastic parameters. That is, twenty-one is the largest number of elastic constants that one might need to describe an anisotropic material uniquely. In an arbitrary oriented coordinate system any non-isotropic medium may have **21** non-vanishing components of the stiffness tensor. Generally, in such a system, most of the **21** parameters are zero. Consider a homogeneous anisotropic medium with **21** elastic constants, we take the Z-axis positive downward. Recall the definition of the strain tensor

$$\epsilon_{ij} = \frac{1}{2}\left(\frac{\partial u_i}{\partial u_j} + \frac{\partial u_j}{\partial u_i}\right) = \frac{1}{2}\left(u_{i,j} + u_{j,i}\right). \tag{2.5}$$

From Newton's second law of mechanics, by using the summation convention the particle motion equation, without body force, can be written as:

$$\rho \partial_t^2 u_i = \sigma_{ij,j} \tag{2.6}$$

where u_i is the ith component of the displacement, and ρ is the density.

2.1.3 Seismic wave velocity in anisotropic media

For a plane harmonic wave with displacement amplitude u_i, wave vector k_j and angular frequency $\omega = 2\pi f$, $x_1 = x$, $x_2 = y$, $x_3 = z$, β_j is a unit vector in the direction of wave normal, i.e., n_j is collinear with the wave vector and the slowness vector ($k_j = n\beta_j$) we have

$$u_i = U_i e^{i(k_j x_j - \omega t)} = U_i e^{i\omega(n_j x_j - t)} \tag{2.7}$$

Let $U_i = U\alpha_i$ and $\omega = 2\pi v/\lambda$, where α_i is the unit vector in the direction of the displacement and λ is the wave length. After substitution of U_i, ω and n_j into equations (2.7) and (2.6), the following can be obtained

$$\rho v^2 \alpha_i = C_{ijkl} n_l n_j \alpha_k \ or \ \rho \alpha_i = C_{ijkl} s_i s_j \alpha_k \tag{2.8}$$

Rewrite as:

$$\begin{cases} \left(C_{ijkl} n_l n_j - \delta_{ik}\rho v^2\right) \alpha_k = 0 \\ \left(C_{ijkl} s_l s_j - \delta_{ik}\rho\right) \alpha_k = 0 \end{cases} \tag{2.9}$$

Using $\mathbf{l} = \{l_1, l_2, l_3\}$ to denote the polar propagating direction, $\alpha = \{\alpha_1, \alpha_2, \alpha_3\}^T$ to denote the particle motion direction of the plane-wave solutions and $\mathbf{k} = \{k_1, k_2, k_3\}$, as the wave vector, above equation 2.9 can be rewritten as:

$$\mathbf{DCD}^T\mathbf{v} = \rho\left(\frac{\omega}{k}\right)^2 \mathbf{v}, \ \mathbf{D} = \begin{bmatrix} l_1 & 0 & 0 & 0 & l_2 & l_3 \\ 0 & l_2 & 0 & l_3 & 0 & l_1 \\ 0 & 0 & l_3 & l_2 & l_1 & 0 \end{bmatrix} \tag{2.10}$$

Where $\mathbf{v}$ is the phase velocity vector. This is a homogeneous system of linear equations in α_k, i.e., in the unit vectors in the direction of polarization for a given direction of wave normal. α_k is also called the eigenvector. From this equation non-trivial solutions exist only if the determinant of the coefficients vanishes, i.e., if the rank of the Kelvin-Christoffel matrix is at most two, the condition can be compressed as (Helbig, 1994)

$$det\left(\Gamma_{ik} - \delta_{ik}\rho v^2\right) = det\left(\Gamma_{ik} - \delta_{ik}\rho\frac{1}{n^2}\right) = 0 \tag{2.11}$$

$$\begin{cases} \Gamma = DCD^T \\ \Gamma_{ik} = \Gamma_{ki} = C_{ijkl}\beta_l\beta_j \end{cases} \tag{2.12}$$

In this equation, v is phase velocity which is defined as the number of wavelengths per unit distance normal to the waveforms (i.e. the velocity with which plane-wave crests and toughs travel through a medium and is expressed as the ratio of frequency of vibration and the wave number). Equations (2.9), (2.11) and (2.12) are the Kelvin-Christoffel equations. There are three roots for the equations since the equations are of order three in ρv^2. Those roots are not only real but also positive if the medium is stable (this is the rather general condition). This means that the $+v,\ and\ -v$ also satisfy ρv^2 as well and also means that in each direction n_i of the wave normal there are at most three values of the square of the velocities for which the velocities in the opposite direction have the same magnitude. In some cases, two or three of the squares of the velocity coincide. Isotropic media are a special case in which there is a single ρv_p^2 and a doubly counting eigenvalue ρv_p^2 for every direction of propagation. The eigenvector corresponding to the single root (P-polarization) is parallel to the wave normal, and the eigenvectors belonging to the double root (S-polarization) are constrained to the plane perpendicular to the wave normal, i.e., parallel to the wave plane in which one is called SV-polarization and the other one is called SH-polarization.

By solving the Kelvin-Christoffel equations, all three squares of velocities in every direction can be obtained. Using these velocities, the so-called slowness surface, and the velocity surface in a 3D system can be calculated. The methods of getting the eigenvalues and eigenvectors for equations (2.9), (2.11) and (2.12) have been reported

by many authors (e.g. Fryer & Frazer 1987, and Gajewski, 1996). The equation is a sixth-order polynomial whose solution needs high degree precision. ANRAY (Gajewski and Psencik, 1995) is a ray tracing package used to solve these equations and is used in this thesis. With the above phase velocity, Kendall and Thomson (1989) presented the formula to calculate the group velocity defined as energy or ray velocity, which is the velocity with which the energy of a wave propagates:

$$g_i = \frac{C_{ijkl} n_l B_{jk}}{Bmm} \tag{2.13}$$

$$B_{ij} = \frac{1}{6} \varepsilon_{ikl} \varepsilon_{jmn} \left(\Gamma_{km} - \rho V^2 \delta_{km} \right) \left(\Gamma_{ln} - \rho V^2 \delta_{ln} \right)$$

Γ_{ik}, n_j, n_l have the same meaning as above. $g_j n_j = 1$. The traveltime can be calculated by ray tracing using the Snell and Fermat approaches, which are the two methods frequently used. The Snell approach relies directly on the phase velocity while the Fermat approach relies on the group velocity (Slawinski, 1996). In practice two tables are built to compute travel time. One is for the phase velocities of the three body waves for a range of incident angles in the sagittal plane at a small angle interval typically 1 or 2 degrees by using the exact equation. The other one contains the group velocities of the three body waves which correspond to the same direction as the phase velocity for the same element in the table.

2.1.4 Seismic amplitude in anisotropic media

There are fundamental differences between wave propagation in isotropic and anisotropic media (Crampin 1977, 1981). Seismic amplitude is one of the most useful attributes of seismic waves in reservoir exploration. The general procedure to obtain amplitude variation with angle is reviewed here. We assume a displacement-stress vector

b whose variables are continuous across any horizontal plane.

$$\mathbf{b} = \begin{pmatrix} u \\ \tau \end{pmatrix}$$

where: $\tau = \frac{-1}{i\omega}(\tau_{xz}, \tau_{yz}, \tau_{zz})^T$ represents the vertical components of the stress tensor, and one of the solutions $\mathbf{u} = \mathbf{U}e^{i\omega(p_x x + p_y y - t)}$ and $\tau = \mathbf{T}e^{i\omega(p_x x + p_y y - t)}$, where $\mathbf{U}$ and $\mathbf{T}$ are the new coefficients of displacement-stress vector. $\mathbf{U} = (U_x, U_y, U_z)^T$, $\mathbf{T} = (T_x, T_y, T_z)^T$, p_x, p_y are horizontal phase slowness and ω is the angular frequency. Mandal and Toksoz (1990) gave the following equations:

$$\begin{cases} \partial_z \mathbf{b}(z) = i\omega \mathbf{A}(z)\mathbf{b}(z) \\ \mathbf{A}(z) = \begin{pmatrix} O & P \\ Q & O^T \end{pmatrix} \\ b(z) = e^{i\omega A(z)(z-z_0)} b(z_0) = P(z, z_0) b(z_0) \\ P(z, z_0) = e^{i\omega \mathbf{A}(z)(z-z_0)} \\ P(z_0, z_0) = I \\ \mathbf{D}^{-1}\mathbf{A}\mathbf{D} = \mathbf{\Lambda} \\ P(z, z_0) = \mathbf{D}e^{i\omega(z-z_0)\Lambda}\mathbf{D}^{-1} \\ \partial_z P(z, z_0) = i\omega A(z) P(z, z_0) \end{cases} \tag{2.14}$$

In equations (2.14), **A** is a 6x6 matrix and is related to the 21 elastic stiffnesses c_{ijkl} ($c_{ijkl} = \frac{C_{ijkl}}{\rho}$, ρ is the density) and the horizontal phase slownesses p_x, p_y and angular frequency ω. **O**, **P** and **Q** are 3X3 submatrices, and **P** and **Q** are symmetric. Λ and **D** are the diagonal matrix of eigenvalues and the eigenvector matrix of matrix $\mathbf{A}(z)$. $P(z, z_0)$ is the propagator of the wavefield in this layer. With these equations, if the 21 elastic stiffnesses, and the wavefield at the depth z_0 are given, the wavefield at any angular and horizontal phase slowness can be calculated step by step even though it is not in the same layer. Firstly, calculate $\mathbf{A}(z)$, then calculate Λ and **D**

which are respectively the diagonal matrix of eigenvalues and the eigenvector matrix of matrix $\mathbf{A}(z)$. Finally we can obtain $p(z)$ and $b(z)$. If we sum all the wavefields at different angular and horizontal slownesses, the complete wavefield in stratified anisotropic media can be calculated.

If the model is composed of a series of uniform anisotropic layers with a free surface z=0 and a half-space at $z > z_L$ (Figure 2.1), how can we compute the reflection and transmission response? From equation (2.14), the relation between the stress-displacement vector at depth 0 and z_L is:

$$b(z_L) = D(z_L+)W(z_L+,0+)D^{-1}(0+)b(0)$$

where

$$D^{-1}(z_L+)b(z_L) = D^{-1}(z_L+)D(z_L+)W(z_L+,0+)D^{-1}(0+)b(0)$$

If:

$$\begin{cases} V(z_L+) = D^{-1}(z_L+)b(z_L) \\ V(0+) = D^{-1}(0+)b(0) \end{cases}$$

we have:

$$V(z_L+) = W(z_L+,0+)V(0+)$$

$$\begin{aligned} V(z_L+) &= \begin{pmatrix} V_U(z_L) \\ V_D(z_L) \end{pmatrix} \\ &= W(z_L+,0+)V(0+) \\ &= \begin{pmatrix} W_{11} & W_{12} \\ W_{21} & W_{22} \end{pmatrix} \begin{pmatrix} V_U(0+) \\ V_D(0+) \end{pmatrix} \end{aligned}$$

In this equation, $W(z_L+,0+) = e^{i\omega(z_L-0)\Lambda}$ is the wave propagator and is portioned into 3x3 submatrices. If we apply the boundary conditions for the wave vector at the free surface (upgoing wave is equal to downgoing wave) and at the half-space (no-upgoing wave) we obtain, respectively

$$V_U(0+) = R_D V_D(0+),\ V_D(z_L+) = T_D V_D(0+)$$

Here, R_D and T_D are the downward reflection and transmission matrices.

$$R_D = \begin{pmatrix} r^D_{PP} & r^D_{P1} & r^D_{P2} \\ r^D_{1P} & r^D_{11} & r^D_{12} \\ r^D_{2P} & r^D_{21} & r^D_{22} \end{pmatrix},\ and\ T_D = \begin{pmatrix} t^D_{PP} & t^D_{P1} & t^D_{P2} \\ t^D_{1P} & t^D_{11} & t^D_{12} \\ t^D_{2P} & t^D_{21} & t^D_{22} \end{pmatrix}$$

where r^D_{ij} means the amplitude of the upgoing wave j generated by the downgoing wave i. i can be P, 1 and 2 which stands for the downgoing qP-wave, qS1 wave and qS2 wave, respectively. j can be P, 1 and 2 which stands for the reflected qP wave, qS1 wave and qS2 wave, respectively.

2.1.5 Classification of anisotropy: symmetries

If there are spatial symmetries in the velocity variation of the material, the general 21 independent parameters can be reduced.

Isotropy - spherical symmetry

In the case of spherical symmetry, or isotropy, the velocity is the same in all directions and there are only two independent elastic parameters, i.e. Lamé parameters λ and μ. μ is the so-called shear-wave modulus which together with the velocity

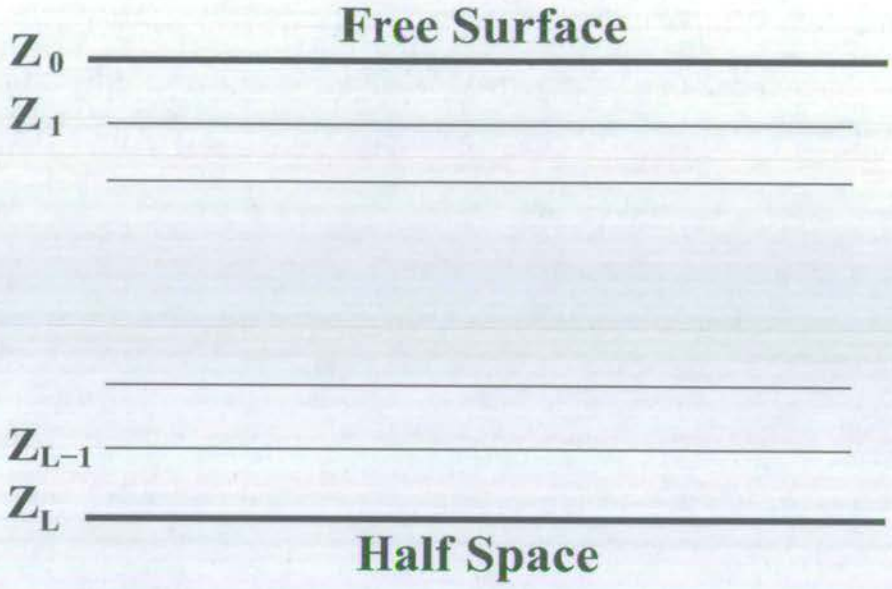

Figure 2.1: A stack of plane-parallel homogeneously anisotropic layers bounded at the bottom z_L by a homogeneous half-space, and at the top z_0 by a homogeneous layer.

controls the velocity of the shear wave. The elastic tensor C_{mn} is simplified to:

$$C_{mn} = \begin{bmatrix} a & \lambda & \lambda & & & \\ \lambda & a & \lambda & & & \\ \lambda & \lambda & a & & & \\ & & & \mu & & \\ & & & & \mu & \\ & & & & & \mu \end{bmatrix} \tag{2.15}$$

where $a = \lambda + 2\mu = K + \frac{4}{3}\mu = \rho V_p^2$. The bulk modulus K gives the fractional change in density due to a change in pressure: $K = \rho(\partial Pressure/\partial\rho)$. The shear modulus $\mu = \rho V_s^2$. V_p and V_s are the velocities of P-wave and S-wave, respectively, in the isotropic media.

Crystals - cubic symmetry class

The cubic matrix has the same form as the isotropic matrix except that all three nonzero elements are independent. The three independent stiffnesses a, b and c, which appear in the second-order stiffness matrix as shown below:

$$C_{mn} = \begin{bmatrix} a & b & b & & & \\ b & a & b & & & \\ b & b & a & & & \\ & & & c & & \\ & & & & c & \\ & & & & & c \end{bmatrix} \tag{2.16}$$

Crystals are optically isotropic, but elastically they are anisotropic (Helbig, 1994). There are no geophysical objects. So they are ignored in exploration industry.

Transverse isotropy - hexagonal symmetry class

Materials with hexagonal symmetry are transversely isotropic. In such media, every plane perpendicular to the axis of symmetry is a plane of symmetry, i.e., for a vertical axis of symmetry, velocities are identical in all the horizontal directions. Five independent stiffnesses, a, b, c, d and e, are required to define such a medium.

$$C_{mn} = \begin{bmatrix} a & b & c & & & \\ b & a & c & & & \\ c & c & d & & & \\ & & & e & & \\ & & & & e & \\ & & & & & \frac{(a-b)}{2} \end{bmatrix} \tag{2.17}$$

A transverse isotropic medium is the next simplest material of most concern in seismic exploration. Based on the direction of the symmetry plane, the TI medium is further classified as a TIV (with vertical symmetry) and TIH (with horizontal) media. Horizontal fracturing and horizontal fine-layering are typical of TIV media. Vertical fractures are typical TIH media. It was found that the polar anisotropy (TIV) can be big (~30%), while azimuthal anisotropy (TIH) is small ($< 10\%$). This thesis will focus on TIH because most of fractured reservoirs found so far are related to vertical fractures. I will discuss it further in the later sections and chapters.

Orthorhombic symmetry

For a system with orthorhombic symmetry, there are three mutually orthogonal planes of symmetry. Nine independent elastic constants are required to describe such a medium. The stiffness tensor is:

$$C_{mn} = \begin{bmatrix} a & b & c & & & \\ b & d & e & & & \\ c & e & f & & & \\ & & & g & & \\ & & & & h & \\ & & & & & i \end{bmatrix} \tag{2.18}$$

The followings are the typical examples of orthorhombic media given in the 2002 EAGE DISC course by Thomsen (?).

- A shale, or a thin-layering sequence, with a single set of vertical fractures in it,

- A shale, or a thin-layering sequence, with orthogonal sets of vertical fractures

in it,

- A massive isotropic sandstone with orthogonal sets of vertical fractures in it,

- An isotropic formation with a single set of vertical fractures in it.

Extreme asymmetry - triclinic symmetry

In such a system, there is no symmetry in the velocities except the trivial symmetry which is 180^o symmetry about a point - the origin. That means that the velocity in one direction is identical to that in the exact opposite direction. The maximum number of stiffness tensor constants, 21 is required to describe such a medium.

2.2 Transverse isotropy and Thomsen's parameters

There are two types of transverse isotropy: TIV and TIH. TIV is the transverse isotropy with a vertical symmetry axis. TIH is the transverse isotropy with a horizontal symmetry axis, also known as azimuthal anisotropy. Although 21 parameters are needed for the general anisotropic medium, only five elastic parameters are needed for the most common TIV and TIH anisotropic media.

2.2.1 Transverse isotropy: TIV

TIV anisotropy is sometimes referred to as polar anisotropy because the velocity varies with the polar angle. In TIV media, the elastic stiffness tensor (equation 2.17) becomes:

$$C_{mn} = \begin{bmatrix} c_{11} & (c_{11}-2c_{66}) & c_{13} & & & \\ c_{11}-2c_{66} & c_{11} & c_{13} & & & \\ c_{13} & c_{13} & c_{33} & & & \\ & & & c_{44} & & \\ & & & & c_{44} & \\ & & & & & c_{66} \end{bmatrix} \tag{2.19}$$

Using the Christoffel equations, the plane wave velocities have the following forms:

$$\begin{cases} V_p^2(\theta) = \frac{1}{2\rho}\left[C_{33}+C_{44}+(C_{11}-C_{33})\sin^2\theta + D\right] \\ V_{s\perp}^2(\theta) = \frac{1}{2\rho}\left[C_{33}+C_{44}+(C_{11}-C_{33})\sin^2\theta - D\right] \\ V_{s\parallel}^2(\theta) = \frac{1}{2\rho}\left[C_{44}\cos^2\theta + C_{66}\sin^2\theta\right] \\ \text{where} \\ D^2 = (C_{33}-C_{44})^2 + 4(C_{13}+C_{44})^2 - 2(C_{33}-C_{44})(C_{11}+C_{33}-2C_{44})\sin^2\theta] \\ +[(C_{11}+C_{33}-2C_{44})^2 - 4(C_{13}+C_{44})^2]\sin^4\theta, \end{cases} \tag{2.20}$$

where θ is the propagation angle of the plane wave: the angle between the symmetry axis and the propagation vector $\mathbf{k}$. Clearly the velocities are independent of azimuthal angle. The three velocities are $V_p(\theta)$, P-wave velocity along the propagation direction, and two S-waves. $V_{s\perp}(\theta)$ is the S-wave polarized with a component perpendicular to the symmetry planes, and is also known as the slow shear wave; in the special case of vertical polar anisotropy, this is called vertical polarization, and this S-wave is called SV. $V_{s\parallel}(\theta)$ is the shear wave velocity polarized parallel to the symmetry planes, which is also known as the fast shear wave; in the special case of vertical polar anisotropy, this is called horizontal (SH) polarization. Equation (2.20) is too complicated to yield much insight about the velocity dependence on elastic

stiffness or anisotropy.

2.2.2 Thomsen's parameters

For TIV, it is common to parameterise the media using Thomsen's five parameters, (Thomsen, 1986), which are defined as:

$$\begin{aligned} V_{p0} &= \sqrt{\frac{C_{33}}{\rho}} \\ V_{s0} &= \sqrt{\frac{C_{44}}{\rho}} \end{aligned} \qquad \begin{aligned} \varepsilon &= \frac{C_{11}-C_{33}}{2C_{33}} \\ \delta &= \frac{(C_{13}+C_{44})^2-(C_{33}-C_{44})^2}{2C_{33}(C_{33}-C_{44})} \\ \gamma &= \frac{C_{66}-C_{44}}{2C_{44}} \end{aligned} \tag{2.21}$$

In the above equations V_{p0} is the vertical P-wave velocity, V_{s0} is the vertical S-wave velocity. The velocities in equation (2.20) can now be compactly written, using Thomsen's parameters, as:

$$\begin{cases} V_p^2(\theta) = V_{p0}^2[1+\varepsilon\sin^2\theta + D'] \\ V_{s\perp}^2(\theta) = V_{s0}^2\left[1+\varepsilon\frac{V_{p0}^2}{V_{s0}^2}\sin^2\theta - \frac{V_{p0}^2}{V_{s0}^2}D'\right] \\ V_{s\parallel}^2(\theta) = V_{s0}^2\left[1+2\gamma\sin^2\theta\right] \\ \texttt{where} \\ D' = \frac{1-\frac{V_{s0}^2}{V_{p0}^2}}{2}[\{1+\frac{4(2\delta-\varepsilon)}{1-\frac{V_{s0}^2}{V_{p0}^2}}\cos^2\theta\sin^2\theta + \\ \frac{4\varepsilon(1-\frac{V_{s0}^2}{V_{p0}^2}+\varepsilon)}{(1-\frac{V_{s0}^2}{V_{p0}^2})^2}\sin^4\theta\}^{\frac{1}{2}} - 1]. \end{cases} \tag{2.22}$$

When the parameters ε, δ and γ are zero, the above equations reduce to the equations for isotropic media. These three parameters therefore define the strength of anisotropy. Weak anisotropy is defined when ε, δ and γ are much less than one. In this case, equation (2.22) can be approximately written, after a Taylor expansion,

as:

$$\begin{cases} V_p(\theta) = V_{p0}[1 + \varepsilon \sin^4\theta + \delta \sin^2\theta \cos^2\theta] \\ V_{s\|}(\theta) = V_{s0}\left[1 + \gamma \sin^2\theta\right] \\ V_{s\perp}(\theta) = V_{s0}\left[1 + \varepsilon \frac{V_{p0}^2}{V_{s0}^2}(\varepsilon - \delta) \sin^2\theta \cos^2\theta\right] \end{cases} \tag{2.23}$$

Consider two special cases: $\theta = 0^o$ and $\theta = 90^o$, the following equations can be derived easily:

$$\begin{cases} \varepsilon = \frac{V_{p90} - V_{p0}}{V_{p0}} \\ \gamma = \frac{V_{s\|90} - V_{s0}}{V_{s0}} \end{cases} \tag{2.24}$$

The formulae show us that in the case of weak anisotropy, the Thomsen parameter ε refers to the fractional difference in vertical and horizontal P-waves velocity and γ refers to the fractional difference between vertical and horizontal polarised shear velocities. In other words, epsilon (ε) captures the difference between horizontally and vertically traveling P-waves; gamma (γ) captures the SH anisotropy. Delta (δ) is a nonintuitive combination of elastic constants which controls the shape of the slowness surface at the intermediate angles. It directly affects AVO and logging responses. These parameters can be measured from seismic data (Thomsen, 2002).

2.2.3 Elliptical anisotropy

From equations (2.22), we notice that $V_{s\|}(\theta)$ is exactly an elliptical wavefront. Hence, γ is the ellipticity of the shear wavefront and the vertical shear velocity gives the short-axis of the ellipse. We also note that, when $(\varepsilon - \delta) = 0$, $V_p(0)$ in equation (2.23) is reduced to $V_p(0) = V_{p0}[1 + \varepsilon \sin^2\theta]$. Therefore, the P-wavefront is also an ellipse when $\varepsilon = \delta$. Thus we can understand why $(\varepsilon - \delta)$ controls the ellipticity of P-wave propagation.

2.2.4 TIH

TIH medium is defined in a similar way to TIV except that its symmetry is perpendicular to that of TIV. In TIH media the elastic stiffness matrix C'_{ijkl} (Li, 1997, 1998) could be expressed as:

$$C'_{ijkl} = \begin{bmatrix} c_{11} & c_{13} & c_{13} & & & \\ c_{13} & c_{33} & c_{33}-2c_{44} & & & \\ c_{13} & c_{33}-2c_{44} & c_{33} & & & \\ & & & c_{44} & & \\ & & & & c_{66} & \\ & & & & & c_{66} \end{bmatrix} \tag{2.25}$$

and the Thomsen's parameters are redefined as:

$$\varepsilon = \frac{C_{33}-C_{11}}{2C_{11}};\ \delta = \frac{2C_{66}+C_{13}-C_{11}}{C_{11}};\ \gamma = \frac{C_{44}-C_{66}}{2C_{66}}. \tag{2.26}$$

In above equations the definition of δ is a simplified version for weak anisotropy. Using these newly defined Thomsen's parameters, we can use equation (2.23) to calculate the three velocities in TIH media as well. In this case, θ is the azimuthal angle.

2.3 Link of fractures and seismic observation

Transversely isotropic media with a horizontal symmetry (TIH) and transversely isotropic media with a vertical symmetry (TIV) can be regarded as the equivalent media of two kinds of natural fractures: vertical and horizontal fractures. Fractured reservoirs behaves anisotropically to seismic waves propagating through them. By using the anisotropic variation of the seismic attributes, it may be possible to extract

reservoir properties that can not be obtained from seismic data processing assuming isotropic media.

2.3.1 Key aspects of fractures

Key aspects of fractures include fracture pattern, orientation, aperture, length or depth, spacing or density; and fracture infill (Doe et al., 1982; Lynn et al., 1996; Hudson and Knopoff, 1989; Liu et al., 2000, Liu and Li, 2000). Natural fractures control fluid flow in many subsurface hydrocarbon reservoirs. Fractures can also strongly influence groundwater flow in the shallow subsurface. For these reasons, techniques to extract fracture and fluid flow parameters, may have significant impact on hydrocarbon production, waste disposal and hydrology.

Economic production from fractured reservoirs requires the fractures to be oriented so that they are open and flowing under the present stress field. Fractures that are open today are most likely those that formed under similar stress orientations to the present, and will impact seismic anisotropy. If the *in situ* stress subsequently changes or rotates, fractures may close. Therefore, reservoir production would be poor or unsustainable. The seismic response of this unit may possibly show an isotropic signature. Therefore the observed seismic anisotropy may mean the existence of open fracturing.

In order to produce hydrocarbons economically from a naturally fractured reservoir, it is critical that a thorough investigation of fracture networks is made. Generally this investigation is performed in two stages. The first stage is an evaluation of the regional geology and geological history of target areas with particular emphasis on the structural history and current *in situ* stress including regional stress and local stress, because stress and tectonic history determine the overall nature and distribution of fractures. The second stage is to investigate the fracture properties

of a 3D area at the depth of interest. Analysis of earthquake focal plane mechanisms gives representations of strain but not directly of stress. Outcrop mapping, remote sensing imagery and airborne surveys may provide references about fracture patterns. However, it must be remembered that the information gathered in this way is mostly from the surface and not at depth where stress may be very different. Core analysis, borehole televiewer or formation logging and borehole stress evaluation from breakout logs may provide direct knowledge about the fracture properties at depth, but then lateral coverage is limited. Seismic reflection techniques based on isotropic wave propagation theory have been proved to be very powerful in the investigation of the infrastructure of underground but not very valuable in providing stress information of the 3D area.

2.3.2 Key aspects of anisotropy

The features or fabric causing anisotropy in sedimentary rock include typically a preferred alignment of anisotropic minerals such as clays, quartz, mica, etc., fractures or micro fractures, and stresses. Elastic anisotropy refers to variation of elastic properties (moduli, velocities) with direction.

Recently, techniques based on anisotropic theory of seismic wave propagation have been used to obtain *in situ* fracture properties at depth. Among these techniques, polar anisotropy and azimuthal anisotropy are the two basic concepts used by the industry for fractured reservoir characterization. The analysis of polar anisotropy using multi-component seismic data, e.g. ocean bottom cable (OBC) data, may provide us with information on the horizontal fine layering or fractures. The analysis of azimuthal anisotropy may give us information about the vertical fractures. The vertical fracture orientation and density can be estimated from an analysis of azimuthal anisotropy using either multi-component data or P-wave seis-

mic data.

The first literature regarding the link between theoretical phenomena of TIV or TIH media and cracks and fractures in the Earth's crust was presented by Crampin and Booth (1985). In this paper, by using three-component studies of microearthquakes near the North Anatolian fault in Turkey, the authors observed shear wave splitting. The leading split shear wave was polarized in a direction parallel or subparallel to the local or regional maximum horizontal principal stress that had been inferred from microearthquake fault plane solutions and related evidence. Subsequent multi-component observations of microseismic events in many different areas (Crampin, 1987), surface-to-surface seismic reflection surveys (Alford, 2000; Willis et al., 1986) and multi-component VSP seismic observations (Johnston, 1986; Becker and Perelberg, 1986) not only confirm this phenomenon but also confirm that crustal seismic anisotropy with a horizontal symmetry axis is widespread in many different geological and tectonic regimes. It is found that the fractures or microcrack structures can in principle readily respond to changes in regional or local stress and strain (Crampin et. al., 1984). A salient feature of fracture-related rock structure is the effective seismic anisotropy of aligned fractures and microcracks (Carnes, 1966; Crampin 1978, 1984b, 1984c; Leary et. al., 1990)

2.3.3 Equivalent medium theory for fracture

Equivalent medium theory is often used to represent a fractured medium in terms of elastic constants. This is an area that has attracted wide interest. Commonly used theories include Hudson (1981, 1990), Zhen (1995); Hudson et al. (1996), Liu et al. (2000) and Schoenberg (1994, 1998). Some of the key results are reviewed below.

The Hudson model (1981) is one of the widely accepted fracture models and is used in this thesis. We are aware that there is no hydraulic connection between

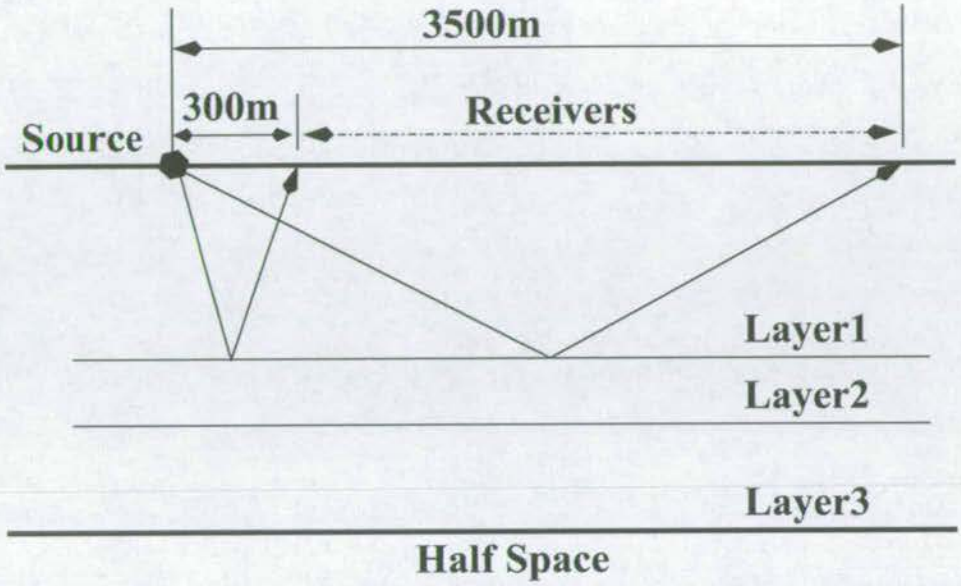

Figure 2.2: A three-layer model (2.1). Layer 1 is isotropic. Layer 2 is formed by vertically fracturing the isotropic medium, which is an azimuthally anisotropic layer. Layer 3 is a strongly anisotropic medium with triclinic symmetry.

cracks in Hudson's model as it therefore assumes zero matrix permeability. The model describes high frequency seismic response in respect of no fluid movement, and a wavelength much longer than the crack radius/spacing. Thomsen (1995) presented a fracture model, which is similar to Brown & Korringa (1975), that has finite matrix permeability but can only simulate the low frequency seismic response. Later on, a lot of excellent work has been done to improve these models (Schoenberg and Sayers, 1995; Sayers and Kachanov, 1995; Pointer et al., 2000). It is not clear, for any given case, whether Hudson or Thomsen is more appropriate. The two approaches will generally give the same fracture strike, but a different estimate of fracture density. The use of frequency dependent anisotropy can be used to discriminate between the Hudson and Thomsen models (Maultzsch et al., 2003).

On the other hand, for improving fractured reservoir characterization, fluid-filled permeable fracture models have developed in recent years (Hudson et al., 1996; Tod, 2001; van der Kolk et al., 2001; Chapman, 2003). Work on this topic is currently

progressing. The radii of fractures and pores may be potentially obtained through an analysis of frequency-dependent anisotropy (Chapman, 2003). The saturation class can also potentially be distinguished by using the frequency dependent anisotropy model (Chapman et al., 2003).

2.4 Seismic responses in fractured-induced media

2.4.1 Numerical modelling

I construct a three-layer synthetic model in which the first layer is composed of an isotropic medium (Table 2.1, Fig. 2.2), and the second and third layers are composed of anisotropic media. The difference between layer 2 and 3 is that the former is an azimuthally anisotropic medium and the latter is a kind of strongly anisotropic medium with triclinic symmetry. The source and receiver are distributed on the surface with an offset range of 300 - 3500m. ANRAY and ANISEIS are used for modelling.

Figure 2.3 shows the azimuthal variation of slowness of upgoing (upper three) and downgoing (lower three) qP, qSV and qSH waves in isotropic medium layer 1. The X-axis and Y-axis are defined by $\cos(\varphi)\sin(\theta)/v$ and $\sin(\varphi)\sin(\theta)/v$, where ϕ is the azimuthal angle and θ is the incidence angle. Figures 2.4 and 2.5 show the azimuthal variation of slowness in the azimuthally anisotropic medium layer 2 and strongly anisotropic medium layer 3, respectively.

Figure 2.6 shows the azimuthal variation of the amplitude at the interface between layer 1 and layer 2 (the interface of isotropic/anisotropic medium). The upper three diagrams are the reflection waves of qP, qSV and qSH for an incident qP. The middle three are the responses for an incident qSV. The lower three are the responses for an incident qSH. Note that the PP amplitudes show elliptical variations,

but PSH is linear and other wave types show more complex variations.

Figure 2.7 shows the azimuthal variation of the traveltime of PP, PSV and PSH reflection waves from the bottom of layer 2. To examine the azimuthal variation in more detail, I focus on the P-wave traveltime. Figure 2.8 is the azimuthal variation of the traveltime of P-wave at offsets of 1500m and 2000m from the bottom of layer 1 and layer 2. It can be seen that the P-wave traveltimes in layer 2 show clear azimuthal changes as compared with those in layer 1. Figure 2.9 is the traveltime variation of P-wave with orthogonal azimuths. There are four lines in this diagram. The lower two lines, marked with hexagons and triangles, are the travel times from the bottom of layer 1 in two directions: $\varphi = 0^o$ and $\varphi = 90^o$ which overlap. This means that the traveltime in layer 1 does not vary with azimuth. However, the upper two lines, marked with circles and diamonds, are the travel times from the bottom of layer 2 in two directions: $\varphi = 0^o$ and $\varphi = 90^o$ and they do not overlap. This confirms that the traveltime of P-wave passing through layer 2 does vary with the azimuth. The azimuthal traveltime variations of SV and SH waves are shown in Figures 2.10 and 2.11, 2.12 and 2.13, respectively.

To summarise, the P-wave attributes (traveltime, velocity, amplitude) show an elliptical variation with azimuth that is diagnostic of fractured media. The long and short axes of the ellipse correspond to the fracture strike and normal. In contrast, other wave types show more complex variation in attribute patterns and are difficult to interpret.

Layer 1: Isotropic	ρ=2.3 g/cm^3, V_p = 3048m/s, V_s = 1574m/s
Layer2: Anisotropic	ρ=2.19 g/cm^3, V_p = 2183m/s, V_s = 1502m/s Aspect ratio: 0.01, Crack density: 10%
Layer3: Anisotropic	ρ=2.0 g/(cm*cm*cm) $\begin{bmatrix} 10.0 & 3.5 & 2.5 & -5.0 & 0.1 & 0.9967 \\ & 8.0 & 1.5 & 0.29 & -0.90 & -0.15 \\ & & 6.0 & 1.0 & 0.42 & 1.5 \\ & & & 5.0 & 0.45 & -0.3532 \\ & & & & 3.0 & -1.0 \\ & & & & & 3.0 \end{bmatrix}$

Table 2.1: The elastic parameters of the model in figure 2.2.

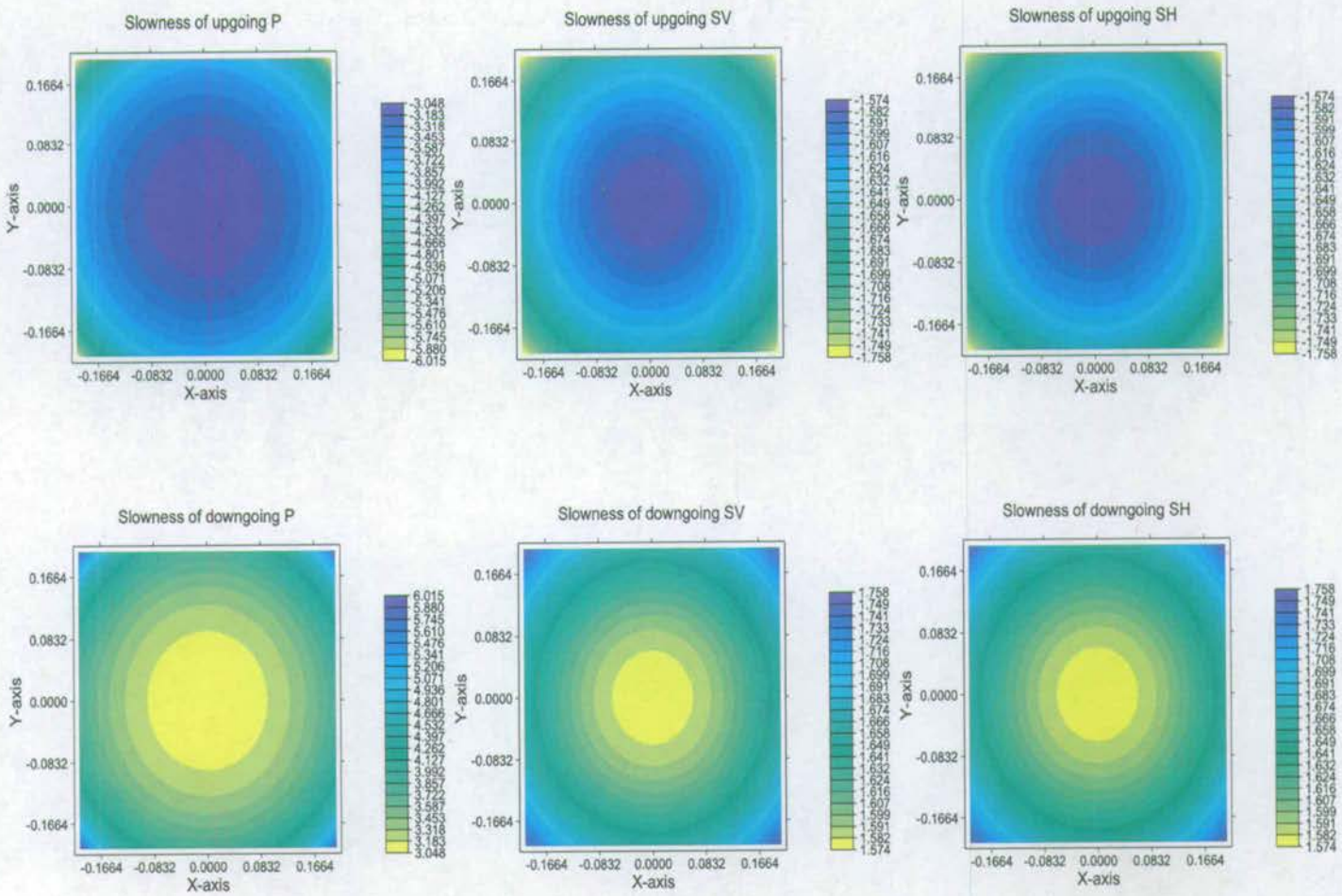

Figure 2.3: The azimuthal variation of slowness of upgoing (upper three) and downgoing (lower three) qP, qSV and qSH waves in isotropic medium layer 1.

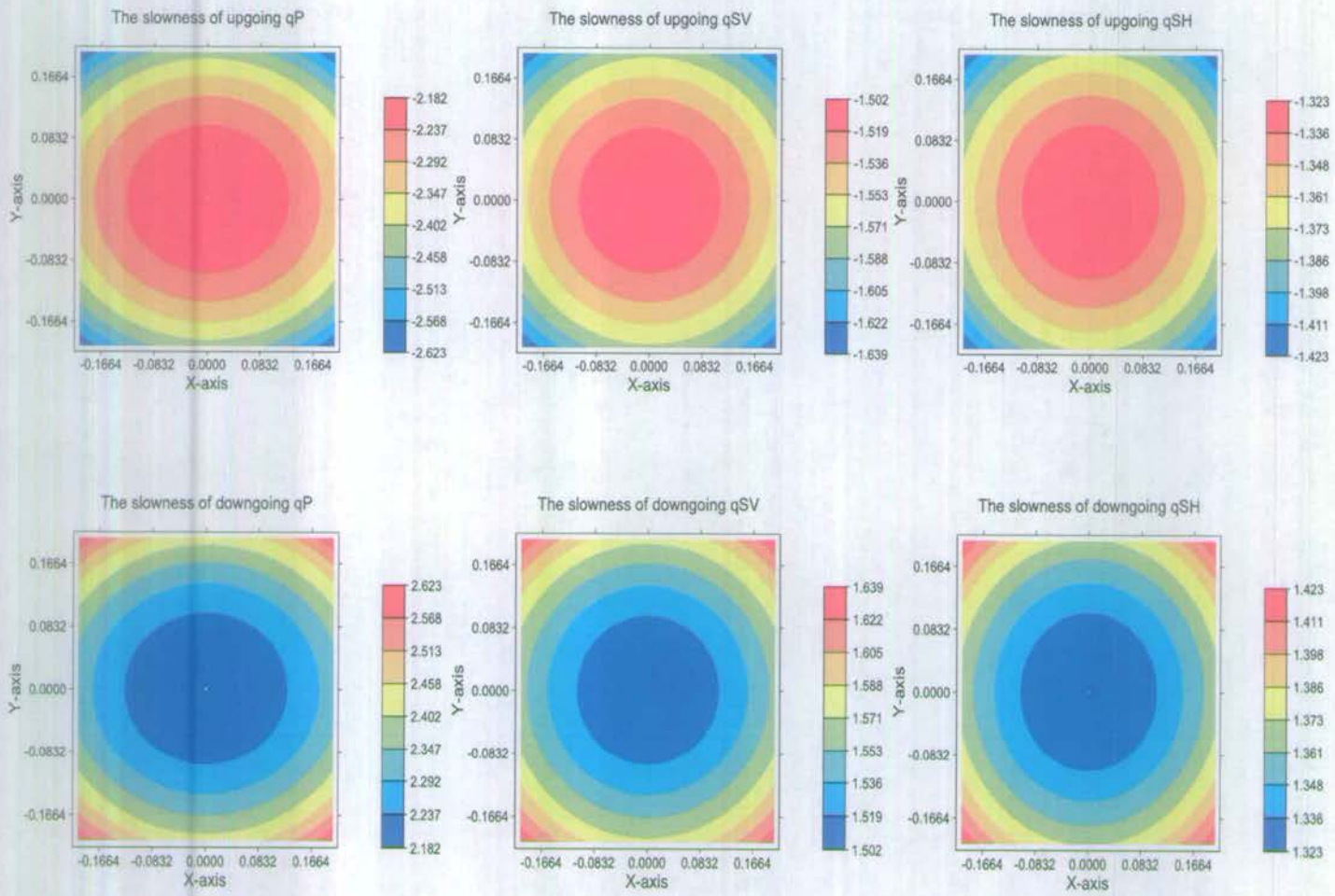

Figure 2.4: The azimuthal variation of slowness of upgoing (upper three) and downgoing (lower three) qP, qSV and qSH waves in vertically fractured medium, an azimuthally anisotropic layer 2.

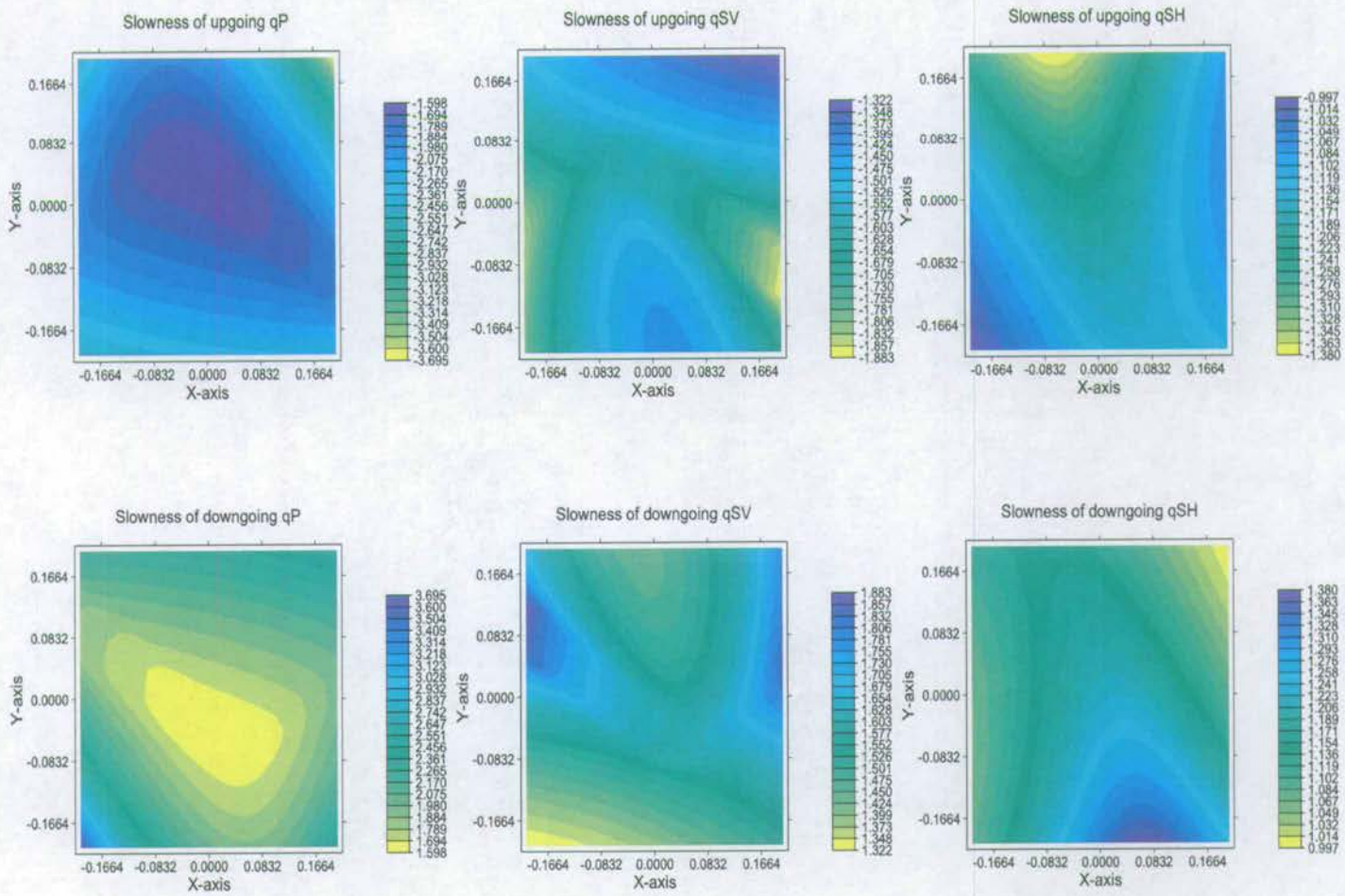

Figure 2.5: The azimuthal variation of slowness of upgoing (upper three) and downgoing (lower three) qP, qSV and qSH waves in strongly anisotropic medium layer 3.

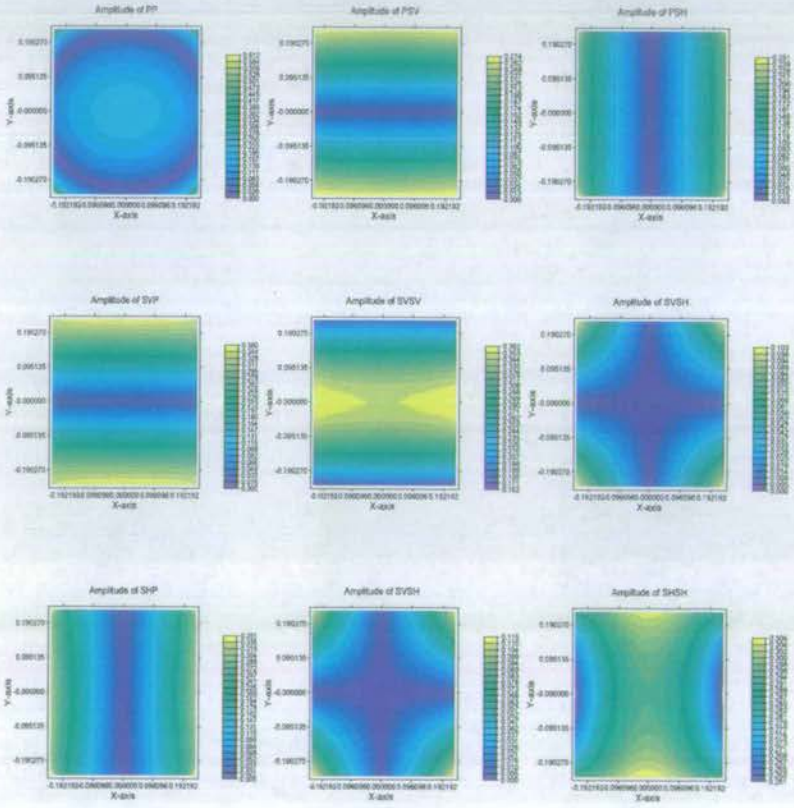

Figure 2.6: The azimuthal variation of amplitude at the interface of layer 1 and layer 2. The upper three diagrams are the responses of qP, qSV and qSH for an incident qP. The middle three are the responses of qP, qSV and qSH for an incident qSV. The lower three are the responses of qP, qSV and qSH for an incident qSH.

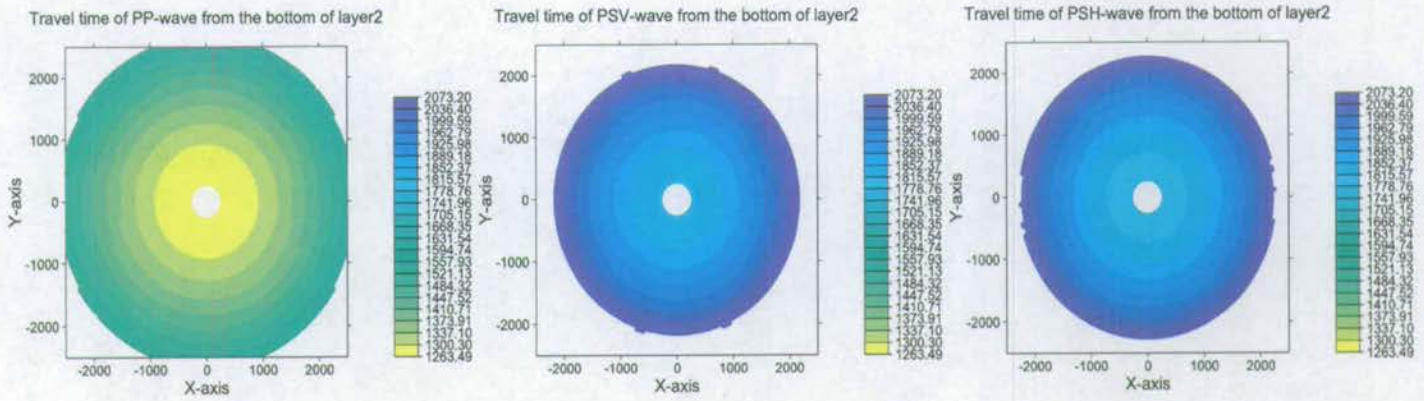

Figure 2.7: The azimuthal variation of traveltime of PP (left), PSV (middle) and PSH (right) waves from the bottom of layer2.

2.4.2 Analytical approximations

We can obtain accurate seismic responses in arbitrary anisotropic or isotropic media by numerical modelling. However, these numerical solutions for special cases offer little help in visualizing how the variation of a particular physical parameter affects the overall trend of seismic attributes. This gap may be filled by analytical approximations. A number of approximations are made to calculate analytically the seismic amplitude, velocity and traveltime in different situations. If the Thomsen's parameter δ is weak-to-moderate (<0.2), Sena (1991) presented an analytical formula for computing the phase and group velocities in TIH-azimuthal anisotropic media:

$$\begin{cases} V^{-2}(\theta) = a_0 + a_1 \sin^2\theta + a_2 \sin^4\theta \\ a)\ quasi-P\ case:\ a_0 = V_{p0}^{-2}(1-2\varepsilon) \\ a_1 = 2V_{p0}^{-2}(2\varepsilon-\delta)\cos^2(\varphi-\phi) \\ a_2 = 2V_{p0}^{-2}(\delta-\varepsilon)\cos^4(\varphi-\phi) \\ b)\ quasi-SV\ case:\ a_0 = V_{s0}^{-2} \\ a_1 = 2V_{s0}^{-2}\frac{V_{p0}^2}{V_{s0}^2}(\delta-\varepsilon)\cos^2(\varphi-\phi) \\ a_2 = 2V_{s0}^{-2}\frac{V_{p0}^2}{V_{s0}^2}(\delta-\varepsilon)\cos^4(\varphi-\phi) \\ c)\ quasi-SH\ case:\ a_0 = V_{S0}^{-2}(1-2\gamma) \\ a_1 = 2V_{s0}^{-2}\gamma\cos^2(\varphi-\phi) \\ a2 = 0 \end{cases} \tag{2.27}$$

where ε, γ and δ are the Thomsen's parameters, $V_{p0} = \sqrt{\frac{C_{33}}{\rho}}$, $V_{s0} = \sqrt{\frac{C_{44}}{\rho}}$ and φ *and* ϕ are the azimuthal angles of the survey line and the fracture strike direction, respectively. In multi-layered azimuthally anisotropic and isotropic media, the traveltime may also be computed by the following formula (Sena, 1991):

$$t^2 = C_1 + C_2X^2 + C_3X^4 + C_4X^6 + \ldots\ldots \tag{2.28}$$

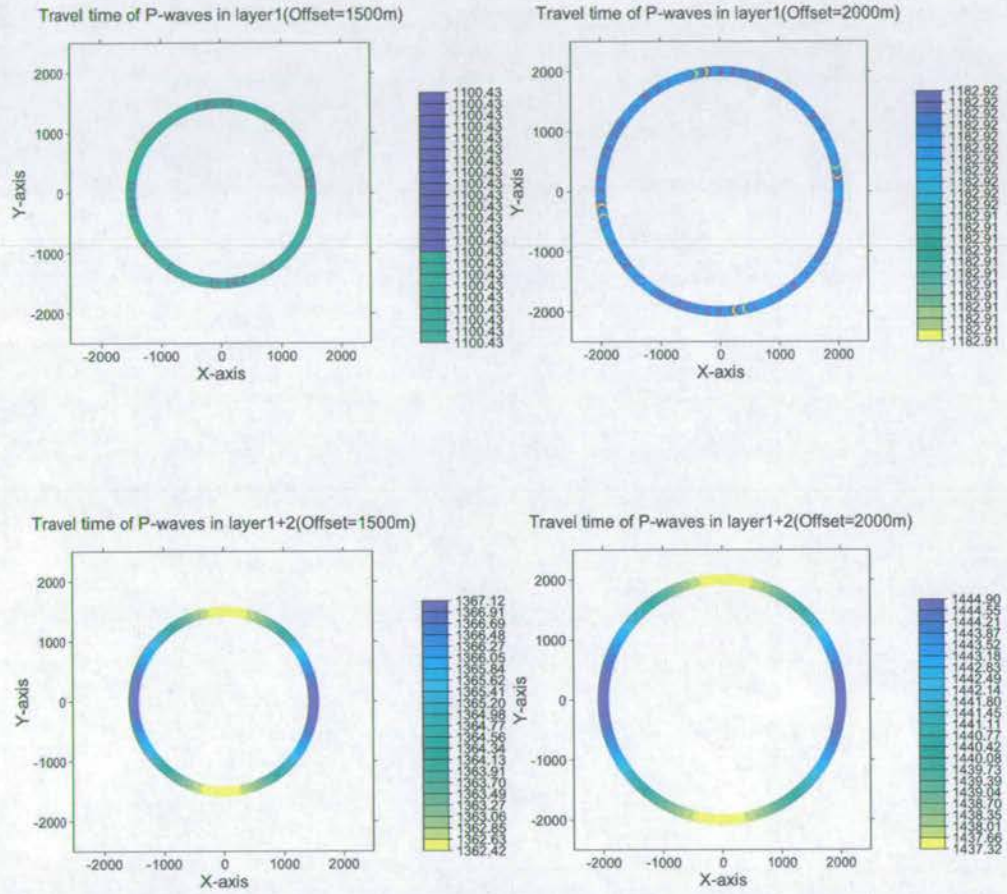

Figure 2.8: The azimuthal variation of traveltime of P-waves from the bottom of layer1 and layer2. The upper two are the the traveltime from the bottom of layer 1 at offsets of 1500m (left) and 2000m (right). The lower two are the traveltime from the bottom of layer 2 at offsets of 1500m (left) and 2000m (right).

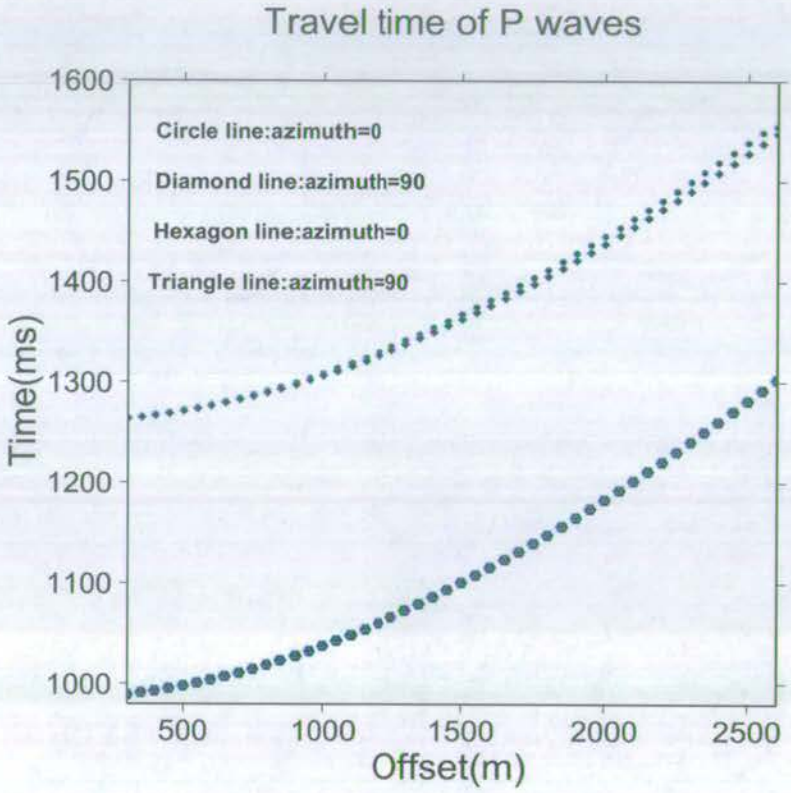

Figure 2.9: The traveltime of P-waves varies at orthogonal azimuths. The lower two curves, marked with hexagons and triangles, are the travel times from the bottom of layer 1 at two azimuthal directions: $\varphi = 0^o$ and $\varphi = 90^o$ which are overlapped. The upper two curves, marked with circles and diamonds, are the travel times from the bottom of layer 2 at $\varphi = 0^o$ and $\varphi = 90^o$.

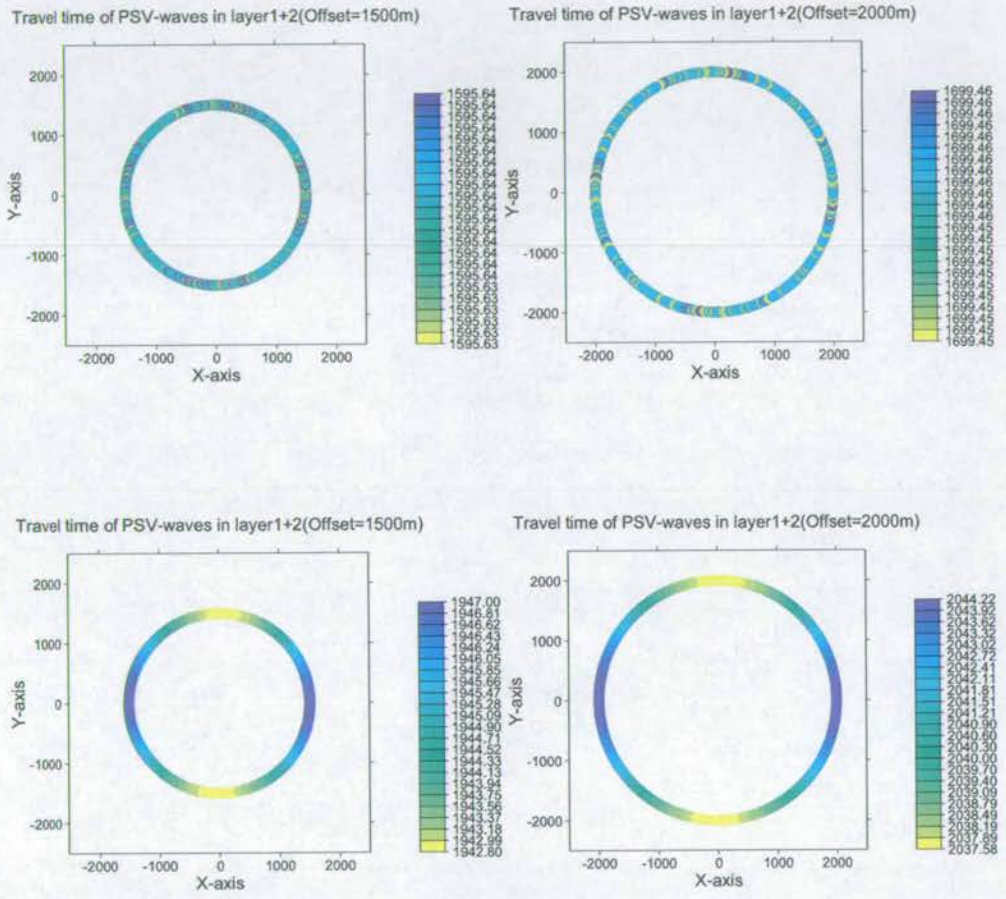

Figure 2.10: The azimuthal variation of traveltime of PSV-waves from the bottom of layer1 and layer2. The upper two are the the traveltime from the bottom of layer 1 at offsets of 1500m (left) and 2000m (right). The lower two are the traveltime from the bottom of layer 2 at offsets of 1500m (left) and 2000m (right).

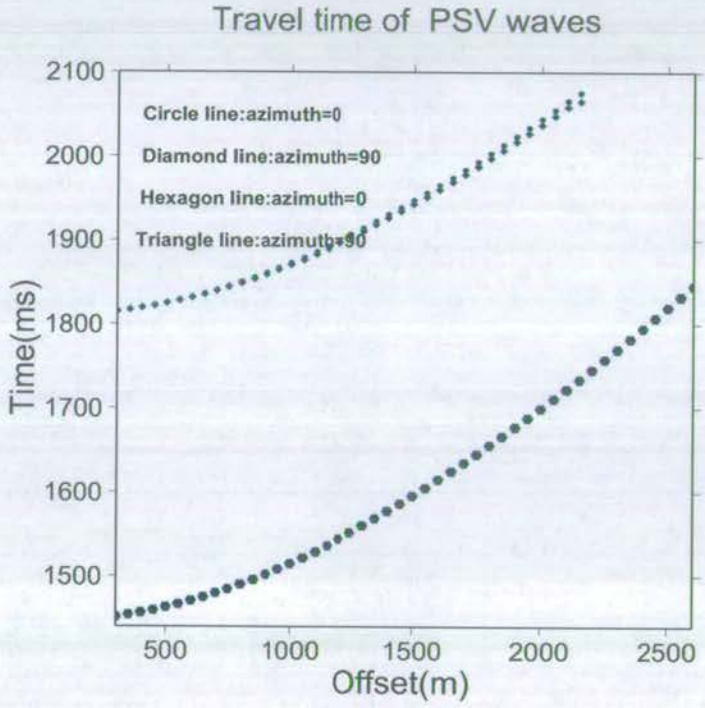

Figure 2.11: The traveltime of PSV-waves varies at orthogonal azimuths. The lower two curves, marked with hexagons and triangles, are the travel times from the bottom of layer 1 at two azimuthal directions: $\varphi = 0^o$ and $\varphi = 90^o$ which are overlapped. The upper two curves, marked with circles and diamonds, are the travel times from the bottom of layer 2 at $\varphi = 0^o$ and $\varphi = 90^o$.

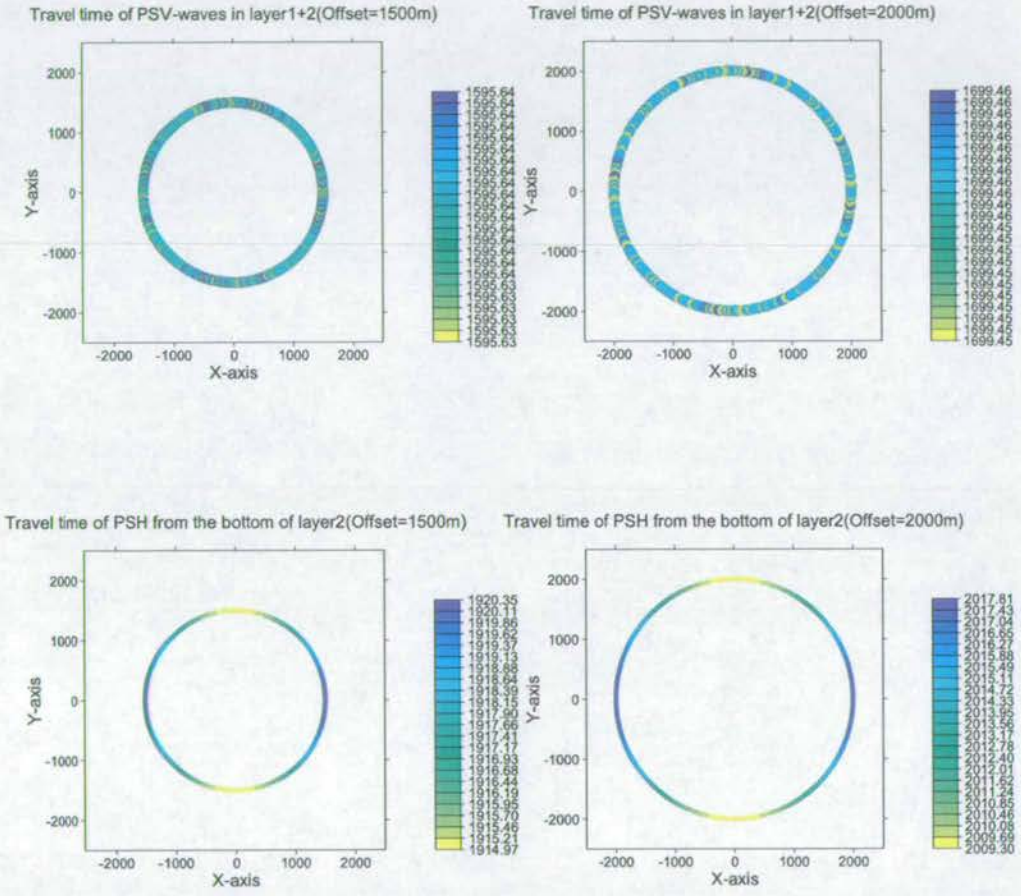

Figure 2.12: The azimuthal variation of traveltime of PSH-waves from the bottom of layer1 and layer2. The upper two are the the traveltime from the bottom of layer 1 at offsets of 1500m (left) and 2000m (right). The lower two are the traveltime from the bottom of layer 2 at offsets of 1500m (left) and 2000m (right).

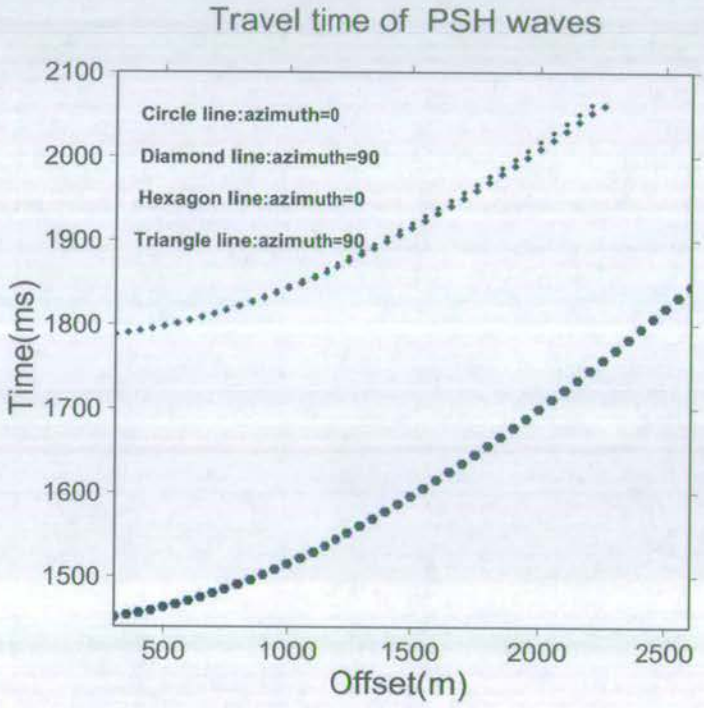

Figure 2.13: The traveltime of PSH-waves varies at orthogonal azimuths. The lower two curves, marked with hexagons and triangles, are the travel times from the bottom of layer 1 at two azimuthal directions: $\varphi = 0^o$ and $\varphi = 90^o$ which are overlapped. The upper two curves, marked with circles and diamonds, are the travel times from the bottom of layer 2 at $\varphi = 0^o$ and $\varphi = 90^o$.

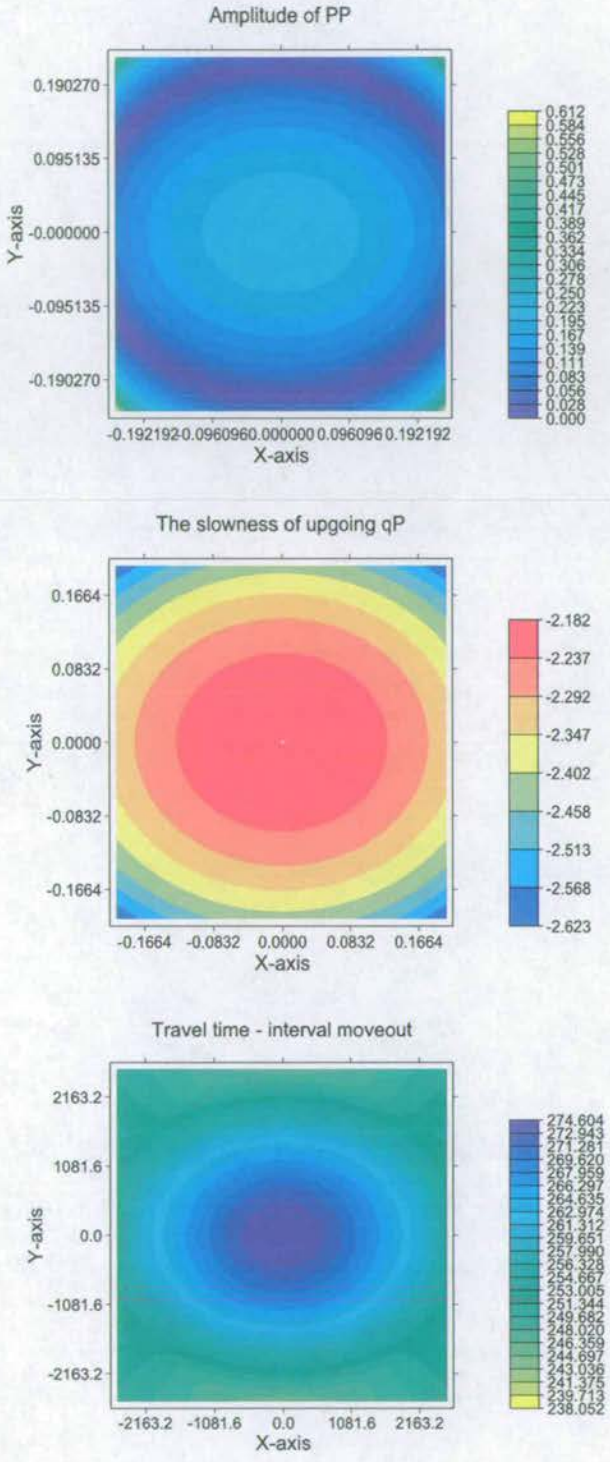

Figure 2.14: Approximate attributes. **Upper:** PP Amplitude at interface of layers 1 and 2. **Middle:** Slowness in layer 2; **Lower:** the interval time of layer 2.

where

$$\begin{cases} V_v^2 = \frac{1}{a_0},\ V_\gamma^2 = \frac{1}{a_0+a_1},\ V_h^2 = \frac{1}{a_0+a_1+a_2} \\ t_k = \frac{d_k}{V_{vk}},\ T_0 = 2\sum_{k=1}^{n} t_k,\ k = 1, 2, 3, ...n \text{ the layer number} \\ C_1 = (2\sum_{k=1}^{n} t_k)^2 \equiv T_0^2 \\ C_2 = \frac{\sum_{k=1}^{n} t_k}{\sum_{k=1}^{n} t_k V_{\gamma k}^2} \equiv \frac{1}{V_{rms}^2} \\ C_{31} = 0.5\sum_{k=1}^{n} t_k V_{\gamma k}^4 \left[4\frac{V_{\gamma k}^4}{V_{vk}^2}\left(\frac{1}{V_{hk}^2} - \frac{1}{V_{\gamma k}^2}\right) - 1\right] \\ C_{32} = 0.25 T_0 V_{rms}^4 \\ C_3 = \frac{1}{T_0^3 V_{\gamma rms}^8}\{C_{31} + C_{32}\} \end{cases} \tag{2.29}$$

V_v, V_γ *and* V_h for qP waves can be written as:

$$\begin{cases} V_v^2 = \frac{C_{33}}{\rho} \\ V_\gamma^2 = V_{p0}^2(1 + 2\varepsilon\sin^2(\varphi - \phi) - 2(\varepsilon - \delta)\cos^2(\varphi - \phi)) \\ V_h^2 = V_{p0}^2(1 + 2\sin^2(\varphi - \phi)(\varepsilon\sin^2(\varphi - \phi) + \delta\cos^2(\varphi - \phi))) \end{cases} \tag{2.30}$$

where θ is the normal direction of the wavefront. Equations (2.28) and (2.29) can be used to calculate the velocities and the traveltime for the model with mixed layers of isotropic and anisotropic media.

The reflection coefficients in the vertical plane perpendicular to the fracture strike can be calculated using the following formula (Li et al., 1996).

$$\begin{cases} r_{pp} = r_{pp0} + \left[\delta_2 - \delta_1 - 2\varepsilon_2 + 2\varepsilon_1 + \frac{8V_{s0}^2}{V_{p0}^2}(\gamma_2 - \gamma_1)\right]\sin^2\theta_P \\ r_{ps} = r_{ps0} + \frac{\sin\theta_P}{2\cos\theta_S}\left(\frac{V_{s0}^2}{V_{p0}^2 - V_{s0}^2}(\delta_2 - \delta_1 - 2\varepsilon_2 + 2\varepsilon_1)\right. \\ \quad + \frac{4V_{s0}^2}{V_{p0}^2}(\gamma_2 - \gamma_1)\cos\theta_p\cos\theta_s \\ \quad - \frac{V_{s0}V_{p0}}{V_{p0}^2 - V_{s0}^2}(\delta_2 - \delta_1 - 2\varepsilon_2 + 2\varepsilon_1)\cos\theta_p\cos\theta_s \\ \quad - \frac{4V_{s0}^2}{V_{p0}^2}(\gamma_2 - \gamma_1)\sin^2\theta_p + (\delta_2 - \delta_1 - 2\varepsilon_2 + 2\varepsilon_1)\sin^2\theta_p \\ \quad \left. - \frac{V_{p0}^2}{V_{p0}^2 - V_{s0}^2}(\delta_2 - \delta_1 - 2\varepsilon_2 + 2\varepsilon_1)\sin^2\theta_p\right) \end{cases} \tag{2.31}$$

Here, θ_p and θ_s are the incident angle for P- and S- wave, respectively. r_{pp0} and r_{ps0} are the amplitude. [When the upper and lower media are composed of the isotropic medium with parameters $V_{p0}(k)$, $V_{ps0}(k)$ and density(k), I can calculate the exact amplitude r_{pp0} and r_{ps0} using the formula given by Aki and Richards (1980)]. The amplitudes at any azimuthal direction can be calculated approximately by the following formula (Teng and Mavko, 1996):

$$\begin{aligned} R_{pp}(\varphi,\theta) &= \tfrac{1}{2}\left(\tfrac{\Delta\rho}{\rho} + \tfrac{\Delta V_p}{V_p}\right) \\ &\quad - \tfrac{2V_s^2}{V_p^2}\left(\tfrac{\Delta\rho}{\rho} + 2\tfrac{\Delta V_s}{V_s}\right)\sin^2\theta \\ &\quad + \tfrac{\Delta V_p}{2V_p}\tan^2\theta \\ &\quad + \left(\tfrac{\Delta\delta_x\cos^2\varphi}{2} + \tfrac{\Delta\delta_y\sin^2\varphi}{2} - 4\tfrac{V_s^2}{V_p^2}\Delta\gamma_{xy}\sin^2\varphi\right)\sin^2\theta \\ &\quad - \left(\tfrac{\Delta\delta_x - \Delta\varepsilon_x}{2}\cos^2\varphi\right. \\ &\quad \left. + \tfrac{\Delta\delta_y - \Delta\varepsilon_y}{2}\sin^2\varphi\right)\sin^2\theta\tan^2\theta \end{aligned} \tag{2.32}$$

where:

$$V_p = \sqrt{\tfrac{C_{33}}{\rho}}\ ;\ V_s = \sqrt{\tfrac{C_{55}}{\rho}};$$

$$\varepsilon_x = \tfrac{C_{11} - C_{33}}{2C_{33}};\ \varepsilon_y = \tfrac{C_{22} - C_{33}}{2C_{33}};$$

$$\delta_x = \frac{(C_{13}+C_{55})^2-(C_{33}-C_{55})^2}{2C_{33}(C_{33}-C_{55})};\ \delta_y = \frac{(C_{23}+C_{44})^2-(C_{33}-C_{44})^2}{2C_{33}(C_{33}-C_{44})};$$

$$\gamma_{xy} = \frac{C_{44}-C_{55}}{2C_{55}};$$

$$\Delta V_p = V_{p2} - V_{p1}\ ;\ \Delta\delta_x = \delta_{x2} - \delta_{x1};\ \Delta\delta_y = \delta_{y2} - \delta_{y1}$$

$$\Delta\gamma_{xy} = \gamma_{xy2} - \gamma_{xy1};\ \Delta\varepsilon_x = \varepsilon_{x2} - \varepsilon_{x1}$$

$$\Delta\varepsilon_y = \varepsilon_{y2} - \varepsilon_{y1}$$

representing the parameters of the two layers.

2.4.3 Accuracy of the approximation

To evaluate the accuracy of these approximate and analytical equations, Figure 2.14 compares the results with the exact results shown in Figures 2.3-2.5, 2.6, 2.7. The general trend of variations in Figure 2.14 agrees with those in Figures 2.3, 2.6 and 2.7.

An example of more detailed comparison for the traveltime equations is shown in Figure 2.15, where I compare the traveltime from the bottom of layer 2 at the azimuthal directions of 0° and 90°. The line with circular symbols is an exact result calculated using ANRAY and that with diamond symbols is calculated using the approximate equation (2.28) after Sena (1991). The two lines superimpose for each azimuth, indicating that the analytical traveltime equation is sufficiently accurate and can be used to develop processing methods to extract the fracture parameters from seismic data. Other detailed comparisons for amplitude and velocity show similar results.

2.5 Basic requirements for fracture detection

To apply the azimuthal anisotropy theory to real data, some general requirements can be derived from the above analysis. First, the diagnostic features for all three

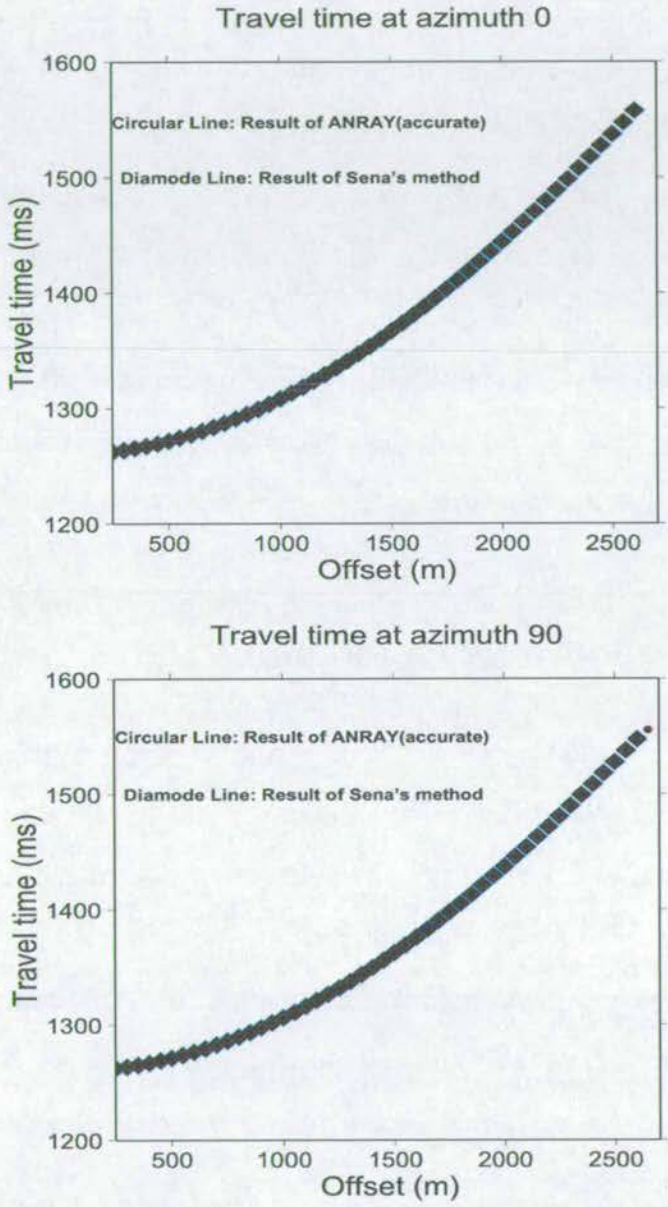

Figure 2.15: The comparison of the traveltime from the bottom of layer 2 at the directions of azimuthal 0° (upper) and 90° (lower) calculated using accurate and approximate methods, respectively.

attributes are associated with the azimuthal variation. Thus multiple azimuthal coverage is necessary. This may not be always possible, particularly in marine seismic surveys. Second, the azimuthal variation increases with offset. Thus it requires sufficiently large offsets to quantify the azimuthal variations. Third as shown in Figure 2.7, there is the requirement of a sufficiently thick layer to be able to identify the top and bottom reflections. In our synthetic model, the bottom and top of the target are sufficiently separated. In practice, we often require other information such as VSPs and well logs to build macro-model which enable us to correlate the horizons and to identify the top and bottom targets. Finally, the model used here consists only of horizontal layers, and this restricts applications to areas with only a gentle structural slope.

2.6 Discussion and conclusions

I have discussed the links between fractures and anisotropy. I have also reviewed the basic theory of seismic wave propagation in anisotropic media. A numerical and analytical analysis is carried out to understand and demonstrate the seismic response in fracture-induced anisotropic media.

The modelling confirms that for HTI the qP-waves show the characteristics of elliptical variations in the horizontal planes, with directions of long and short axes indicating the fracture strike and normal (the symmetry direction of the model). The analytical approximation provides good accuracy to describe the P-wave seismic response in weakly anisotropically fractured media. In general, the earth is weak anisotropy, so those can be applied to natural data.

In conclusion, media with aligned vertical fractures give rise to azimuthal anisotropy in seismic data, and the synthetic P-wave attributes show an approximately elliptical variation with azimuth. The direction of the axis indicates the fracture orientation,

and the ratio of the long-to-short axis is proportional to the fracture intensity or density. The seismic attribute (amplitude and travel time) variation with azimuth may therefore potentially be used to estimate fracture parameters (orientation, intensity and the spatial distribution). This requires multi-azimuthal coverage and large offsets and brings a whole set of issues related to data analysis, methodology and uncertainties. What can we really obtain from seismic data? What are the best practices? The rest of this thesis addresses these questions.

Chapter 3

The P-wave Azimuthal Attribute Analysis (3A)

Abstract

This chapter introduces my contributions to the methodology for fracture detection using P-wave seismic, which is called azimuthal attribute analysis, AAA or 3A for short. Equations using azimuthal amplitude versus offset (AVO), AVO gradient, slowness and traveltime are derived for fracture orientation and intensity calculations. I also find a universal generalization which can be used to describe the azimuthal variation of these four seismic attributes. The tests using synthetic data demonstrate that the 3A technique can be used to estimate fracture parameters. The general application procedures under different P-wave acquisition environments are discussed in this chapter and three case studies are presented in Chapters 6, 7 and 8.

3.1 Introduction

As shown in Chapter 2 by analyzing the attributes of the seismic data of P-, S- and PS converted waves from anisotropic modelling, one may estimate the azimuthally anisotropic model parameters. Applying a suitable equivalent medium theory, these estimated parameters may link to fracture properties and therefore help to characterise fractured reservoirs.

Generally speaking, there are four main kinds of seismic attributes: traveltime, velocity, amplitudes and AVO gradient. As far as traveltime is concerned, again three kinds of traveltimes are widely used in seismic exploration: first arrival traveltime, reflection traveltime and refraction traveltime. First arrival traveltimes are the key parameters for static correction, and velocity estimation using VSPs. Refraction traveltimes are also mainly used for the static estimation in complex surface environments, such as desert and mountain areas. Reflection traveltimes are generally used to map the subsurface geological structure, and also used together with the application of velocity models to map depth images. These traveltimes may show azimuthal variation in the presence of vertical fractures, as demonstrated in Chapter 2 (Booth and Crampin 1983, Sena 1991, Sayers and Ebrom 1997), and they can be used to compute the fracture orientation and intensity.

Velocity is another important attribute of seismic data. By building up the velocity model we can construct the geological structure of the subsurface. Analysis of velocities, derived from crosswell seismic data collected at the USGS Fractured Rock Research Site by Ellefsen et al. (1999), shows that the velocities are related to the hydraulic conductivities of the fractured bedrock and the low velocities (less than 5100 ft/s) are indicative of a wide range of conductivities. In contrast, high velocities (greater than or equal to 5100 ft/s) are indicative of low conductivities. Velocity can also be used to estimate the pore-pressure and fracture pressure that are

essential information for optimizing the mud weight which can prevent well blow-out as well as formation damage. The inversion of pore aspect ratio using velocity has also been reported (Ludwig et. al. 1998). It is well known that seismic velocities often mistie to the well control. One possible cause is velocity anisotropy. In TIH media, NMO velocity and slowness shows elliptical variation with azimuth (Corrigan et. al. 1997, Grechka et. al. 1997, 1998b).

Seismic depth imaging is limited to the interpretation of geological structures. Although a suitable geological structure that can act as a trap is a necessary condition for hydrocarbons in the subsurface, it is not a sufficient condition. For subsurface hydrocarbons to exist, reservoir rocks must be present for hydrocarbon formation and pooling which can be identified by analyzing the seismic response amplitudes. AVO analysis has enjoyed considerable success at distinguishing brine-filled reservoirs from gas and oil filled reservoirs. Research shows that many reservoir rocks are anisotropic (e.g. Crampin 1985) and azimuthal seismic variation may be an indication of the existence of vertical open fractures.

What is the effect of anisotropy on AVO? The AVO trend can change, or even be reversed, even when we are dealing with weak anisotropy (Floridia and Teles 1998). As we know that seismic anisotropy is the large-scale manifestation of ordered, small-scale heterogeneity, anisotropic AVO analysis using prestack seismic data may provide a potential tool to reveal the rock parameters involving lithologic discrimination that is impossible to obtain using isotropic AVO analysis. Vertical fractures may generate azimuthal AVO variation in the seismic data (Li and Mavko 1996, Lynn and Beckham 1998). Therefore, if we have full-azimuthal seismic data, we can theoretically use one or all of these attributes: traveltime, velocity, amplitude and AVO gradient, or even more, to determine the fracture orientation and intensity. Thus uncertainties may be reduced.

Based on the seismic lines or the azimuthal directions available, the technologies

of fracture detection using P-waves can be sorted out into three types: three-line method, four-line method and multi-line method. In each method different attributes can be used to characterize fractures. Therefore I may apply a group of methods to estimate fracture parameters from the same seismic data. I shall begin by presenting the four-line method where the lines form an orthogonal pattern, that simplifies the processing method. This is followed by the three-line and multi-line methods. In each method multifracture mappings are possible from the same seismic data using different attributes. In the following sections, I discuss respectively the estimation of fracture orientation and intensity using traveltimes, amplitude, or AVO gradient, and velocity.

3.2 Three assumptions for fracture estimation

Current techniques based on the analysis of P-wave azimuthal moveout, amplitude and velocity are derived from some basic assumptions. First, at any CMP locations, at least three azimuthal seismic records should be provided. Second, the top and bottom of the reservoirs should be distinguishable and, lastly, the underlying fractured reservoir is assumed to be overlain by an isotropic sedimentary overburden.

1 *Multi-azimuthal coverage (Figure 3.1a).* Multi-azimuthal coverage can be achieved by selecting repeated 2D lines from vintage surveys. It can also be achieved through multi-azimuthal recording (Figure 3.1b). The excited signal at the shot point is recorded at different azimuthal directions. The multi-azimuthal coverage is thus obtained by multi-source-receiver acquisition.

2 *Well logs (Figure 3.2).* The well logs are used to compute synthetic seismic records to help to distinguish the reflection events from the top and bottom interfaces of the target from other events. From several well-logs, the P-wave velocity, S-wave

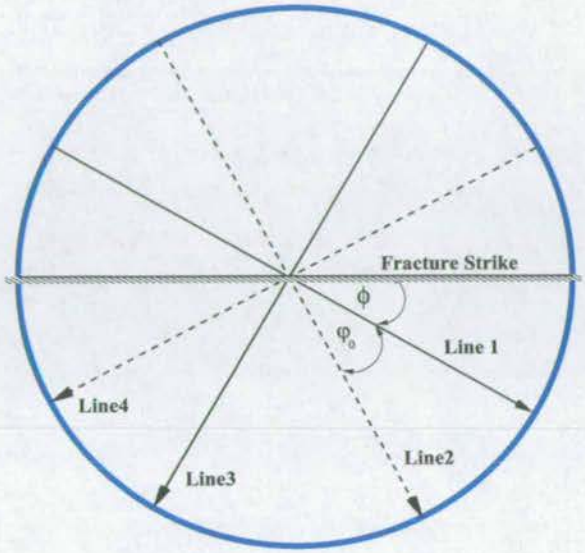

a)

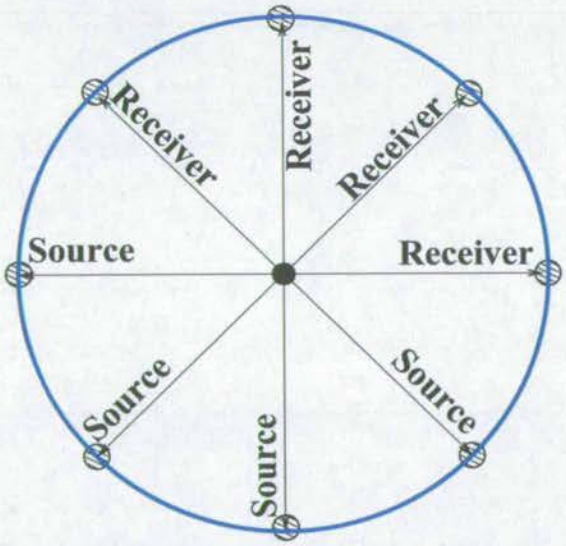

b)

Figure 3.1: (a) Orthogonal lines system: two sets of orthogonal lines or four azimuthal directions for the CMPs with the same crosspoint. Line 1 and Line 3, Line 2 and Line 4 are two sets of orthogonal lines. φ_0 is the angle between Line 2 and Line 1. Φ is the angle between the fracture strike and Line 1. (b) Multi-azimuthal recording system.

velocity, density and all the elastic parameters for the target can be calculated. Using equivalent medium theory, I can compute the one-dimension seismic record from these elastic parameters. Comparison of the synthetic record with the field seismic record can discern reflection times for the target top and bottom interfaces. The procedure is as follows:

$$\left[\begin{array}{c} Well-logs \\ \Downarrow \\ Elastic\,parameters \\ \Downarrow \\ Equivalent\,medium\,theories \\ \Downarrow \\ Source\ signature + Synthetic\,record \\ \Downarrow \\ Comparing\,synthetic\,and\,field\,records \end{array}\right]$$

3 *ISO+ANISO model.* Figure 3.3 shows a simple geological model which consists of two flat layers: the upper one is an isotropic layer and the lower one is an anisotropic layer - TIH layer. This model will be used in my synthetic tests. If the overburden is not an isotropic one but not an azimuthally anisotropic one, it will not bring any new azimuthal variations to seismic attributes from the underlying layer, therefore it has no effects on fracture detection. So we can at least relax this assumption to VTI+ANISO.

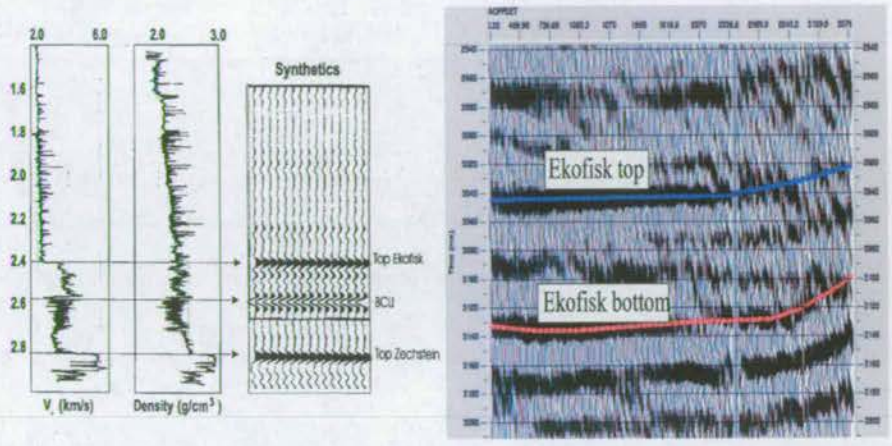

a) b)

Figure 3.2: a) Well-logs at the crosspoint from which the synthetic seismic record can be calculated by the equivalent medium theory (From MacBeth et. al. 1998). b) A field CMP gather. Comparing the synthetic and field records makes it possible to distinguish the reflection from the top and bottom of the target from other events.

Figure 3.3: ISO+ANISO model. The upper layer is a flat isotropic layer. The lower layer is an horizontally anisotropic layer which is a fractured medium and can be described using equivalent medium theory.

3.3 Fracture detection using orthogonal lines

3.3.1 Special four-line configuration

The four lines (Figure 3.1a) are two sets of orthogonal lines with a common intersection, or there are four special CMP gathers at the crosspoint for each CMP gather in which all the traces have the same shot-receiver azimuthal direction and the four CMPs are composed of two sets of orthogonal azimuthal CMPs.

3.3.2 Azimuthal moveout response(AMR)

For a survey line at the azimuthal angle φ to the fracture strike in a single-layered TIH medium, the reflection moveout can be written as (following Sayers and Ebrom, 1997),

$$t^2(\varphi, x) = t_0^2 + \frac{x^2}{V_{nmo}^2} - \frac{Ax^4}{x^2 + t_0^2 V_{p0}^2}, \tag{3.1}$$

where $t(\varphi, x)$ is the reflection traveltime at offset x, t_0 is the two-way zero-offset traveltime, V_{nmo} is the NMO velocity and A is a moveout coefficient. Equation (3.1) is obtained for weak anisotropy (see also Sena, 1991; Li and Crampin, 1993), and for general anisotropy, an empirical but more accurate equation is given by Al-Dajani et al. (1998). From Al-Dajani et al. (1998), V_{nmo} and coefficient A can be written, to the first order in the anisotropy parameters, as

$$\frac{1}{V_{nmo}^2} = \frac{1}{V_{p0}^2}[1 - 2(\delta - 2\varepsilon)\sin^2\varphi], \tag{3.2}$$

$$A = \frac{2(\varepsilon - \delta)}{V_{p0}^2}\sin^4\varphi. \tag{3.3}$$

Note the coefficient $A = -t_0^2 V_{p0}^2 A_4$, where A_4 is the quartic moveout coefficient defined by Al-Dajani et al. (1998). Also, $\delta - 2\varepsilon \approx \delta^{(V)}$ in the weak-anisotropy approximation, where $\delta^{(V)}$ is the effective Thomsen's parameter defined by Tsvankin

(1997).

Substituting equations (3.2) and (3.3) into equation (3.1), taking the square roots and linearizing with respect to the anisotropic parameters ε and δ gives

$$t(\varphi, x) = \sqrt{t_0^2 + \frac{x^2}{V_{p0}^2}} \left[1 - (\delta - 2\varepsilon)\sin^2\theta\sin^2\varphi - (\varepsilon - \delta)\sin^4\theta\sin^4\varphi\right], \tag{3.4}$$

where θ is the incident (ray) angle at the reflector measured from vertical. The square-root term in equation (3.4) is a standard normal moveout term. Introducing $t_{\|}$ and $t_{\perp}$ as the reflection moveouts at offset x for the survey lines parallel and perpendicular to the fracture strike, respectively, yields

$$t_{\|}(x) = t(\varphi = 0, x) = \sqrt{t_0^2 + \frac{x^2}{V_{p0}^2}}\ ; \tag{3.5}$$

$$\begin{aligned} t_{\perp}(x) &= t(\varphi = \pi/2, x) \\ &= t_{\|}(x) - t_{\|}(x)(\delta - 2\varepsilon)\sin^2\theta - t_{\|}(x)(\varepsilon - \delta)\sin^4\theta\ . \end{aligned} \tag{3.6}$$

Substituting equations (3.5) and (3.6) into equation (3.4) yields

$$\begin{aligned} t(\varphi, x) &= t_{\|}(x)\cos^2\varphi + t_{\perp}(x)\sin^2\varphi \\ &+ t_{\|}(x)(\varepsilon - \delta)\sin^4\theta\sin^2\varphi\cos^2\varphi. \end{aligned} \tag{3.7}$$

I now assume two orthogonal CMP (common-mid point) lines at azimuths φ and $\pi/2 - \varphi$ measured from the fracture strike in a single-layered medium (Figure 3.1a). The azimuthal moveout response (AMR) of a fracture target is defined as the traveltime difference (Δt) between the two orthogonal lines from the bottom of the target:

$$\Delta t(\varphi, x) = t(\pi/2 - \varphi, x) - t(\varphi, x). \tag{3.8}$$

As shown in equation (3.4), the traveltime equation explicitly contains the square-

root moveout term. Sometimes, it may be convenient to apply a common hyperbolic moveout correction to both azimuthal lines before the calculation of Δt. This implies the rearrangement of equation (3.8) as:

$$\Delta t(\varphi, x) = \left[t(\pi/2 - \varphi, x) - \sqrt{t_0^2 + \frac{x^2}{V_{nmo}^2}} \right] - \left[t(\varphi, x) - \sqrt{t_0^2 + \frac{x^2}{V_{nmo}^2}} \right], \quad (3.9)$$

where V_{nmo} is the chosen moveout velocity. From equation(3.7), Δt can be written as

$$\Delta t(\varphi, x) = (t_\perp - t_\parallel) \cos 2\varphi = B_0(x, \varepsilon, \delta) \cos 2\varphi, \quad (3.10)$$

where, to the first order in the anisotropy parameters, I have

$$B_0(x, \varepsilon, \delta) = \frac{x}{V_{p0}} \sin\theta \left[2\varepsilon - \delta - (\varepsilon - \delta) \sin^2\theta \right]. \quad (3.11)$$

As $B_0(x, \varepsilon, \delta)$ is independent of azimuth, equation (3.10) shows that in the weak-anisotropy approximation, the AMR is a function of $\cos 2\varphi$ for a fixed offset. The AMR, $\Delta t(\varphi_i, x)$, at different azimuth φ_i and a fixed offset x can be picked from the CMP gather. By fitting those interval times to equation (3.10), the directions with maximum and minimum interval time can be obtained, which are the fracture normal and strike directions, respectively. This feature allows us to determine the fracture strike without the need to know $t_\perp$ and $t_\parallel$.

This section reviews the analysis procedure for a single-layered TIH medium. Figure 3.4 shows a model and the resulting CMP synthetic gather. The configurations of the four lines are shown in Figure: 3.1a. Φ is the angle from the fracture strike to the Line 1, φ_0 is the angle between Line 1 and Line 2. T_{top} and T_{bottom} are the reflection times picked for the same offset X. Δt_1^{31} and Δt_2^{42} are the AMR of the two sets of orthogonal lines for the same offset which are defined by equations 3.13 and 3.15. Defining $\Delta t_{Line1} = (T_{bottom} - T_{top})_{Line1}$, I have:

$$\tan 2\Phi = \frac{\Delta t_2^{42'}}{\Delta t_1^{31}} \tag{3.12}$$

where:

$$\Delta t_1^{31} = (T_{bottom} - T_{top})_{Line3} - (T_{bottom} - T_{top})_{Line1} \tag{3.13}$$

$$\Delta t_2^{42'} = \frac{\Delta t_1^{31} \cos 2\varphi_0 - \Delta t_2^{42}}{\sin 2\varphi_0} \tag{3.14}$$

$$\Delta t_2^{42} = (T_{bottom} - T_{top})_{Line4} - (T_{bottom} - T_{top})_{Line2} \tag{3.15}$$

and

$$\left.\begin{aligned} \Delta t_{Line1} &= A + B\cos 2\varphi_1 \\ A = 0;\ B &= \tfrac{x\sin\theta}{V_{p0}}\left[2\varepsilon - \delta - (\varepsilon - \delta)\sin^2\theta\right] \end{aligned}\right\} \tag{3.16}$$

3.3.3 Fracture detection using AVOZ

Many published papers show that seismic amplitude varies with azimuthal angle. Here I derive the analytic formula which is similar to equation (3.12), to calculate the fracture orientation directly. First of all, let us see how the amplitude varies with the azimuth.

As shown in equation (2.32), the amplitude from the top interface of the target is related to the azimuth, the incident angle (which is related to the offset), and to the

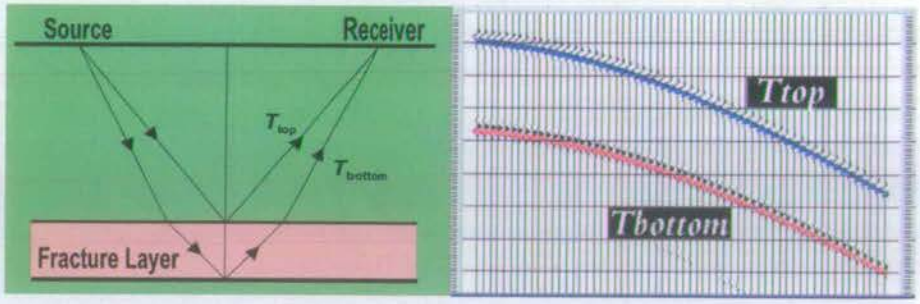

a) b)

Figure 3.4: a) A geological model and b) the synthetic CMP gather calculated for this model using ANISEIS at the fracture normal direction.

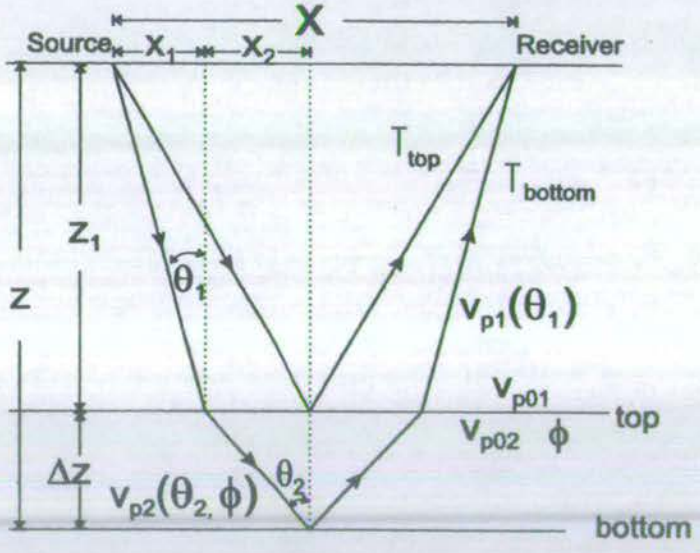

Figure 3.5: The ray path of P-P reflections from the top (interface1) and the bottom of a fractured reservoir (after Li, 1997). X is the offset and T_{top} and T_{bottom} are the top and bottom reflection times, respectively.

elastic parameters of the two layers. If the layer parameters and azimuth are fixed, I can obtain the relationship between amplitude and offset, which is the conventional AVO. If the offset and azimuth are fixed, I can obtain the relationship of amplitude with every parameter of the two layers based on the effect of velocity difference of the interface. If I fix the layer parameters and offset, I can obtain the relationship between amplitude and azimuth. Equation (2.32) is very complex and it isn't easy to get a clear idea about how the amplitude varies with offset and azimuth. I may rewrite equation (2.32) by separating it into the following three level of formula:

$$\left[\begin{array}{c} \textit{The first level formula : related to elastic parameters} \\ \Downarrow \\ \textit{The second level : related to offset} \\ \Downarrow \\ \textit{The third level : related to azimuth} \end{array}\right]$$

and the rewritten result is:

$$R_{pp}(\varphi,\theta) = R_{pp1}(\theta)\cos^2\varphi + R_{pp2}(\theta)\sin^2\varphi + R_{pp3}(\theta) \tag{3.17}$$

where:

$$R_{pp1}(\theta) = \frac{\Delta\delta_x}{2}\sin^2\theta - \frac{\Delta\delta_x - \Delta\varepsilon_x}{2}\sin^2\theta\tan^2\theta \tag{3.18}$$

$$R_{pp2}(\theta) = \frac{\Delta\delta_y}{2}\sin^2\theta - \frac{\Delta\delta_y - \Delta\varepsilon_y}{2}\sin^2\theta\tan^2\theta - 4\frac{V_s^2}{V_p^2}\Delta\gamma_{xy}\sin^2\theta \tag{3.19}$$

$$R_{pp3}(\theta) = \frac{1}{2}\left(\frac{\Delta\rho}{\rho} + \frac{\Delta V_p}{V_p}\right) - \frac{2V_s^2}{V_p^2}\left(\frac{\Delta\rho}{\rho} + 2\frac{\Delta V_s}{V_s}\right)\sin^2\theta + \frac{\Delta V_p}{2V_p}\tan^2\theta \tag{3.20}$$

Equation (3.17) shows much more clearly how the amplitude varies with azimuth.

Equations (3.18), (3.19) and (3.20) show how the amplitude varies with the offset and elastic parameters.

If all the elastic coefficients of the two layers are known, and the depths and thicknesses of the layers are also available, then the reflection amplitude variation with azimuth can be computed by equation (3.17), as suggested by Teng and Mavko (1996). On the other hand, if the amplitudes are known in some azimuthal directions and offsets, can we invert for the parameters such as the fracture strike angle? Mallick et. al. (1996) presented a solution to this question for the three-line configuration. From their equation, if the amplitudes at the same offset in three different azimuthal directions are given, the fracture strike can be estimated. Here I derive an analytic formula to calculate fracture strike directly from azimuthal amplitude and velocity for the four lines. Equation (3.17) can be rewritten as :

$$\begin{aligned} R_{pp}(\varphi,\theta) &= R_{pp1}(\theta)\cos^2\varphi + R_{pp2}(\theta)(1-\cos^2\varphi) + R_{pp3}(\theta) \\ &= (R_{pp1}(\theta) - R_{pp2}(\theta))\cos^2\varphi + R_{pp2}(\theta) - R_{pp3}(\theta) \\ &= \tfrac{R_{pp1}(\theta)-R_{pp2}(\theta)}{2} + R_{pp2}(\theta) + R_{pp3}(\theta) + (\tfrac{R_{pp1}(\theta)-R_{pp2}(\theta)}{2})\cos 2\varphi \end{aligned}$$

or

$$R_{pp}(\varphi,\theta) = A + B\cos 2\varphi \tag{3.21}$$

where :

$$\left.\begin{aligned} A &= \tfrac{R_{pp1}(\theta)-R_{pp2}(\theta)}{2} + R_{pp2}(\theta) + R_{pp3}(\theta) \\ B &= \tfrac{R_{pp1}(\theta)-R_{pp2}(\theta)}{2} \end{aligned}\right\}$$

It is clear that if we have three equations, or if three amplitudes are known in three different azimuthal directions, the fracture strike angle φ can be solved exactly.

If we have the real seismic records in three different azimuthal directions, for each offset, a set of φ, A, B can be picked up, so a series of φ, A, B can be computed for different offsets. Therefore, to obtain the fracture strike in this way, three lines are the minimum that are required. From each set of φ, A and B, the vertical velocity V_{p0}, the Thomsen's anisotropy parameter $\delta^{(V)}$ and the azimuthal angle Φ of the symmetry plane in a transversely isotropic medium with a horizontal symmetry axis can be calculated.

However, Al-Dajani et. al. (1998) show that the inversion result of V_{p0}, $\delta^{(V)}$ and Φ is very sensitive to the angular separation between the three survey lines. Azimuths for the source-to-receiver directions 60^o apart are required for maximizing the accuracy and stability of the parameter estimation. Now I deal with four lines, or two sets of orthogonal lines, the following present an alternative way to simply and robustly compute the fracture strike.

Under our fourline configuration in Figure 3.1, for the same offset there will be the same incident angle θ for the reflection from the same depth. I use $\varphi_1, \varphi_2, \varphi_3$ *and* φ_4 to denote the azimuthal angles of the four lines and φ_0 to denote the angle between line 2 and line 1. Line 3 and line 1 are orthogonal, and line 4 and line 2 are orthogonal. Here, lines 1, 2, 3 and 4 are in a clockwise direction in order. φ_1 is the angle between the fracture strike and line 1 and it is positive if it is in the clockwise direction, and it is negative if it is in an anticlockwise direction. So, one of the pre-processing steps for fracture detection is to redefine the line number in clockwise order. Then, φ_0 is always positive and

$$\varphi_2 = \varphi_1 + \varphi_0,\ \varphi_3 = \varphi_1 + 90\ ,\ \varphi_4 = \varphi_2 + 90$$

I have,

$$\Delta A_{31} \ = \ R_{pp}(\varphi_3, \theta) - R_{pp}(\varphi_1, \theta)$$

$$
\begin{aligned}
&= R_{pp1}(\theta)\cos^2\varphi_3 + R_{pp2}(\theta)\sin^2\varphi_3 + R_{pp3}(\theta) - \\
&\quad R_{pp1}(\theta)\cos^2\varphi_1 - R_{pp2}(\theta)\sin^2\varphi_1 - R_{pp3}(\theta) \\
&= \cos 2\varphi_1 (R_{pp2}(\theta) - R_{pp1}(\theta))
\end{aligned}
$$

because : $\theta = \theta(x_i)$, so:

$$
\begin{aligned}
\Delta A_{31} &= R_{pp}(\varphi_3, \theta) - R_{pp}(\varphi_1, \theta) \\
&= \cos 2\varphi_1 (R_{pp2}(x_i) - R_{pp1}(x_i))
\end{aligned} \tag{3.22}
$$

In the same way , I can obtain:

$$
\begin{aligned}
\Delta A_{42} &= R_{pp}(\varphi_4, \theta) - R_{pp}(\varphi_2, \theta) \\
&= \cos 2\varphi_2 (R_{pp2}(x_i) - R_{pp1}(x_i))
\end{aligned} \tag{3.23}
$$

$$
\frac{\Delta A_{31}}{\Delta A_{42}} = \frac{\cos 2\varphi_1}{\cos 2\varphi_2} = \frac{\cos 2\varphi_1}{\cos 2(\varphi_1 + \varphi_0)}
$$

$$
\tan 2\Phi = \frac{\Delta A'_{42}}{\Delta A_{31}} \tag{3.24}
$$

$$
\Delta A'_{42} = \frac{\Delta A_{31}\cos 2\varphi_0 - \Delta A_{42}}{\sin 2\varphi_0}
$$

3.3.4 NMO velocity and azimuthal AVO gradient

Equations for Using Azimuthal NMO Velocity

Grechka and Tsvankin (1997, 1998b, 1998a) gave the following formula for the variation of velocity with azimuth in a TIH medium:

$$V_{nmo}^2(\varphi) = \frac{1}{\frac{\sin^2\varphi}{V_{s2}^2} + \frac{\cos^2\varphi}{V_{s1}^2}}, \tag{3.25}$$

where φ is the angle between the fracture strike and survey line. $V_{nmo}(\varphi)$ is the NMO velocity in azimuth direction φ and V_{s1}, V_{s2} are the NMO velocities in the two vertical symmetry planes (x,z), and (y,z). Let:

$$\eta_{nmo}(\varphi) = \frac{1}{V_{nmo}(\varphi)}$$

$$\eta_{s1} = \frac{1}{V_{s1}}, \ \eta_{s2} = \frac{1}{V_{s2}}$$

So:

$$\eta_{nmo}^2(\varphi) = \eta_{s2}^2 \sin^2\varphi + \eta_{s1}^2 \cos^2\varphi \tag{3.26}$$

For our fourline configuration, the azimuths of lines 1, 2, 3 and 4 have the following relationships ($\varphi_1, \varphi_2, \varphi_3, \varphi_4$ and the order of lines 1, 2, 3, 4 are defined as above).

$$\varphi_2 = \varphi_1 + \varphi_0, \ \varphi_3 = \varphi_1 + 90, \ \varphi_4 = \varphi_2 + 90$$

Therefore:

$$\eta_{nmo}^2(\varphi_1) = \eta_{s2}^2 \sin^2\varphi_1 + \eta_{s1}^2 \cos^2\varphi_1$$

$$\eta^2_{nmo}(\varphi_2) = \eta^2_{s2}\sin^2\varphi_2 + \eta^2_{s1}\cos^2\varphi_2$$

$$\eta^2_{nmo}(\varphi_3) = \eta^2_{s2}\sin^2\varphi_3 + \eta^2_{s1}\cos^2\varphi_3 = \eta^2_{s2}\cos^2\varphi_1 + \eta^2_{s1}\sin^2\varphi_1$$

$$\eta^2_{nmo}(\varphi_4) = \eta^2_{s2}\sin^2\varphi_4 + \eta^2_{s1}\cos^2\varphi_4 = \eta^2_{s2}\cos^2\varphi_2 + \eta^2_{s1}\sin^2\varphi_2$$

$$\Delta\eta_{nmo31} = \eta^2_{nmo}(\varphi_3) - \eta^2_{nmo}(\varphi_1) = \cos 2\varphi_1(\eta^2_{s2} - \eta^2_{s1}) \tag{3.27}$$

In the same way, I have

$$\Delta\eta_{nmo42} = \eta^2_{nmo}(\varphi_4) - \eta^2_{nmo}(\varphi_2) = \cos(2\varphi_1 + 2\varphi_0)(\eta^2_{s2} - \eta^2_{s1}) \tag{3.28}$$

Then, dividing equation 3.27 by equation 3.28, I have

$$\frac{\Delta\eta_{nmo31}}{\Delta\eta_{nmo42}} = \frac{\cos 2\varphi_1}{\cos(2\varphi_1 + 2\varphi_0)}$$

As a result:

$$\tan 2\Phi = \frac{\Delta\eta'_{42}}{\Delta\eta_{31}} \tag{3.29}$$

$$\Delta\eta'_{42} = \frac{\Delta\eta_{31}\cos 2\varphi_0 - \Delta\eta_{42}}{\sin 2\varphi_0}$$

Alternatively, another equation can be derived from equation 3.26. It is rewritten as:

$$\eta^2_{nmo}(\varphi) = \eta^2_{s2}(1 - \cos^2\varphi) + \eta^2_{s1}\cos^2\varphi = A + B\cos 2\varphi \tag{3.30}$$

where:

$$\left.\begin{aligned} A &= \tfrac{(\eta_{s1}^2+\eta_{s2}^2)}{2} \\ B &= \tfrac{(\eta_{s1}^2-\eta_{s2}^2)}{2} \end{aligned}\right\} \tag{3.31}$$

Equations for Using Azimuthal AVO Gradient

Azimuthal AVO can be used to estimate fracture orientation and intensity. Seismic-derived AVO gradient and intercept provide quantitative answers to reservoir size, location and fluid saturation. Recently, it was realized (Rüger, 1996c) that the AVO gradient from the interface of a fractured reservoir shows azimuthal variation and I suggest that it can also be used to estimate fracture orientation and intensity as well. From equation (3.17), I can derive the following equation:

$$\mathrm{R_{pp}}(\varphi,\theta) = I + G(\varphi)\sin^2\theta + C(\varphi)\sin^2\theta\tan^2\theta \tag{3.32}$$

where,

$$\begin{aligned} I &= \tfrac{1}{2}\left(\tfrac{\Delta\rho}{\rho} + \tfrac{\Delta V_p}{V_p}\right), \\ G(\varphi) &= A_1 + B_1\cos 2\varphi, \\ C(\varphi) &= \left(\tfrac{\Delta V_p}{2V_p} - \tfrac{\Delta\delta_x-\Delta\varepsilon_x}{2}\cos^2\varphi - \tfrac{\Delta\delta_y-\Delta\varepsilon_y}{2}\sin^2\varphi\right)\sin^2\theta\tan^2\theta, \\ A_1 &= \tfrac{\Delta V_p}{2V_p} - \tfrac{2V_s^2}{V_p^2}\left(\tfrac{\Delta\rho}{\rho} + 2\tfrac{\Delta V_s}{V_s}\right) + \tfrac{\Delta\delta_y+\Delta\delta_x}{4} - 2\tfrac{V_s^2}{V_p^2}\Delta\gamma_{xy}, \\ B_1 &= \left(\tfrac{\Delta\delta_x-\Delta\delta_y}{4} + 2\tfrac{V_s^2}{V_p^2}\Delta\gamma_{xy}\right), \end{aligned} \tag{3.33}$$

I and $G(\varphi)$ are the AVO intercept and gradient, respectively. When weak anisotropy is assumed, $C(\varphi)$ can be neglected. Four azimuthal gradients: $G(\varphi_1)$, $G(\varphi_2)$, $G(\varphi_3)$ and $G(\varphi_4)$ can be inverted using equation (3.32) from AVO inversion.

Similarly, I obtain the following equation to calculate fracture strike angle ϕ:

$$\tan 2\Phi = \frac{\Delta G'_{42}}{\Delta G_{31}}, \tag{3.34}$$

where, $\Delta G_{31} = G(\varphi_3) - G(\varphi_1)$, $\Delta G_{42} = G(\varphi_4) - G(\varphi_2)$ and $\Delta G'_{42} = \frac{\Delta G_{31}\cos 2\varphi_0 - G A_{42}}{\sin 2\varphi_0}$.

3.4 General formula

From equations (3.12), (3.24), (3.29) and (3.34), we can see that the four azimuthal attribute equations have the same form. Two general formulae can be built. One is for the calculation of fracture parameters, and the other is for describing the variation of the attributes.

$$\left.\begin{aligned} \tan 2\Phi &= \frac{F'_{42}}{F_{31}} \\ F'_{42} &= \frac{F_{31}\cos 2\varphi_0 - F_{42}}{\sin 2\varphi_0} \end{aligned}\right\} \tag{3.35}$$

$$F(\theta,\ j) = A(\theta) + B(\theta)\cos 2\varphi + C(\theta)\cos 4\varphi \tag{3.36}$$

where $F = (\theta,\ \varphi)$ represents either P-wave amplitude, AVO gradient, inverse of the squared NMO velocity ($1/V^2_{nmo}$), or traveltime; $A(\theta)$, $B(\theta)$ and $C(\theta)$ are azimuthally invariant coefficients.

3.5 Synthetic tests for fracture detection using orthogonal lines

In the three-layer model shown in Figure 3.6, the isotropic medium is shale and the thickness is 1500 m. The fractured layer striking normal to X-axis is azimuthally anisotropic, its background material is isotropic with a P-wave velocity of 2183m/s, a

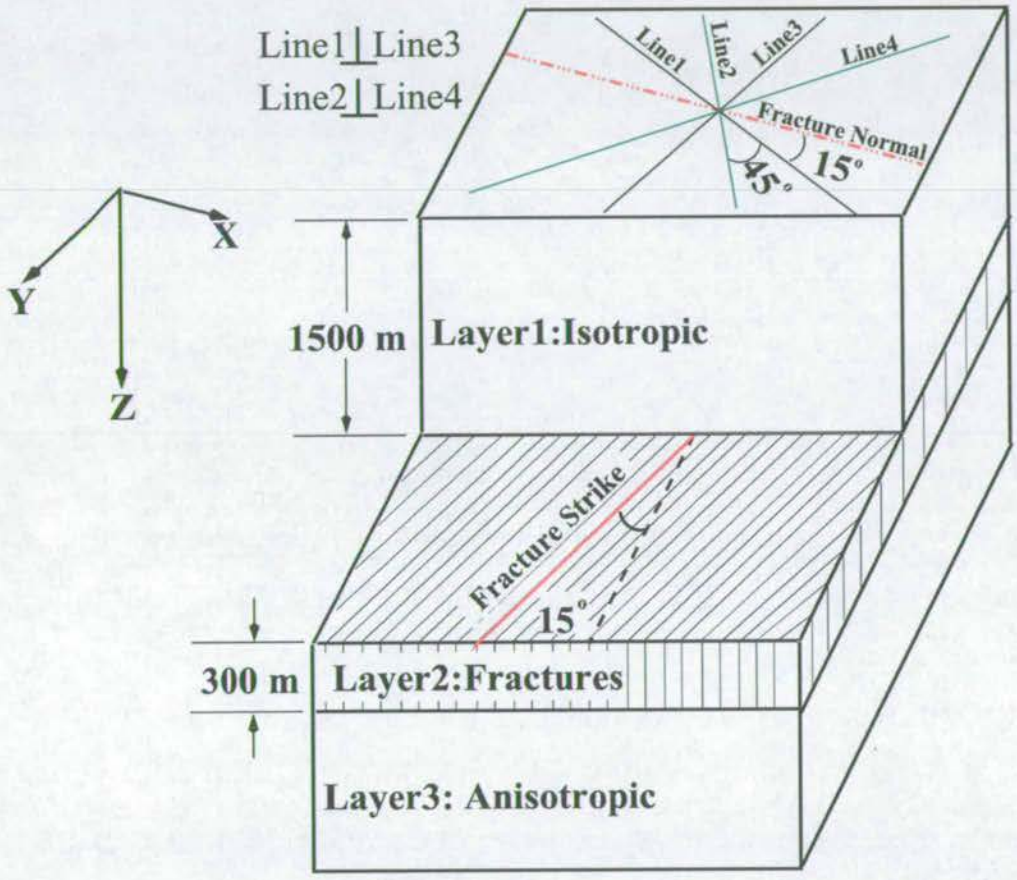

Figure 3.6: The orthogonal acquisition geometry for fractured reservoir estimation of layer 2 which is an equivalent medium of a fractured layer using Hudson theory (1981).

quasi-S-wave velocity of 1502m/s and a density of 2.19 g/cm^3. Then I add fractures to this background material using Hudson (1981) theory so I obtain the TIH media. The thickness of this layer is 300 m. The synthetic seismic records are calculated using the ANISEIS package (Taylor, 1990). The elastic stiffnesses C_{mn} $(10^9 pa)$ were computed using the same parameters as in Table 2.1.

$$C_{mn} = \begin{bmatrix} 6.252 & 0.333 & 0.333 & & & \\ & 10.425 & 0.543 & & & \\ & & 10.425 & & & \\ & & & 4.941 & & \\ & & & & 3.833 & \\ & & & & & 3.833 \end{bmatrix} \tag{3.37}$$

Figure 3.7 shows the synthetic seismic records from the model in Figure 3.6. All the traces from CMP1001, 1002, 1003 and 1004 have the same coordinates. The azimuthal angles for CMP1001, 1002, 1003, 1004 are 15, 60, 105, 150 degrees to X-axis in a clockwise direction. Figure 3.8 shows the NMO gathers of the four lines. CMP 1001, 1002, 1003, 1004 are from Line 1, Line 2, Line 3 and Line4, respectively. This figure shows that the bottom residual moveout time varies with offset and azimuth. Figure 3.9 is the reflection amplitude from the top interface; a), b), c) and d) are from Line 1, Line 2, Line 3 and Line 4, respectively. To examine the azimuthal and offset variation in more detail, Figures 3.10a and b show the picked amplitudes and bottom reflection times, respectively. The amplitudes are picked from Figure 3.9 and the reflection times from Figure 3.7. Figure 3.10 shows only the variation in four azimuthal directions. Figures 3.11 a and b show the variations of traveltime and amplitude with all offsets and azimuth; Figure 3.12 shows the variations of velocity with all azimuths. These confirm the elliptical variation as discussed in Chapter 2.

Figure 3.13 shows the results of azimuthal moveout analysis. Figure 3.13a shows

the moveout difference between the the orthogonal lines calculated by equations 3.13 and 3.15. The star red line stands for the moveout difference between Line 3 and Line 1 for each offset; the dot blue line stands for the moveout difference between Line 4 and Line 2. Figure 3.13b is a cross plot in which "dt1" means Δt_1^{31} [equation (3.13)], "dt2p" means $\Delta t_2^{42\prime}$[equation (3.14)]. This plot gives us a direct sense of the fracture strike. Figure 3.13c shows the variation of fracture strike calculated by equation 3.12 for each offset; from this plot the detection error variation with the offset can be seen clearly. The larger the offset, the smaller the error.

Figure 3.14 shows the results of the azimuthal amplitude analysis. The figure is arranged in the same way as Figure 3.13, where Figure 3.14a is the amplitude difference pair, Figure 3.14b is the cross plot of $\Delta A'_{42}$ versus ΔA_{31}, in which "da1" and "da2p" mean $\Delta A_{31}$and $\Delta A'_{42}$ respectively and Figure 3.14c shows how the fracture strike calculated by equation 3.24 for offset. Again the bigger the offset, the smaller the error.

In this synthetic test, the results of azimuthal moveout and amplitude always show similar accuracy and sensitivity, as compared in Figures 3.13 and 3.14. However, the implications of the two methods are quite different. The moveout method is based on the bottom reflector, which implies that the reservoir has to be sufficiently thick. The amplitude method is based on the top reflector, which implies that it may be suited for thin-layer reservoirs.

From the CMP gather in Figure 3.8, the traveltimes from the bottom interface can be picked for velocity analysis as in Table 3.2. Time1, Time2, Time3 and Time4 are the picked times from Lines 1, 2, 3 and 4, respectively. Based on the following formula:

$$t^2 = t_0^2 + \frac{Offset^2}{V_{nmo}^2} \tag{3.38}$$

	AVO Intercept	AVO Gradient
CDP 1001	2201	1024
CDP 1002	2127	1010
CDP 1003	2105	1016
CDP 1004	2185	1014

Table 3.1: The calculated AVO gradients and intercepts from four CMPs: 1001, 1002, 1003 and 1004.

and the least square method, the NMO velocity can be calculated from the above picked traveltimes, as

$$\begin{cases} V_{nmo_{Line1}} = 2825(m/s) \\ V_{nmo_{Line2}} = 2866(m/s) \\ V_{nmo_{Line3}} = 2877(m/s) \\ V_{nmo_{Line4}} = 2836(m/s) \end{cases}$$

Applying formula 3.29, the fracture strike is: $\Phi = 15^o$. This result agrees with that obtained by moveout and amplitude analysis. In a similar way to the above analysis, by picking the amplitudes at the target top, fitting equation 3.32 at each azimuthal direction using least-squares, the AVO gradient and intercept are calculated (Table 3.1). Applying formula 3.34, the fracture strike from AVO gradient analysis is: $\Phi = 14^o$. This result also agrees with that obtained by moveout and amplitude analysis.

The azimuthal variations of NMO velocity and AVO gradient are both less than 2.5% in this case. Even though the correct model parameters are estimated, these two attributes may be less reliable in the case of very weak anisotropy for application to real data, and we will need to use either an AMR analysis or an amplitude analysis scheme. The P-wave azimuthal velocity and AVO gradient methods are different from the methods of P-wave azimuthal moveout and amplitude. In the former, the velocity or AVO gradient is calculated from all the picked reflection times or amplitudes, one velocity or gradient for one azimuth and then only one

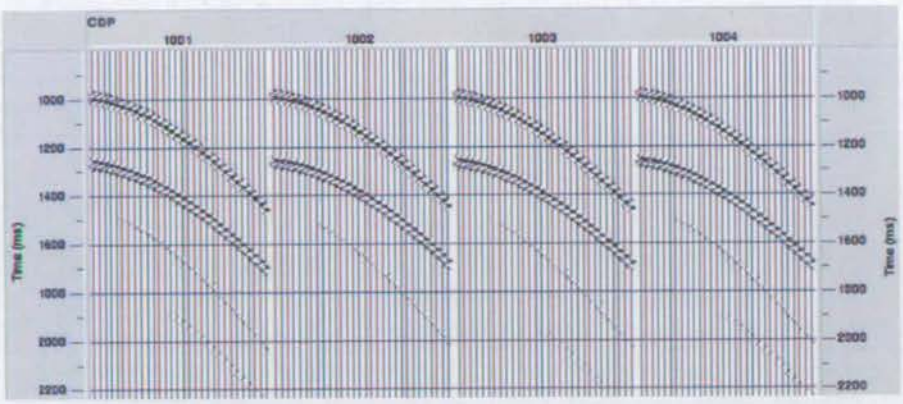

Figure 3.7: The four CMP gathers for the four lines. 1001-Line1, 1002-Line2,1003-Line3, 1004-Line4.

fracture strike angle can be calculated from the velocities or gradients for all the offsets. In the latter, one angle can be calculated for each offset, and the final angle is computed by using least-squares linear regression.

3.6 Sensitivity analysis

From the above analysis we have learnt that the precise of the fracture detection technologies may heavily depend on the accuracy of the amplitude and travel time picking, which always brings some picking errors. Therefore, a sensitivity investigation of the estimation results to picking errors is necessary for the real data application of these technologies. Two groups of researches, total twelve tests, are finished based on AVAZ analysis (Figure 3.16) and TVAZ analysis (Figure 3.15), respectively. Here only the prediction error histograms for fracture orientation estimation are presented as examples. The procedures of generating the two groups of diagrams are briefly described as below.

In the case of the four orthogonal lines (Figure 3.7), for TVAZ and AVAZ based fracture analysis methods, a set of fracture orientation and intensity can be estimated from each group of common-offset traces by using either travel time or

Offset(m)	Time1(ms)	Time2(ms)	Time3(ms)	Time4(ms)
500.00000	1279.07629	1278.67004	1278.55603	1278.95996
550.00000	1281.66003	1281.17688	1281.05005	1281.53406
600.00000	1284.48474	1283.92004	1283.77881	1284.34998
650.00000	1287.56006	1286.89990	1286.72998	1287.40454
700.00000	1290.88672	1290.10999	1289.89929	1290.68994
750.00000	1294.44995	1293.54211	1293.30005	1294.19861
800.00000	1298.23328	1297.19995	1296.94397	1297.93994
850.00000	1302.23999	1301.08704	1300.81006	1301.92175
900.00000	1306.47571	1305.19995	1304.87659	1306.13000
950.00000	1310.93994	1309.53357	1309.16003	1310.54968
1000.00000	1315.63025	1314.07996	1313.67603	1315.18994
1050.00000	1320.54004	1318.83228	1318.41003	1320.05908
1100.00000	1325.66235	1323.80005	1323.34521	1325.15002
1150.00000	1331.00000	1328.99109	1328.47998	1330.45312
1200.00000	1336.55408	1334.39001	1333.81506	1335.95996
1250.00000	1342.31995	1339.97961	1339.35999	1341.66492
1300.00000	1348.29138	1345.77002	1345.12207	1347.57996
1350.00000	1354.45996	1351.77039	1351.07996	1353.71448
1400.00000	1360.81958	1357.96997	1357.21313	1360.05005
1450.00000	1367.38000	1364.35522	1363.54004	1366.56628
1500.00000	1374.14954	1370.93005	1370.07800	1373.27002
1550.00000	1381.10999	1377.69824	1376.81006	1380.16907
1600.00000	1388.24268	1384.65002	1383.71643	1387.26001
1650.00000	1395.56006	1391.77563	1390.79004	1394.53625
1700.00000	1403.07361	1399.07996	1398.02881	1401.98999
1750.00000	1410.77002	1406.56775	1405.44995	1409.61389
1800.00000	1418.63293	1414.22998	1413.06714	1417.41003
1850.00000	1426.66003	1422.05664	1420.85999	1425.38184
1900.00000	1434.85071	1430.05005	1428.80457	1433.53003
1950.00000	1443.20996	1438.21216	1436.90002	1441.85156
2000.00000	1451.74060	1446.53003	1445.14868	1450.32996
2050.00000	1460.43005	1454.99231	1453.56006	1458.94958
2100.00000	1469.26428	1463.60999	1462.14124	1467.71997
2150.00000	1478.25000	1472.39392	1470.88000	1476.65161
2200.00000	1487.39368	1481.32996	1479.76147	1485.73999
2250.00000	1496.68005	1490.40222	1488.78003	1494.97644

Table 3.2: The picked reflection traveltimes from the bottom interface. "Time1, Time2, Time3 and Time4" are the picked times from Line 1, Line 2, Line 3 and Line 4, respectively.

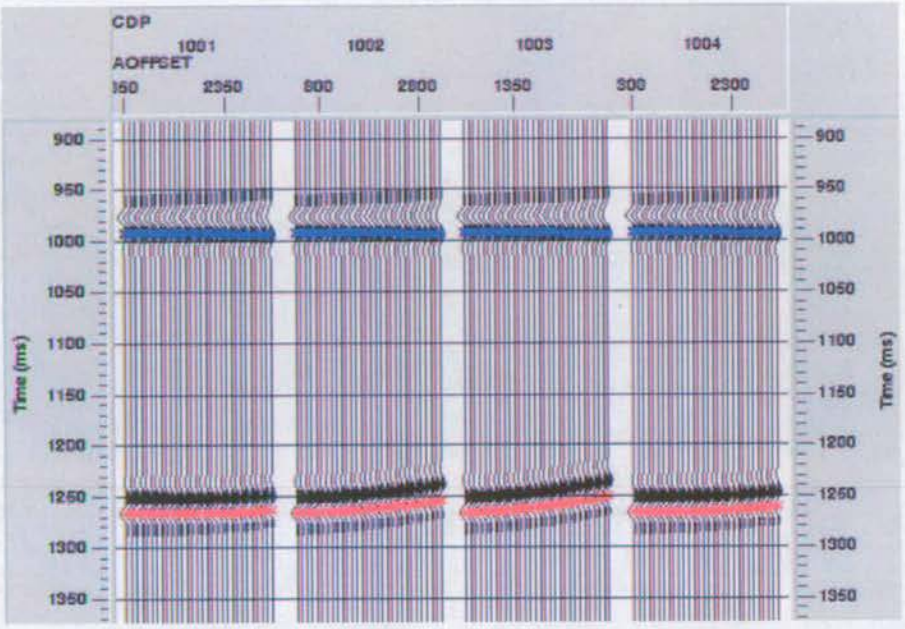

Figure 3.8: The CMP(NMO) gathers of the four lines. CMP 1001, 1002, 1003 and 1004 are from Line1, Line2, Line3 and Line4 separately. These plots show the bottom residual moveout time variation with offset and azimuth.

amplitude picked from noise-free data. Total sixty common-offset gathers will produce sixty strikes and intensities. Subtracting the estimated orientation from the modelling value, we are able to produce one error histogram on which we should be able to see the error distribution of the measurements. By adding different level of picking error to either the travel time or amplitude and repeat above procedure, we should be able to obtain a new error histogram. By comparing a series of error histograms we may be able to see the sensitivity of our estimation to different picking error. Figures 3.16a), b), c), d), e) and f) are six histograms of the estimated orientation error generated by using TVAZ analysis. Their picking errors are respectively, 0ms, 1ms, 2ms, 4ms, 6ms and 8ms. The maximum azimuthal time variation from the target bottom is 6ms when offset/depth=1. Figures 3.15a), b), c), d), e) and f) are six histograms of the estimated orientation error generated by using AVAZ analysis. Their picking errors are respectively, 0%, 3%, 9%, 18%, 36% and 72% of

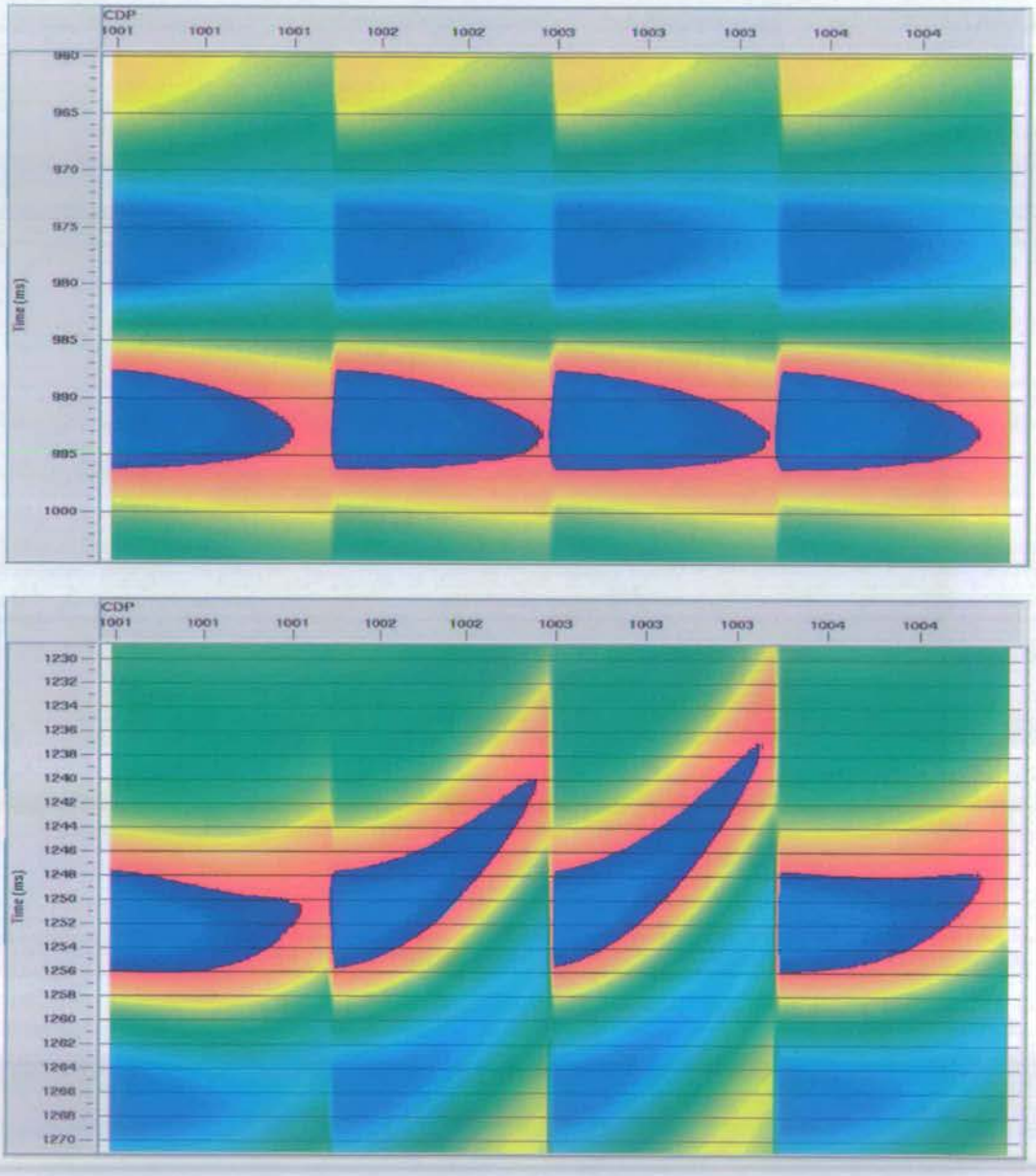

a) (b) (c) d)

Figure 3.9: The reflection amplitude from the target top (upper pane) and bottom (lower pane) interfaces, a), b), c) and d) are from Line1, Line2, Line3 and Line4 separately. It is showing that amplitude varies with offset and azimuth.

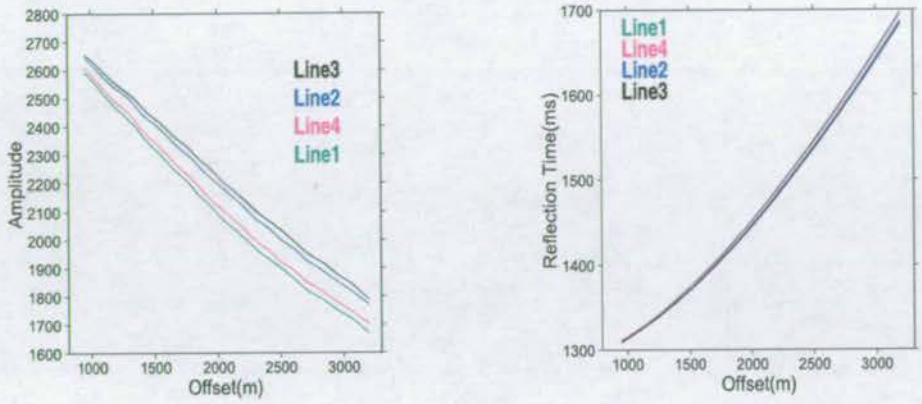

a) b)

Figure 3.10: a) Amplitudes picked from the synthetic traces in Figure 3.9. b) reflection times picked from the bottom reflectors in Figure 3.8. The green, blue, black and pink line stand for the amplitude or traveltime of Line 1, Line 2, Line 3 and Line 4 respectively.

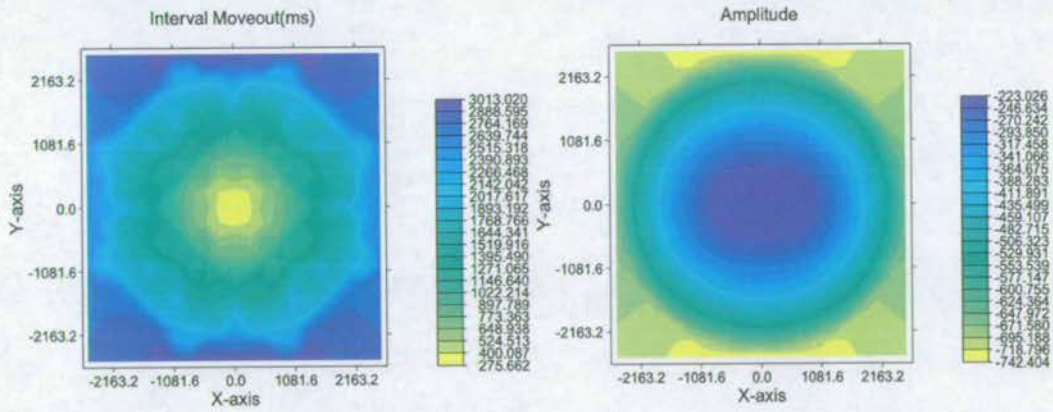

a) b)

Figure 3.11: . This plot shows how the moveout time and the amplitude vary with the azimuthal directions. a) the variation of interval moveout with any azimuthal direction and offset range of 0-2600 m. b) the variation of amplitude with any azimuthal direction and offset range of 0-2600 m. (X,Y)=(0.0, 0.0) is the crosspoint, in which $Offset = \sqrt{X^2 + Y^2}$.

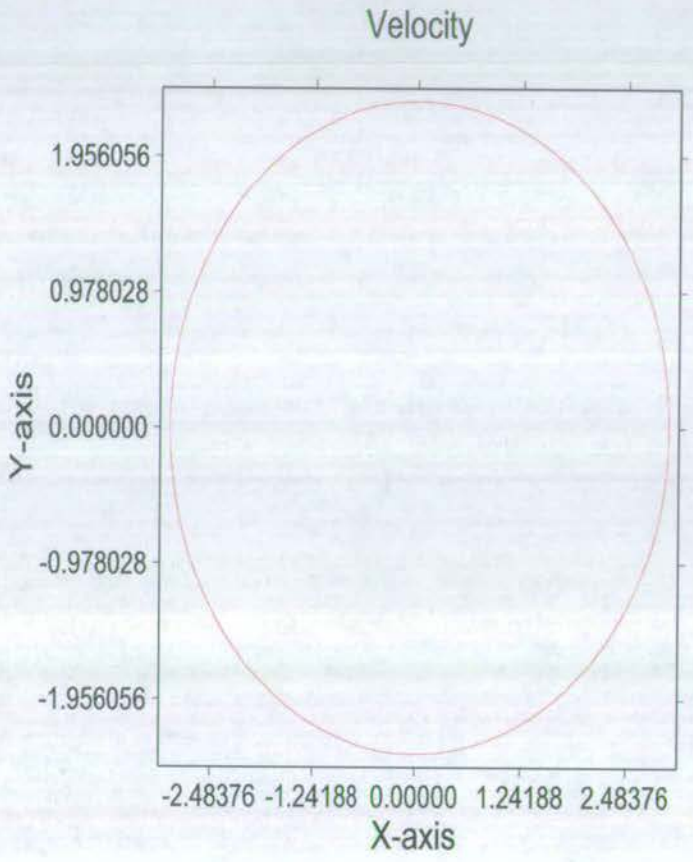

Figure 3.12: Velocity variation with any azimuthal direction and offset range from 0-2600 m $Offset = \sqrt{X^2 + Y^2}$. X and Y means the velocity component in X and Y direction.

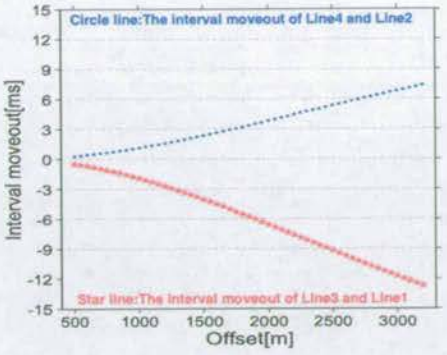

a)

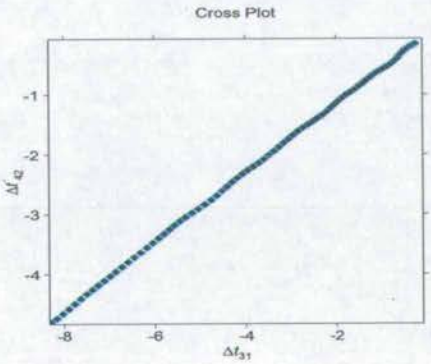

b)

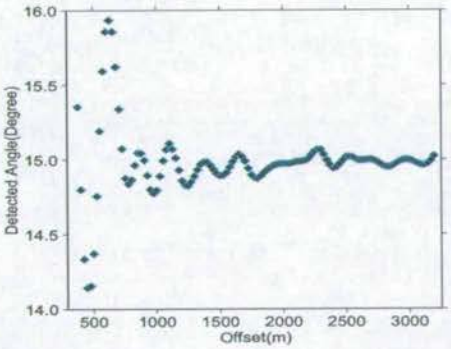

c)

Figure 3.13: The application results of azimuthal moveout analysis. a) the moveout difference pair between the orthogonal lines calculated by equations 3.13 and 3.15. The star red line represents the moveout difference of Line 3 and Line 1. The dot blue line stands for the moveout difference of Line 4 and Line 2. b) shows $\Delta t_2^{42\prime}$ versus Δt_1^{31}. In this plot, "dt1" means Δt_1^{31}(equation 3.13), "dt2p" means $\Delta t_2^{42\prime}$(equation 3.14). c) The fracture normal calculated by equation 3.12 for each offset.

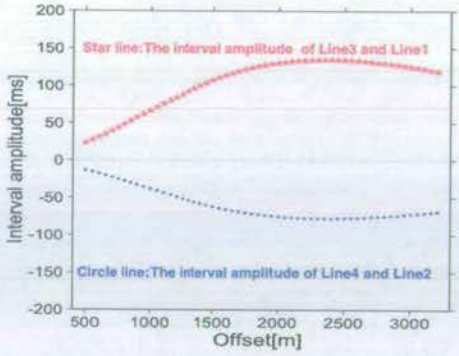

a)

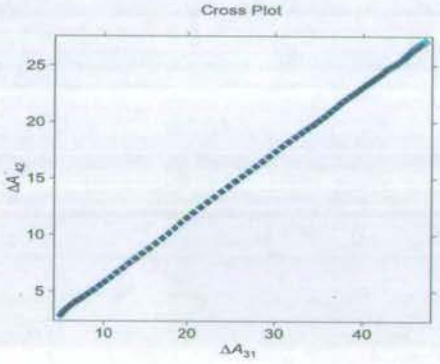

b)

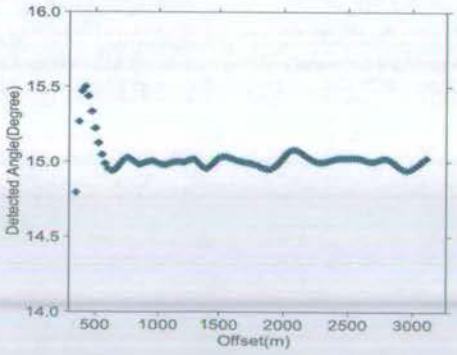

c)

Figure 3.14: The application results of azimuthal amplitude analysis. a) the amplitude difference pair between the the orthogonal lines (calculated by equations 3.22 and 3.23). The red star line stands the amplitude difference of Line 3 and Line 1. The blue dot line stands for the amplitude difference of Line 4 and Line 2. b) Shows $\Delta A'_{42}$ versus ΔA_{31}. In this plot, "da1" and "da2p" means ΔA_{31}, $\Delta A'_{42}$ respectively. c) The fracture normal by equation 3.24 for each offset.

the RMS amplitude. From these values, an average orientation and density can be obtained. Thus the deviation can be calculated straightforward.

A normal distribution of these errors is observed from either Figures 3.16 or 3.15. From the first group of diagrams, I notice that an angle close to the model strike can be inferred even through the random picking error of traveltime is as large as 100%. From the second group of diagrams, I observed that the correct angle can be reckoned even through the random picking error of amplitude is as large as 72%. By comparsion the six pairs of diagrams I find that the TVAZ analysis seems more robust than AVAZ analysis.

3.7 Three-line configuration and robust AVO analysis

3.7.1 Three-line configuration

If I have three lines such as Lines 1, 2 and 3 as shown in Figure 3.17, and the angle between any two lines is arbitrary, I have, from equation (3.36)

$$\begin{cases} F(\theta,\ \phi_1) = A(\theta) + B(\theta)\cos 2(\phi_1 + \Phi_0), \\ F(\theta,\ \phi_2) = A(\theta) + B(\theta)\cos 2(\phi_2 + \Phi_0), \\ F(\theta,\ \phi_3) = A(\theta) + B(\theta)\cos 2(\phi_3 + \Phi_0), \end{cases} \tag{3.39}$$

Where, ϕ_1, ϕ_2 and ϕ_3 are the azimuthal directions of the three lines, respectively. Therefore, for the same incident angle θ_i or offset r_i along the three azimuth directions, by solving equation 3.39, I can obtain a set of $A(\theta_i) = A(r_i)$, $B(\theta_i) = B(r_i)$ and $\Phi_0(r_i)$. $\Phi_0(r_i)$ is the angle of fracture orientations. The average angle is used as the fracture orientation by smoothing all the $\Phi_0(r_i)$ (i = 1, ..., N). If I display all the directional angles $\Phi_0(r_i)$ (i = 1, ..., N) in a circle with the radius showing the

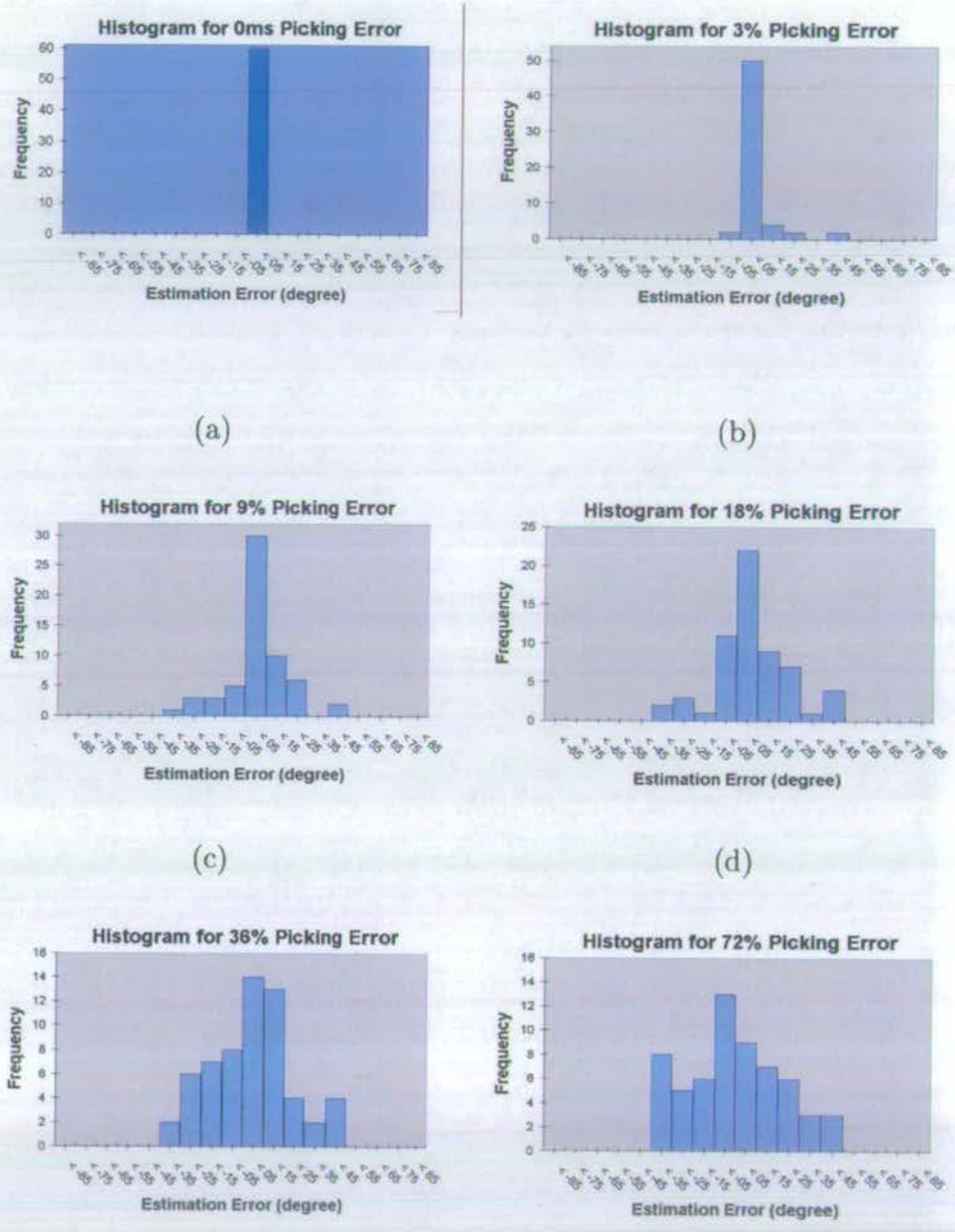

Figure 3.15: a), b), c), d), e) and f) are six histograms of the estimated orientation error for investigating the sensitivity of the AVAZ analysis (amplitude versus azimuth) to the picking errors of amplitudes. Their picking errors are respectively, 0%, 3%, 9%, 18%, 36% and 72% of the RMS amplitude.

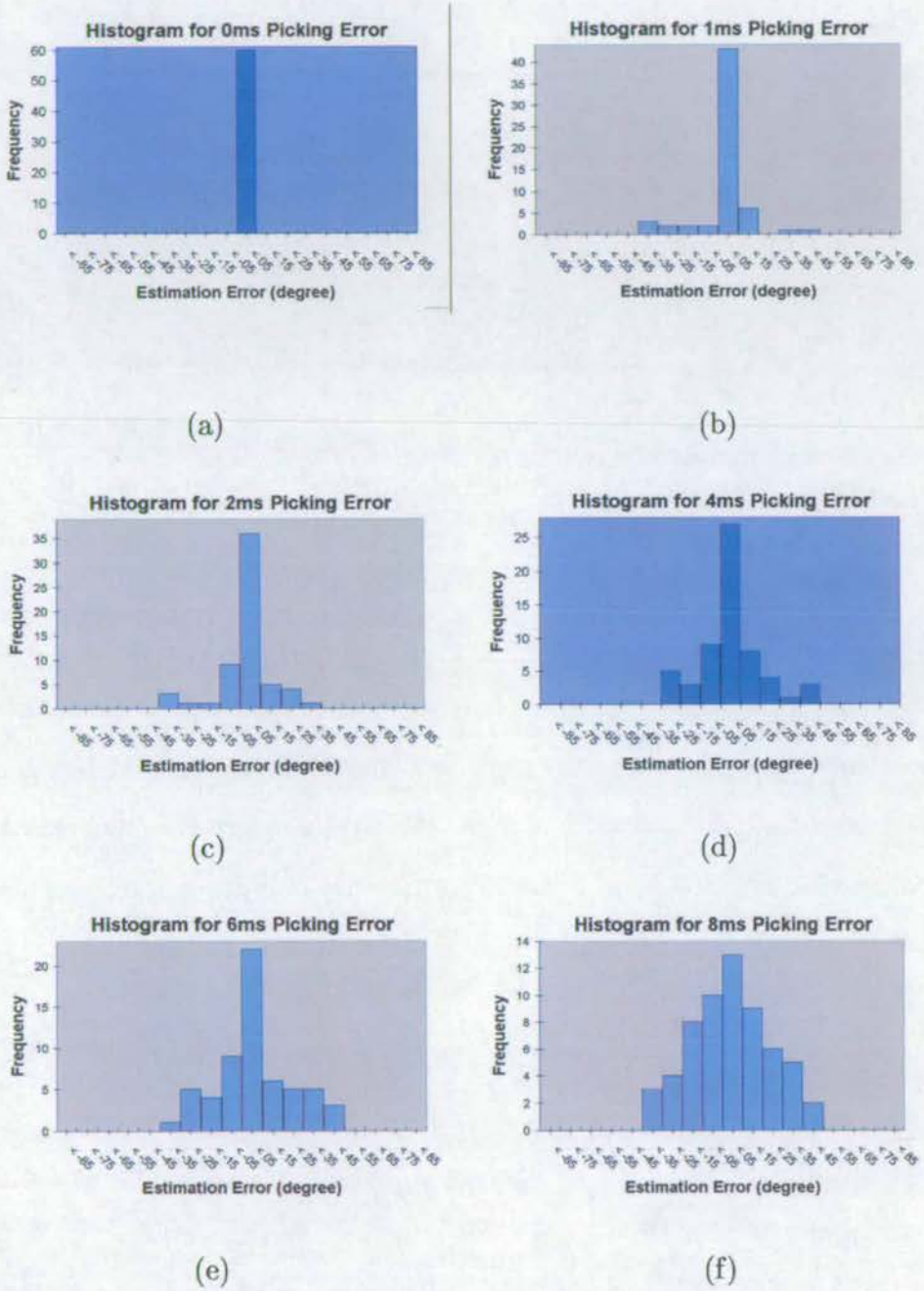

Figure 3.16: a), b), c), d), e) and f) are six histograms of the estimated orientation error for investigating the sensitivity of the TVAZ analysis (travel time versus azimuth) to the picking errors of travel times. Their picking errors are respectively, 0ms, 1ms, 2ms, 4ms, 6ms and 8ms.

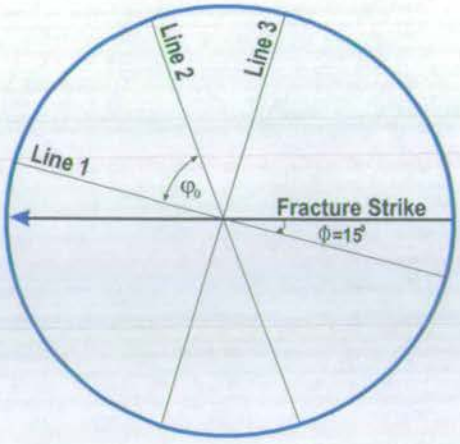

Figure 3.17: An example of three lines configuration. Line 1, 2 and 3 are arbitrary distributed lines.

fracture density, a rose diagram can be formed.

I can use any of the attributes (moveout, amplitude, gradient and velocity) to estimate fracture strike. So there are four possible ways to calculate fracture orientations. These angles should be the same for synthetic data, but may be different for real data because the travel time may be affected by incorrectly statics correction, velocity may be affected by the structure dipping, amplitude may be affected by attenuation and all these attributes may be affected by anisotropic overburden.

3.7.2 Robust AVO analysis

Among attributes amplitude, travel time, gradient and velocity, amplitude / gradient is clearly more sensitive to any noise interruption than the other two. When the reflector of a target layer is not smooth, the reflection scatter may also affect the AVO trend. A sensitivity test of the AVO analysis is thus necessary.

For comparison with field data, the source-receiver (S-R) configuration in Figure 3.18 should be used in my modelling. First, a uniformly defined CMP gather is extracted from which a common offset supergather may be formed. There are a

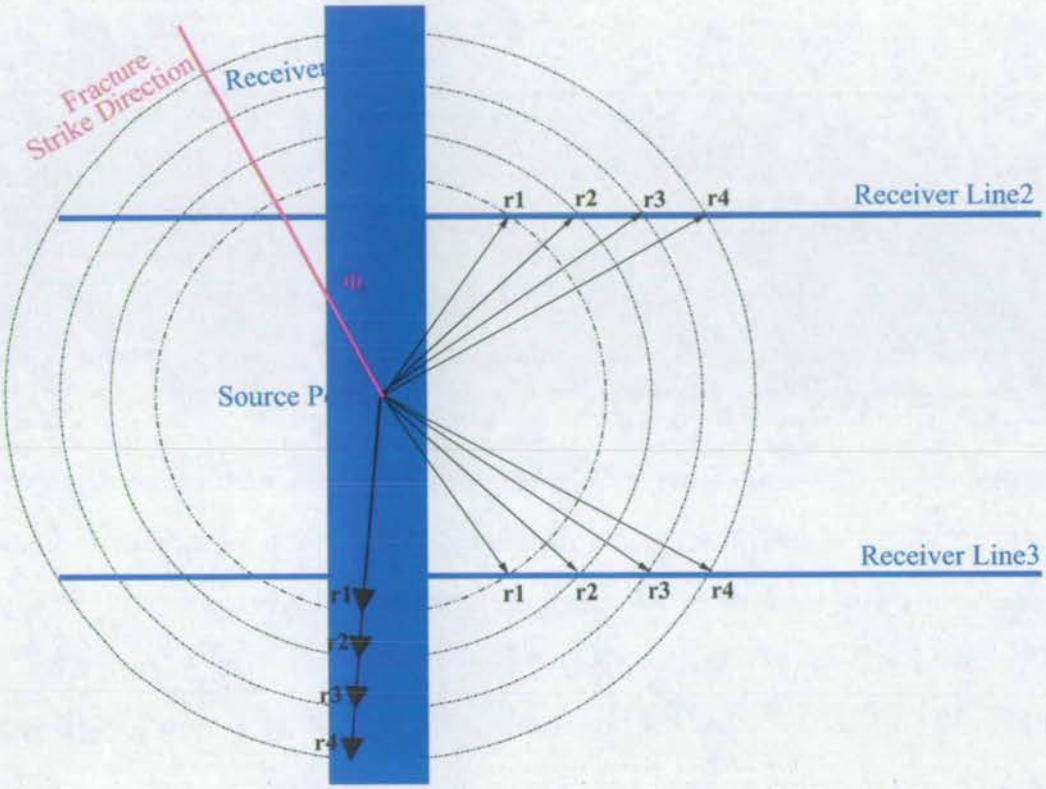

Figure 3.18: Special three lines configuration. *Line*2 || *Line*3. The source point is located only on line 1. r1, r2, r3 are three offset instances. If a CMP point is in the same position as the Source Point and such a CMP gather exists, a serial of fracture orientation angles could be calculated from its sorted offset gathers.

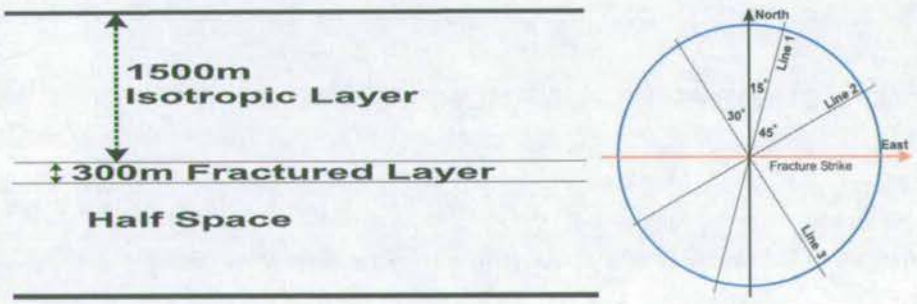

Figure 3.19: Assuming a three layers model (Left). The lines intersected each other and were distributed in azimuthal directions of -30^0, 15^0 and 60^0 respectively (Right). The designed fracture strike is in an East-West direction (Azimuth=90^0).

total of sixty common-offset traces. There is one trace in each azimuth along Lines 1, 2 and 3, and the total number of traces is three for each offset. If more than one trace is found in each azimuth, a least-squares fitting method is used to obtain the best solution. Therefore sixty common-offset gathers will lead to sixty estimated orientations, and the results are then plotted in a rose diagram. In the test examples, random noise is added. I add different levels of noise to the same synthetic data, and repeat the processing procedure, and finally I obtain a suite of rose diagrams. The sensitivity of this method to noise is shown by comparing all the rose diagrams containing different levels of noise. The construction of a synthetic record for the configuration as shown in Figure 3.18 is very time consuming, instead the same model with three-line configuration (Figure 3.19) is used here.

I have tested the method by systematically adding random noise of 0%, 10%, 20%, 30%, 50% to the same supergather, and the results are shown in Figures 3.20 and 3.21. These figures show that the azimuthal anisotropy parameters estimation technique using amplitude information is not affected seriously by random noise. Even when 100% random noise is added to the synthetic data, the main fracture orientation can still be estimated. If there were more traces in each azimuthal direction, the calculated result would be improved (Figures 3.22), but not by much.

3.8 Discussion and conclusions

So far, I have presented a four-line configuration for fracture detection using P-wave attributes such as traveltime and amplitude. For this configuration, there are a few special features worth noting. Firstly, for the nearest line to the fracture normal, the NMO velocity must be the smallest. If this velocity is used for NMO correction, the reflection event in the nearest line will be flat, but the reflection events of the other three lines will be overcorrected as shown in Figure 3.8. Similarly, for the

(a) 0%

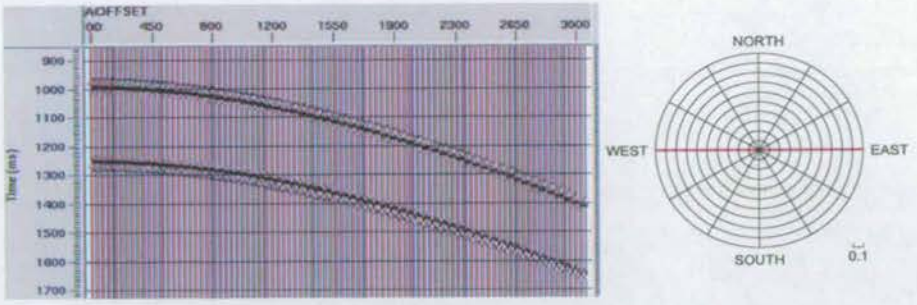

(b) 10%

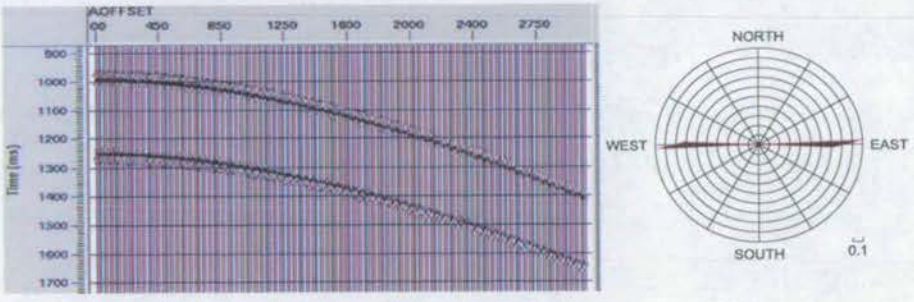

(c) 20%

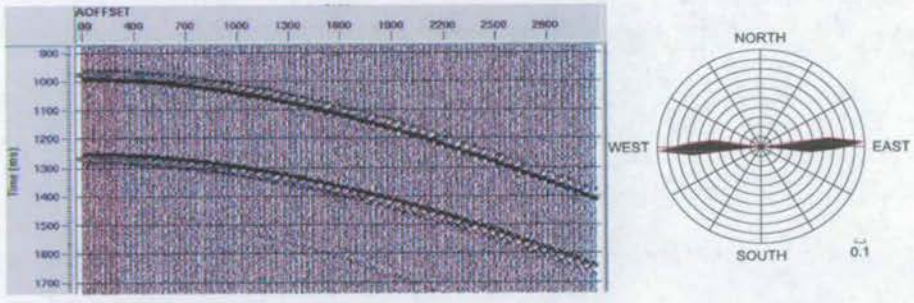

(d) 30%

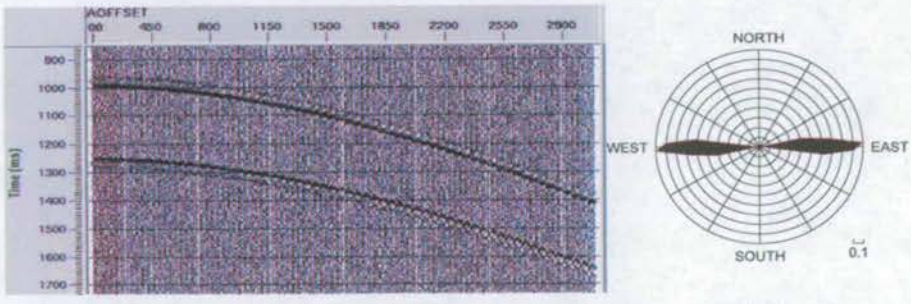

Figure 3.20: Noise test: (a) Noise free synthetic supergather (Left) which contains common-offset traces composed of the three CMP gathers from the three directional lines. All the calculated orientation angles at each offset are shown in the rose diagram (Right). (b), (c) and (d) are the same as (a) but with 10%, 20% and 30% random noise added, respectively.

(a) 50%

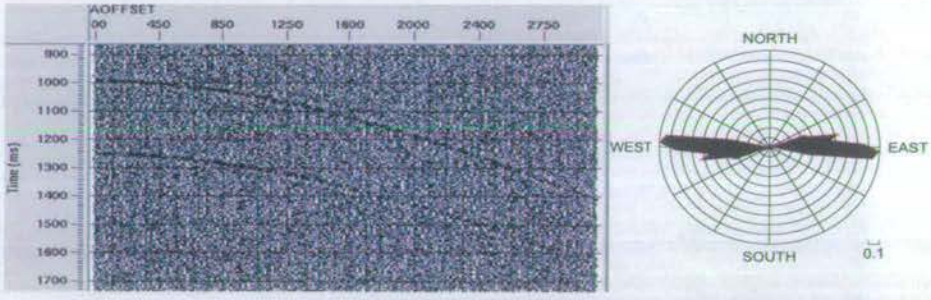

(b) 100%

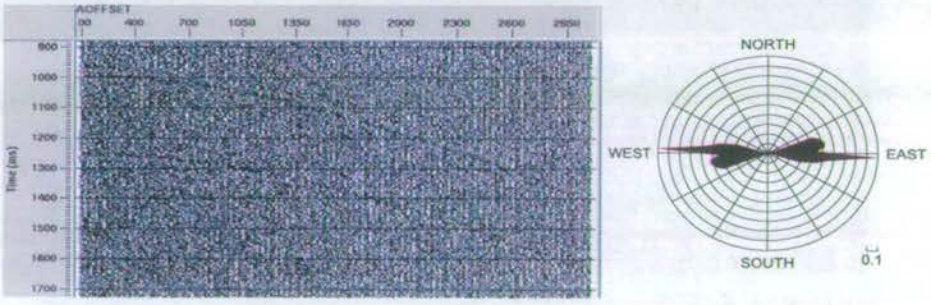

Figure 3.21: (a) and (b) are the same as Figure 3.20 but with 50% and 100% random noise added, respectively.

(a) 3

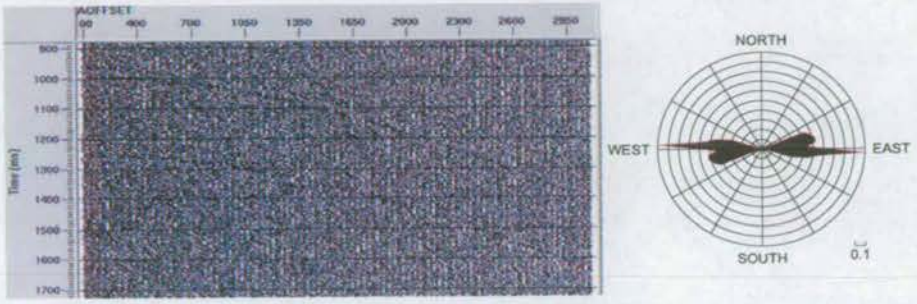

(b) 15

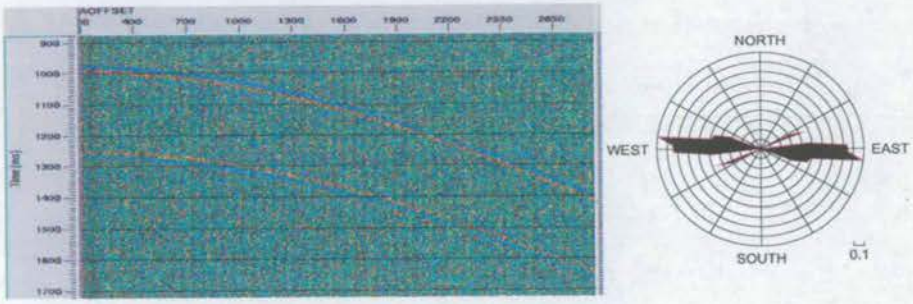

(c) 30

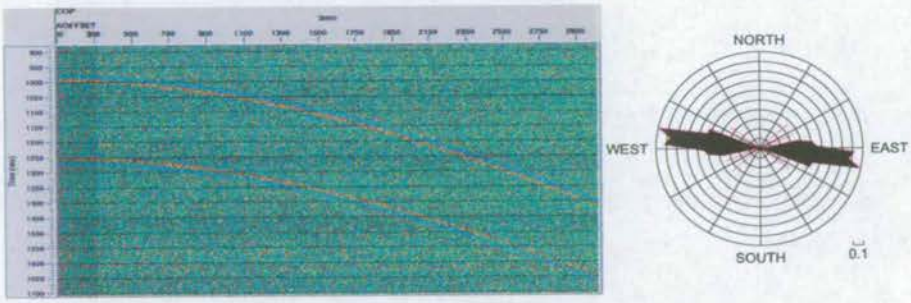

Figure 3.22: Comparison of the effects of the trace numbers within a common offset gather on orientation estimation: (a) 3 traces, (b) 15 traces and (c) 30 traces, respectively.

nearest line to the fracture strike, its NMO velocity must be the biggest one. If this velocity is used for NMO correction, the reflection event in the nearest line to the fracture strike will be flat, but the reflection events of the other three lines will be undercorrected. In my synthetic example shown in this chapter, I use the line which possesses the smallest NMO velocity as Line 1. So, the calculated angle is the fracture normal. Of course, one can also redefine the line order and use Lines 2 or 3 as the starting point 1, one can then calculate the fracture strike. A positive calculated angle means that the fracture normal is actually in the same direction as assumed.

Secondly, note that the same fracture normals are calculated from the four different P-wave azimuthal attributes (moveout, amplitude, AVO gradient and velocity). Although the four methods may give the same result, the requirements for applying them to real data are different. For example, traveltime or velocity is usually more robust but it requires targets to be sufficiently thick, whilst the amplitude or AVO gradient is usually more sensitives and requires good signal to noise ratio, but it may be possible to apply the amplitude and gradient techniques to thin reservoirs.

Thirdly, we find that both of the analyses of AVAZ and TVAZ are robust and even through the picking error is as large as 100% of the maximum azimuthal variation, it is still possible to infer the real fracture parameters.

Finally, the accuracy of these methods is very dependent on the offset coverage, as shown in Figures 3.13c and 3.14c. Often the larger the offset is, the higher the accuracy is. Generally it is required that the ratio of offset to the depth of target is greater than 0.6.

I conclude from the study in this chapter that fracture orientation can be determined using P-wave different attributes using a four-line configuration, the four lines forming two orthogonal pairs at the interesting point, and the four attributes that are: traveltime(or moveout), amplitude, velocity and AVO gradient. The fracture

orientation at the intersecting point can be obtained by cross-plotting the traveltime or amplitude differences between the two orthogonal pairs. It can also be directly calculated from the velocity difference or AVO gradient difference between the orthogonal pairs.

Compared with the traditional three-line configuration, the four-line configuration is more robust and accurate to fracture detection than three-line configuration. The three-line method considers only elliptical variations (the $\cos 2\varphi$ term only), and is strictly valid only for NMO velocity and AVO gradient. In contrast, the four-line method also considers the $\cos 4\varphi$ term, and can be applied directly to traveltime or amplitude.

The methods have been tested using synthetic data. Real data applications are shown in Chapter 6 and 7, after examining two special issues: the layer stripping covered in Chapters 4 and 5, respectively. For multi-azimuth coverage (more than four), least-squares surface fitting may be used. This is discussed in detail in Chapter 8.

Chapter 4

Layer Stripping for Azimuthal Attribute Analysis

Abstract

This chapter presents a layer-stripping procedure to determine interval measurements of fracture parameters in multi-layered fractured media with vertically varying strike direction. The procedure is based on the P-wave traveltime difference between two orthogonal seismic survey lines, and this difference is referred to as the P-wave azimuthal moveout response (AMR). The interval AMR of a fracture target for a fixed offset is a function of $\cos 2(\varphi - \Phi_i)$ with respect to the line azimuth φ and the fracture-strike azimuth Φ_i when there is no polar anisotropy. Consequently two pairs of orthogonal survey lines can be used to determine the local fracture strike Φ_i if the interval AMR of the target is known.

In the case of a weakly fractured overburden (about 3% azimuthal anisotropy or less) underlain by a heavily fractured target (about 10%), the layer stripping can be achieved through the alignment of the top-target event by performing NMO-correction separately for all survey lines. The interval AMR of the target layer may

then be calculated from the residual moveout of the bottom-target event, if there is any. In general, a ray tracing procedure, similar to that used in AVO analysis, is required to perform effective layer-stripping. Full-wave modelling using ANISEIS is used to verify and illustrate these procedures.

4.1 Introduction

Chapter 3 considers only an isotropic layer overlying the fractured target. When there are more than one azimuthally anisotropic layers overlying the target layer, the observed azimuthal variation of attributes consist of the accumulated variations of all the layers. This makes azimuthal attribute analysis difficult. To determine the anisotropy strength of the underlying target layer, one must first know the fracture parameters for all the overburden layers, i.e., a layer stripping technique must be applied. Theoretically, all the attributes can be used to estimate the azimuthal parameters layer by layer.

Li (1999) presented an approach for fracture detection in marine streamer data, as part of an overall effort intended to overcome some of the practical difficulties often encountered in the use of azimuthal P-wave AVO and NMO velocity analysis (Al-Dajani and Alkhalifah, 1997). The new approach is based on the P-wave travel-time (moveout) difference between two orthogonal survey lines, and this difference is referred to as the P-wave azimuthal moveout response (AMR, as discussed in Chapter 3). This approach requires a configuration of four intersecting survey lines which form two orthogonal pairs. The fracture orientation can be obtained by analysing the cross-plot of the two corresponding AMRs. This technique is straightforward and is particularly useful in marine exploration with repeated surveys of various vintages where continuous azimuthal coverage is often not available. However, this technique, as originally formulated, is restricted to an azimuthally isotropic overburden.

Here, I extend the above approach to media with vertically varying fracture orientation. I present analytical expressions for quantifying the interval AMR of any given layer in the multi-layered media. Layer-stripping procedures are then formulated to obtain the interval AMR. Cross-plotting analysis may then be performed on these interval AMRs to obtain the local fracture orientation. Full-wave modelling and synthetic data examples are used to illustrate the methodology.

4.2 AMR analysis: multi-layered media

In Chapter 3, I introduced the algorithm to calculate fracture parameters in a single azimuthal layer using orthogonal lines. Here I consider the more general case of multi-layered fractured TIH media with arbitrary fracture orientations, and the case with uniform fracture orientation is treated as a special case. I first introduce the traveltime equation and the concepts of total and interval AMRs, and then derive the expressions for these AMRs which are needed to establish the layer-stripping procedure.

4.2.1 Traveltime equation

Consider multi-azimuth seismic surveys over a stack of n TIH layers with arbitrary fracture orientations. Assume a reflection ray from the bottom of the n-th layer with offset x at the k-th line with azimuth angle φ from North. This ray is referred to as $L_{nk}(x)$ (Figure 4.1). Here I compute the traveltime, $t(\varphi, x)$, from the bottom of the n-th layer for offset x and for the k-th line azimuth at angle φ from North [ray $L_{nk}(x)$, Figure 4.1].

For the i-th layer, I introduce the following azimuthally-invariant interval properties: V_{p0i}, vertical P-wave velocity; t_{0i}, one-way zero-offset traveltime; ε_i and δ_i, Thomsen's parameters; Φ_i, fracture-strike azimuth from North. For the ray segment

in the i-th layer corresponding to the k-th line-azimuth, I use x_{ki} and θ_{ki} as the horizontal component and incidence angle of the ray segment, respectively, and t_{ki} as the traveltime along the ray segment (Figure 4.1b).

The total traveltime $t(\varphi, x)$ for the given ray $L_{nk}(x)$ is, as shown in Figure 4.1,

$$t(\varphi, x) = 2\sum_{i=1}^{n} t_{ki} \ , \tag{4.1}$$

where offset x satisfies,

$$x = 2\sum_{i=1}^{n} x_{ki}. \tag{4.2}$$

Equation (4.2) implies that the ray is confined to the incident plane and is valid only for weak azimuthal anisotropy. t_{ki} can be written as equation 3.5

$$\begin{aligned} t_{ki} &= \sqrt{t_{0i}^2 + \frac{x_{ki}^2}{V_{p0i}^2}} \left[1 - (\delta_i - 2\varepsilon_i)\sin^2\theta_{ki}\sin^2(\varphi - \Phi_i)\right. \\ &- \left.(\varepsilon_i - \delta_i)\sin^4\theta_{ki}\sin^4(\varphi - \Phi_i)\right]. \end{aligned} \tag{4.3}$$

Let's introduce $t_{\|i}$ and $t_{\perp i}$ as the traveltime inside the i-th layer for the survey lines parallel and perpendicular to the fracture strike of the i-th layer, respectively, and $x_{\|i}$, $\theta_{\|i}$, $x_{\perp i}$ and $\theta_{\perp i}$ as the corresponding ray-segment components with the same total offset x. To the first order of the anisotropy parameters, I obtain,

$$t_{\|i}(x_{\|i}) = \sqrt{t_{0i}^2 + \frac{x_{\|i}^2}{V_{p0i}^2}} \ , \tag{4.4}$$

$$t_{\perp i}(x_{\|i}) = t_{\|i} - t_{\|i}(\delta_i - 2\varepsilon_i)\sin^2\theta_{\|i} - t_{\|i}(\varepsilon_i - \delta_i)\sin^4\theta_{\|i} \ , \tag{4.5}$$

and

$$t_{ki}(x_{\|i}) = t_{\|i}\cos^2(\varphi - \Phi_i) + t_{\perp i}\sin^2(\varphi - \Phi_i)$$

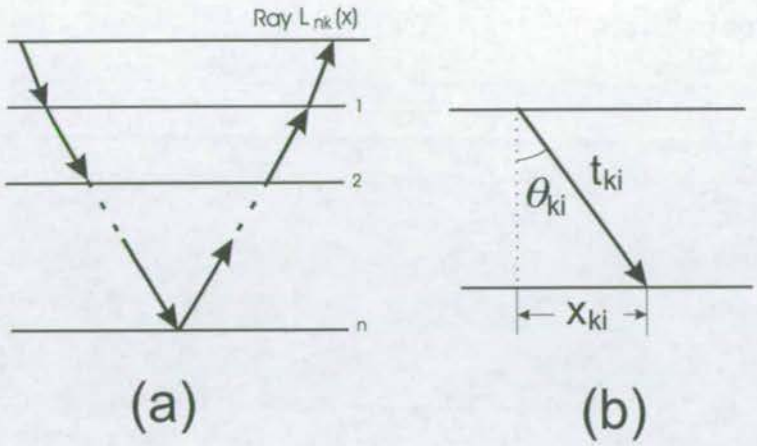

Figure 4.1: (a) A cross-section of multi-layered azimuthally anisotropic media. $L_{nk}(x)$ marks the ray path at offset x from the bottom of the $n-th$ layer for the $k-th$ line azimuth in a multi-azimuthal survey. (b) The down-going ray segment components for the $l-th$ layer.

$$+ \quad t_{\|i}(\varepsilon_i - \delta_i)\sin^4\theta_{\|i}\sin^2(\varphi - \Phi_i)\cos^2(\varphi - \Phi_i) \tag{4.6}$$

These lead to,

$$\begin{aligned} t(\varphi,\, x) &= 2\sum_{i=1}^{n} t_{ki} = 2\sum_{i=1}^{n}\left[t_{\|i}\cos^2(\varphi - \Phi_i) + t_{\perp i}\sin^2(\varphi - \Phi_i)\right] \\ &+ 2\sum_{i=1}^{n} t_{\|i}(\varepsilon_i - \delta_i)\sin^4\theta_{\|i}\sin^2(\varphi - \Phi_i)\cos^2(\varphi - \Phi_i) \\ &- 2\sum_{i=1}^{n}\frac{\sin\theta_{\|i}}{V_{p0i}}x_{\|i}V_{\perp i}\sin^2(\varphi - \Phi_i)\ . \end{aligned} \tag{4.7}$$

Note that the only azimuthal variable in the above equation is line azimuth φ and fracture strike azimuth Φ_i. Thus it is possible to use different azimuthal lines to recover fracture parameters.

4.2.2 Total AMR

The total AMR for the stack of n layers associated with ray $L_{nk}(x)$ is defined as:

$$\Delta t_{1n}(\varphi,\, x) = t(\varphi + \pi/2, x) - t(\varphi, x), \tag{4.8}$$

where $t(\varphi, x)$ is the traveltime for the k-th line azimuth and $t(\varphi + \pi/2, x)$ is the traveltime for the line perpendicular to the k-th line azimuth. Subscript $1n$ denotes that the AMR is defined from layer "1" to layer n.

Noting equation (4.7) gives,

$$\begin{aligned}
\Delta t_{1n}(\varphi,\, x) &= t(\varphi + \pi/2, x) - t(\varphi, x) \\
&= 2\sum_{i=1}^{n}\left(t_{\perp i} - t_{\|i} - \frac{\sin\theta_{\|i}}{V_{p0i}} x_{\|i} V_{\perp i}\right)\cos 2(\varphi - \Phi_i) \\
&+ 2\sum_{i=1}^{n}\frac{\sin\theta_{\|i}}{V_{p0i}} x_{\|i}(V'_{ki} - V_{ki}).
\end{aligned} \tag{4.9}$$

Using equations (4.4) and (4.5) yields

$$\Delta t_{1n}(\varphi, x) = \sum_{i=1}^{n} B_i(\varepsilon_i, \delta_i, x_{\|i})\cos 2(\varphi - \Phi_i), \tag{4.10}$$

where

$$B_i(\varepsilon_i, \delta_i, x_{\|i}) = \frac{2x_{\|i}}{V_{p0i}}\sin\theta_{\|i}\left[2\varepsilon_i - \delta_i - (\varepsilon_i - \delta_i)\sin^2\theta_{\|i}\right]. \tag{4.11}$$

Note that the ray-segment components $x_{\|i}$ and $\theta_{\|i}$ are used in all the above equations, and should be evaluated at the azimuthal direction parallel to the local fracture strike.

4.2.3 Interval AMR

Since equation (4.11) has the same form as the single-layer case (Equation 3.12), but in terms of the local interval quantities at the direction parallel to the fracture strike, I then define,

$$\Delta t_i(\varphi - \Phi_i, x_{\|i}) = B_i(\varepsilon_i, \delta_i, x_{\|i}) \cos 2(\varphi - \Phi_i), \tag{4.12}$$

as the interval AMR for the i-th layer. Comparing the definition of (4.12) with the single-layer response equation (3.11) in Chapter 3 reveals that the interval AMR is the traveltime difference between two-orthogonal lines within the i-th layer with offset $x_{\|i}$.

Thus, the total AMR for the stack of n layers is the sum of the interval AMR for each individual layer,

$$\Delta t_{1n}(\varphi, x) = \sum_{i=1}^{n} \Delta t_i(\varphi - \Phi_i,\ x_{\|i}), \tag{4.13}$$

where offset x satisfies,

$$x = 2\sum_{i=1}^{n} x_{\|i}, \tag{4.14}$$

Note that equation (4.14) implies that the ray is confined to the incident plane and is only valid for weak azimuthal anisotropy.

As the interval AMR Δt_i also shows $\cos 2\varphi_i$ variations, where $\varphi_i = \varphi - \Phi_i$, the same four-line configuration and cross-plotting procedure as in the single-layer case can be used to determine the local fracture orientation φ_i, if Δt_i can be extracted from the total AMR (4.13) by some form of layer stripping. Also as equations (4.4), (4.5), and (4.6) all have the same form as the single-layer case, the same procedure as in the single-layer case can also be used to estimate $t_{\|i}$ and $t_{\perp i}$, and to obtain the fracture intensity.

4.3 Special cases: uniform fracture orientation and isotropic ray tracing

4.3.1 Uniform fracture orientation

Assume the target fractured layer is the n-th layer in the media. For the special case of multi-layered media with a uniform fracture-strike azimuth $\Phi_i \equiv \Phi$. Total AMR in equation (4.9) is reduced to

$$\begin{aligned}\Delta t(\varphi, x) &= 2\cos 2(\varphi-\Phi)\sum_{i=1}^{n}\left(t_{\perp i}-t_{\|i}\right) - 2p\cos 2(\varphi-\Phi)\sum_{i=1}^{n} x_{\|i}V_{\perp i} \\ &= (t_\perp - t_\|)\cos 2(\varphi-\Phi) = B(x,\varepsilon,\delta)\cos 2(\varphi-\Phi) \qquad (4.15)\end{aligned}$$

Note that $\sum_{i=1}^{n} x_{\|i}V_{\perp i} \equiv 0$. If the target layer is embedded in an azimuthally isotropic background, $B(x,\varepsilon,\delta)$ is evaluated locally at the fractured target,

$$B(x,\varepsilon,\delta) = B_n = \frac{2x_{\|n}}{V_{p0n}}\sin\theta_{\|n}\left[2\varepsilon-\delta-(\varepsilon-\delta)\sin^2\theta_{\|n}\right]. \qquad (4.16)$$

Equation (4.16) has exactly the same form as the single-layer medium (Equation 3.12). Thus, the same analysis procedure derived for a single-layer can also be used for multi-layered media with uniform fracture orientation. In this case, layer stripping is not required to estimate the fracture orientation, but is required to invert for the anisotropic parameters.

4.3.2 Isotropic ray tracing

For the i-th layer (Figure 4.1), I introduce x_i and θ_i as the ray-segment components obtained by isotropic ray tracing. For weak anisotropy, x_i and θ_i satisfy,

$$x_{\|i} = x_i(1+V_i); \quad \theta_{\|i} = \theta_i + \Delta\theta_i, \qquad (4.17)$$

where V_i and $\Delta\theta_i$ are small quantities of the same order as the anisotropic parameters ε_i and δ_i. Substituting equation (4.17) into (4.11), and linearizing over the small quantities gives

$$B_i(\varepsilon_i, \delta_i, x_i) = \frac{2x_i}{V_{p0i}} \sin\theta_i \left[2\varepsilon_i - \delta_i - (\varepsilon_i - \delta_i)\sin^2\theta_i\right]. \tag{4.18}$$

Thus, isotropic ray tracing can replace anisotropic ray tracing to obtain the ray segment components, and the error introduced into the AMR is of the second-order of the anisotropic parameters.

4.4 Layer-stripping procedures and results

4.4.1 Layer-stripping using isotropic ray tracing

From equations (4.12) and (4.13), one can see that the layer-stripping requires knowing the ray-segment components $x_{\|i}$ and $\theta_{\|i}$. Accurately determining these ray-segment components requires anisotropic ray tracing. Since the anisotropic parameters are unknown at this stage of data processing, anisotropic ray tracing is thus not feasible. Fortunately, as shown in equation (4.18) in the previous section, the error introduced into the AMRs by performing isotropic ray tracing is of second-order in terms of the anisotropic parameters. Thus, for multi-layered weakly TIH media, we may use the isotropic ray tracing, in a similar way to AVO analysis, to perform layer stripping. The full layer-stripping procedure may be summarized as follows:

Data preparation

1. Locate four CMP gathers at the intersecting point of the four orthogonal lines (Figure 3.2), and perform velocity analysis for each CMP gather separately to

build an optimum velocity model.

2. Pick traveltimes for the four CMP gathers without NMO correction and build the traveltime table for all layers.

3. Perform isotropic ray-tracing and build an offset/ray-segment-component table for each layer.

4. For layer 1,

$$\Delta t_1^{31}(x) = line\,3\,(layer\,1) - line\,1\,(layer\,1)$$

$$\Delta t_1^{42}(x) = line\,4\,(layer\,1) - line\,2\,(layer\,1)$$

perform cross-plot analysis using the single-layer method to determine Φ_1, and store $\Delta t_1^{31}(x)$ and $\Delta t_1^{42}(x)$ in a table for future use.

Main stripping loop

1. For layer 2, select one of the orthogonal pairs (for example lines 1 and 3) and calculate

$$\Delta t_{12}^{31}(x) = line\,3\,(layer\,2) - line\,1\,(layer\,2) = \Delta t_1^{31}(x_1) + \Delta t_1^{31}(x_2)$$

where x_1 and x_2 are the ray segment components in layers 1 and 2 respectively, calculated in preparation step 3.

2. From the offset-$\Delta t_1(x)$ table stored in preparation step 4, estimate $\Delta t_1^{31}(x_1)$, calculate

$$\Delta t_2^{31}(x_2) = \Delta t_{12}^{31}(x) - \Delta t_1^{31}(x_1)$$

and store the results in a table for future use.

3. Repeat the above procedures for lines 2 and 4, and obtain $\Delta t_2^{42}(x_2)$.

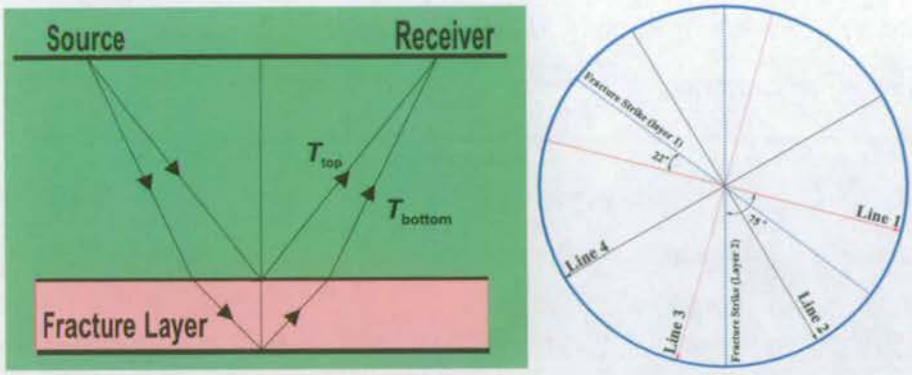

a) b)

Figure 4.2: (a) A cross section of a two-layer model for illustrating overburden correction. The model consists of a fractured target overlain by an azimuthally anisotropic overburden. (b) A plan view of a multi-azimuthal survey. The survey consists of four intersecting lines forming two orthogonal pairs.

4. Cross plot the two interval AMRs, Δt_2^{31} and Δt_2^{42} to determine Φ_2.

5. Repeat the above four steps for the remaining layers.

4.4.2 Layer-stripping using NMO correction

Frequently, we may approximate multi-layered TIH media in terms of an overburden underlain by a target layer with respect to the vertical variation of the azimuthal anisotropy (Figure 4.2). In this way, the layer-stripping is reduced to a form of overburden correction. For a weakly anisotropic overburden with its thickness far greater than the thickness of the target layer and with weak impedance contrast, this overburden correction of azimuthal anisotropy may be accomplished simply by NMO correction within the conventional near-to-mid offset ranges. This is because, in such a case, x_1 is often far greater than x_2. Thus one may approximate $\Delta t_1(x_1)$ by

$$\Delta t_1(x_1) \approx \Delta t_1(x), \tag{4.19}$$

whilst $\Delta t_1(x)$ can be compensated for by NMO correction alone. The procedure can be summarized as follows.

1. Locate four CMP gathers at the intersection point, and carefully select the overburden and target horizons.

2. Perform velocity analysis and NMO correction to the overburden horizon for each CMP gather separately, so that the overburden horizons in all four gathers are aligned properly. In this way, the azimuthal AMR in the overburden is completely removed.

3. Apply NMO correction to the target horizon (the bottom of the target) using the same velocity as the overburden, so that the amount of moveout removed from the target horizon is almost the same as $\Delta t_1(x)$.

4. Pick the residual moveout for the target horizon. Using equations 3.3 and 3.4 gives

$$\Delta t_1^{31}(x) = \textit{Residual moveout}\ (\textit{line}\ 3) - \textit{Residual moveout}\ (\textit{line}\ 1)$$

$$\Delta t_1^{42}(x) = \textit{Residual moveout}\ (\textit{line}\ 4) - \textit{Residual moveout}\ (\textit{line}\ 2) \qquad (4.20)$$

5. Perform cross-plotting of $\Delta t_2^{31}(x)$ and $\Delta t_2^{42}(x)$ to quantify the fracture strike of the target.

4.4.3 Testing with full-wave synthetic data

A three-layer model is constructed to illustrate the layer-stripping procedure using full-wave synthetics calculated using the reflectivity method (Taylor 1990). As shown

Layer 1: Fractured	ρ=2.3 g/cm^3, $v_p = 3048m/s$, $v_s = 1574m/s$. Aspect ratio: 0.01, Crack density: 10% . Thickness=1.5km	Strike 75°
Layer2: Fractured	ρ=2.19 g/cm^3, $v_p = 2183m/s$, $v_s = 1502m/s$ Aspect ratio: 0.01, Crack density: 10% . Thickness=0.3km	Strike 45°
Layer3: Isotropic	ρ=2.3 g/cm^3, $v_p = 3048m/s$, $v_s = 1574m/s$. Half space	n/a

Table 4.1: The elastic parameters for the model in Figure 4.2 a. Layer 1 is a fractured overburden, layer 2 is the fractured target and layer 3 is an isotropic basement.

in Table 4.1 and Figure 4.2a, the first layer is 1500m thick, representing a weakly anisotropic overburden with 3% azimuthal anisotropy and a fracture strike of 22° from line 1. The second layer is 300m thick, representing a fractured target with 10% azimuthal anisotropy and a fracture strike of 75° from line 1. The four lines are separated by 45° ($\Phi_0 = 45°$, Figure 4.2b). The calculated CMP gathers at the intersecting point of the four lines are shown in Figure 4.3, and traveltime picks of the top- and bottom-target events are marked with red and the blue lines, respectively.

First, I apply the single-layer method to each individual event. From the traveltime picks, I calculate Δt_1^{31}=line 3-line 1 and Δt_1^{42}=line 4-line 2 for the top event, and Δt_{12}^{31}=line 3-line 1 and Δt_{12}^{42}=line 4-line 2 for the bottom event. Noting $\Phi_0 = \pi/4$ here, I cross-plot Δt_1^{31} versus t_1^{42}, Δt_{12}^{31} versus t_{12}^{42} (Figures 4.4a and 4.4c). I also calculate the fracture orientation using equation (3.2) for each individual offset (Figures 4.4b and 4.4d).

Figure 4.4a reveals a very good linear trend, confirming the prediction of equation (3.2), and the trend is in a direction of 44° ($2 \times 22°$) and the estimations for each individual offset yield 22° on average. All this agrees with the model parameters (Table 4.1). However, analysis of the bottom event without taking the effects of the anisotropic overburden into account shows a deviated trend (Figure 4.4c) and individual offset estimation gives an average angle of 30°, very close to the fracture orientation in the overburden. This is not surprising since the total AMR for the

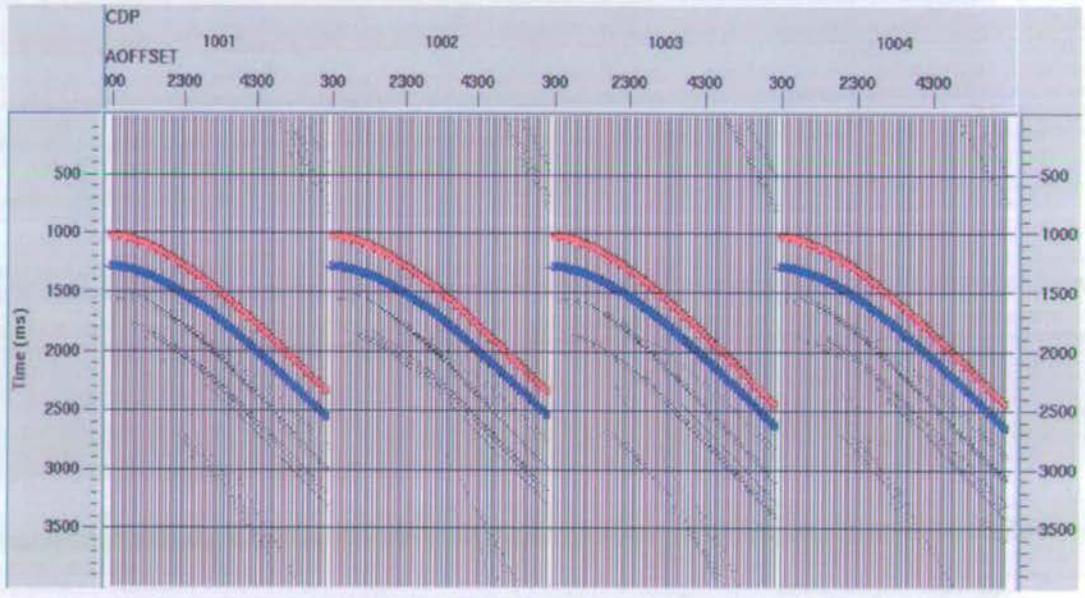

Figure 4.3: The four CMP gathers at the intersection point in Figure 4.2b, calculated for the two-layer model in Figure 4.2a with the parameters listed in Table 4.1. The red line marks the traveltime picks along the top target event and the blue line marks the bottom-target event. The lines are: CMP 1001-line 1, 1002-line 2, 1003-line 3, and 1004-line 4.

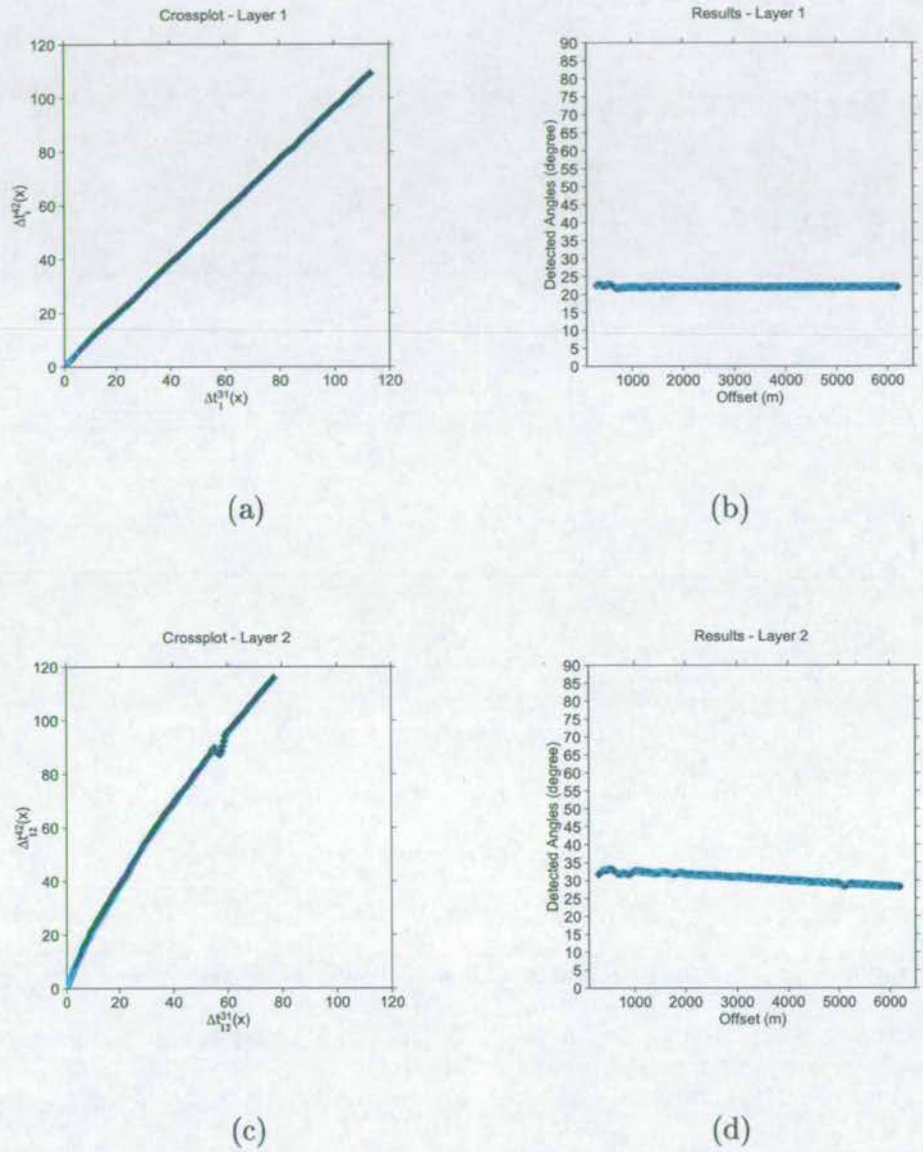

Figure 4.4: AMR analysis using the single-layer method directly without layer-stripping. (a) Cross-plotting of $\Delta t_{12}^{31}(x)$ versus $\Delta t_{12}^{42}(x)$ from the top target event, and (b) the estimating the fracture orientation of the overburden for each individual offset using equation (3.1). (c) and (d) are the same as (a) and (b) but for the bottom-target event.

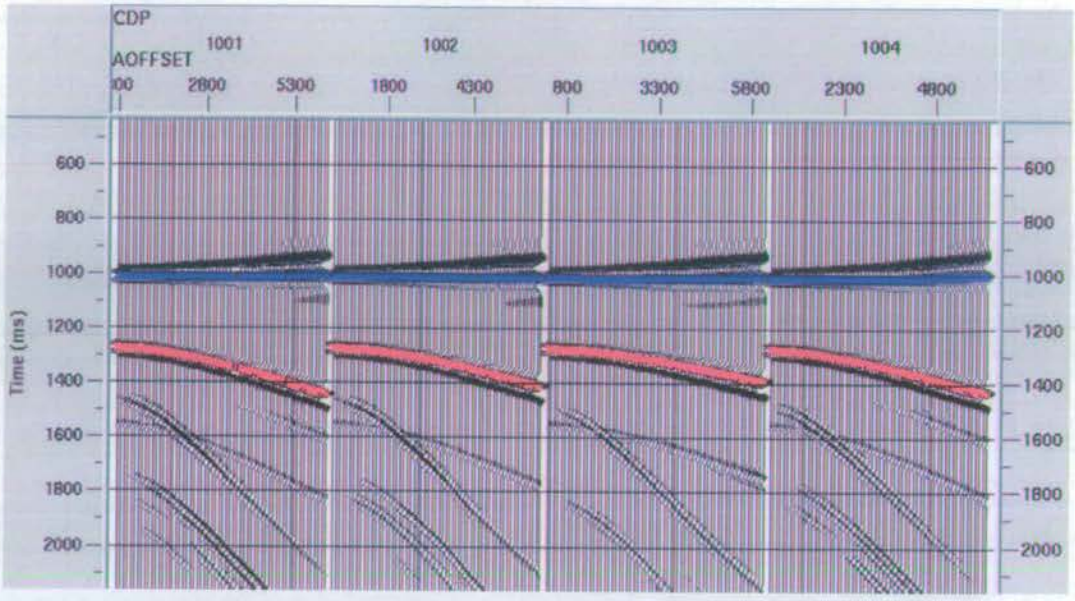

Figure 4.5: The same CMP gathers as in Figure 4.3 but after NMO correction which aligned the top events in all four lines.

two layers is largely due to the overburden because of its thickness.

Second, I perform layer stripping using the ray-tracing procedure in order to estimate the fracture orientation in the target. From the picked travel times and the ray segment components, the interval AMR is calculated: $\Delta t_2^{31}(x_2) = \Delta t_{12}^{31}(x) - \Delta t_1^{31}(x_1)$ and $\Delta t_2^{42}(x_2) = \Delta t_{12}^{42}(x) - \Delta t_1^{42}(x_1)$. The cross-plot and the individual offset estimation are shown in Figures 4.6a and 4.6b. Now the linear trend for the target event is improved with an angle of 150° ($2 \times 75°$) and the average angle from the individual offset estimation is 75°. This confirms the validity of the ray-tracing-based layer-stripping procedure.

Thirdly I perform the overburden-correction procedure based on NMO correction. Figure 4.5 shows the NMO corrected CMP gathers. The top events in all four lines are reasonably flat and show almost no azimuthal variation, that is, the AMR of the overburden is fully compensated. However, there are significant residual moveouts in the bottom target events, which also clearly display azimuthal varia-

tions. The picked residual moveout of the bottom target was then input to equation (4.20) to calculate the interval AMR. Figures 4.6c and 4.6d show the cross-plot and the estimation for each offset. The cross-plot shows a slightly degraded linear trend. However, the overall trend direction is 150° and the average angle from each offset is 75°. These results are consistent with the model and the ray tracing result.

To sum up, the analysis of AMRs is a straightforward way to quantify the local fracture orientation. In the presence of azimuthal anisotropy in the overburden, both a ray-tracing procedure and an effective NMO procedure can be used to perform overburden correction. The results after overburden correction are in agreement with the model.

4.5 Discussion and conclusions

Traditionally, azimuthal anisotropy has been largely associated with shear-wave splitting (birefringence). Since the early 1980's, much effort has been focused on the analysis of shear-wave splitting by recording multicomponent shear-wave data (Crampin 1985). These studies revealed that depth dependence of the principal direction of azimuthal anisotropy is common in the Earth's crust, and a layer-stripping process is thus necessary to obtain the interval measurements of azimuthal anisotropy.

In recent years, the use of azimuthally varying information in P-waves for studying azimuthal anisotropy has become common practice. However, all of these studies assumes either an azimuthally isotropic overburden, or a depth-invariant principal direction of azimuthal anisotropy. To overcome this restriction, Grechka and Tsvankin (1998b) extend the NMO approach of Tsvankin (1995) to vertically inhomogeneous anisotropic media. In practice, the NMO approach requires careful data processing to minimise the error propagation and magnification through various

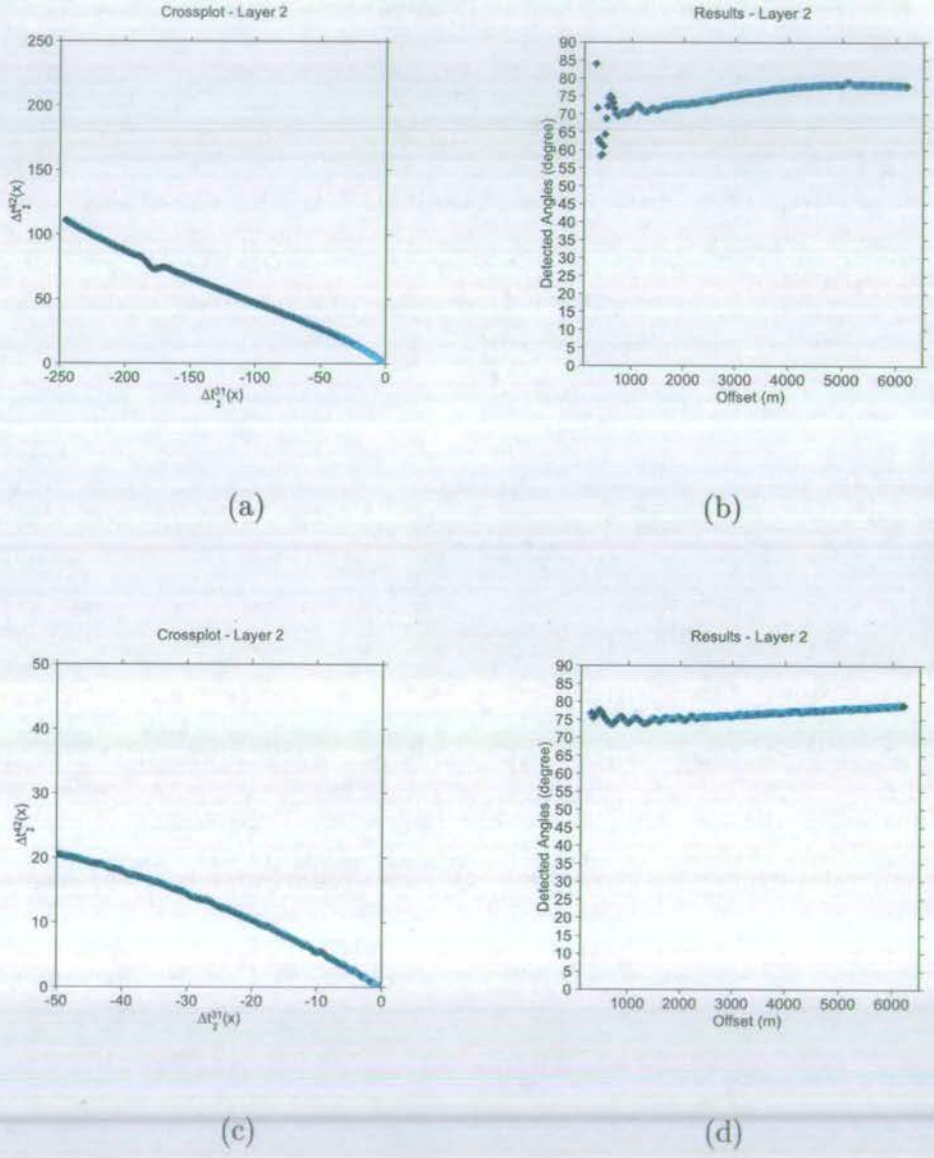

Figure 4.6: Analysis results for the fractured target after layer-stripping. (a) and (b) are the results using a ray-tracing procedure; (c) and (d) are those with NMO correction procedure.

processing steps (Al-Dajani and Alkhalifah, 1997), and this limits the application of the technique to some extent. In this chapter, I have presented an alternative approach based on the P-wave azimuthal moveout response to achieve layer stripping of azimuthal anisotropy. The interval AMR for a fixed offset is a function of $\cos(\varphi - 2\Phi_i)$ with respect to line azimuth φ and fracture strike azimuth Φ_i in multi-layered azimuthal anisotropic media with vertically varying fracture orientations. Thus the cross-plot of two corresponding AMRs from two pairs of orthogonal lines can be used to determine the local fracture orientation $\varphi_i = \varphi - 2\Phi_i$, if the interval AMR can be extracted from the moveout data. In the real data application, the picking of amplitude and traveltime from the moveout data may bring some picking errors. The sensitivity of the detected results to picking error has been discussed in Chapter 3.6 (Figures 3.15 and 3.16) for isotropic overburden case. In the case of weak anisotropy overburden, I believe that this stripping technology have similar sensitivity to the picking error as discussed above. The removal of background noises and trace interpolation using a fine sample interval are the two major measures to reduce picking errors, which may create a better error histogram and a better fracture estimation.

In the case of a weakly fractured overburden underlain by a heavily fractured target, the layer-stripping can be effectively achieved using normal moveout correction. Each line should be processed separately so that the top event of the target is properly aligned. The residual moveout of the bottom target event, after the moveout correction, can then be used to calculate the interval AMR. In general, in a similar way to AVO analysis, the ray tracing can be used to calculate the ray segment components in each layer using the velocity model built from stacking velocity analysis, and layer-stripping can then be performed using these ray-segment components.

Chapter 5

Effects of Thin Layering on AVO/AVOZ

Abstract

This chapter is dedicated to the discussion of the thin layering problem. Using the picked amplitude as the effective reflection coefficient is a normal procedure in current AVO (amplitude versus offset) and AVOZ (amplitude versus offset and azimuth) analysis. This substitution may give serious errors in the presence of thin layers because of the discrepancies between picked amplitudes and expected reflection coefficients. Those discrepancies have been discussed in the literature (Swan, 1991; Dong, 1999). However, I still feel that it is helpful to produce 3D (time, thickness, offset) and 4D (time, thickness, offset, azimuth) synthetic datasets covering the thickness and incidence ranging from 0.01λ to 10λ and from zero to the critical angle, respectively, to understand the effects of thin layering on AVO, AVOZ and the fracture characterisation (Here $\lambda = 88$m is the dominant wavelength with centre frequency of 25 Hz, wave speed of 2180m/s). In this chapter, I discuss the effects of the discrepancies on both isotropic and azimuthal AVO analysis, and the

estimation of anisotropic parameters. A range of thickness models is constructed by sandwiching an isotropic or anisotropic layer between two isotropic layers. Full-wave seismograms are calculated for each of these models. From these gathers I study the effects of thin layers on AVO and AVOZ. I then apply azimuthal AVO analysis to the synthetic seismograms, I find that fracture orientation and intensity can be estimated accurately if the thickness of the thin layers is larger than a quarter of the wavelength. However, there are large discrepancies in the orientation and intensity estimates when the thickness is less than this limit. I finally present a new procedure to improve the detectability of azimuthal anisotropy in the presence of thin layers.

5.1 Introduction

Many methods such as those in Chapters 3 and 4 have been developed for estimation of fracture parameters from P-wave seismic data. However, these methods assume that distinct reflections from the top and bottom of reservoirs can be clearly identified. If a reservoir is thin, it is extremely difficult to pick amplitude and traveltime differences with sufficient precision to characterise the anisotropy, mainly because of interference between the reflections and transmissions from the top and bottom of the layer. This motivates us to study the effects of thin layers on AVO, AVOZ and the estimation of the fracture parameters, to find some other method for identifying intensely fractured zones in thin layers and to estimate lateral changes in fracture strike and intensity.

Thin layers result in distortions both in the amplitude and the phase of reflected waves. Widess (1973) concluded that for layers with thickness less than $\frac{1}{8}$ of the dominant wavelength, the reflected amplitude is less than that expected from a simple interface and this may affect the vertical resolution.

As far as the boundaries of the thin layers are concerned, the vertical resolution

may be defined as the minimum separation between two successive geological interfaces before their separate identity is lost in the resultant seismic data. As far as an object is concerned, it can also be defined at the threshold of detectability as the minimum thickness that a layer must have in order to produce a visible reflection (de Voogd and den Rooijen, 1983). In fracture estimation using interval times, I need to know the boundaries of thin layers. However, in the estimation using amplitudes, I need only the top of the layer to produce a visible reflection, therefore the vertical resolution is sometimes method-dependent.

Slack et al. (1993); Grechka (1998); Dong (1999), Schoenberg (1994) and Schoenberg et al. (1999) have demonstrated that the vertical resolution can be improved by either eliminating the apparent AVO behaviour or building precise new AVO analytic equations. Therefore thin reservoirs may still be detectable using AVO and AVOZ analysis.

In this chapter, beginning with an analysis of the discrepancies between amplitude and reflection coefficient, followed by comprehensive full-wave modelling, I investigate the effect of reservoir thickness on the AVO and AVOZ analysis and the estimation of fracture parameters using synthetic seismograms. I demonstrate that thin layers can have a serious effect on P-wave AVO and AVOZ, and I propose a new procedure to compensate for the effects of thin layers.

5.2 Amplitudes and P-wave AVOZ of thin layers

5.2.1 Seismic amplitude and reflection coefficient

Consider a geological model consisting of a series of horizontally homogeneous layers, i = 1, 2, 3, ...n, and the impulse response of the earth is known,

$$G_{pp}(t),\ t = t_1, t_2, ..., t_n$$

Based on the convolutional model, the noise-free seismic responses S(t) of primary P-wave received on the surface may be be written as

$$S(t) = G_{pp}(t) * W(t), \tag{5.1}$$

where $W(t)$ is the source function or wavelet and * means convolution. $G_{pp}(t) = \{g_{t_1}, g_{t_2}, ..., g_{t_n}\}$ denotes the impulse response time series, or the Green's function of the earth which is determined by the source and receiver geometry and the properties of the media. g_{t_i} is the response coefficient from *ith* layer. I use $R_{k(k+1)}$ and T_{jk} to denote the reflection coefficient at the interface of layer k and (k+1), and the transmission coefficient from layer j to k, respectively. Then g_{t_i} (i=1,2,.....,n) are listed as the following (only primary P-waves are considered, that is, interval multiples, converted waves are ignored) :

$$\begin{cases} g_{t_1} = R_{12} \\ g_{t_2} = R_{23}T_{12}T_{21} \\ g_{t_3} = R_{34}T_{12}T_{23}T_{32}T_{21} \\ ..... \\ g_{t_n} = R_{n(n+1)} \prod_{k=1}^{k=n-1} T_{k(k+1)} \prod_{k=n-1}^{k=1} T_{(k+1)k} \end{cases} \tag{5.2}$$

$G_{pp}(t)$ can be rewritten as

$$G_{pp}(t) = [g_{t_1}, g_{t_2}, g_{t_3}....., g_{t_n}]$$
$$= G_{pp1}(t) + G_{pp2}(t) + ... + G_{pp(n-1)}(t) + G_{ppn} \quad (t) \tag{5.3}$$

$$\begin{cases} G_{pp1(t)} = [g_{t_1}, 0, 0, ..., 0] \\ G_{pp2}(t) = [0, g_{t_2}, 0, ..., 0] \\ G_{pp3}(t) = [0, 0, g_{t_3} ....., 0] \\ \qquad\qquad ..... \\ G_{ppn}(t) = [0, 0, 0, ..., g_{t_n}] \end{cases}$$

$$W(t) = \begin{bmatrix} w_{-M} & w_{-M+1} & ..... & w_{-1} & w_0 & w_1 & ..... & w_{N-2} & w_{N-1} & w_N \end{bmatrix}^T \quad (5.4)$$

M and N are positive integers. I see that equation (5.1) can be rewritten as:

$$\begin{aligned} S(t) &= G_{pp1}(t) * W(t) + G_{pp2}(t) * W(t) + ... + G_{ppn}(t) * W(t) \\ &= g_{t_1} W(t - t_1) + g_{t_2} W(t - t_2) + ... + g_{t_n} W(t - t_n) \end{aligned} \quad (5.5)$$

The exact angle-dependent reflection and transmission coefficients of plane P-wave in isotropic media are given by Aki and Richards (1980). Under the assumption of small contrasts across the media and moderate, precritical angles, Shuey (1985); Swan (1993) and Hilterman et al. (1996) presented the approximate formulation of reflection coefficients. All of these have the form of linearised expansions of the plane-wave reflection coefficients as a function of incident angle. Swan's (1993) small-angle linearisation of P-wave reflection coefficient R_{t_i} as a function of incident phase angle θ is:

$$R_{t_i} = A_i + B_i \cos 2\theta + C_i \cos^2 2\theta \quad (5.6)$$

Here, A_i, B_i, C_i are the coefficients related to the velocities and densities of the two layers above and below the interface. The incident angle θ is related to the offset. Assuming total number of layers is n=3, applying equations (5.6) and (5.2)

to equation (5.5), I have:

$$\begin{aligned} S(t) &= g_{t_1}.W(t-t_1) + g_{t_2}.W(t-t_2) \\ &= (A_1.W(t-t_1) + A_2T_{12}T_{21}W(t-t_2)) \\ &+(B_1.W(t-t_1) + B_2T_{12}T_{21}W(t-t_2))\cos 2\theta \\ &+(C_1.W(t-t_1) + C_2T_{12}T_{21}W(t-t_2))\cos^2 2\theta \end{aligned} \tag{5.7}$$

To a normally-incident plane pressure wave, the reflection response at time $t = t_1$ is:

$$S(t_1) = W(0)(A_1 + B_1 + C_1) + W(\Delta t = t_1 - t_2)T_{12}T_{21}(A_2 + B_2 + C_2) \tag{5.8}$$

From this equation, it is clear that the received seismic response or amplitudes show an approximately linear relationship with $\Delta t = t_1 - t_2$, or the thickness of the second layer when Δt is quite small compared with the dominant wave period. However, for angle-dependent reflections, the amplitude shows a complex relationship with thickness in the presence of a thin layer. Clearly, in either condition the discrepancy between $S(t = t1)$ and $R(t = t1)$=R_{12} exists. This discrepancy is extremely complex if the second layer is a fractured reservoir layer. As shown equation (3.1), in each medium the reflection coefficient has a similar form to equation (5.6),

$$R_{ti} = A_i(\theta) + B_i(\theta)\cos 2\varphi + C_i(\theta)\cos^2 2\varphi, \tag{5.9}$$

where φ is the azimuth along the source-receiver spread direction. $A_i(\theta)$, $B_i(\theta)$ and $C_i(\theta)$ are the coefficients related to source-receiver geometry, the velocities, fracture parameters and the densities of the two layers and they are independent of azimuth. Then, the seismic response in equation (5.1) from this three layered model may be

written as:

$$\begin{aligned} S(t) &= g_{t_1}.W(t-t_1) + g_{t_2}.W(t-t_2) \\ &= (A_1(\theta).W(t-t_1) + A_2(\theta)T_{12}T_{21}W(t-t_2)) \\ &+(B_1(\theta).W(t-t_1) + B_2(\theta)T_{12}T_{21}W(t-t_2))\cos 2\varphi \\ &+(C_1(\theta).W(t-t_1) + C_2(\theta)T_{12}T_{21}W(t-t_2))\cos^2 2\varphi \end{aligned} \tag{5.10}$$

I define $A_i^{'}(\theta)$, $B_i^{'}(\theta)$ and $C_i^{'}(\theta)$ as:

$$\begin{cases} A_1^{'}(\theta) = A_1(\theta).W(t-t_1) + A_2(\theta)T_1T_2W(t-t_2) \\ B_1^{'}(\theta) = B_1(\theta).W(t-t_1) + B_2(\theta)T_1T_2W(t-t_2) \\ C_1^{'}(\theta) = C_1(\theta).W(t-t_1) + C_2(\theta)T_1T_2W(t-t_2) \end{cases} \tag{5.11}$$

Thus, I have

$$S(t) = A_1^{'}(\theta) + B_1^{'}(\theta)\cos 2\varphi + C_1^{'}(\theta)\cos^2 2\varphi \tag{5.12}$$

Comparing the two pairs of equations (5.6) and (5.7), and (5.9) and (5.10), shows the discrepancies between the reflection coefficient and the seismic amplitude in scale and composition. The reflection coefficient is not related to the wavelet and the thickness of the layers, and is determined by the properties of the media and the source-receiver geometry, incidence angle and azimuth, or slowness. The magnitude of the seismic response from *the mth* layer is a cumulative result of source function, primary reflection from *mth* layer and all the other waveforms such as multiples, converted P- and S- waves which arrive at a similar time. When the layer is thin, the internal multiples, converted P- and S-waves may contribute significantly to the recorded seismic amplitude (Ziolkowski and Fokkema, 1986; Juhlin and Young, 1993). Therefore, in the presence of thin layers, the substitution of $S(t = t1)$ to $R_{t=t1}$ may affect AVO and AVOZ.

The above analysis shows that the discrepancies between recorded seismic amplitude and expected reflection coefficients manifest themselves in two ways. One is the difference in the scale and I call it the scaling problem. The other one is the difference in the composition waveforms mainly because of the thin layers; I call this the thin layering problem. A discussion follows on how these two discrepancies affect the estimation of fracture parameters.

5.2.2 Effect of thin layering: 2D lines case

I consider that the four seismic records are $S_1(t) = S(t, \varphi_1)$, $S_2(t) = S(t, \varphi_2)$, $S_3(t) = S(t, \varphi_3)$ and $S_4(t) = S(t, \varphi_4)$ in the azimuthal directions of φ_1, φ_2, φ_3 and φ_4, respectively, which intersect at the same surface point. The four azimuths have the relationship: $\varphi_3 = \varphi_1 + 90^o$ and $\varphi_4 = \varphi_2 + 90^o$. In Chapters 3 and 4 I proposed a procedure for estimating azimuthal anisotropy parameters using interval times which requires that the top and bottom of the target layer can be distinguished or the boundaries of the reflection layer are visible. When the layer is thinner, it is difficult to define the boundaries of the target, but I can pick the target top at least. I therefore may have to use amplitude as an alternative constraint. As shown in Chapter 3 the ratio of amplitude difference $R_{31}(t_1)/R_{42}(t_1)$ can be used to estimate the azimuthal anisotropic parameters. Ideally, the difference of the reflection coefficients $R_{mn}(t_1)$ of the orthogonal line pair, $R_m(t_1)$ and $R_n(t_1)$, should be used:

$$R_{31}(t_1) = R_3(t_1) - R_1(t_1), \quad R_{42}(t_1) = R_4(t_1) - R_2(t_1) \tag{5.13}$$

and I define $\Omega_R = \frac{R_{31}(t_1)}{R_{42}(t_1)}$ as:

$$\Omega_R = \frac{B_1(\theta)\cos 2\varphi_3 + C_1(\theta)\cos^2 2\varphi_3 - B_1(\theta)\cos 2\varphi_1 - C_1(\theta)\cos^2 2\varphi_1}{B_1(\theta)\cos 2\varphi_4 + C_1(\theta)\cos^2 2\varphi_4 - B_1(\theta)\cos 2\varphi_2 - C_1(\theta)\cos^2 2\varphi_2} \tag{5.14}$$

In practice, the differences of amplitudes picked from the seismic records are used as the difference of reflection coefficients, i.e:

$$S_{31}(t_1) = S_3(t_1) - S_1(t_1), \quad S_{42}(t_1) = S_4(t_1) - S_2(t_1) \tag{5.15}$$

and $\Omega_S = \frac{S_{31}(t_1)}{S_{42}(t_1)}$ is defined as:

$$\Omega_S = \frac{B_1'(\theta)\cos 2\varphi_3 + C_1'(\theta)\cos^2 2\varphi_3 - B_1'(\theta)\cos 2\varphi_1 - C_1'(\theta)\cos^2 2\varphi_1}{B_1'(\theta)\cos 2\varphi_4 + C_1'(\theta)\cos^2 2\varphi_4 - B_1'(\theta)\cos 2\varphi_2 - C_1'(\theta)\cos^2 2\varphi_2} \tag{5.16}$$

are used as the replacements of equations (5.13) and (5.14). Clearly, if the source function $W(t)$ does not vary with azimuth, the scaling problem seems to have less effect on the estimation of fracture parameters. However, the thin layering can have serious effects on fracture estimation. When the thickness is less than $\frac{\lambda}{2}$ (here λ is the seismic wave length), the reflection from the target top and all the other waves generated from the bottom and top will interfere strongly, and it is therefore very difficult to distinguish the top reflection from the bottom reflection. Thus the above replacement (i.e equations 5.15 and 5.16) may have significant errors.

5.2.3 Effect of thin layering: further discussions

In the case where I do not have orthogonal source-receiver lines, but there are three or more irregularly distributed azimuthal lines, least-squares fitting to equation (5.9) can be used to estimate the fracture strike and intensity of the underlying layer. Again, because of the same reason as in the previous discussion, equations (5.11)

Layer No.	Media Type	Vp(m/s)	Vs(m/s)	ρ	σ	ε
1	Shale	3048	1574	2.3	0	0
2	Gas sand	2183	1502	2.19	0	0
3	Shale	3048	1574	2.3	0	0

Table 5.1: Materials used in Figure 5.1 for isotropic modelling. The interface of Layer 1-2 is a high impedance to low one. The up-going reflection coefficient at this interface is negative. The up-going reflection coefficient from the target bottom, 2-3, is positive.

and (5.12) are applied to the picked azimuthal amplitudes. If the target layer is thick enough, the terms $A_2(\theta)T_1T_2W(t_1-t_2)$, $B_2(\theta)T_1T_2W(t_1-t_2)$ and $C_2(\theta)T_1T_2W(t_1-t_2)$ in equation (5.11) may be neglected and this equation becomes:

$$\begin{cases} A_1'(\theta) = A_1(\theta)W(0) \\ B_1'(\theta) = B_1(\theta)W(0) \\ C_1'(\theta) = C_1(\theta)W(0) \end{cases} \tag{5.17}$$

This equation shows that the scaling problem has a negligible effect on the normalised AVO gradient and intercept estimation from which strike and intensity can be estimated, but this is subject to an invariant wavelet in the area where there are multiple CMPs from different physical location. In this case, equation (5.12) can be used to replace equation (5.9) to calculate the normalised values of $A_1(\theta)$, $B_1(\theta)$ and $C_1(\theta)$. However, the thin layer will violate the above assumption and therefore the estimation results from the fitting may also contain a serious error.

I next use full-wave modelling seismograms generated by ANISEIS to show the thickness-dependent fracture estimation variation in the following sections.

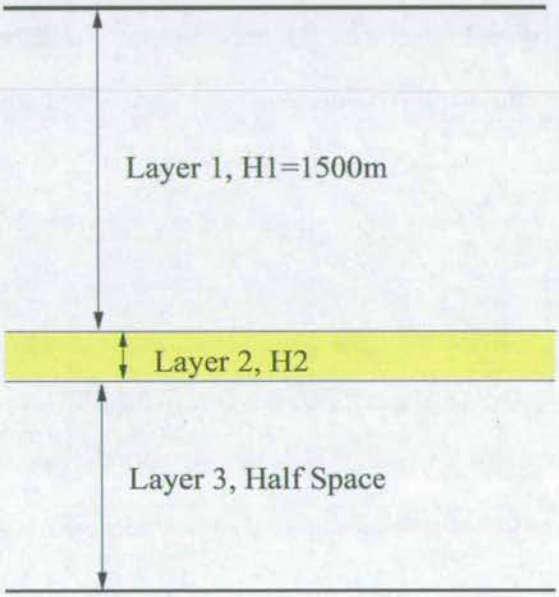

Figure 5.1: The three layer geological model is used. The thickness of Layer 1 is fixed at 1500m for all the modelling in the chapter, and it is made of shale with velocities of 3048m/s and 1574m/s for P- and S-wave respectively. Layer 3 is a half-space made of the same material as Layer 1 (Table 5.1). Layer 2 is our target layer whose variable thicknesses are listed in Table 5.4.

5.3 Synthetic modelling

To investigate the effects of thin layers, I use a simple model made of three plane layers to generate synthetic seismograms. Layer 1 is made of isotropic shale with a thickness of 1500m (Figure 5.1 and Table 5.1). Layer 2 is the target reservoir layer with 30 designed thicknesses (Table 5.4). Layer 3 is the same as Layer 1. I fix the thickness of Layer 2, and use a 3050m spread with 50m interval to construct full-wave synthetic seismograms using the reflectivity method. A total of 30 CMP gathers are produced. To study the effect of the thickness on AVOZ, a similar model with three layers is constructed by sandwiching a fractured gas sand between two isotropic layers (Table 5.2). The target layer is still the second layer. The fracture strike is north. Six CMP gathers are generated along the azimuths at 0^o, 15^o, 60^o, 90^o, 105^o and 150^o for the same thickness model. (Table 5.5). A total of 30x6=180 models are calculated. Each model corresponds to a fixed thickness or 'thickness model', for which I calculate the full-wave synthetic CMP gather using ANISEIS (Taylor, 1990).

From the analysis and comparison of these full-wave synthetic records, I expect to find answers to the question: Are there any clues to tell us whether a reflective layer of interest is an azimuthally anisotropic layer? Given the isotropic material for all the three layers, an isotropic 3D dataset (time, offset, thickness) is produced from which an AVO-thickness diagram of the target top is created. For the models with a fractured layer, the fracture strike is north and a 4D dataset (time, offset, thickness, azimuth) can be created. Using these 3D and 4D datasets, I extract parameters such as variation of amplitude with thickness and offset, and variation of azimuthal amplitude difference with thickness and offset, from which I can investigate the effects of thin layers on AVO/AVOZ.

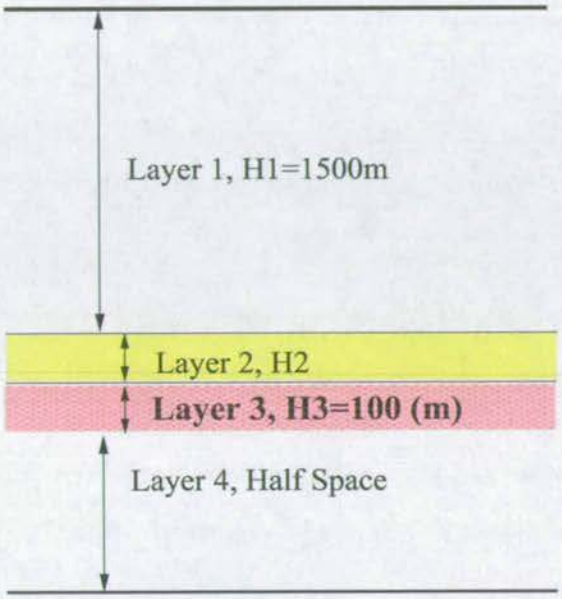

Figure 5.2: The four layer geological model is used. The properties of Layer 1 are as in Figure 5.1. Layer 3 is a 100m thick isotropic medium. Layer 4 is a half-space made of the same material as Layer 1 (Table 5.3). Layer 2 is our target layer whose variable thicknesses are listed in Table 5.6.

Layer No.	Media Type	Vp(m/s)	Vs(m/s)	ρ	σ	ε
1	Shale	3048	1574	2.3	0	0
2	Fractured gas sand	2183	1502	2.19	10%	0.005
3	Shale	3048	1574	2.3	0	0

Table 5.2: Materials used in Figure 5.1 for anisotropic modelling. The parameters are the same as those in Table 5.1 except for those of Layer 2 to which I add some cracks with the strike direction north.

Layer No.	Media Type	Vp(m/s)	Vs(m/s)	ρ	σ	ε
1	Shale	3048	1574	2.3	0	0
2	Fractured gas sand	2183	1502	2.19	10%	0.005
3	Sand	2743	1466	2.30	0	0
4	Shale	3048	1574	2.3	0	0

Table 5.3: Model parameters for Figure 5.2 used for checking new procedure.

5.3.1 Effect of thin layers on isotropic AVO

Reflection coefficients do not vary with the thickness of the underlying layer, Layer 2. However, the recorded seismic amplitude from the interface between the two layers is affected by the interferences between neighbour layers. The synthetic seismograms (Figure 5.4) give an overall view of the effects of thickness on the amplitudes of all the seismic waves, including P-waves and converted waves, from the top and bottom of the target. Clearly, the measured amplitude from the top varies with thickness. The two scaled 3D diagrams of AVO-Thickness (Figure 5.5) focus well on the effects of thickness on reflection amplitudes of the top of the target. A complex offset and thickness-dependent variation of amplitudes is shown on both Figures 5.4 and 5.5. The amplitudes from the top of the target at a fixed offset in different CMP gathers increase linearly with increasing thickness from 0.02m to 10.24m (Figures 5.4 and 5.5b). When the thickness is greater than 25m, the AVO curves show a slight variation with thickness (Figures 5.4, 5.5a and 5.5b). Comparing the amplitude variations with thickness at offsets 300m and 3000m, I find that the amplitudes from far offsets (3000m) show a clearer and periodic variation with thickness and have stronger variations than those from the near offsets (300m) (Figure 5.5a). In other words, thickness variation has a greater effect on far-offset amplitudes than on those at near offsets in this case.

5.3.2 Effect of thin layers on AVOZ

Figures 5.6a and 5.6b and Figures 5.7a and 5.7b are the synthetic CMP gathers generated in the orthogonal source-receiver azimuths of 0^o (fracture normal) and 90^o, 60^o and 150^o, respectively. The thickness of the target layer and its observation azimuth are labelled on the diagrams. The amplitude difference in the two CMP gathers along azimuth 0^o and 90^o at thickness of 0.16m can be seen in Figures 5.6a and 5.6b. Figures 5.8a, 5.8b, 5.8c and 5.8d are the AVO-thickness maps picked from the top of the target along four azimuthal directions. The maps show that the reflection amplitude from the target top increases with increasing thickness when the thickness is less than 10m, and that the AVO varies slightly with thickness when the thickness of the second layer $H2 > \lambda/2$. I find that all the amplitudes are thickness-dependent to some extent when $H2$ is small, which is similar to what I find from the isotropic modelling. Moreover, I find that the AVO is azimuth and thickness dependent to some extent, especially when the layer is quite thin (Figures 5.9a and 5.9b). I also find that there is a large difference between the maximum amplitude difference of the two pairs of orthogonal CMPs; one is about 150, but the other is about 60. This confirms that the amplitude difference will have a maximum value among the two CMPs which lie approximately along the fracture strike and the normal directions. Another interesting fact is that the maximum amplitude difference shows up in the thickness ranges of less than 22m ($\lambda/4$) in which I have problems in detecting thin layers using normal methods. This strong azimuthal variation of amplitude in the presence of thin layers may provide a means to detect azimuthal anisotropy in thin layers. When the thickness is greater than 44m ($\lambda/2$), the amplitude differences of the orthogonal CMPs are very stable.

Further analysis on AVOZ is shown on Figure 5.10. Figure 5.10a is calculated by finding the minimum and maximum amplitude among each bin of thickness and

offset. The Z-axis of the diagram is the difference of the minimum and maximum amplitude. Figure 5.10b is different from 5.10a in its vertical axis which is the percentage of the difference calculated by the equation $100 \times \frac{Maximum-Minimum}{(Maximum+Minimum)/2}$. The amplitude difference between two azimuthally-orthogonal directions reaches its maximum when $H2 \doteq \lambda/4$. From the two diagrams I find that the amplitude difference varies slightly with thickness larger than $\lambda/2$ and the ratios of the amplitude differences are also stable for the thickness larger than $H2 > \lambda/2$. The ratios are 8% and 2% when Offset=2xD2 and Offset=0.5xD2, respectively (offset is the source-receiver distance).

I also find other interesting phenomena when I compare anisotropic and isotropic supergathers of the same thickness model which are formed via the same three-step processing for each thickness modelling: 1) sorting the merged traces from all the observation azimuths with offset; 2) flattening the reflection event from the target top on the NMO gather; and 3) applying inverse NMO (Figure 5.11). On this supergather I find that a strong periodic "static problem" exists on the event from the bottom of the target. This can be used to identify azimuthal anisotropy inside a layer.

5.3.3 Effect of thin layering on the estimation of fracture parameters

For convenience of processing, I define a series of CMP numbers for different thickness gathers which are from the same thickness model. Therefore I have a total of 180 azimuthal CMP gathers, and form 30 CMP supergathers from the anisotropic modelling. In this section I apply a fracture estimation method to all the thickness supergathers to analyse the effect of thin layering on fracture strike and intensity estimation. I calculate the Strike- and Strike_Error-Offset-Thickness, Density- and

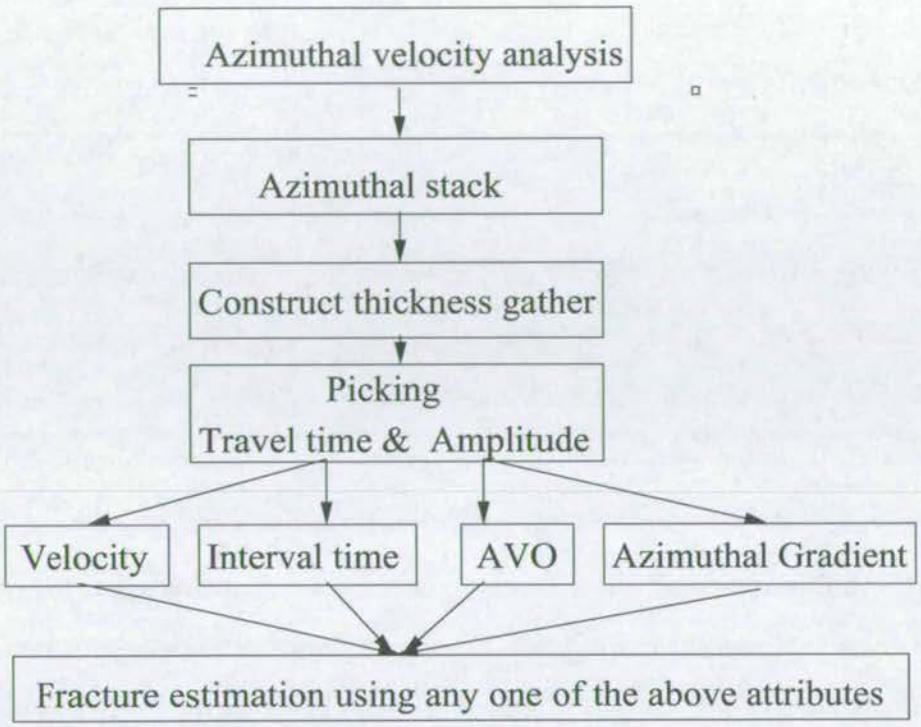

Figure 5.3: The procedures for fracture estimation from thickness supergathers

Density_Error-Offset-Thickness diagrams, respectively.

The procedures for estimation of strike and intensity from these data are briefly described as follows (Figure 5.3). First, complete the velocity analysis on the CMP gather with the same azimuth, I then have 30 azimuthal velocity functions (Figure 5.12a). Second, I apply the velocity function to the same azimuthal CMP gathers for all the thickness models to form an azimuthal stack section (Figure 5.12b) for picking the monitoring time window of the top and bottom of the target. Third, for each thickness model, I merge the calculated azimuthal CMP gathers from the same two pairs of orthogonal directions selected to form a thickness gather. I then have 30 thickness gathers, or one supergather, on which the periodic residual statics can be seen (Figure 5.12c and 5.12d). Fourth, I sort each supergather first by offset then by azimuth. There are therefore 56 common offset groups inside each supergather. The offset ranges from 50 - 3050m with an interval of 50m. Among each offset gather,

there should be four azimuthal traces. Fifth, I pick precise amplitudes and travel times from the top and bottom of the target for all the traces of all the supergathers. My previous tests show that the time interpolation of the seismic trace has critical effects on the estimation of fracture parameters when $H2 < \lambda/4$. From the time interpolation seismic data, I find that the estimated fracture orientations from the CMPs with thickness greater than 30m are almost the same as the true value (90^o), whereas for the CMPs with thickness less than 30m, there are large discrepancies between the estimated value of the fracture orientation and the true value. A similar conclusion can be drawn for the fracture intensity estimation.

Finally, I interpolate all the seismograms and use azimuthal variation of P-wave amplitudes to estimate fracture orientation and intensity for every offset group in each supergather. This is repeated over all the models, and finally two 3D diagrams are produced (Figures 5.13a and 5.13b). Error analysis of strike and density yields another two diagrams (Figures 5.13c and 5.13d). The obtained orientation values are almost exact even when the layer is as thin as 1m, as shown in Figures 5.13a and 5.13c (the true orientation value is 90^o). Figures 5.13b and 5.13d show that the estimated fracture intensity from the CMPs with thickness greater than 10.24m is almost the same as the true value (7%), whereas for the CMPs with thickness less than 10.24m, there are certain discrepancies between the estimated value and the true value and the estimated value is less than the true value.

To find the limit of estimation for real data, I add 50% of random noise to the synthetic data (Figure 5.14a) and then apply the AVOZ technique to estimate fracture parameters. Subtracting the model parameters from the estimated values yields two error diagrams, as shown in Figures 5.14b and 5.14c. The histograms in the error diagrams show that the estimated values are still close to the true values when $H2 > \lambda/4$. This means that the AVOZ technique used for estimation of fracture parameters is not sensitive to random noise when $H2 > \lambda/4$. I find that

noise can make it difficult when thin layers are present, but the effect of thickness is a more significant issue than noise when $H2 > \lambda/4$. This result confirms that there exists a limit beyond which the estimation of fracture parameters may not be reliable. This is consistent with the minimum resolution limit, i.e. $\lambda/4 = 22$m in our synthetic case. In practice, I have not only random noise but also other sources of noise, therefore to achieve a reasonable estimation, the requirement of Offset > 0.5xD2 should be met because the azimuthal variation is too small in this range of offsets to pick up, as shown in Figure 5.10b.

Figure 5.15a is the amplitude spectrum of the target wavelet I will achieve after deconvolution. From the wavelet shaped data, the strike and intensity are estimated using the same procedure as above. After comparing Figures 5.14b and 5.15b, and Figures 5.14c and 5.15c, respectively, I find that the the deconvolution processing improved the estimated results.

5.4 Compensation for the effect of thin layers

I here present a procedure to improve the detectability of thin fractured layers. It is noted that the azimuthal variation of P-wave amplitudes or $\Delta T_{pp}(t, \varphi) = T_{pp}(t_{bottom}, \varphi) - T_{pp}(t_{top}, \varphi)$ (the interval time of the target layer in the azimuthal direction of φ) is approximately an ellipse for fracture-induced azimuthal anisotropy, and if I add a constant to this ellipse, its basic shape will be similar and the directions of the long and short axes of the ellipse will not change, but the ratio of the long to the short axes will be smaller. This forms the basis of the new analysis procedure. In the four-layer models shown in Figure 5.2 and Table 5.3, I assume that the target layer, Layer 2, is a variable thickness layer, and below a reasonable depth (say 1500m) (Table 5.6). Therefore the variation with azimuth in P-wave raypaths to the top and bottom of the target for a fixed offset is very small. In other words,

the traveltime for the raypath to the bottom of the new target layer (Layers 2+3) equals the traveltime in the thin layer (true target) plus a constant traveltime which is the traveltime in the isotropic layer. I can then apply the AVOZ technique to the new target layer (Layers 2+3), and this will give the same information about the fracture orientation as the true target (Layer 2). If Layer 3 is properly selected, there should be no difficulty in picking $\Delta T_{pp}(t, \varphi)$.

To test this idea, 180 synthetic CMPs are generated (Figure 5.16a), with 25% random noise added to the synthetic seismograms. I can see that the top and bottom reflections are still evident for Layer 2+3 even when the thickness of Layer 2 is smaller than $\lambda/4$ and the reflections from the top and bottom of the target cannot be identified. I use the traveltime from the top and bottom of Layer 2+3 to estimate fracture orientation and density, and find that the error (estimated value - true value) in orientation is in the range from -10^o to $+10^o$ (average error of 0^o) (Figure 5.16b). This shows that our method is reliable and can be used to estimate fracture orientation even if the target layer is as thin as 10.24m in our case. The error (estimated value - true value) in intensity is between -7% and -4% (average error of -5.5%) (Figure 5.16c). The reason for the large discrepancy between the estimated average intensity (1.5%) and the true value (7%) is that the isotropic Layer 3 essentially dilutes the effect of the fractures. Interestingly, this discrepancy and the calculated strike values are stable for all the models in which the thickness of Layer 2 ranges from 10 to 600m. This means that the estimation errors are independent of the thickness of thin layers, but are related to the thickness of the underlying layer. This procedure decreases the detectable limit from $\lambda/4$ to $\lambda/8$.

5.5 Summary

The effect of thin layers on AVO and AVOZ is not a new topic, and has been studied before in many papers. If we have 4D maps of AVO versus thickness and azimuth, the amplitude variations with offset, thickness and azimuth may be studied conveniently. To obtain the maps, I design a series of thickness models for which the thickness varies from zero to a 1000 metres and the observation with full azimuths for all the precritical angles is calculated. In this chapter, I have presented such AVO and AVOZ versus thickness maps for the designated isotropic and azimuthally anisotropic models, respectively. The comprehensive synthetic modelling provides an opportunity to investigate the details of amplitude variation with either thickness or offset or both. I find that the thin layer has the following effects on AVO and AVOZ:

- The synthetic seismograms confirm that AVO variation is azimuth-dependent at the interface of isotropic and azimuthally anisotropic media, and the amplitude is proportional to thickness when $H2 < \lambda/4$ (here $H2$ denotes the thickness of the target layer and λ is the dominant wavelength).

- Amplitude varies greatly with increased thickness and reaches its maximum value in the whole 3D amplitude-offset-thickness distribution when $H2 \cong \lambda/4$, and shows a slight and stable variation when $H2 > \lambda/2$.

- Thickness has more effect on the responses from far offsets than on those from near offsets.

- The amplitude difference between two azimuthally orthogonal directions is proportional to the thickness when $H2 < \lambda/4$ and it varies slightly when $H2 > \lambda/2$.

- This difference reaches its maximum when $H2 \doteq \lambda/4$ and this value is greater than that when $H2 > \lambda/2$. This is true over all the precritical incident angles.

- The ratios of the amplitude differences are also stable over a thickness larger than $\lambda/2$. They are 8% and 2% when $Offset = 2 \times D2$ and $Offset = \frac{1}{2} \times D2$, respectively (here $Offset$ is the source-receiver distance, and $D2$ is the depth of the target layer). A lower value of the ratio means smaller visible azimuthal variation of amplitude and diminished possibility of using AVOZ to estimate azimuthal anisotropy.

The following findings are also obtained from our evaluation of the effects of thin layers on fracture estimation:

- My work shows that a sufficiently small interval of time sample for the seismic data is required to identify the anisotropy of thin layers. The noise cancellation processing with amplitude preserved is important to improve the detectability of thin layers.

- For noise-free data, and using the AVOZ method, the fracture strike is correctly estimated for a layer as thin as 1m and correct intensity can be estimated if $H2$ is larger than $\lambda/8$. The intensity estimated from the layer with thickness $H2 < \lambda/8$ is smaller than the true value. This is true in either near or far offsets.

- The vertical resolution of thin layers is method-dependent, as, from the same dataset, I do not obtain similar estimation results using the traveltime based method.

- For noisy data, because azimuthal variations that are too small are submerged by noise when $H2 < \lambda/4$ and Offset $<$ 0.5xD2, it is difficult to obtain the true

values for either fracture strike or intensity. But when $H2 > \lambda/4$ and Offset $>$ 0.5xD2 meet, the orientation and density can be estimated correctly, and the results are robust.

- For synthetic data with peak frequency of 25Hz and velocity of 2183m/s, the minimum fractured layer thickness that can be identified is between 20 - 30m, i.e around $\lambda/4$.

- If there is an isotropic layer below a target reservoir (i.e. a fractured thin reservoir), the proposed new procedure can provide reliable information about fracture orientations and density even if the thickness of reservoirs is as low as $\lambda/8$.

modelling No.	Line No	Thickness of H2 (metre)
1	2	0.02
2	4	0.04
3	8	0.08
4	16	0.16
5	32	0.32
6	64	0.64
7	128	1.28
8	256	2.56
9	512	5.12
10	1024	10.24
11	2048	20.48
12	2519	25.19
13	3098	31.0
14	3811	38.1
15	4687	46.9
16	5765	57.9
17	7091	70.9
18	8723	87.2
19	10730	107.3
20	13197	132.0
21	16232	162.3
22	19965	199.7
23	24557	245.6
24	30206	302.1
25	37153	371.5
26	45699	457.0
27	56209	562.1
28	69138	691.4
29	85039	850.4
30	104599	1046.0

Table 5.4: The 30 designed thicknesses of the target layer for investigating the effect of thickness on the recorded amplitude from the top of Layer 2. Using each thickness in this table, I calculate full-wave CMP seismograms with source-receiver offsets ranging from 300m to 3050m at 50m interval. Therefore a total of 30 CMP gathers is generated.

modelling No.	Model No. (Line No.)	Thickness of H2 (metre)	Azimuth
1	2	0.02	15, 60, 105, 150, 0, 90
2	4	0.04	15, 60, 105, 150, 0, 90
3	8	0.08	15, 60, 105, 150, 0, 90
4	16	0.16	15, 60, 105, 150, 0, 90
5	32	0.32	15, 60, 105, 150, 0, 90
6	64	0.64	15, 60, 105, 150, 0, 90
7	128	1.28	15, 60, 105, 150, 0, 90
8	256	2.56	15, 60, 105, 150, 0, 90
9	512	5.12	15, 60, 105, 150, 0, 90
10	1024	10.24	15, 60, 105, 150, 0, 90
11	2048	20.48	15, 60, 105, 150, 0, 90
12	2519	25.19	15, 60, 105, 150, 0, 90
13	3098	31.0	15, 60, 105, 150, 0, 90
14	3811	38.1	15, 60, 105, 150, 0, 90
15	4687	46.9	15, 60, 105, 150, 0, 90
16	5765	57.9	15, 60, 105, 150, 0, 90
17	7091	70.9	15, 60, 105, 150, 0, 90
18	8723	87.2	15, 60, 105, 150, 0, 90
19	10730	107.3	15, 60, 105, 150, 0, 90
20	13197	132.0	15, 60, 105, 150, 0, 90
21	16232	162.3	15, 60, 105, 150, 0, 90
22	19965	199.7	15, 60, 105, 150, 0, 90
23	24557	245.6	15, 60, 105, 150, 0, 90
24	30206	302.1	15, 60, 105, 150, 0, 90
25	37153	371.5	15, 60, 105, 150, 0, 90
26	45699	457.0	15, 60, 105, 150, 0, 90
27	56209	562.1	15, 60, 105, 150, 0, 90
28	69138	691.4	15, 60, 105, 150, 0, 90
29	85039	850.4	15, 60, 105, 150, 0, 90
30	104599	1046.0	15, 60, 105, 150, 0, 90

Table 5.5: The 30 designed thicknesses of the target layer and observation azimuths for investigating the effect of thickness on AVOZ. Six full-wave CMP seismograms with the same source-receiver geometry as isotropic modelling are generated for each thickness model. Therefore a total of 180 CMP gathers is generated which forms 30 supergathers.

modelling No.	Model No. (Line No.)	Thickness of H2 (metre)	Azimuth
1	2	0.02+100.0	15, 60, 105, 150, 0, 90
2	4	0.04+100.0	15, 60, 105, 150, 0, 90
3	8	0.08+100.0	15, 60, 105, 150, 0, 90
4	16	0.16+100.0	15, 60, 105, 150, 0, 90
5	32	0.32+100.0	15, 60, 105, 150, 0, 90
6	64	0.64+100.0	15, 60, 105, 150, 0, 90
7	128	1.28+100.0	15, 60, 105, 150, 0, 90
8	256	2.56+100.0	15, 60, 105, 150, 0, 90
9	512	5.12+100.0	15, 60, 105, 150, 0, 90
10	1024	10.24+100.0	15, 60, 105, 150, 0, 90
11	2048	20.48+100.0	15, 60, 105, 150, 0, 90
12	2519	25.19+100.0	15, 60, 105, 150, 0, 90
13	3098	31.0+100.0	15, 60, 105, 150, 0, 90
14	3811	38.1+100.0	15, 60, 105, 150, 0, 90
15	4687	46.9+100.0	15, 60, 105, 150, 0, 90
16	5765	57.9+100.0	15, 60, 105, 150, 0, 90
17	7091	70.9+100.0	15, 60, 105, 150, 0, 90
18	8723	87.2+100.0	15, 60, 105, 150, 0, 90
19	10730	107.3+100.0	15, 60, 105, 150, 0, 90
20	13197	132.0+100.0	15, 60, 105, 150, 0, 90
21	16232	162.3+100.0	15, 60, 105, 150, 0, 90
22	19965	199.7+100.0	15, 60, 105, 150, 0, 90
23	24557	245.6+100.0	15, 60, 105, 150, 0, 90
24	30206	302.1+100.0	15, 60, 105, 150, 0, 90
25	37153	371.5+100.0	15, 60, 105, 150, 0, 90
26	45699	457.0+100.0	15, 60, 105, 150, 0, 90
27	56209	562.1+100.0	15, 60, 105, 150, 0, 90
28	69138	691.4+100.0	15, 60, 105, 150, 0, 90
29	85039	850.4+100.0	15, 60, 105, 150, 0, 90
30	104599	1046.0+100.0	15, 60, 105, 150, 0, 90

Table 5.6: Layer thicknesses for checking the new method using Anisotropic+Isotropic layer as a composite anisotropic layer. Again, a total of 180 new CMP gathers is generated which forms 30 new supergathers

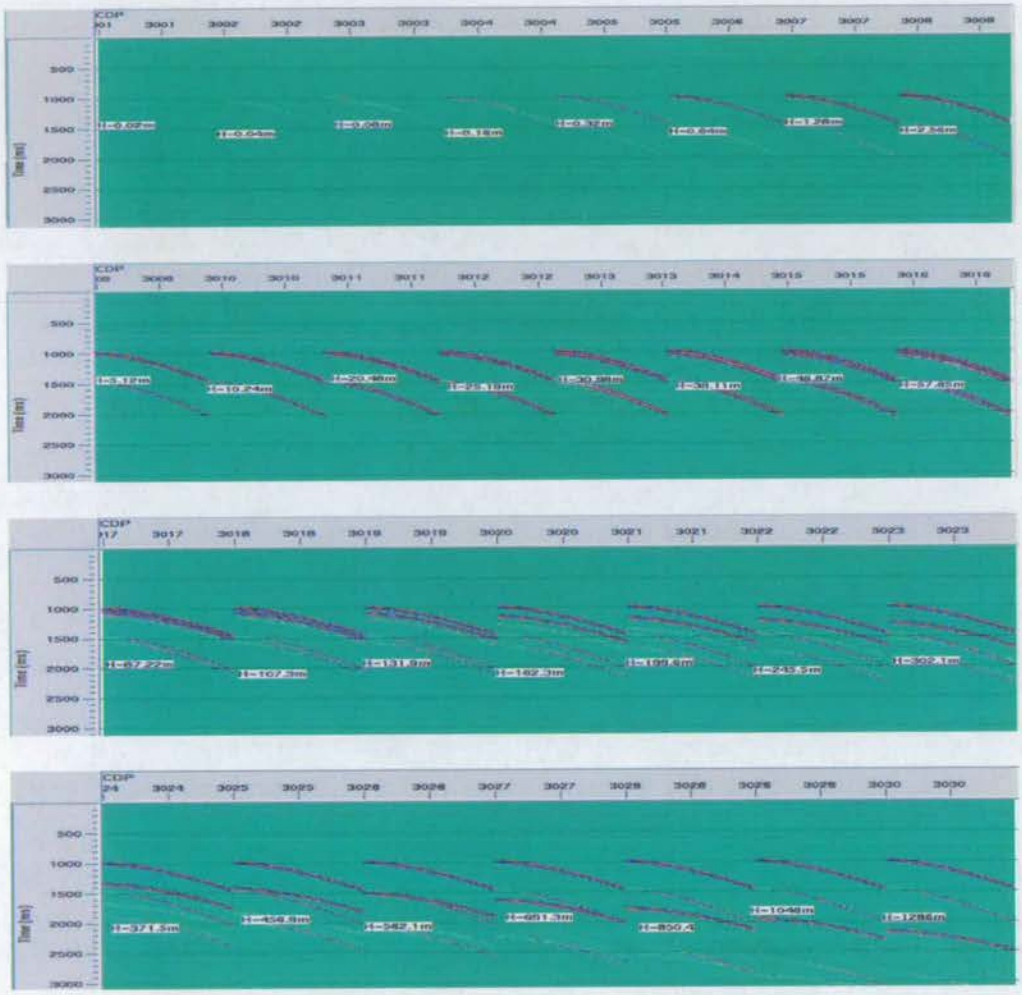

Figure 5.4: The full-wave synthetic seismograms generated using ANISEIS. The thickness is designated on the diagram for each synthetic gather using "H". The thickness dependent AVO variation can be seen clearly when H2 varies from 0.02m to 850.4m. The amplitudes at a fixed offset in different CMP gathers became progressively larger when the thickness varies from 0.02m to 10.24m. When the thickness is greater than 107.3m, the AVO has no apparent variation.

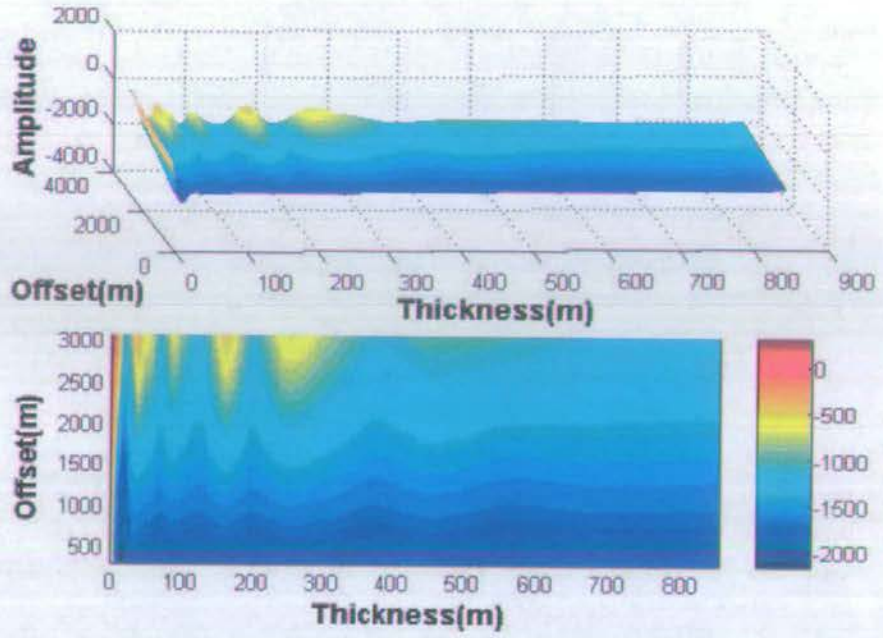

(a)

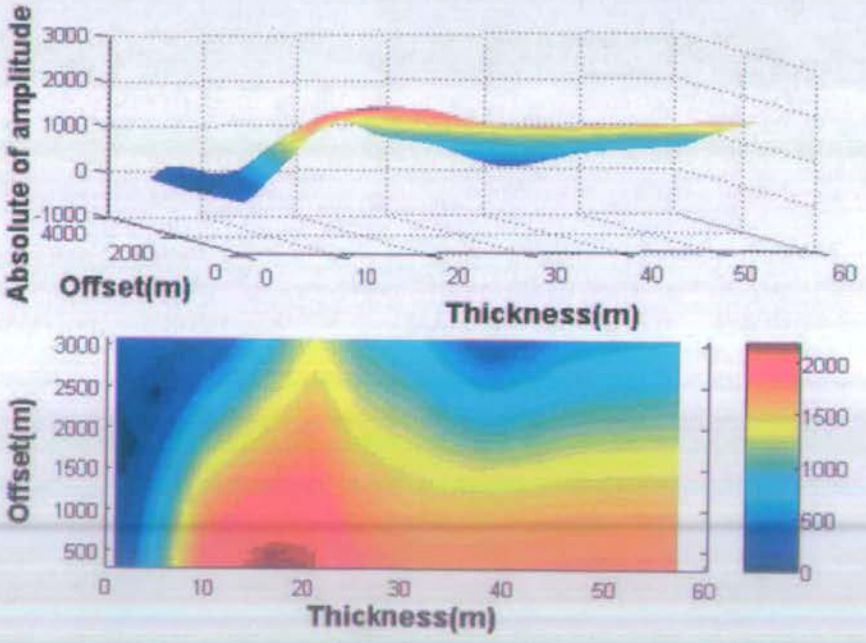

(b)

Figure 5.5: The AVO-Thickness 3D diagram at larger scale (a: thickness ranges 0.02m - 850.4m) and small scale (b: thickness ranges 0m - 60m).

(a)

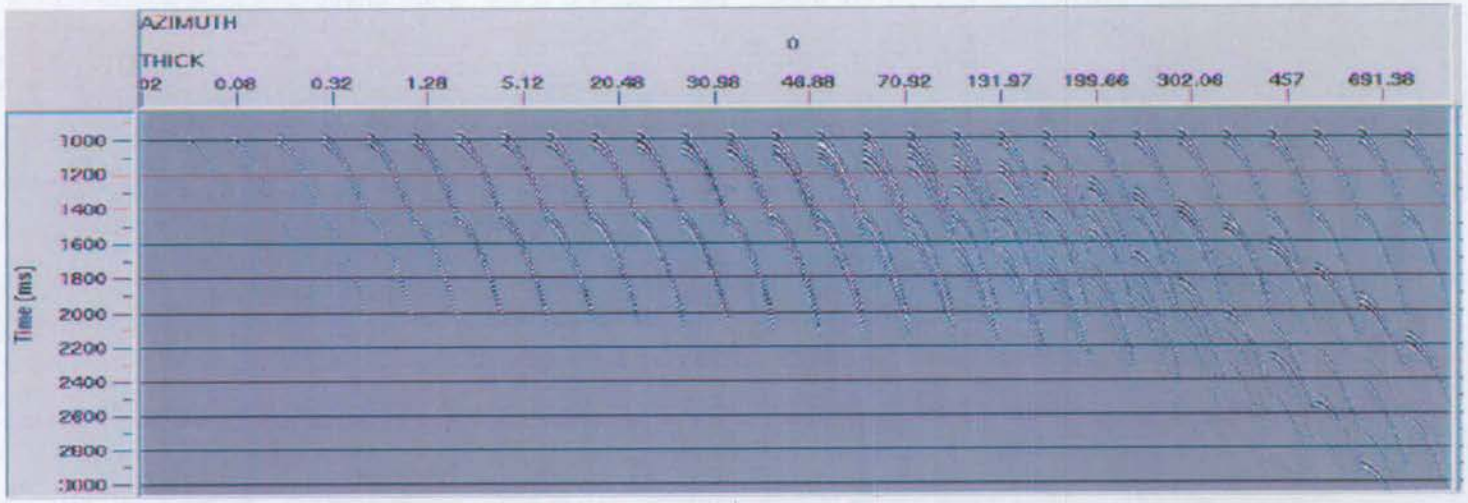

(b)

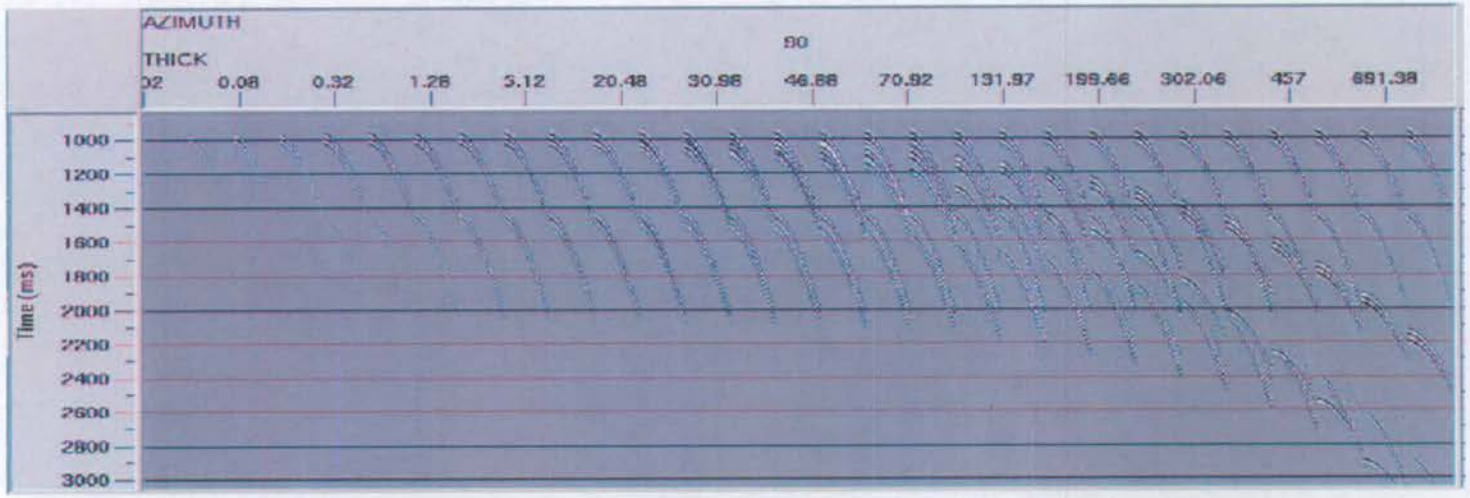

Figure 5.6: The ful-wave synthetic CMP gathers generated in the orthogonal source - receiver azimuths of 0^o(a) and 90^o(b). The thickness of the target layer and the shot azimuth are labelled on the diagrams.

Figure 5.7: The synthetic CMP gathers generated in the orthogonal source-receiver azimuths of 60°(a) and 150°(b). The

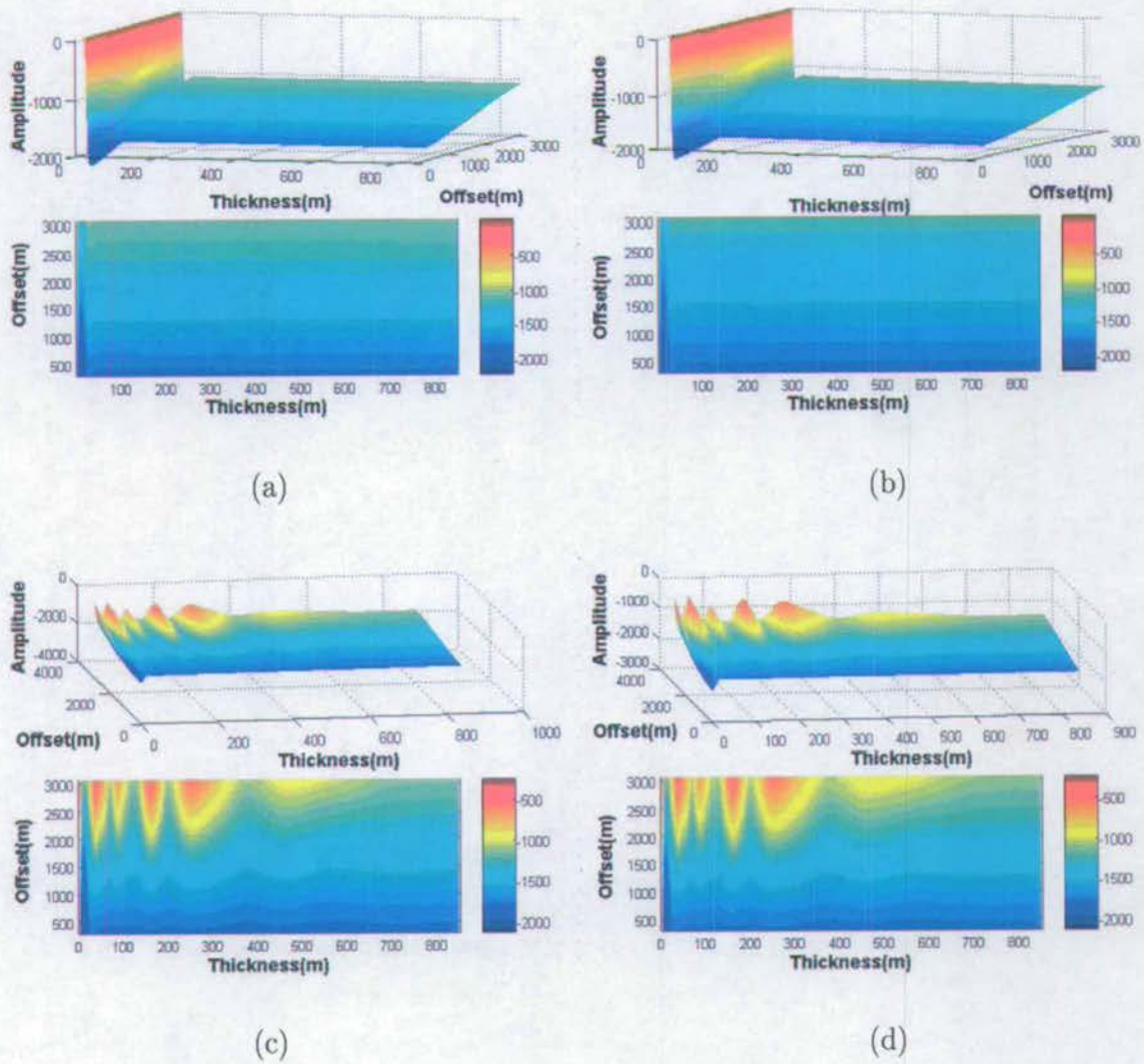

Figure 5.8: The amplitudes picked at the target top from the 30 supergathers along the azimuths of 0^0(a), 90^0(b), 60^0(c) and 150^0(d), respectively.

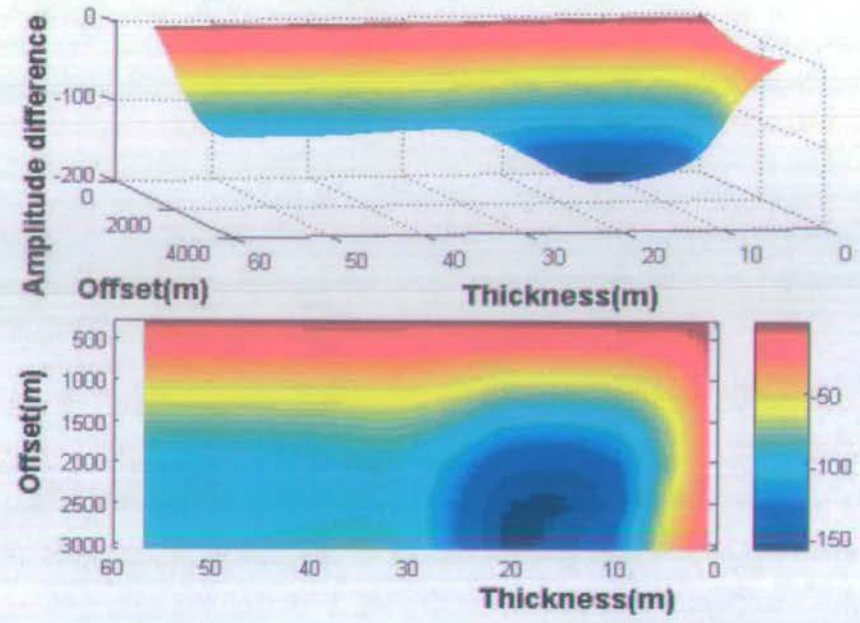

(a)

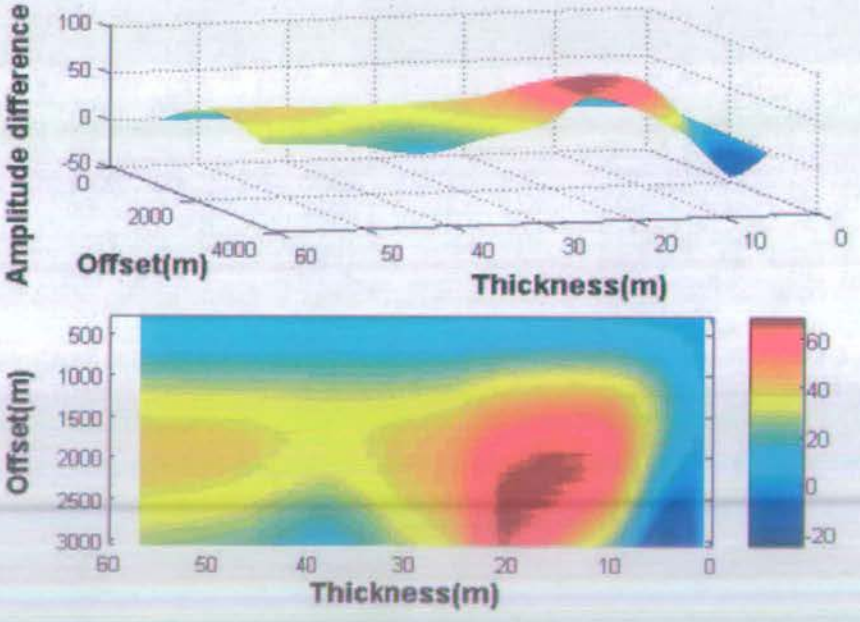

(b)

Figure 5.9: The amplitude difference between azimuths of 0^0 and 90^o(a) and 60^o and 150^0(b), respectively. Clearly, the amplitude difference is azimuthal and thickness dependent as well. The maximum value in (a) is twice that in (b). The maximum shows up only when the $H2 < \lambda/4$. The difference values are much smaller and stable when $H2 > \lambda/2$.

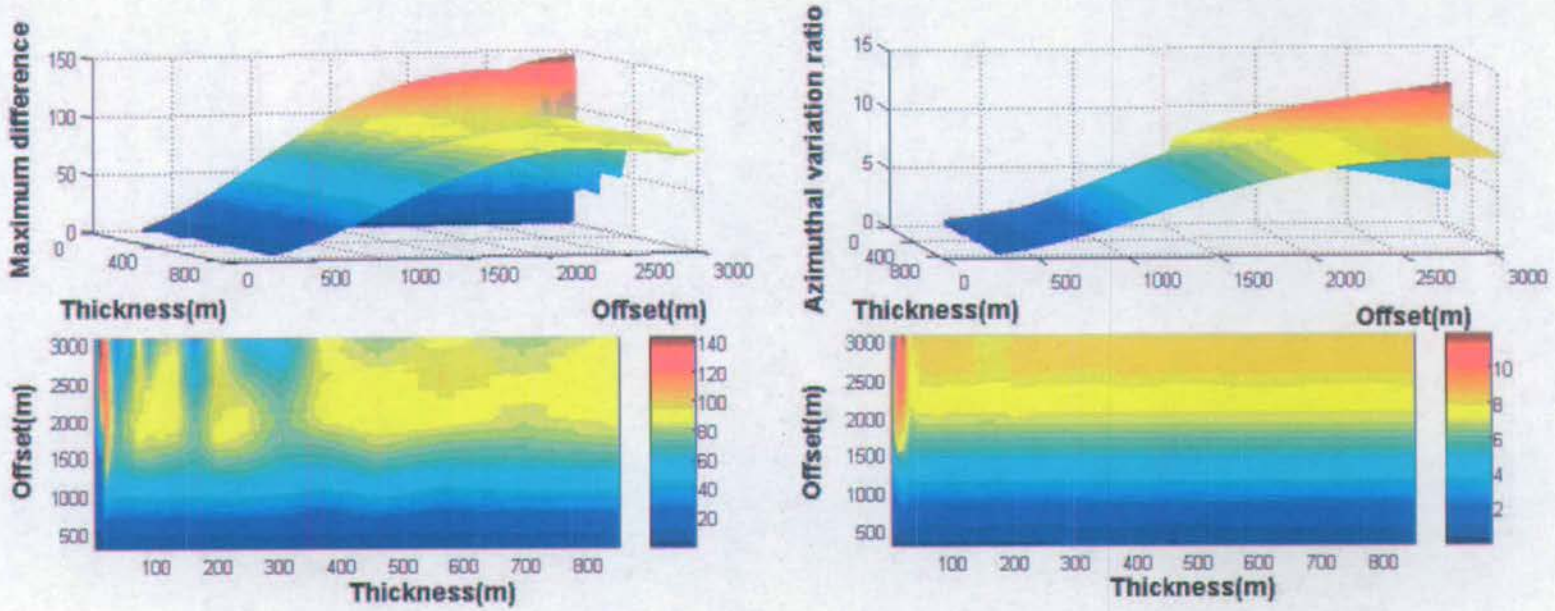

(a) (b)

Figure 5.10: The azimuthal variation of amplitude among the common offset group (a) and the variation ratio (b), respectively. The variation ratio in (b) is calculated by the equation $100 * \frac{Amplitude_{max} - Amplitude_{min}}{Amplitude_{average}}$ in each thickness-offset bin.

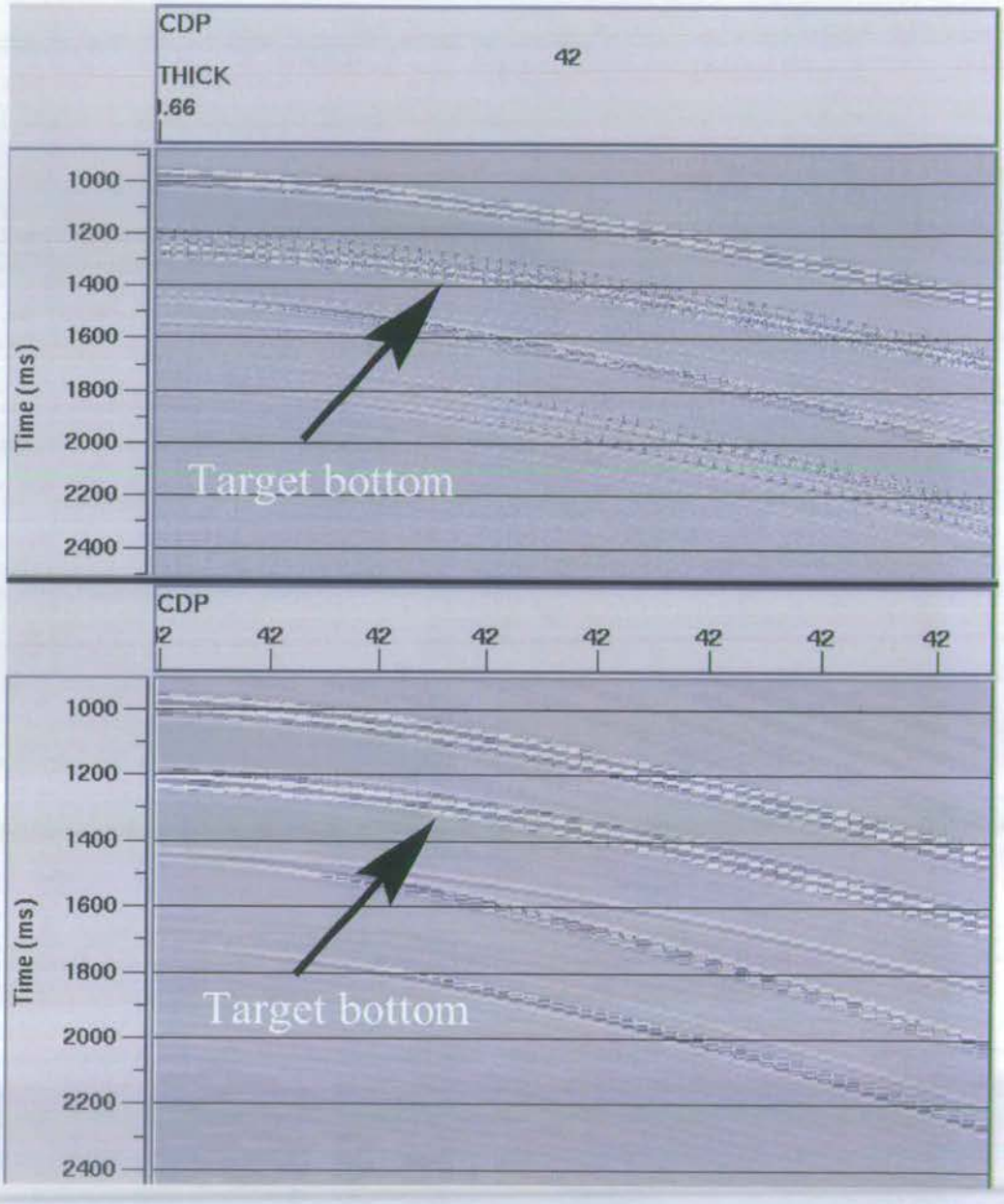

Figure 5.11: Comparison of a supergather from isotropic (Lower part) and anisotropic (Upper part) material. The supergather of a CMP point is constructed via three-step processing. Firstly, sorting the merged traces of all the observation azimuths with offset. Secondly, flattening the top event of the target on the NMO gather. Thirdly applying the inverse NMO.

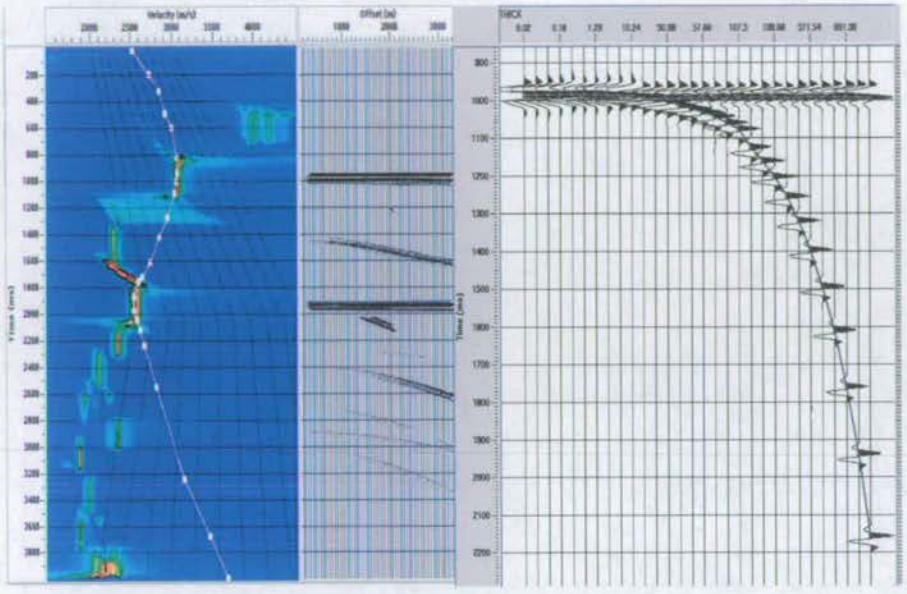

(a) (b)

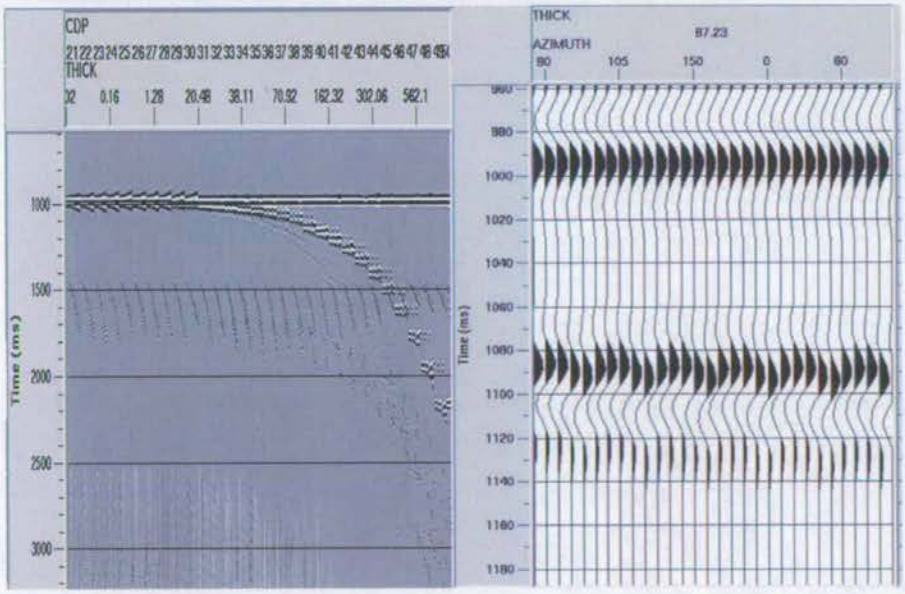

(c) (d)

Figure 5.12: (a) Velocity analysis for one of the thickness gathers. (b) Azimuthal stack section of all the thickness CMP gathers. (c) Thirty NMO supergathers corresponding to the thickness ranges 0.02m - 850.4m. (d) Zoom-in of the supergather at thickness 87.23m, again, periodic residual static phenomena are clearly seen.

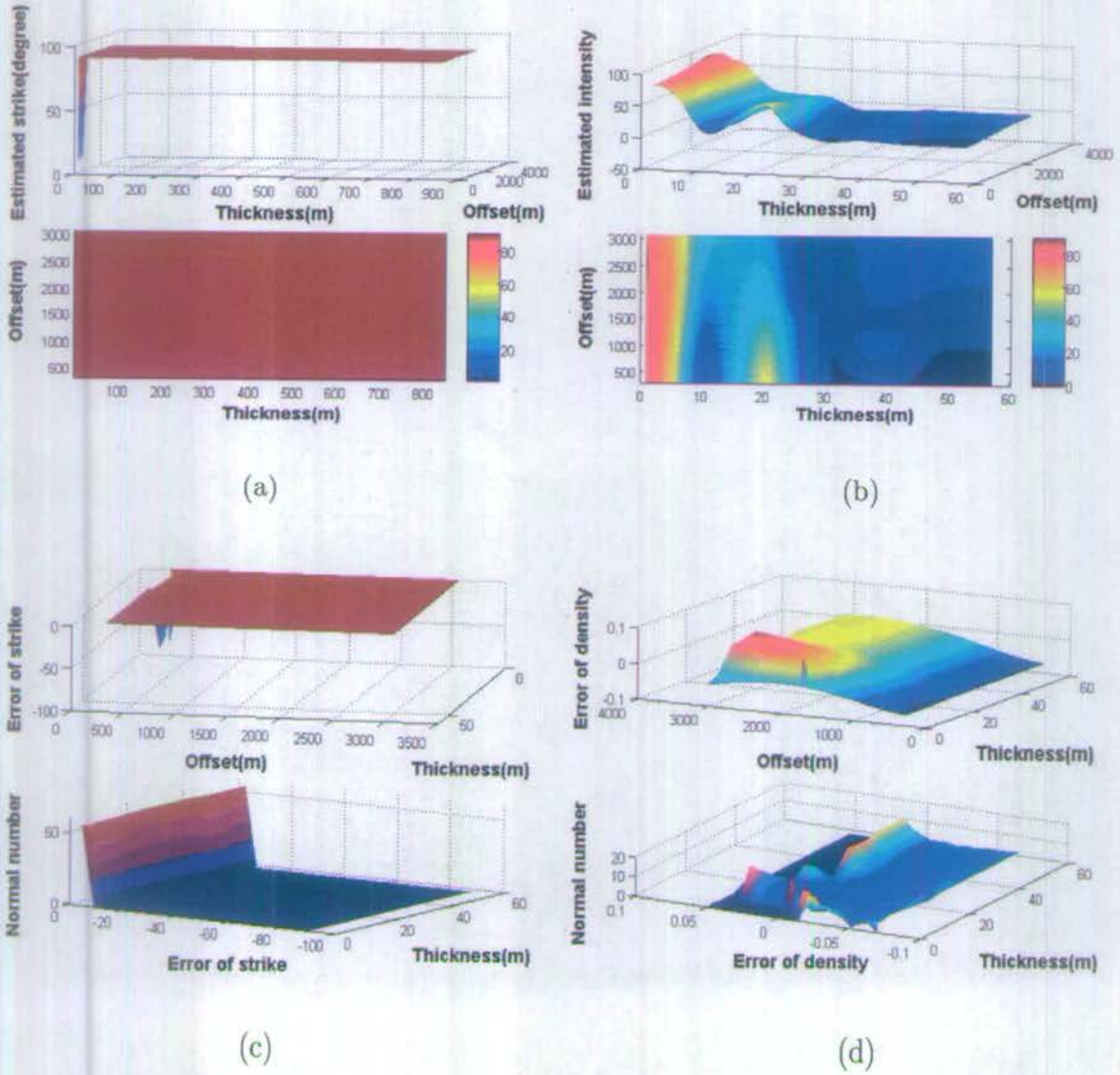

Figure 5.13: Estimated strike (a) and density (b) variations with offset and thickness (0m - 60m). Error analysis result of estimated strike (c) and density(d). When the thickness of the target layer is greater than 60m, the estimated results present very small variations compared to the true values.

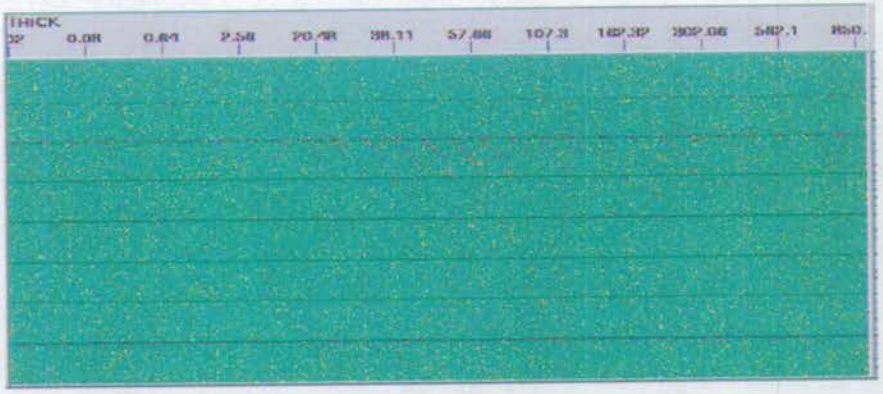

(a)

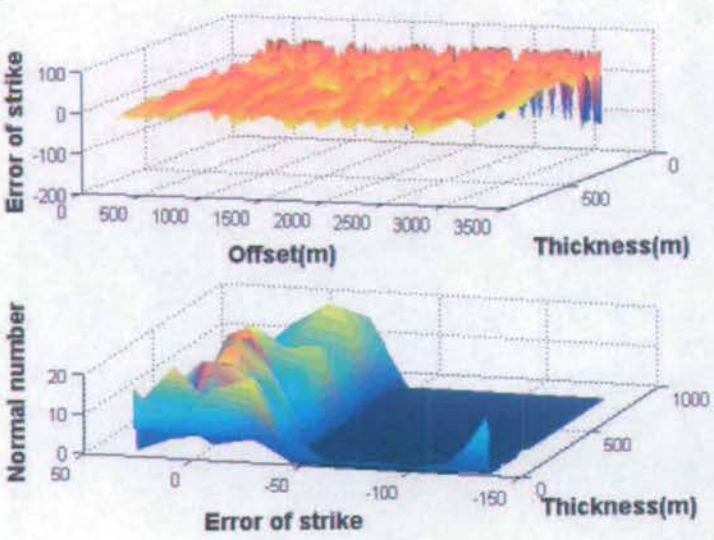

(b)

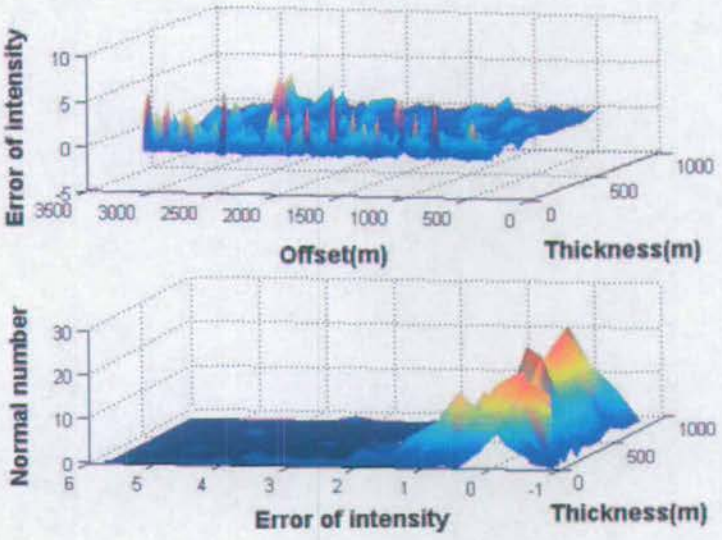

(c)

Figure 5.14: All supergathers to which AGC has been applied for enhancement purposes, with 50% added noise. Estimated

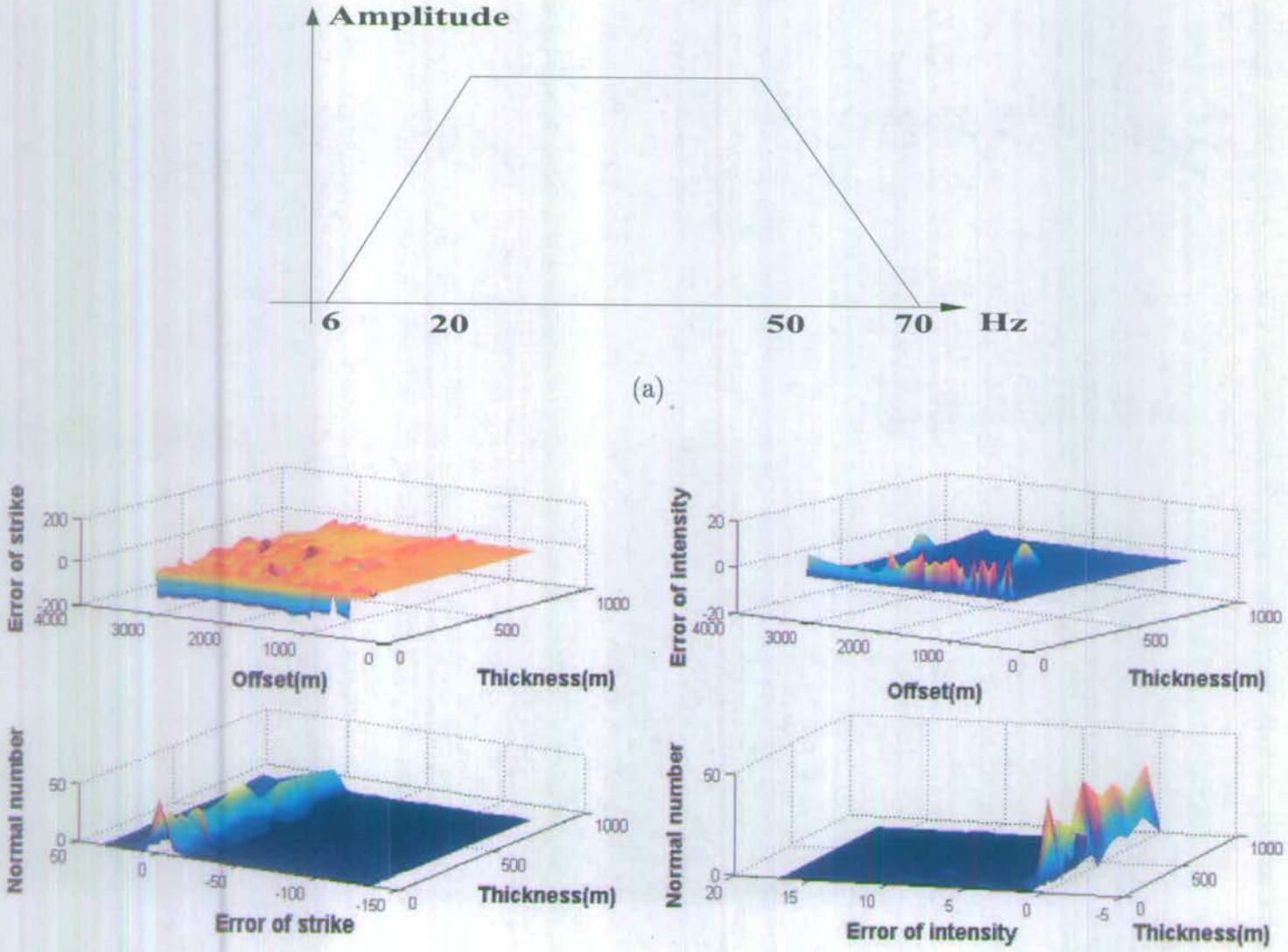

(a)

(b)

(c)

Figure 5.15: I shaped the wavelet to the shape (a), then applied the normal fracture detection procedure using azimuthal

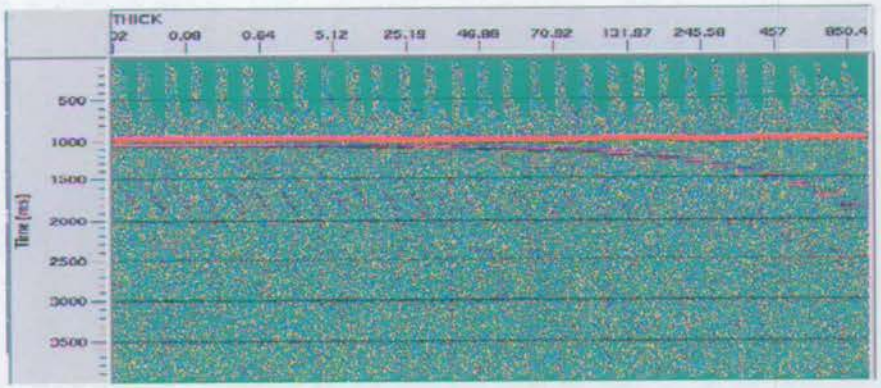

(a)

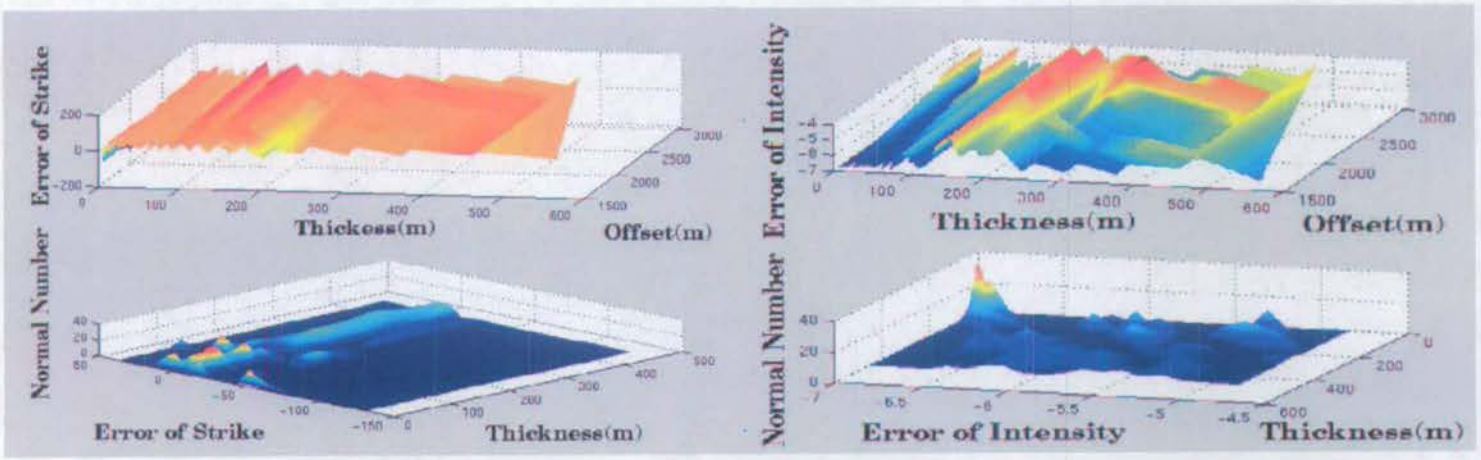

(b) (c)

Figure 5.16: (a) The synthetic NMO supergathers with respect to the parameters in Table 5.6 and Figure 5.2. (b) and (c) show the error analysis of detection results of fracture strike (orientation) and intensity (density), respectively.

Chapter 6

Fracture Detection Using 2D Orthogonal Lines

Abstract

In this chapter, I apply the 3A technology using orthogonal lines described in Chapter 3 to a field dataset from the North Sea supplied by TotalFinaElf. The dataset consists of four 2D lines, that intersect at a well and form two orthogonal intersecting pairs, which is ideally suited to test the 3A technology. From this dataset four azimuthal observations with near and far offset information exist can be found, and the subsurface fracture orientation and intensity at the intersecting point can be interpreted. My analysis shows that the interpreted fracture orientation is consistent with the major fault system at the target layer.

6.1 Geological setting

The dataset is from Fina Exploration (now Total). The targets are the Ekofisk and Tor formations of the Chalk sequence. Figure 6.1a shows the depth map of the top

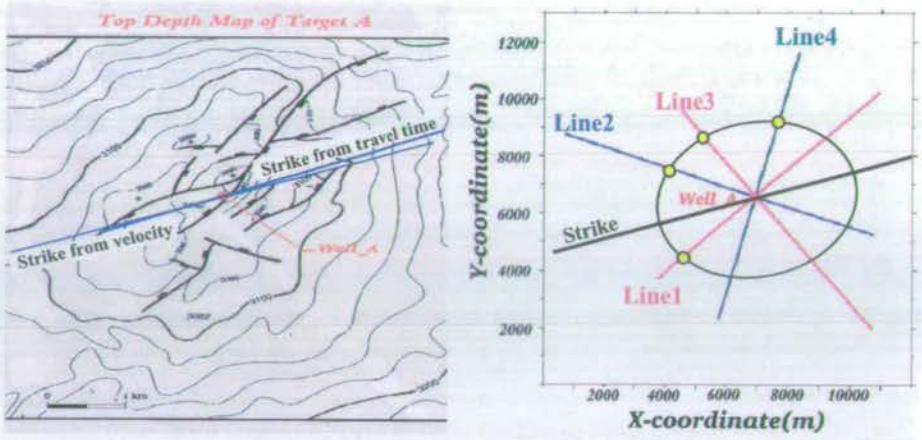

a) b)

Figure 6.1: (a) The depth map of the top target, the Ekofisk. (b) Configuration of the four lines. There is a common intersection for the four lines. Lines 1 and 3 are orthogonal, and lines 2 and 4 are orthogonal.

of the Ekofisk and reveals intensive faulting near the top. Four seismic lines are selected from this area and the four lines intersect each other at the well location (Well A, Figure 6.1b). The fractured chalk sequence is about 200m thick (Figure 6.2a). High hydrocarbon saturations are believed to be related to fractured/fault zones in the Ekofisk and Tor Formations (Figure 6.2b). On testing, this interval produced 200-250 barrels per well per day (BPWPD) with 6-20% oil-cut. Neither the Ekofisk nor the Tor show abrupt changes in porosity.

6.2 Data processing

Four streamer lines (Figure 6.1b) were acquired in 1986 by Western Geophysical. Figure 6.3 shows four CMP gathers selected from the four lines. The data are of reasonable quality. The top and bottom of the target can be clearly identified from the final stacked section supplied by FINA, which reveals complex fault zones

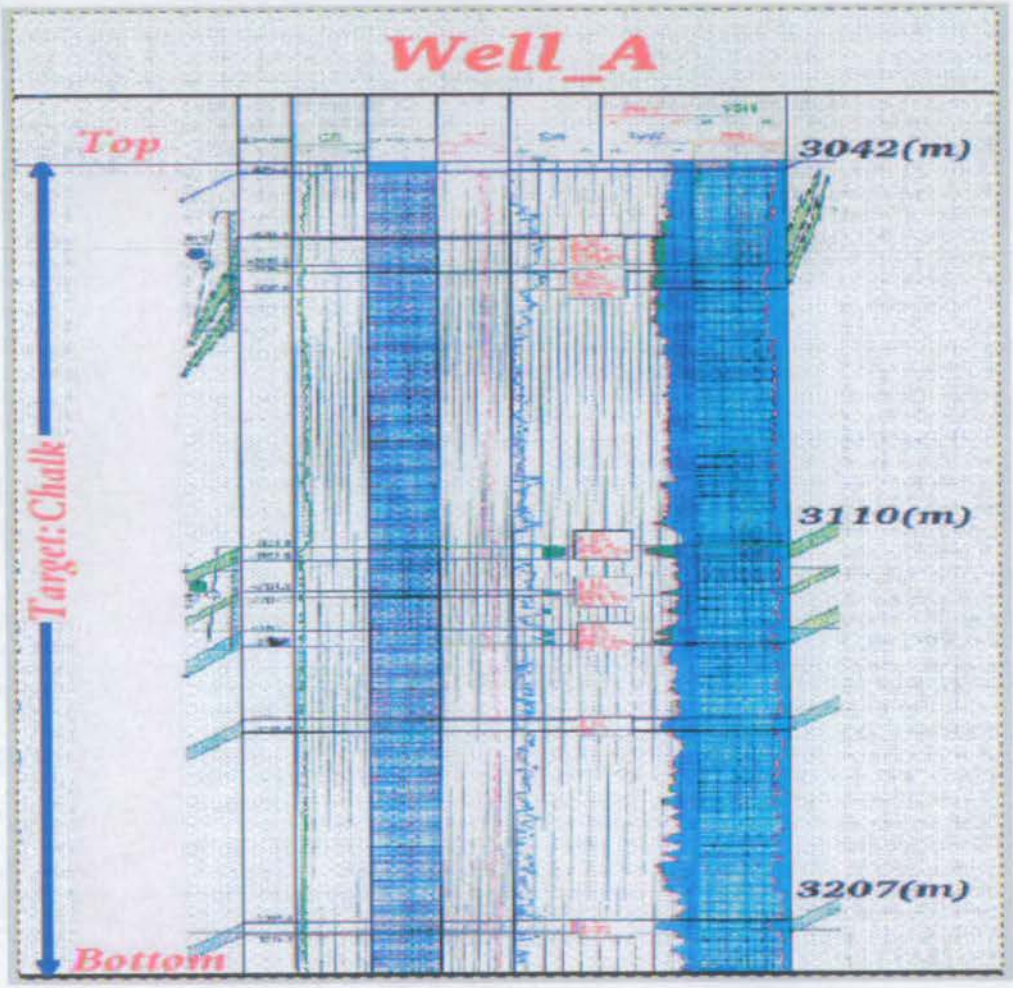

(a) (b)

Figure 6.2: The well logs at the intersecting point Well A.

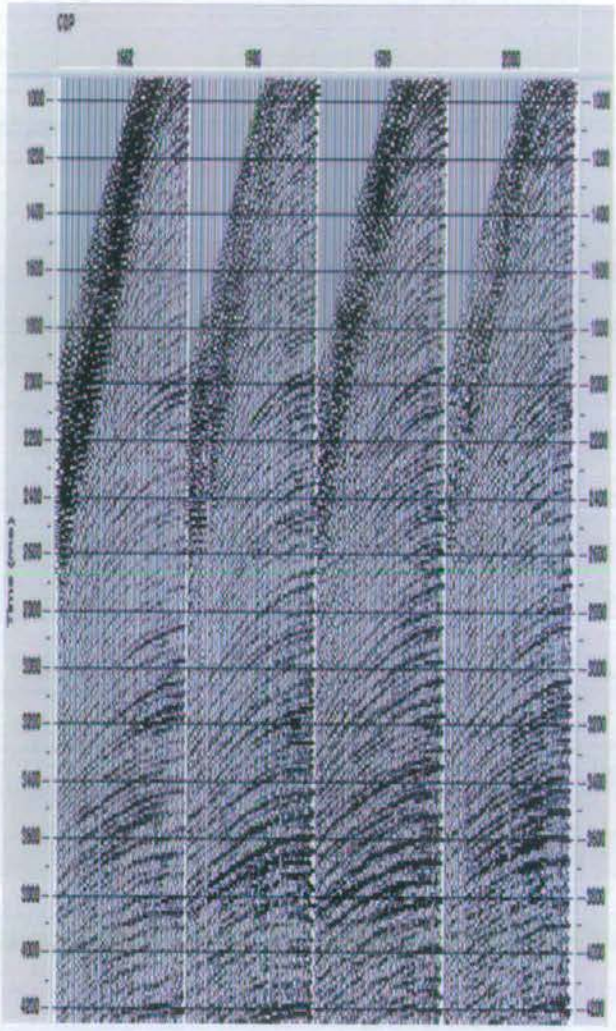

Figure 6.3: The CMP samples at the intersection point of the four lines, Well A.

(Figure 6.4).

Different processing procedures are needed for the application of traveltime and amplitude analyses. Traveltime analysis including azimuthal moveout and velocity requires the relative time shift between different events and different azimuths to be maintained, whilst amplitude analysis requires the relative changes in amplitude to be maintained.

Among these steps, editing bad shots and traces is very important, but time consuming. As we know, bad shots and traces can degrade the quality of the stacked

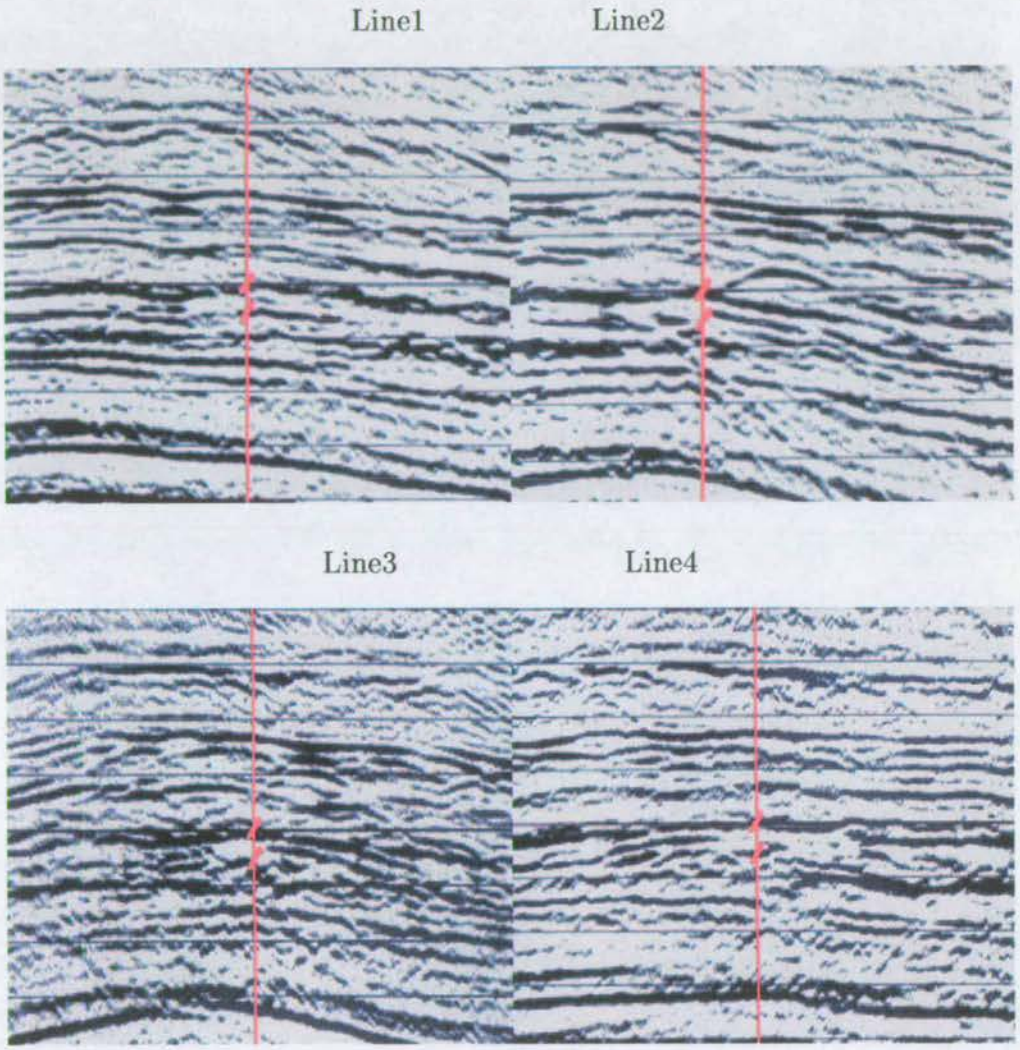

Figure 6.4: The final stacked sections for lines 1, 2, 3 and 4. The red vertical lines in the sections mark the crosspoint of the four lines and the position of Well A, and two intersecting short lines mark the top and bottom of the seismic target.

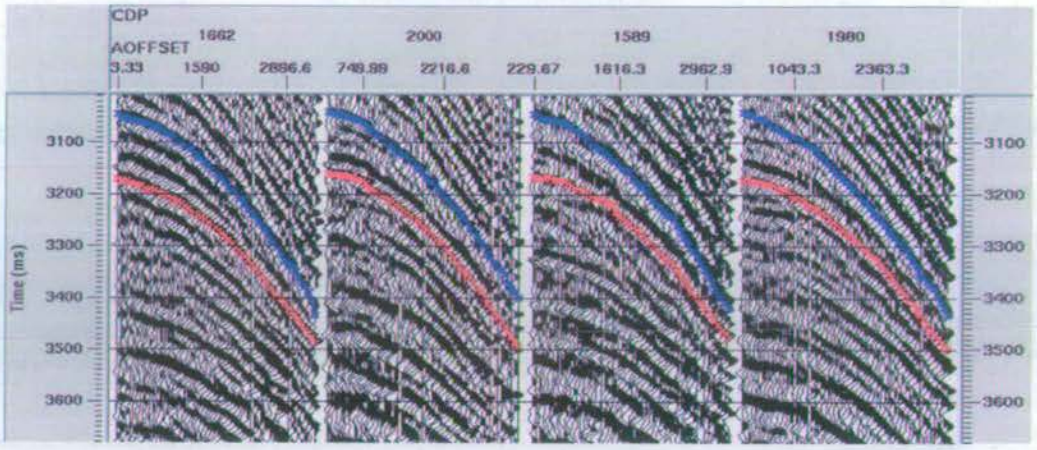

Line 1 Line 2 Line 3 Line 4

Figure 6.5: CMP gathers at Well A for lines 1, 2, 3 and 4.

section substantially. Artificial intelligence techniques such as neural networks may be used to pick up bad shots and traces. Here I use the basic interactive picking method.

Velocity analysis is critical to obtain a good quality stack. Here the data are good, and reliable velocities can easily be picked from semblances (Figure 6.6). Deconvolution is crucial for shortening the wavelet and properly separating the reflections from the top and bottom of the target. The Surface Consistent Deconvolution and Spiking/Predictive Deconvolution in ProMAX system are used in the processing. The former is used to improve the lateral continuity of events and the latter is used to improve the resolution.

6.3 Results of azimuthal attribute analysis

From the well log in Figure 6.2 three interfaces can be identified at depths of 3042m (two-way travel time 3019ms), 3110m and 3207m (two-way traveltime 3134ms). The depth of 3042m is near the top of the Ekofisk. Considering that a layer of

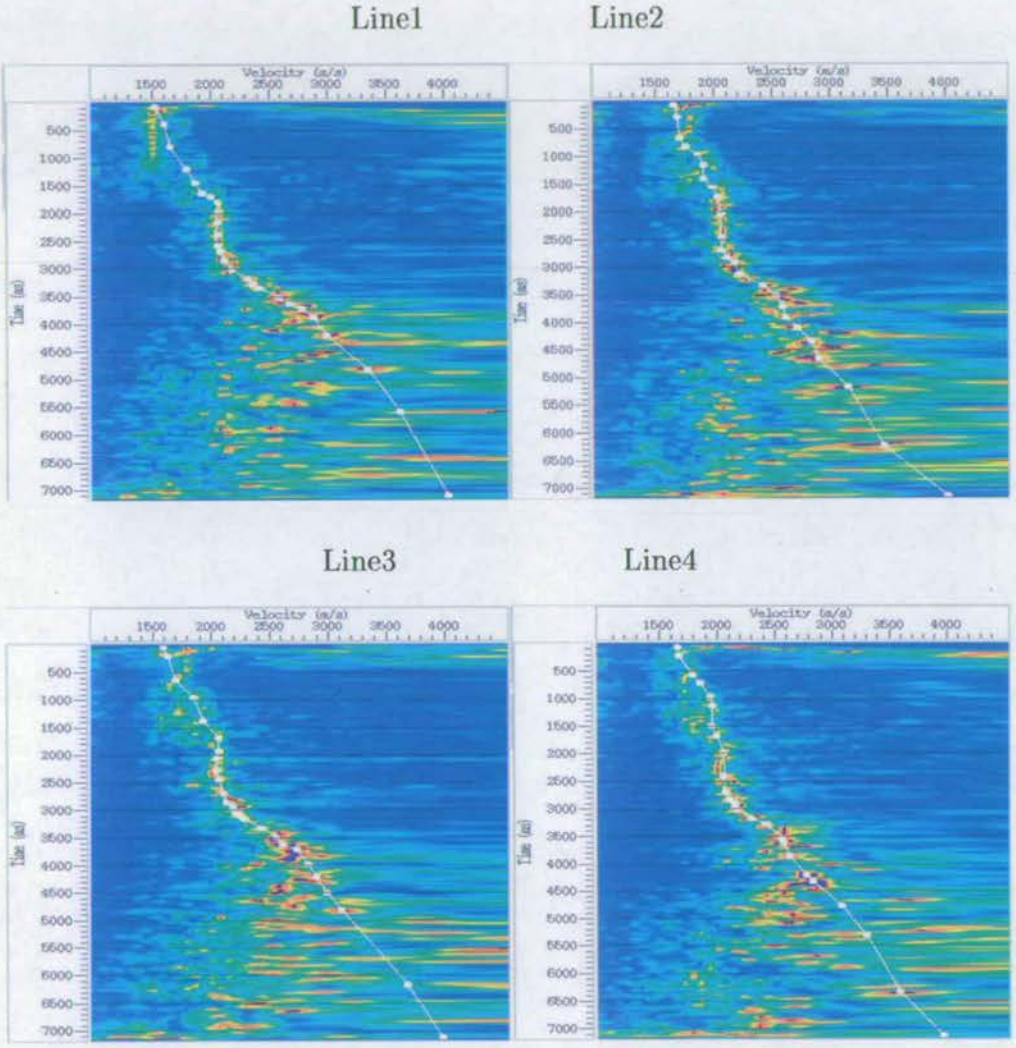

Figure 6.6: The four velocity spectra of line 1, line 2, line 3 and line 4 respectively, in Figure 6.3.

70m between 3042m and 3110m is difficult to distinguish from the seismic record, the interface at 3207m is used as the new target bottom for anisotropy analysis (Figure 6.4). Based on the theoretical analysis in Chapter 5, the result obtained from this enlarged interval should represent the results of the original 70m target with sufficient accuracy.

Velocities for the four lines can be analysed from the processed CMP gather (Figure 6.5). The four velocity spectra corresponding to the CMP gathers are shown in Figure 6.6. Using the interactively picked velocities as guide cures, the more accurate traveltimes in the four azimuthal directions can be picked. By fitting the picked traveltimes at the target to four cures using least-square inversion, the more accurate NMO velocities are calculated as 2259.13, 2242.72, 2178.25 and 2197.92 m/s. Applying the azimuthal velocity analysis method, I obtained a fracture strike of $\Phi_v = N75^oE$ (Figure 6.1b). Therefore the angle estimation error by using velocity should be similar to that by direct using traveltimes.

To examine the azimuthal variation of moveout (traveltime) and amplitude, we often apply NMO-correction to the data (Figures 6.7 and 6.8). The top event for all four lines is relatively flat, whilst the bottom event for Lines 1, 2 and 4 is overcorrected, and the degree of over-correction varies among the lines. This reveals a clear azimuthal variation of traveltime. The pattern of the variation suggests that Line 3 is close to the fracture normal. This is because the NMO velocity along the fracture normal is slow and when a slow velocity is used for NMO correction overcorrection occurs. The amplitude variation and corresponding picks are shown in Figure 6.8. The variation of the residual moveout complicates the picking of the amplitude.

The final cross-plotting results of the traveltime and amplitude are shown in Figures 6.9a and 6.9c. The traveltime cross-plot reveals a relative good trend, and the calculated angle at the offsets larger than half of the target depth is $26^o \pm 7.5^o$ from line 1 ($\Phi_t = N73^o \pm 7.5^oE$, Figure 6.1a) which is in good agreement with the

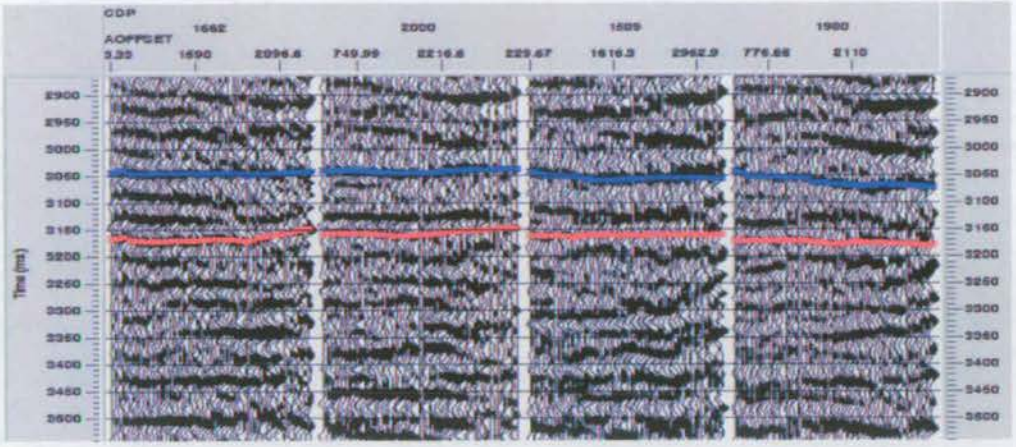

Figure 6.7: The CMP gathers after moveout correction at Well A.

result of the azimuthal velocity analysis. However, the amplitude results are more scattered, as expected, and a good result is not apparent.

6.4 Discussion and conclusions

In a fractured anisotropic medium, the P-wave amplitude and gradient, NMO velocity (slowness) and interval traveltime (moveout) may show elliptical variation with azimuth (Chapters 2 and 3). These ellipses have the same major axis direction as the direction of the anisotropic symmetry axis. In the case study, the angles estimated from interval moveout and NMO velocity analysis are consistent with each other.

Azimuthal AVO relies on the detection of subtle amplitude variations, and is time consuming to implement in repeated surveys of various vintages because different sources and receivers were used. Extensive effort must be placed on wavelet shaping and matching to make this analysis possible. For azimuthal NMO velocity analysis, magnification of errors is of some concern both in the Dix equation for interval

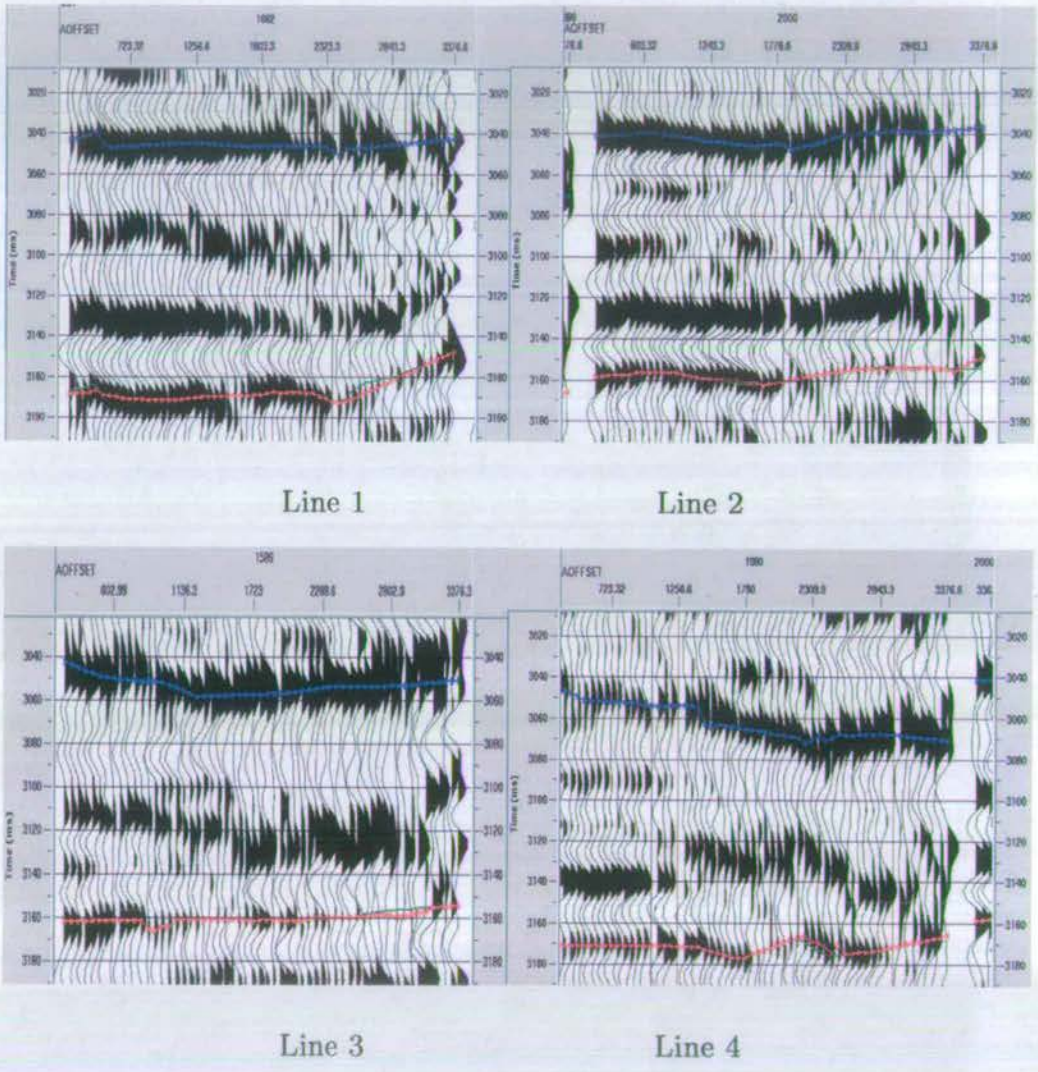

Figure 6.8: Windowed CMP gathers showing the azimuthal variation of the amplitude. The lines indicate the top and bottom of the target.

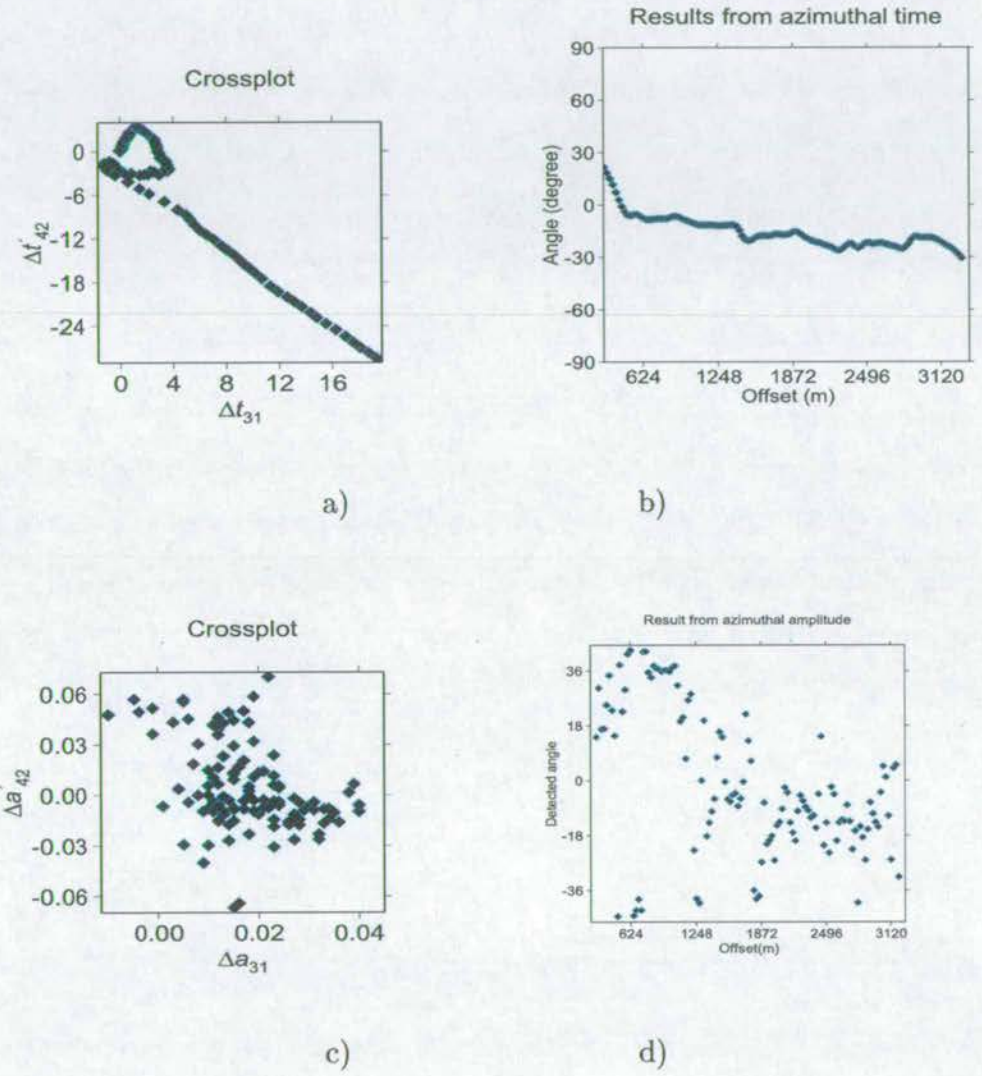

Figure 6.9: Azimuthal interval time analysis results: (a) The cross-plot of Δt_{31} versus $\Delta t'_{42}$ and (b) the detected angles for each offset for the real data in Figure 6.3. Azimuthal amplitude analysis results: (c) The cross-plot of ΔA_{31} versus $\Delta A'_{42}$ and (d) the detected angles for each offset.

measurements and in the least-squares fitting of the NMO ellipse.

The use of differential attributes between two orthogonal lines shows potential in overcoming some difficulties in azimuthal AVO and NMO velocity for marine seismic data. The methods have good flexibility in handling variations in acquisition conditions. These variations include inconsistency in source signatures, offset and azimuthal sampling, and spatial variation in target depth and thickness. The orthogonal distribution of azimuthal lines also improves the reliability of the NMO velocity analysis and the results of NMO velocity agree with the results of azimuthal moveout analysis.

This case study of the four-line configuration confirms the effectiveness of the 3A technology presented in Chapter 3 and 4. It also uses the concept in Chapter 5 to enlarge the thin target layer of 70m by adding an extra interval. However, it is worth noting that after all these efforts, the method only yields results at the intersecting point. It does not provide any information on the spatial variation of subsurface fractures. For this purpose, multiple cross 2D lines, or cross 2D and 3D data are required, and this is discussed in the next chapter (Chapter 7).

Chapter 7

Fracture Detection Using Crossed 2D and 3D Marine Data

Abstract

In this chapter, I present a case study of fracture estimation using crossed 2D and 3D surveys from the North Sea. I develop data matching procedures to integrate such datasets and demonstrate the potential of using repeated 3D surveys of different vintages for improving spatial coverage as compared with the case of crossed 2D lines in Chapter 6.

The dataset includes ten crossed 2D lines, and a 3D survey shot over ten years ago using a two-streamer boat. Supergathers are formed from the 3D data combined with the crossed 2D lines to overcome the lack of azimuthal coverage. This gives rise to at least three traces in an azimuthal gather for each CMP point along any particular crossed 2D lines. The approach requires careful data processing to match acquisition geometries, and the phase and amplitude characteristics of the 2D and 3D surveys. Fracture orientations along the ten lines are estimated and plotted as rose diagrams. In this way, the lateral variation in fracture orientations can be

determined. These results agree with the previous analysis of orthogonal 2D lines in Chapter 6.

7.1 Introduction

So far, I have demonstrated the 3A technology and its application using both synthetic and real datasets. We know that aligned subvertical fractures cause azimuthal variations in seismic attributes such as traveltime, velocities and amplitudes. The 3A technology involves the analysis of azimuthal variations in P-wave traveltime, amplitudes, NMO velocity and AVO gradient. This technology is also sometimes referred to as P-wave AVD (attributes versus direction) technology (MacBeth and Li, 1999). The application of the AVD technology to 3D streamer data is still a problem because of the lack of good azimuthal coverage. Marine 3D streamer data are usually recorded in a different way from land 3D data, with streamers parallel to each other, giving rise to a very narrow azimuthal coverage that decreases with increasing offset. This limits the application of P-wave AVD analysis for fracture detection. In Chapter 6, I utilized crossed 2D lines from different vintage surveys to compensate for the lack of azimuthal coverage. But the spatial resolution is limited and the results are only applicable to the intersection point. Here I examine the possibility of combining 3D surveys with crossed 2D lines for improving spatial coverage. In this case study, azimuthal gather containing at least three-azimuthal traces can be formed along each CMP point crossing each 2D line, which makes it possible to obtain fracture orientations along all the ten 2D lines. The results are shown in rose diagrams to help interpretation.

I conclude from this study that the azimuthal coverage necessary is the "Source-Receiver" (S-R) azimuth coverage, but not the "Shot Line-Receiver Line" (SL-RL) azimuth coverage, and that if the joint data - composed of marine 3D data and

crossed single 2D data - are available, the attribute versus direction (AVD) technique can then be applied. Thereafter, such marine 3D datasets could be used for extracting azimuthal anisotropy information about subsurface cracks and fractures. This reveals a great potential for further application to modern 3D marine surveys with wide azimuthal coverage.

7.2 Field data application

7.2.1 Study area

There are two wells 2km apart in the study area (Figure 7.1, Wells 1 & 2). The target formations marked inline and cross line (Figure 7.2) are the Ekofisk Formation and the Tor Formation. Core study and well testing results indicate that these two formations are associated with residual oil within fractured and fault zones (Hall et al., 2002). Based on core and CPI control it is inferred that the Ekofisk Formation in both wells consists of essentially non-reservoir, basinal facies. Amplitude mapping in this area also confirms that no hydrocarbon reservoir has been assigned to the Ekofisk Formation in this structure. However, drill stem testing of the upper Tor Formation in Well 1 indicates the presence of movable oil within the structure. Water produced during the same testing indicates the presence of a water/transition zone within the test interval. Based on CPI analysis, the base of producible oil is interpreted to be at the top of the lowermost porous bed with a depth of about 3100 m to 3200 m. Well 2 also encounted the top of the water-bearing Tor Formation at a depth of about 3160 m, which supports this interpretation.

The Tor Formation is an attractive layer in this area, and is found to be related to the fault and fractured zone in two wells and is in the Chalk sequence. The top and bottom of the Tor formation are at approximately 3.13 s and 3.2 s in the

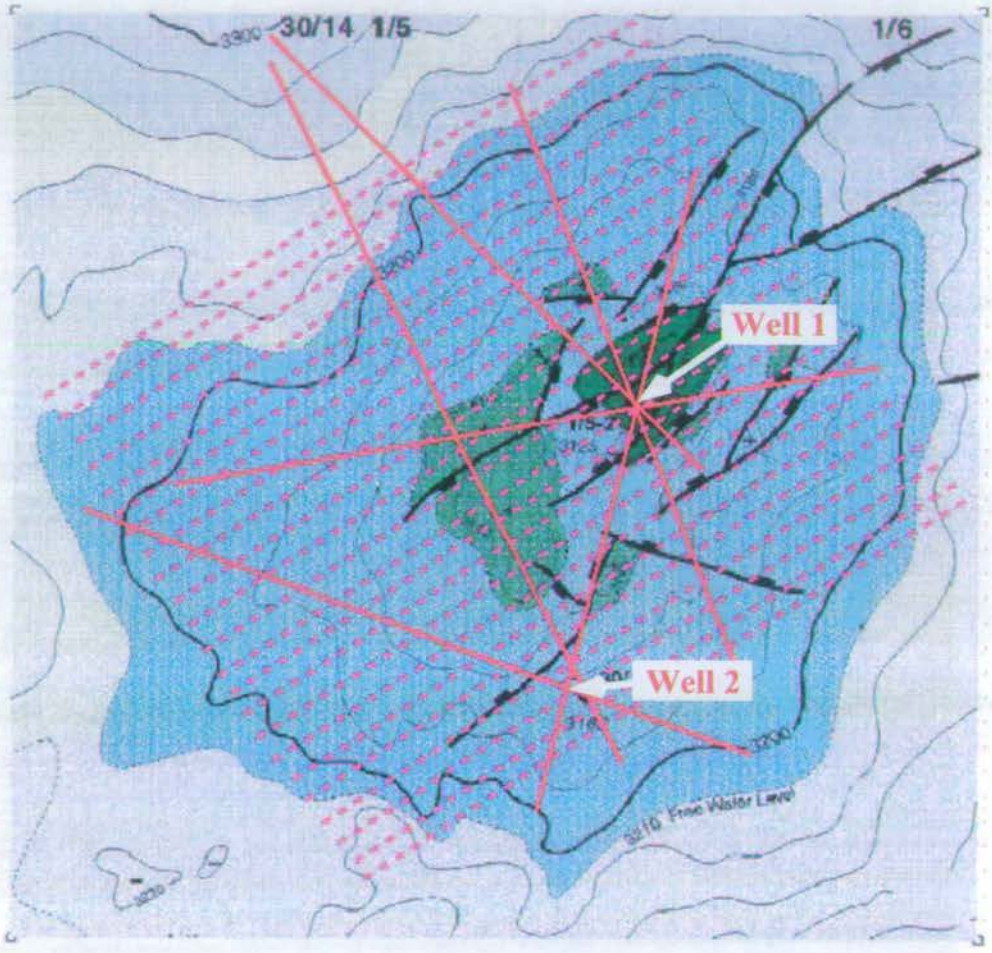

Figure 7.1: Dataset area shown on the target depth map. The parallel lines show marine 3D streamer sailing directions which are crossed by a few different directional 2D single streamer lines which were shot at different times. Both of the cored wells 1 and 2 are located in the fault/fracture zone to the right of the area.

	Shot Interval (m)	Receiver Interval (m)	Traces /Shot	Date	Shots	Size (GB)	Record Length (ms)	Sample Interval (ms)
2D	26.6/50	13.3/25	240/120	1986 1989	10,000	10	7000	2
3D	50	25	240	1989	50,000	56	7000	2

Table 7.1: The acquisition parameters of the 2D and 3D marine data

two-way time section, respectively (Figure 7.2). We note that, for the same target layer, there are about 100ms system time-shift between the provided data (Figure 7.2) and our merged data (Figure 7.14). I believe that this is because no unified datum was used in processing. The Chalk sequence is approximately 200 m thick and is known to be fractured from boreholes. High hydrocarbon saturations are believed to be related to these fractured and fault zones.

In my previous study, I find that there were two pairs of orthogonal 2D lines intersecting at Well 1, from which fracture orientation of about $N73^0E$ were estimated in Chapter 6. In this chapter, I address the problems of estimating fracture orientations from 3D data and attempt to extract fracture information for the Tor Formation at the other positions without core information or any drilling. If this proves to be possible, it will be useful to extend current interpretation results of Well 1 and Well 2 to the study area.

7.2.2 Acquisition configuration

In the previous section, the S(ource)-R(eceiver) azimuthal direction is overlapped by SL-RL azimuth direction. In other words sources and receivers are located on exactly the same line. In this section, my joint data have a special "three-line" configuration as shown in Figure 7.3. There are three receiver lines in different directions, and a source is located on one of the receiver lines, e.g. Line 1, but not

on the other two receiver lines. For all receivers on Lines 2 and 3, the S-R azimuthal directions are different. Clearly, S-R direction is not always the same as either the SL or RL direction.

For a fixed CMP point (i.e. same as the Source Point in Figure 7.3) and a fixed offset such as r1, r2, r3, ..., at least one trace from each azimuthal direction can be obtained and a total of three traces can be found for each offset. After solving equation (3.36) or applying a least-squares fitting procedure (if there are more than three traces) to equation (3.36), I may obtain a series of $A(r_i)$, $B(r_i)$ and $\Phi_0(r_i)$ (i = 1, 2, ... K).

7.2.3 Datasets

Three data blocks in the study area are provided known as Blocks 1, 2 and 3. Block 1 consists of four 2D lines labelled 55, 59, 62 and 64 and the data were recorded in 1986. Block 2 consists of six 2D lines labelled 01, 02, 03, 04, 07 and 08 and the data were acquired in August 1989. All the ten 2D lines were shot in different directions (Figure 7.1). Block 3 is composed of 90 swathes of marine 3D data and the survey was carried out in December 1989 (Table 7.1). All data were recorded over a salt-induced structure in the Central North Sea with intensive faulting (Figure 7.1). A total of 88 swathes in the 3D data are used and there are two parallel receiver lines (Figures 7.4 and 7.5). The difference in SR-RL azimuth is zero and both SL and RL are in the direction of $N57^0E$ which is approximately parallel to one of the fault strikes at $N30^0-70^0E$. The other fault strike is in the range of $N30^0-70^0W$. These datasets were shot about ten years ago and the acquisition parameters are given in Table 7.1. The azimuth of the 3D swathes is also parallel to one of the main fault systems at the target depth (Figure 7.1). Initially it appears to be impossible to extract fracture information from this 3D dataset as the azimuthal coverage is very

(a) Inline

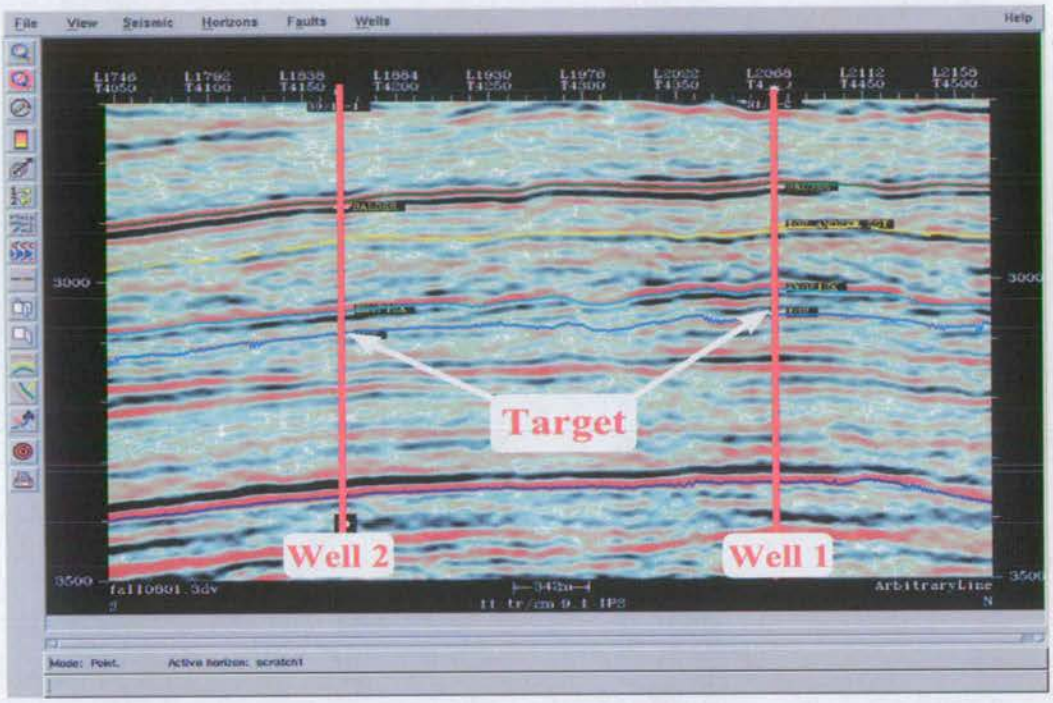

(b) Crossline

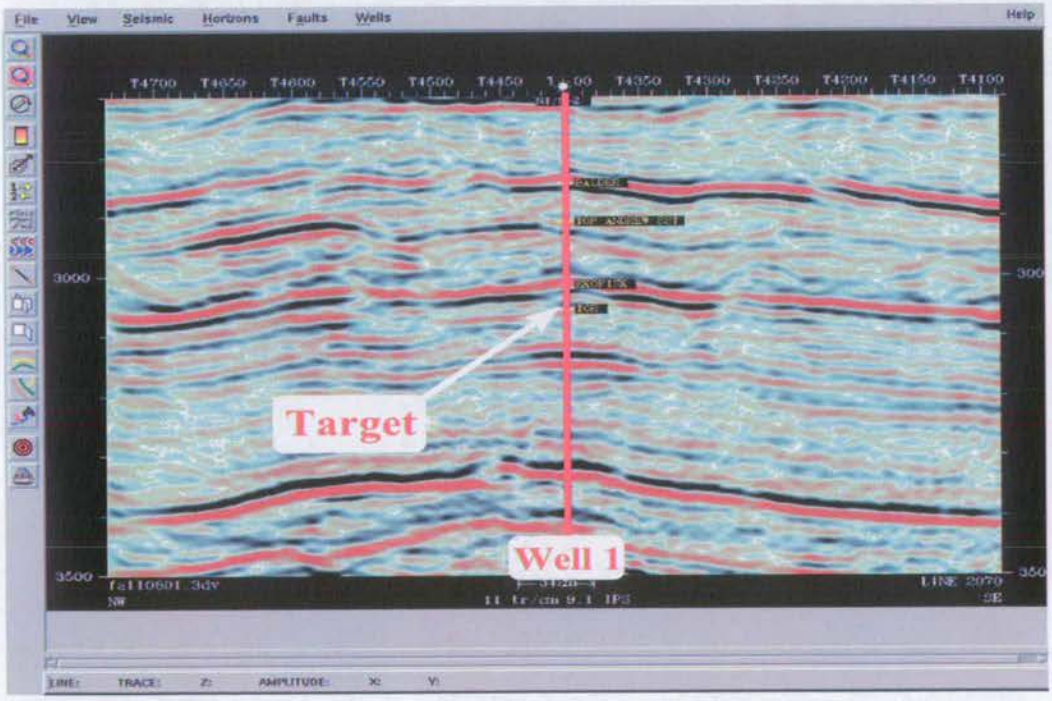

Figure 7.2: The well tie between Wells 1 & 2. My target is the underlying layer of Ekofisk and Tor at traveltime of about 3000 ms. The core shows that Tor is a fault/fracture zone which could be found in both wells. (a) inline section (North-West); (b) cross section (South-East). The two sections intersect at Well 1.

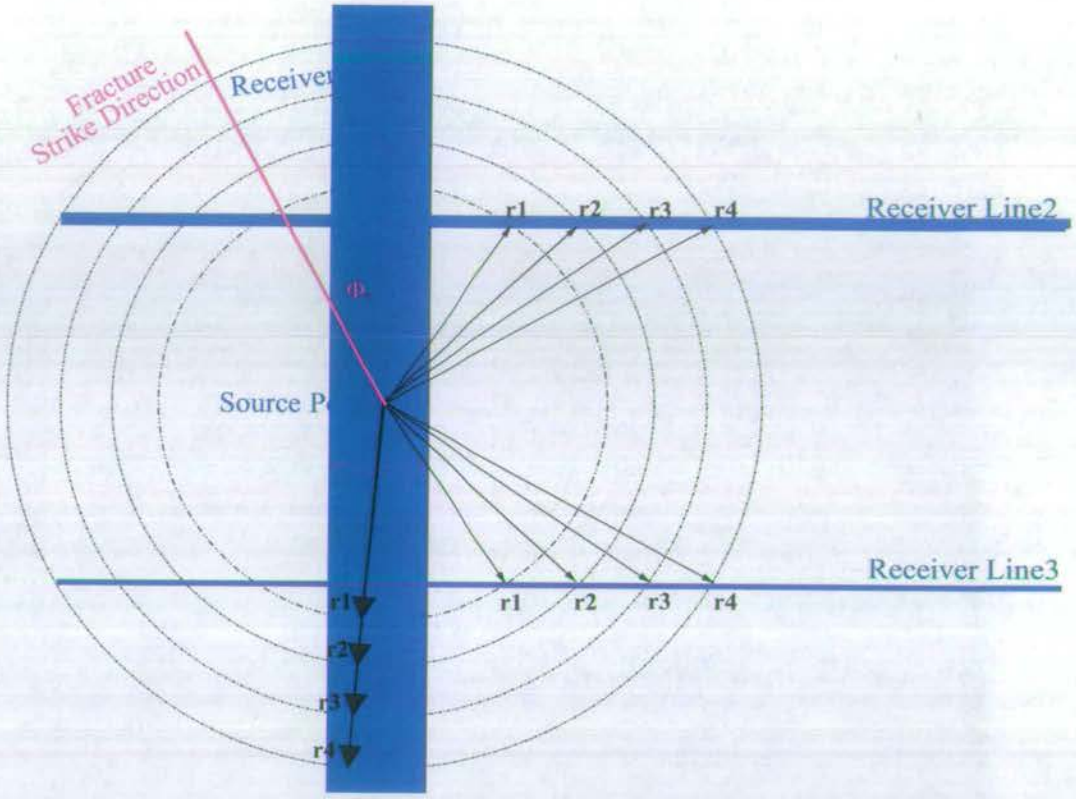

Figure 7.3: Special three-line configuration. *Line*2 || *Line*3 and 100m apart from each other. The source point is located only on line 1. r1, r2, r3 are three offset instances. If a CMP point is in the same position as the Source Point and such a CMP gather exists, a series of fracture orientation angles could be calculated from its sorted offset gathers.

limited. However, my previous experience of analysing this kind of 3D data (Figure 7.3) shows that there are two traces with different azimuths that can be found for each offset in one CMP gather, and three traces can be found for each offset in each supergather. This condition meets the basic requirement of combining these 3D data with 2D lines. But we also notice that the azimuth difference of the two traces from 3D data will decreases when the offset increases. Therefore the azimuthal traces are only available inside a limited offset range.

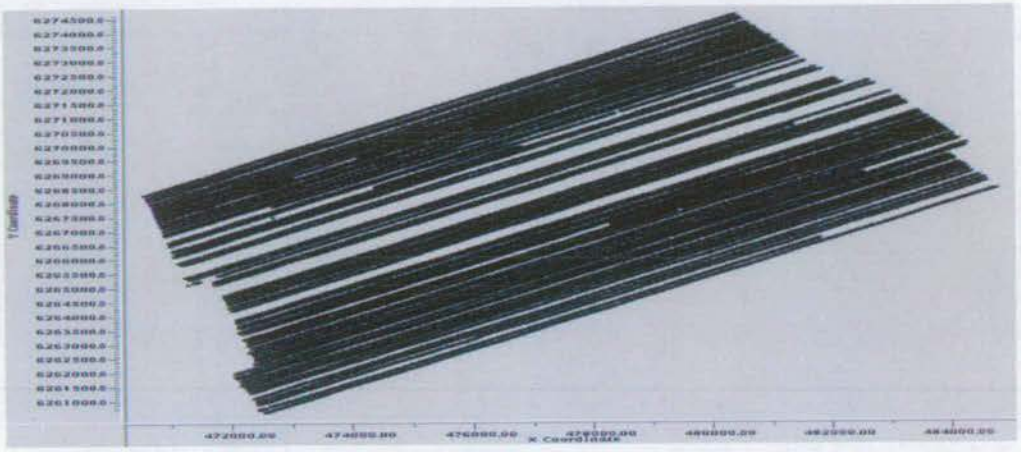

Figure 7.4: Regional coverage of the 3D survey. There are 88 swathes separated by 100m from each other.

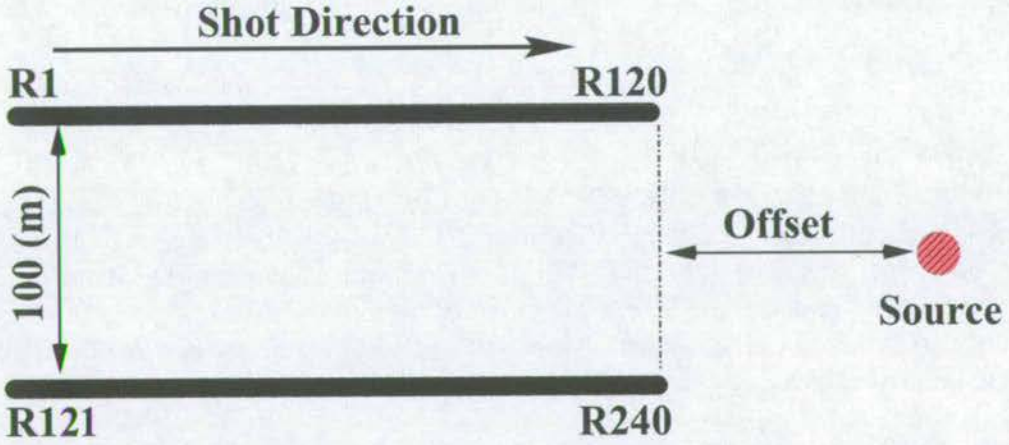

Figure 7.5: Streamer configuration of the 3D survey. It was a two-streamer 3D boat with 120 receivers on each streamer. The "Offset" in the diagram equals about 100 metres.

Tape No.	Line No.	Start Source (FFID)	Stop Source (FFID)	Total Traces
07	1	23911 (18)	24155 (262)	240
07	1	24156 (263)	24156 (263)	239
07	1	24157 (264)	24421 (528)	240
07	2	24422 (18)	24514 (110)	240
07	2	24515 (112)	24799 (396)	240
07	2	24800 (396)	24800 (396)	241
07	2	24801 (397)	24933 (529)	240
07	3	24934 (18)	24936 (20)	240
07	3	24937 (28)	25439 (530)	240
07	4	25440 (18)	25955 (533)	240
07	5	25956 (18)	25957 (19)	240
07	5	25958 (19)	25958 (19)	480
07	5	25959 (19)	25959 (19)	481
07	5	25960 (22)	26299 (361)	240
07	5	26300 (367)	26300 (367)	240
07	5	26301 (369)	26449 (517)	240
07	5	26450 (517)	26454 (521)	240

Table 7.2: Data inputting summary for Tape 07 (one of 45 tapes). Ideally, each shot contains 240 traces. The FFID should be continuous. However, because of traces or shots missing or partially missing, only 239 traces were read from FFID 263, one trace was repeated for FFID 396. The boundary of FFID 19 and 21 (Line 5) was missing and traces 19 to 21 were mixed wrongly. From the Navigation file I could also extract similar tables. After editing the data or navigation files, both of the summary tables can be output again and should be matched completely.

7.3 Data Processing

Before I perform azimuthal AVO analysis, I first need to form a common offset supergather for all the crossed surface points which have three azimuthal records from all 88 swathes of marine 3D streamer data and ten 2D single streamer lines. The 2D lines were shot in different directions with different patterns, and the different swathes in the 3D data were also shot in different patterns. The main differences are recording time, source type, source and receiver depths, difference of exploration times among data blocks, source energy and wavelets. In this section, I focus on how to form the matched supergathers, and for this purpose a three-stage matching scheme is designed on the ProMAX system including geometry matching (Match 1), CMP matching (Match 2), and data matching (Match 3).

7.3.1 Match 1 - Geometry matching

I have a unified coordinates and source index for all data blocks after geometry matching, and a universal 3D geometry file from which no trace in any data block is excluded. I assume that FFID numbers from all shots and shot/receivers coordinates are stored in a Navigation File. The same FFID numbers are also included in the data header. The following eight steps are used in this stage.

Step 1. Unify coordinate systems of shots and receivers from different blocks.

Step 2. Match data and navigation information.

The data can be loaded into ProMAX separately and the universal index Source Number for each shot was built. At the same time, I define a unique Line Number as a block identifier number which will be used in the data matching stage. FFID numbers are used as an identifier number for the coordinates of each shot. Ideally, the data on tape and navigation file should match each other exactly by using the seismic data header entry FFID number. Unfortunately, when I input this 10

years old dataset, traces are sometimes missing, or the whole shot may not be read correctly. An example summary of 3D data inputting is given in Table 7.2. From the Navigation file I may also extract similar tables. When I match data with the Navigation file, I need to edit both the input data and the navigation tables. This process is very time consuming.

Step 3. Find left, right, top and bottom boundaries for each data block such as 3D swathes and all 2D lines. In Figure 7.6, C11, C12, C13 and C14 are the boundary corners of 3D streamer data. C21, C22, C23 and C24 are the boundary corners of all the 2D and 3D lines. C31, C32, C33 and C34 are the boundary corners of the extending area, or the common 3D grid area.

Step 4. Find the common boundary from the result of Step 3 (Figure 7.6).

Step 5. Determine inline and crossline directions. Here the 3D inline direction is used as the main geometry inline direction.

Step 6. Extend the boundary found in Step 3 so that all CMP positions are included in the unified CMP grids, so that I can build a set of geometry parameters for the common 3D grid which will include all 3D and 2D lines.

Step 7. Define a geometry file for each data block using the common parameters and its own data.

Step 8. Upload header values from geometry files to all seismic trace headers separately.

7.3.2 Match 2 - CMP Matching

After CMP matching, ten new 2D lines will be extracted which are located in exactly the same geographic location as the previous ten and which are composed of big bin supergathers. These supergathers are formed by gathering 2D and 3D big binning gathers. The original universal 3D grid bin size is $50m \times 50m$. Now $150m \times 150m$ is

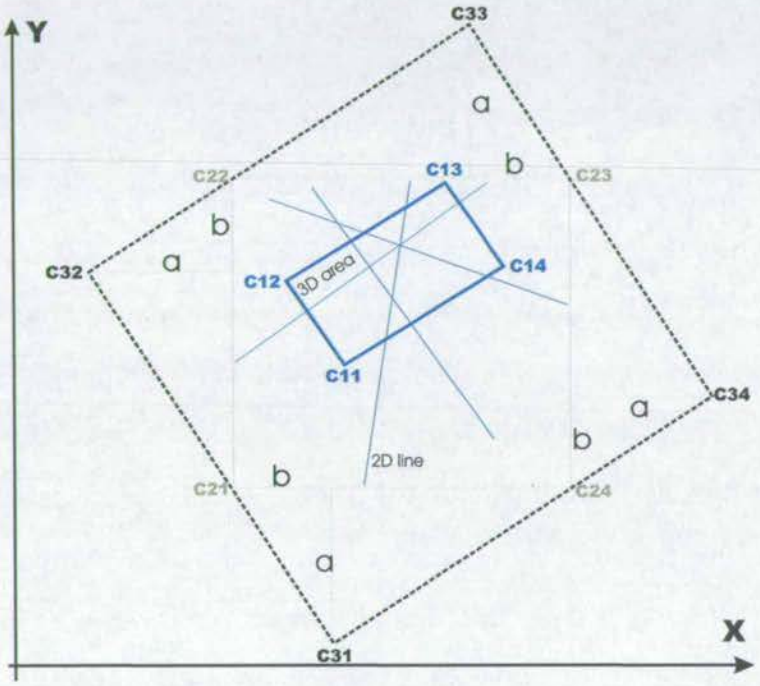

Figure 7.6: How to obtain the extended 3D grid. C11, C12, C13 and C14 are the boundary corners of 3D streamer data. C21, C22, C23 and C24 are the boundary corners of all the 2D and 3D lines. From the coordinates of C21, C22, C23 and C24 and the known angle of the 3D inline direction, "a" and "b" can be calculated. Then the coordinates of C31, C32, C33 and C34 can be computed. These are the boundary corners of the extending area, or the common 3D grid area.

used as the big binning size. The big binning gathers may be sorted by ProMAX if the following two requirements are met: (1) Enough disk space exists. The original data size is 60 GB, and each original bin is a possible supergather bin point. So I need to form the supergather bin by bin, thus the storage space for this one job needs $5 \times 60 + 60 = 360$ GB; (2) A ProMAX module is available to withdraw an arbitrary 2D line from a 3D dataset. However I had none of these. Even if I had both of them, this will be very time consuming. I have therefore developed a procedure described in the following eight steps to solve this problem.

Step 9. Calculate coordinate rotation equations for each 2D CMP central line in which the new X-coordinate on this 2D line equals a nominal number (here 2000 is used). Figure 7.7 shows that in general my real CMP points line is a CMP points beam. The following steps are listed for each of the ten lines: calculating central CMP line; calculating coordinate system linear transformation parameters of the central line; rotating coordinate system; defining a new inline and cross line number; and defining a new CMP number based on the new defined inline and cross line numbers. All the steps are repeated ten times on these 3D data using parameters used for different 2D lines, and finally I obtain the common new CMP range for 2D and 3D data and gather the supergathers including all possible traces located in this big bin.

The coordinate rotations or linear transformation parameters for ten 2D lines are listed in Table 7.3. Now I show how to obtain the parameters $X0, Y0$ and *Azimuth or* α in Table 7.3. First, input all source and trace coordinates; Second, compute CMP X, Y coordinates: $X(i)$ and $Y(i)$, and its azimuthal angle $Azimuth(i)$ for each trace; and third, using equation (7.1), calculate X0, Y0 and azimuth (the angle begins with Y-axis and is positive in a clockwise direction).

$$\begin{cases} X0 = \frac{1}{K}\sum_{i=1}^{K} X(i) \\ Y0 = \frac{1}{K}\sum_{i=1}^{K} Y(i) \\ Azimuth = \frac{1}{K}\sum_{i=1}^{K} Azimuth(i) \end{cases} \tag{7.1}$$

For any given 2D line, if the calculated azimuth is negative (Figure 7.8 Left) or positive (Figure 7.8 Right), the coordinate rotation equation parameter "Constant" (Table 7.3) can be calculated using equations 7.2 and 7.3 respectively as shown in Table 7.3.

$$Constant = 2000.0 - \sqrt{X0 * X0 + Y0 * Y0} * \cos(90 - |\alpha| - \arctan\frac{X0}{Y0}) \tag{7.2}$$

$$Constant = 2000.0 - \sqrt{X0 * X0 + Y0 * Y0} * \cos(90 + |\alpha| - \arctan\frac{X0}{Y0}) \tag{7.3}$$

Using X1 and Y1 to denote the original CMP X-axis and Y-axis, the new CMP coordinates (Table 7.4) can be calculated using the following equations:

$$\begin{cases} \alpha 2 = \arctan|\frac{X1}{Y1}| \\ oa = \sqrt{X1^2 + Y1^2} \\ angle = 90.0 + \alpha - \alpha 2 \\ X_{new} = oa * \sin(angle) + Constant \\ Y_{new} = oa * \cos(angle) \end{cases} \tag{7.4}$$

All the new X-coordinates on the Central CMP lines of all ten lines should be equal to the chosen nominal number (here 2000). This is a key design feature to achieve a high processing efficiency.

Step 10. Rotate all 2D lines with equation 7.4 using parameters in Table 7.3.

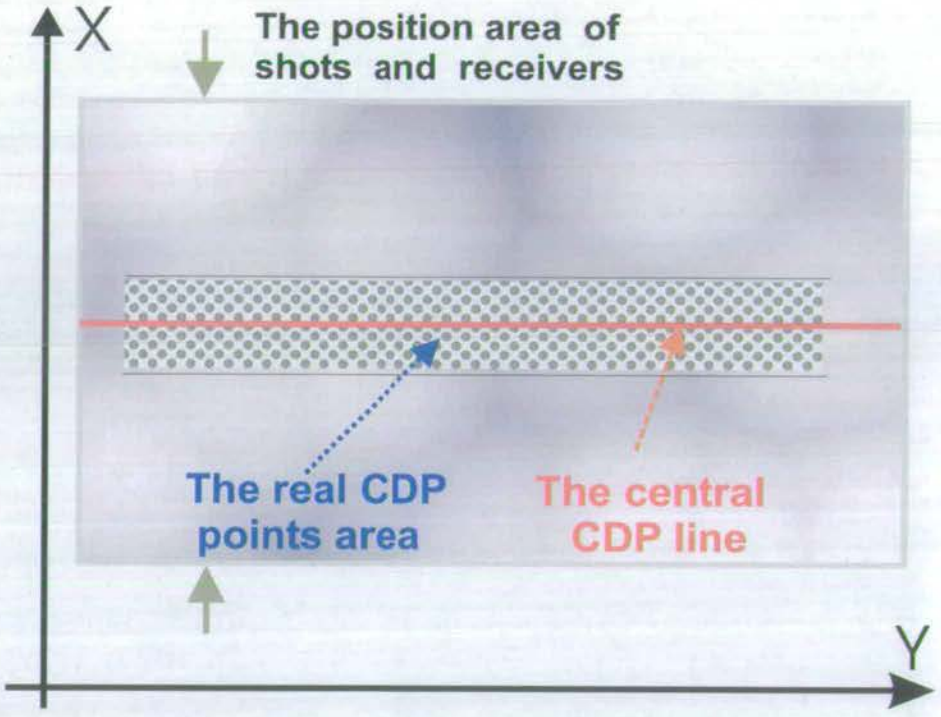

Figure 7.7: The real CMP line of all the 2D lines is not exactly a straight line; it is actually a CMP points beam. For merging 2D and 3D, I need to get a straight CMP line. Here the central CMP line of the real CMP points beam is used as the straight CMP line (Straight red line).

Step 11. Rotate 3D data coordinate system ten times by applying the same equation and parameters as in Step 10, then the values of the twenty new data header entries given in Table 7.4 are calculated and inserted into the trace headers of all 3D data.

Step 12. For any 2D line, insert three new header entries for the newly defined CMP number, inline and crossline numbers by using new X and Y coordinates which, with a new CMP number will always begin with 12001, and the new inline number will always be 2001. This task is repeated for every 2D line.

Step 13. Repeat Step 12 for 3D data; ten runs are required;

Step 14. Find new common CMP range with the traces from both 2D and 3D datasets for all ten new lines.

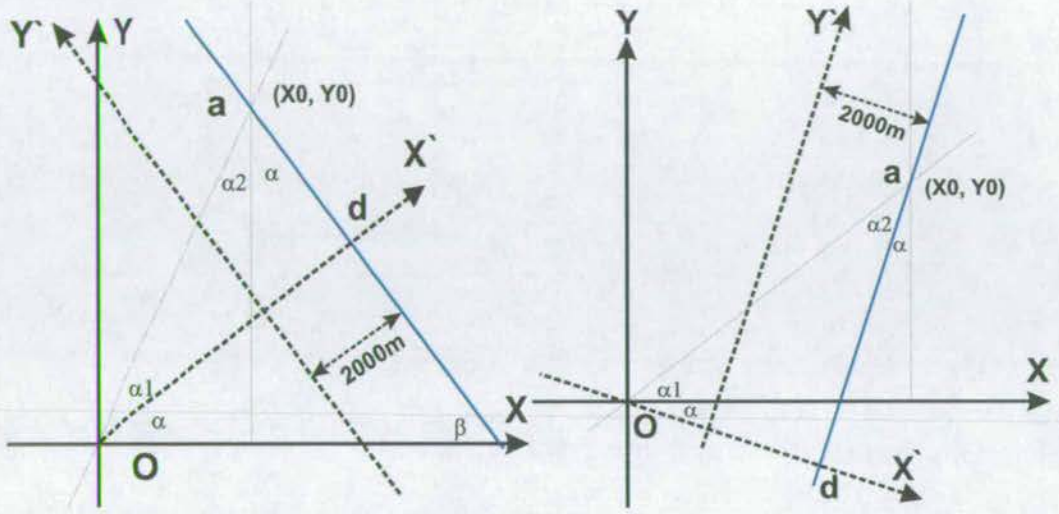

Figure 7.8: The rotation of the coordinate when the angle from Y-axis for any 2D line is negative (Left) or positive (Right). In the new system, the value of $X' - axis$ always equals 2000.0 from the central CMP line.

Line	X0	Y0	Azimuth(α)	Constant
Line 01	480572.	6.26414E+06	-22.2962	-2.81923E+06
Line 02	474723.	6.27396E+06	-44.0465	-4.70114E+06
Line 03	475271.	6.26294E+06	19.5043	1.64506E+06
Line 04	475260.	6.27010E+06	79.7967	6.08875E+06
Line 07	474931.	6.27264E+06	-33.4528	-3.85205E+06
Line 08	473917.	6.26908E+06	-82.8427	-6.27728E+06
Line 55	478396.	6.27100E+06	47.7531	4.32250E+06
Line 59	478819.	6.26953E+06	-39.0746	-4.32160E+06
Line 62	478222.	6.27153E+06	15.4038	1.20680E+06
Line 64	476776.	6.27099E+06	-70.7420	-6.07534E+06

Table 7.3: The coordinate rotation or linear transformation parameters calculated for the ten 2D lines. The whole 3D data will be rotated ten times using the ten listed sets of parameters for extracting the geographically identical supergathers from 2D and 3D datasets.

Line No.	New CDP X-axis Entry	New CDP Y-axis Entry
Line 01	F2d01_X	F2d01_Y
Line 02	F2d02_X	F2d02_Y
Line 03	F2d03_X	F2d03_Y
Line 04	F2d04_X	F2d04_Y
Line 07	F2d07_X	F2d07_Y
Line 08	F2d08_X	F2d08_Y
Line 55	F2d55_X	F2d55_Y
Line 59	F2d59_X	F2d59_Y
Line 62	F2d62_X	F2d62_Y
Line 64	F2d64_X	F2d64_Y

Table 7.4: The ten pairs of trace-header entries are inserted into the trace header which will be used as the new X- and Y-axes.

Step 15. Using the new common CMP range as a primary sort key, the sorted data from both 2D and 3D are merged to form supergathers of the 2D line - or the new 2D line; Figure 7.9 is a windowed supergather of CMP 12017 from line 59. The processing steps before merging 2D and 3D datasets are the same. Line_no "3.7813e+05" is the original 2D line identifier, "5.3473e+06" is the original 3D data identifier. I immediately find a larger difference in traveltime and energy between the original 2D and 3D datasets.

7.3.3 Match 3 - Data matching

In the above stages, ten merged supergathers for 2D lines are extracted, and all lines are in their original inline directions for processing convenience. Match 3 is designed to complete the last match - Data matching, used to eliminate any data differences due to time shift, source energy and wavelets, or perhaps differences in sensitivities of the receivers.

Step 16. Separate merged 2D lines into two 2D lines whose traces are only from original 2D and 3D datasets using the trace header entry Line Number.

Step 17. Process two datasets with the same parameters and comparing stacked

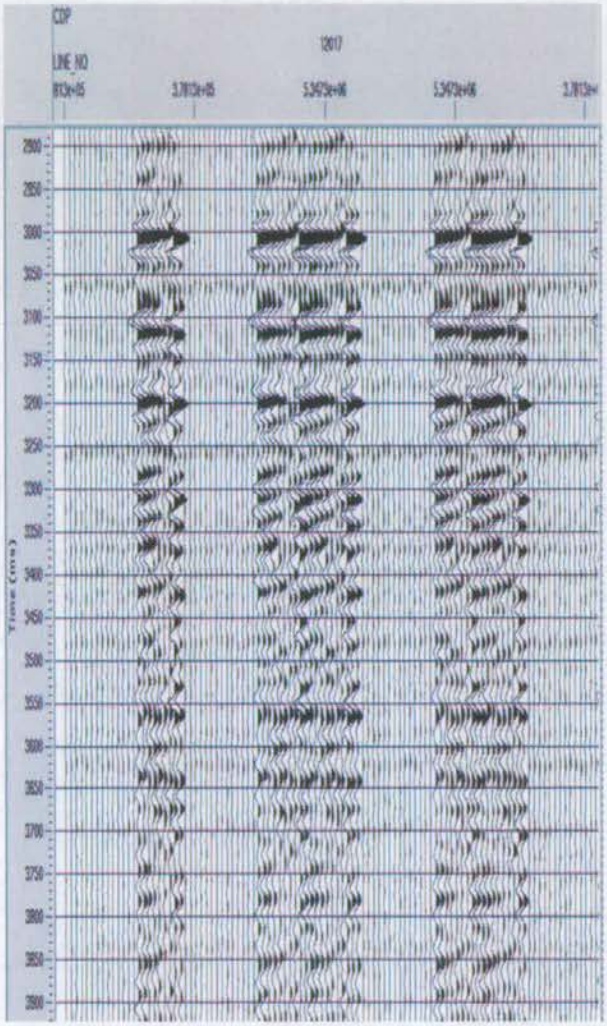

Figure 7.9: Merged supergather without data match processing gather. A windowed no scaled common offset supergather of CMP 12017 from line 59. The processing steps before merging for 2D and 3D datasets are the same. The line_no "3.7813e+05" is the original 2D line identifier, while "5.3473e+06" is the original 3D data identifier. At once a bigger difference in traveltime and energy can be found between the original 2D and 3D datasets.

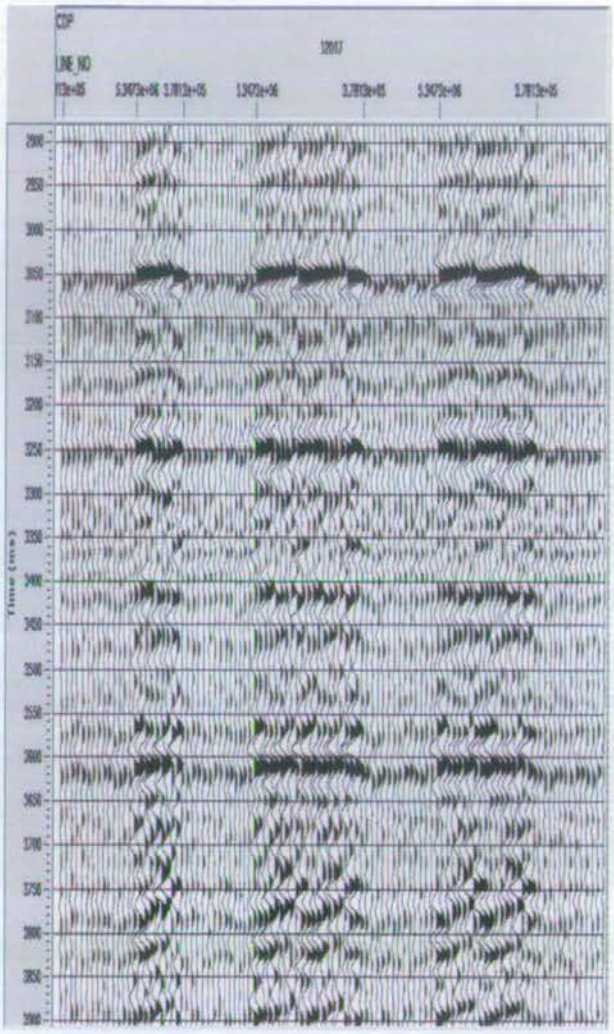

Figure 7.10: The same as Figure 7.9 but after data matching processing. Compared to the unmatched gather in Figure 7.9, the differences in traveltime and energy are at once found reduced.

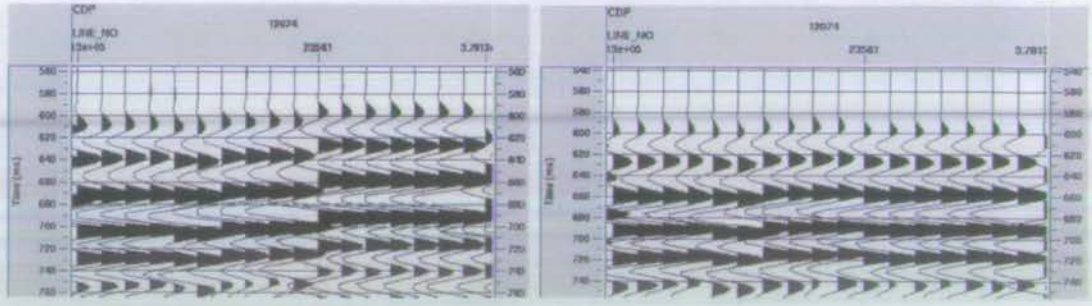

Figure 7.11: One of a windowed supergather of line 01. Results of unmatched (Left) and matched (Right).

sections to find its time shift and frequency difference.

Step 18. Shift one of the 2D lines in time. Sometimes time shifts are needed for both 2D lines. If there are some differences among the acquisition parameters, surface consistent scaling/deconvolution is normally suggested. Any single trace processing should be avoided to preserve the true amplitude. If difference only exists among the sources, a source deconvolution is used to compensate for the difference in source energy. Let $R(t)$ and $R(\omega)$, $\xi(t)$ and $\xi(\omega)$, $S(t)$ and $S(\omega)$ be, respectively, the seismic record and its Fourier transformation; the reflectivity and its Fourier transformation; and the source wavelet and its Fourier transformation. If the inverse of a source wavelet Fourier transformation $S^{-1}(\omega)$ from the 2D and 3D dataset can be extracted, the reflectivity coefficients in equation 7.6 for 2D and 3D can be calculated from the seismic records in equation 7.5. The source wavelet $S(t)$ may be estimated from the first break of near offset traces.

$$\begin{cases} R_{2D}(t) = \xi_{2D}(t)\nabla S_{2D}(t) \\ R_{3D}(t) = \xi_{3D}(t)\nabla S_{3D}(t) \end{cases} \tag{7.5}$$

$$\begin{cases} R_{2D}(\omega) = \xi_{2D}(\omega)S_{2D}(\omega) \\ R_{3D}(\omega) = \xi_{3D}(\omega)S_{3D}(\omega) \end{cases}$$

$$\begin{cases} R_{2D}(\omega).S_{2D}^{-1}(\omega) = \xi_{2D}(\omega)S_{2D}(\omega).S_{2D}^{-1}(\omega) = \xi_{2D}(\omega) \\ R_{3D}(\omega)S_{3D}^{-1}(\omega) = \xi_{3D}(\omega)S_{3D}(\omega).S_{3D}^{-1}(\omega) = \xi_{3D}(\omega) \end{cases}$$

$$\begin{cases} \xi_{2D}(\omega) = R'_{2D}(\omega) = R_{2D}(\omega).S_{2D}^{-1}(\omega) \\ \xi_{3D}(\omega) = R'_{3D}(\omega) = R_{3D}(\omega)S_{3D}^{-1}(\omega) \end{cases}$$

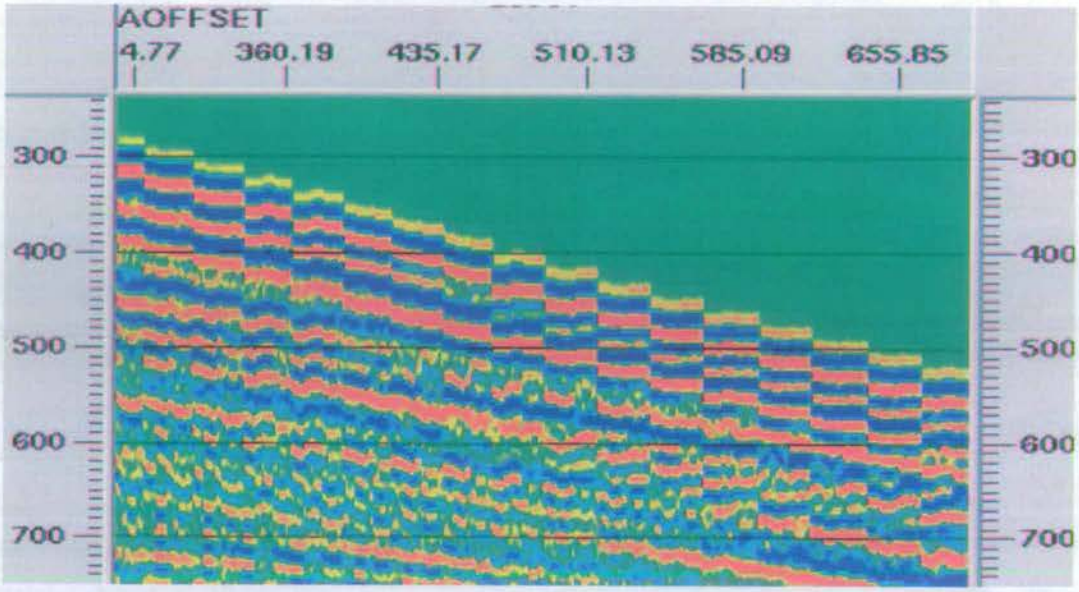

Figure 7.12: A windowed display of a supergather of the combined 2D and 3D surveys. Common-offset traces with different azimuths show constant first break times, and the attribute analysis is performed on these common-offset traces in which there are about 20 traces.

$$\begin{cases} \xi_{2D}(t) = R_{2D}(t)\nabla S_{2D}^{-1}(t) \\ \xi_{3D}(t) = R_{3D}(t)\nabla S_{3D}^{-1}(t) \end{cases} \tag{7.6}$$

Step 19. Merge two separately reprocessed 2D lines to form the last supergathers for each 2D line. Figure 7.10 is the result after data-matching for Line 59. It is clear that the data match each other much better than before if I compare results here with those in Figure 7.9. If there is no difference because of time-lapse, the energy differences in this diagram between original 2D and original 3D whose SL azimuth directions are perpendicular to each other show a clear azimuthal variation in amplitude. Figure 7.11 is a windowed gather which compares the unmatched and matched processing results from Line 1. Figure 7.12 is a windowed supergather after common offset sorting.

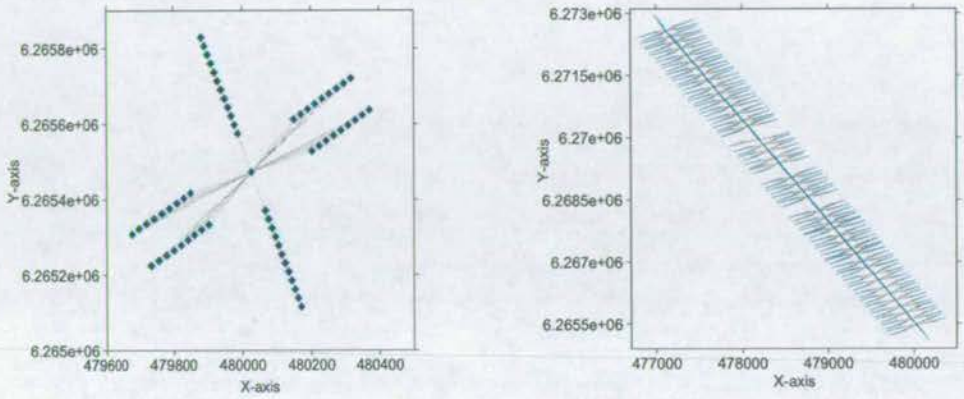

Figure 7.13: Azimuth distribution analysis. Left - the distribution for a given CMP. Right - the distribution for all CMPs along a crossed 2D line.

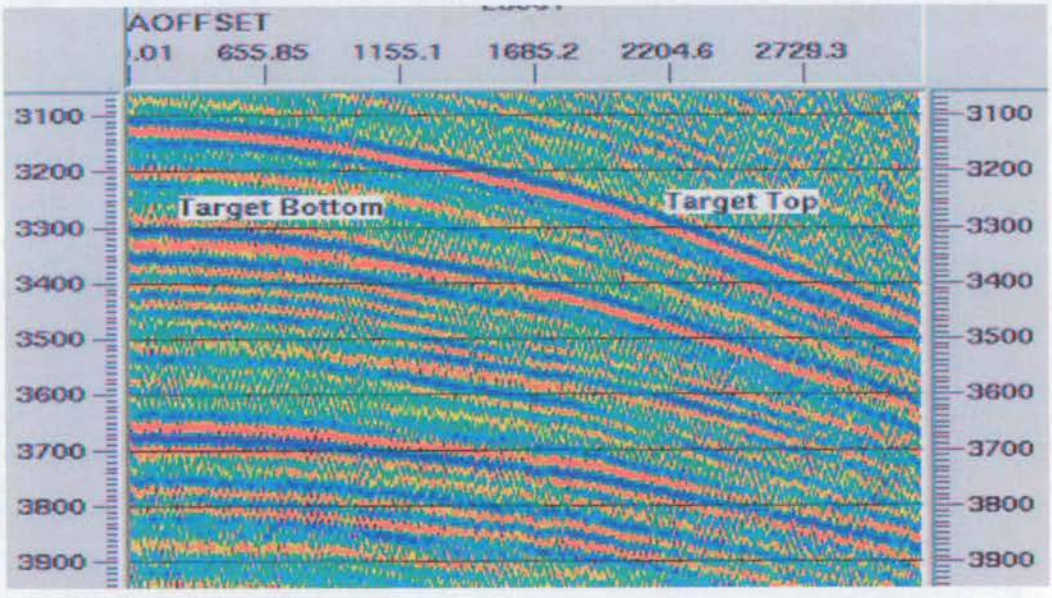

Figure 7.14: The top and bottom reflections from the target as identified in the super gather of the combined 2D and 3D surveys.

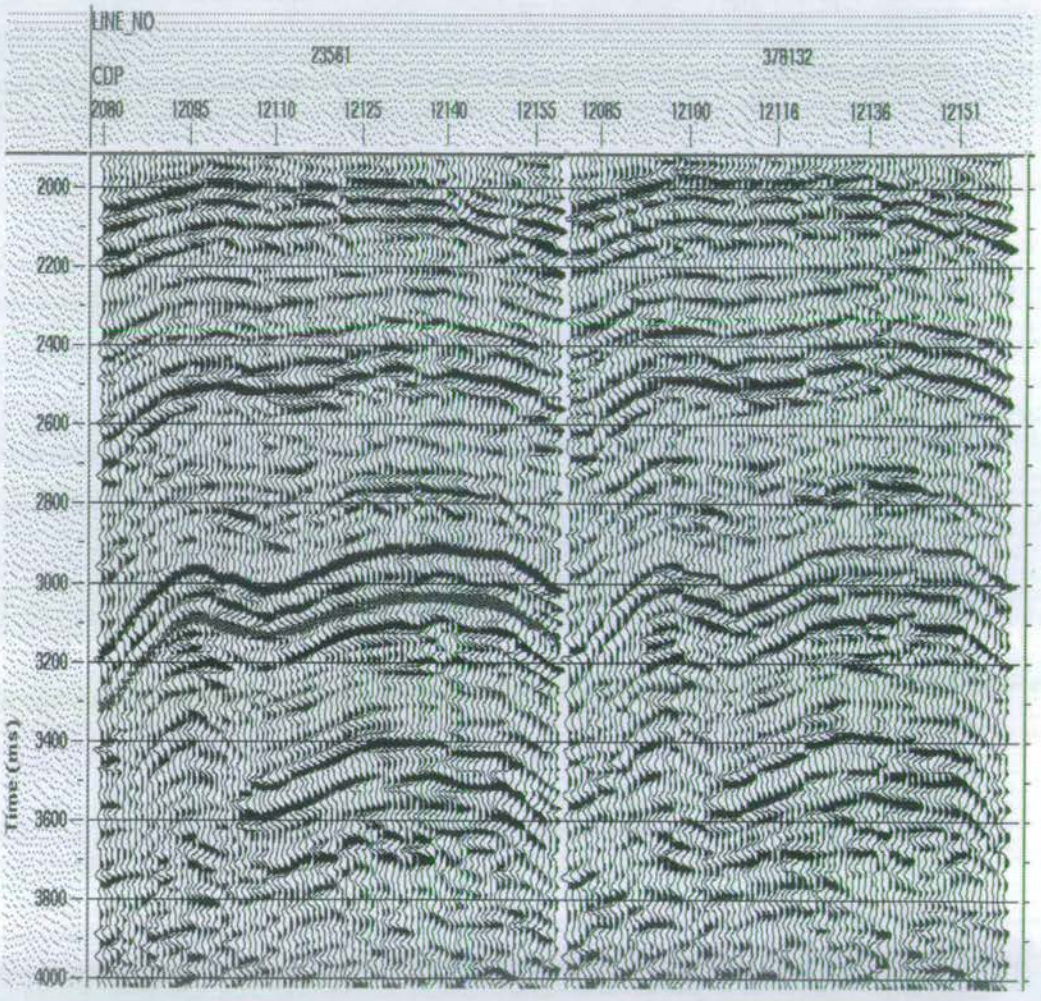

Figure 7.15: Stacked sections along azimuth Line-03. Left: the data extracted from the 2D line which were shot in the line direction. Right: the data extracted from the 3D volume which were shot in a different direction.

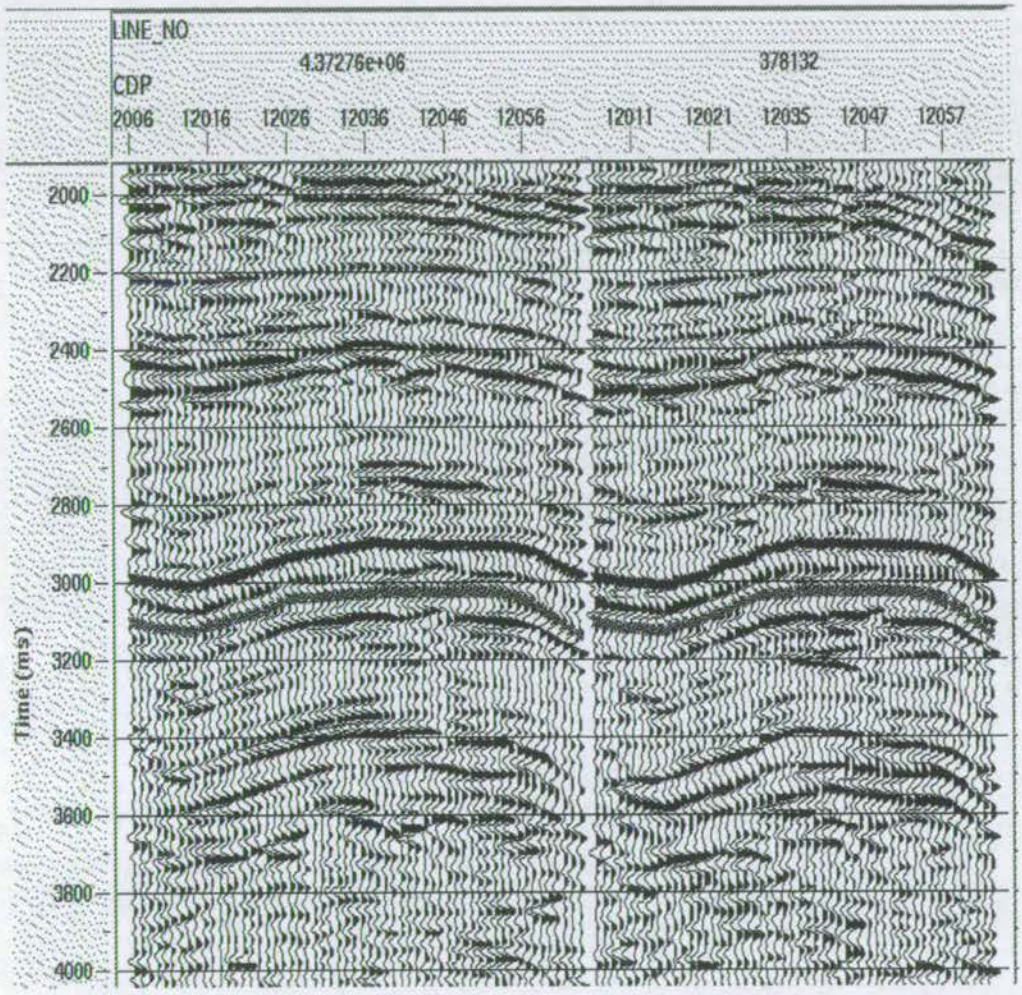

Figure 7.16: Stack sections along azimuth Line-62. Left: the data extracted from the 2D line which were shot in the line direction. Right: the data extracted from the 3D volume which were shot in a different direction.

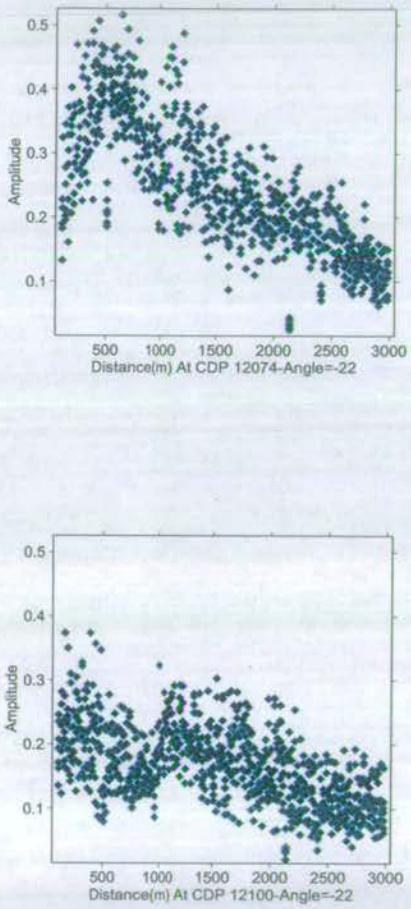

Figure 7.17: Variations of amplitude with offset for a given azimuth. Upper - CMP 12074; Lower- CMP 12100.

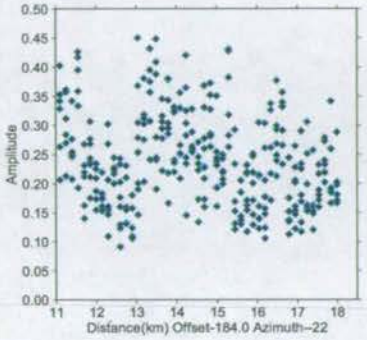

Figure 7.18: Amplitude variations with CMP points at a given offset for azimuths at 22^0.

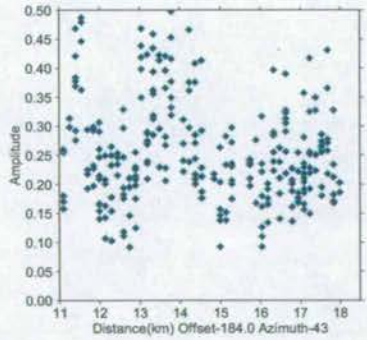

Figure 7.19: Amplitude variations with CMP points at a given offset for azimuths at 43^0.

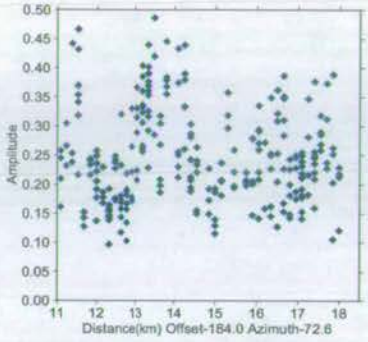

Figure 7.20: Amplitude variations with CMP points at a given offset for azimuths at 73^0.

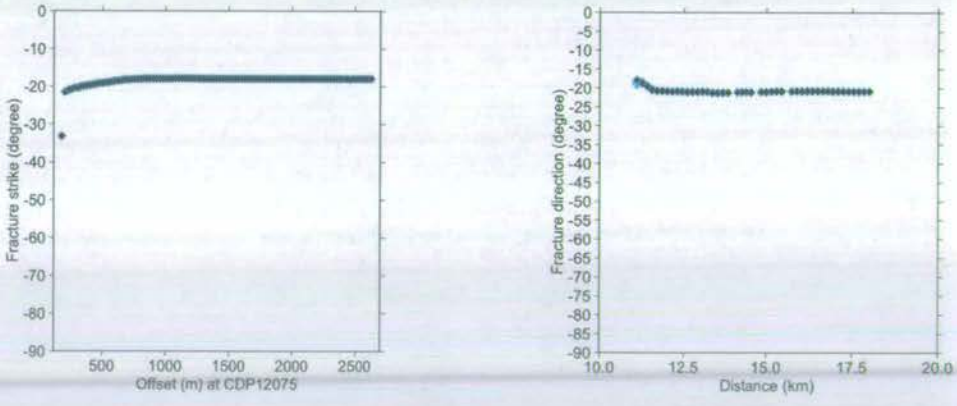

Figure 7.21: Results of azimuth AVO analysis. The fracture orientation calculated for each offset distribution for a given CMP (left) and the fracture orientation for each CMP along a given crossed 2D line (right).

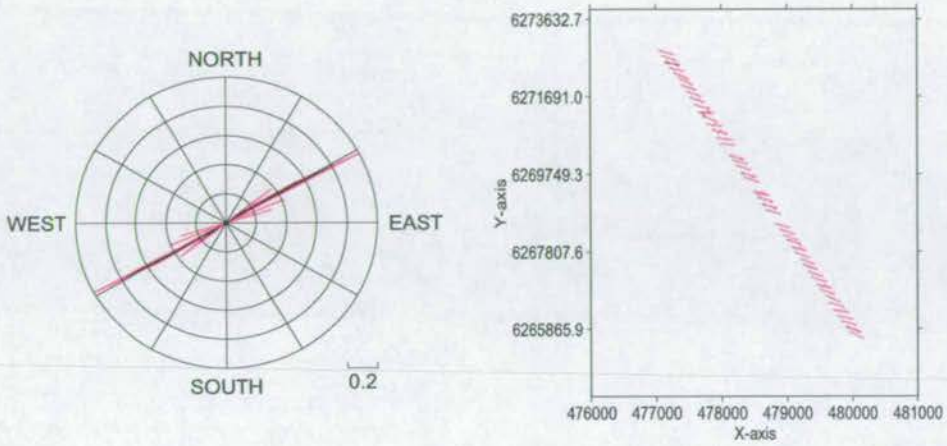

Figure 7.22: Left: Inferred fracture orientations displayed as a rose diagram for one of the CMPs in Line-04. Right: Rose diagrams of line 01.

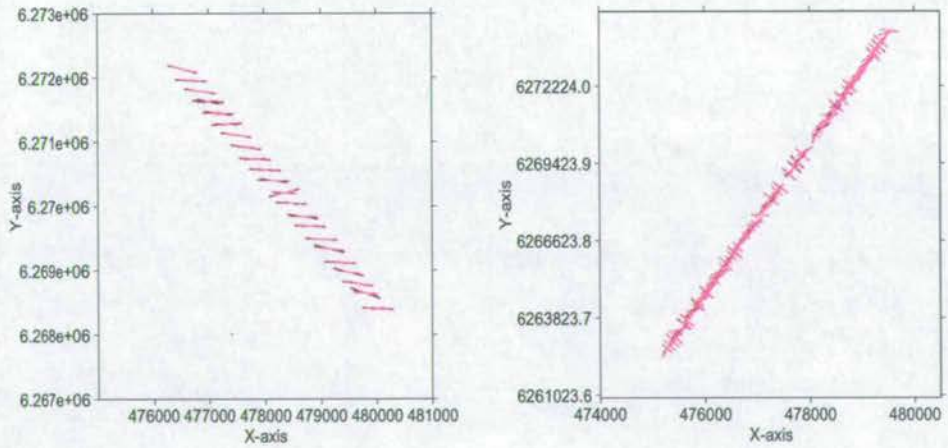

Figure 7.23: Rose diagrams of line 02 (Left) and line 03 (Right).

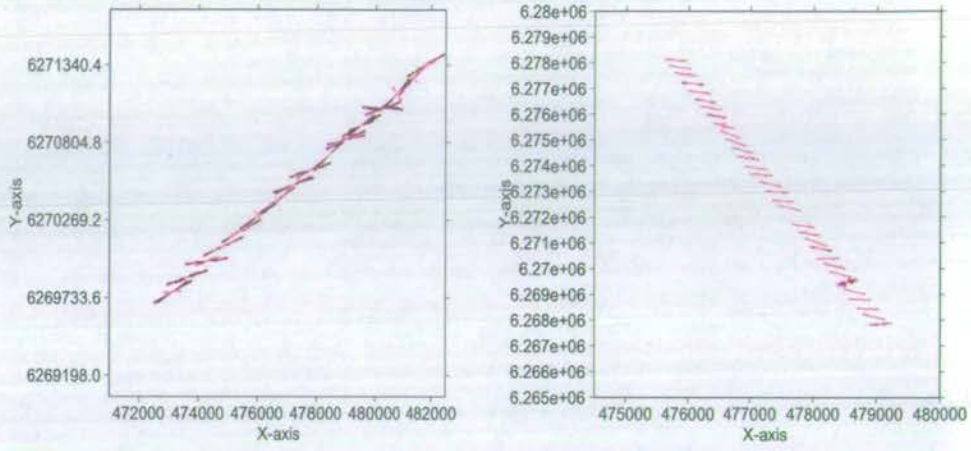

Figure 7.24: Rose diagrams of line 04 (Left) and line 07 (Right).

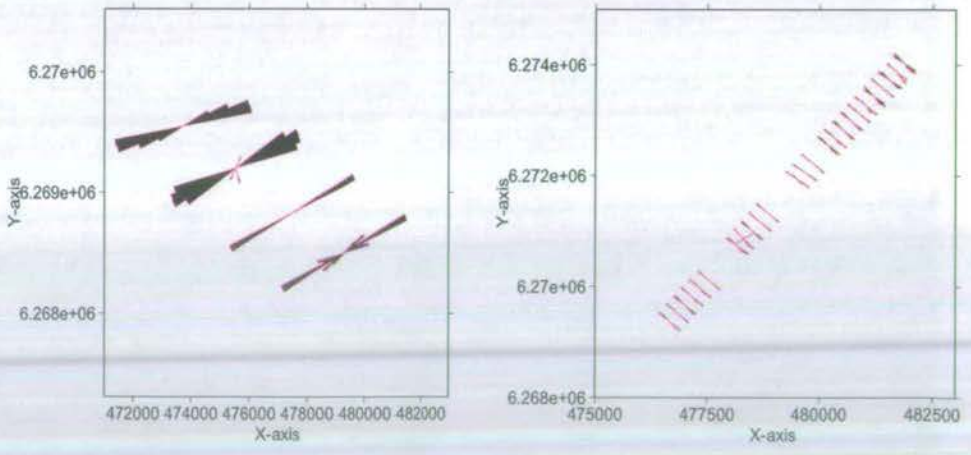

Figure 7.25: Rose diagrams of line 08 (Left) and Line 55 (Right).

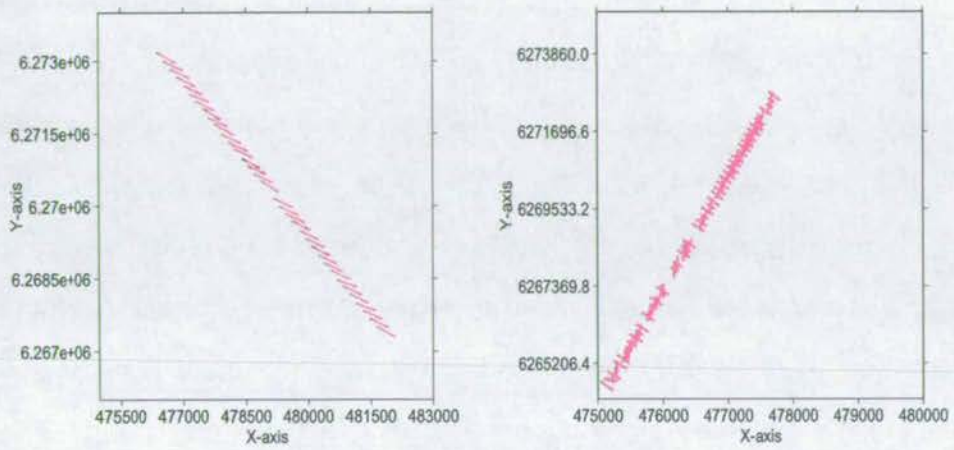

Figure 7.26: Rose diagrams of line 59 (Left) and Line 62 (Right)

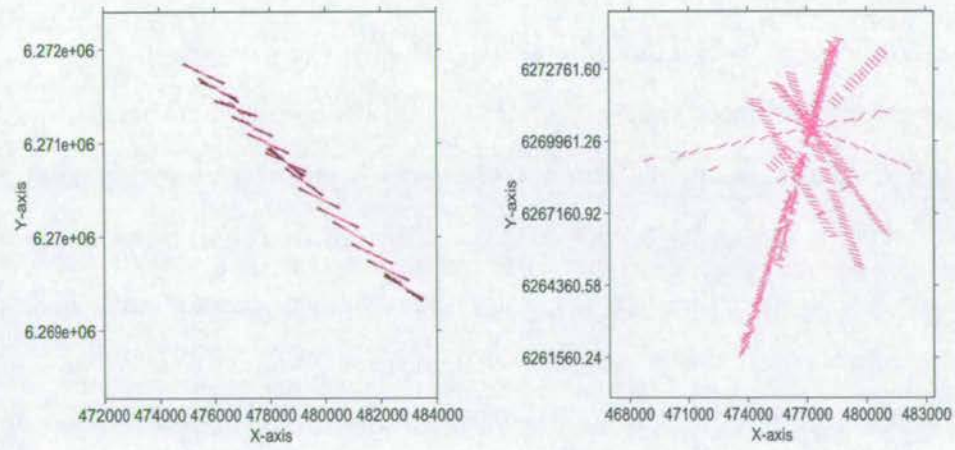

Figure 7.27: Rose diagrams of line 64 (Left) and all the ten lines (Right).

7.4 Quality control for processing

The above joint data processing has nineteen steps and is quite complex. For such a procedure and processing of old data, Quality Control (QC) is required at each step. My last QC results are obtained in the following three steps: (a) all the ten 2D lines in which all the traces are from original 2D lines are extracted from the final matched new 2D lines; (b) another ten 2D lines in which all the traces are from original 3D data are also extracted from the final matched 2D lines; (c) stacking both of the extracted ten 2D lines with exactly the same processing steps and parameters, then ten pairs of stack sections are obtained. Figure 7.15 shows the stacked section pair along azimuth Line-3. Figure 7.16 showes the stacked section pair along azimuth Line-62. These figures show almost identical features. Comparing the stack section pairs, I am confident that all the processing steps are correct.

7.5 Azimuthal AVO analysis

To apply the velocity method, I need a relatively long spread and both of the near offset and far offset traces. As for the amplitude method, a relatively smooth reflector is usually assumed. To analyse the moveout attribute, far offset receiver traces and recognisable target layer top and bottom reflection times are required.

In the special three line case, if I assume that there are enough near and far offset gathers and clear top and bottom traveltimes for the target, I have to decide which attributes to use. Firstly, I examine the possibility of extracting velocity for three S-R directions. It is clearly shown in Figure 7.3 that the velocity can be analysed in the direction of Line 1. However, there are not enough traces for velocity analysis in any other S-R direction. Therefore the velocity method cannot be used for fracture detection in this case. Secondly, I see if I can pick target moveouts. From the far

offset gathers, there are traces from all three lines. However, the larger the offset, the smaller the difference between S-R angles for the traces from Lines 2 and 3; and the nearer the offset, the smaller the moveout and the greater the picking errors are. Therefore although the moveout method appears an ideal choice, it can not be used here. Finally, to apply the amplitude attributes, I need to know if I have a relatively smooth reflector for this target area and if I can pick amplitudes from different S-R directions. The average dip of the Tor formation in this area is about 5^o (Figure 7.2), so this can be effectively considered as a horizontal bedding layer although in some small areas steeper dips were found. The difference in amplitudes from common far offset traces is small because of the narrow azimuthal angles. The smaller the offset, the smaller the azimuthal variation. As I have shown in Figure 7.5, the distance between Lines 2 and 3 is only 100 m, and far offset traces can not be treated as two S-R directions. When the offset is 1500 m, the difference in "source-receiver" angles for the same offset traces on both of the lines is less than 10^o. Based on the above description, I conclude that only in the near offset range between 50 and 1000 m have I three common offset traces from three azimuthal directions, and only the amplitude attribute can be used to extract fracture information. It is noted that the near offset traces are used for anisotropy analysis.

I begin by picking amplitudes at the top target interface from all offsets, and then sum up traces with offset separation less than 10m. Figure 7.17 shows examples of the amplitude variations with offset for different CMPs at a given azimuth, and Figures 7.18, 7.19 and 7.20 show amplitude variations with CMP points at a given offset for different azimuths. The next step is to use equation 3.36 for azimuthal AVO analysis. I use a least-squares linear inversion scheme to calculate the three parameters for different offsets. For each offset distribution, a set of A, B and Φ are calculated, and from these the fracture intensity may be estimated as well. Then the results are averaged over all offsets for a given CMP (see Figure 7.22). Finally,

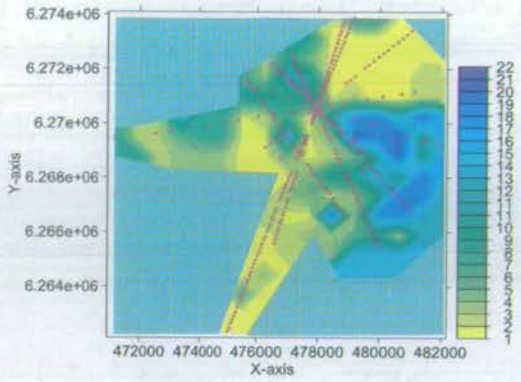

Figure 7.28: Fracture estimation result - fracture intensity and data positions. The large value in the colour bar means large intensity.

AVO analysis is carried out CMP-by-CMP and line-by-line, and the inferred fracture orientations are displayed in rose diagrams. Figures 7.23, 7.24, 7.25, 7.26 and 7.27 are the fracture orientation diagrams (rose diagrams) for the ten lines respectively. Figures 7.28 and 7.29 are the maps of interpreted fracture intensity and orientation, respectively. These maps reveal clearly that there are mainly two sets of fractures: N75E and N40W. Those trends are consistent with what I see from the target depth map. Figure 7.30 superimposes the fracture orientation on top of the intensity map. The colour displays the fracture intensity and the rose diagrams displays fracture orientation.

7.6 Evaluation of fracture parameters

I succeeded in extracting fracture parameters from the joint data along all the intersected 2D lines by using AVAZ analysis. To further evaluate these estimated parameters, I create the following four statistic histograms (Figure 7.31) for a) orientation, b) orientation prediction error, c) density and d) density prediction error. None of

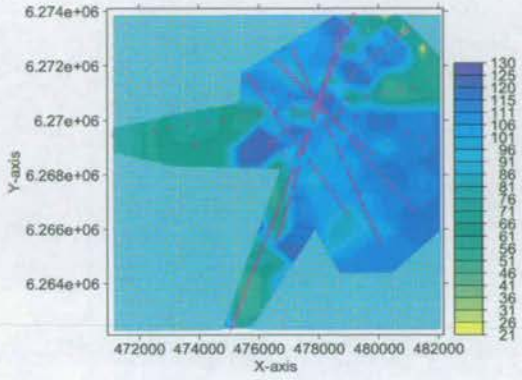

Figure 7.29: Fracture map - fracture orientation and data positions. The large value in the colour bar means large orientation angle.

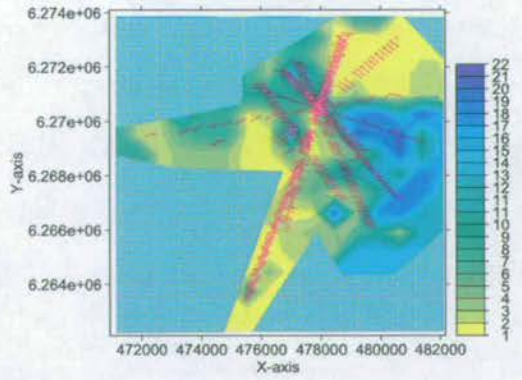

Figure 7.30: Fracture map - fracture intensity and orientation trend. The large value in the colour bar means large intensity.

the fracture parameters are excluded in generating these statistical histograms. Figure 7.31a shows us the orientation distribution of all the fractures encounted along the ten 2D lines. I found that the fractures strike at various directions but with a dominant fracture strike between 85^0 and 120^0. Figure 7.31c shows that three fifths of these fractures have relative low fracture density (<10%), one fifth of the fractures results in medium anisotropy and the other one fifth of fractures results in strong anisotropy (>30%). Based on these two histograms we can infer that at the target depth in this project area of $250^2 km$, the high density fractures only exist in a small zone. This may be confirmed from Figure 7.1. Figures 7.31b and 7.31d are generated using the prediction error at each crossed CDP of 2D and 3D. Clearly the well distributed error bars on both of the diagrams confirm that we have a reliable prediction results.

7.7 Discussion and Conclusions

Aligned subvertical fractures caused azimuthal variations in seismic attributes such as traveltime, velocities and amplitudes. The analysis of ***P***-wave attribute variation with azimuth has been successfully used for interpreting fracture patterns in reservoirs in land seismic surveys. However, it is a challenge to apply attribute analysis techniques to marine 3D streamer data. The key issue that determines the application is whether sufficient azimuth coverage is available, as a minimum of three azimuthal directions is needed at each CMP. Marine 3D streamer data are normally recorded in quite different patterns from those of land 3D surveys because almost all the shot lines are parallel to receiver lines, which means that the differences of azimuthal angles between lines of receivers and shots are almost zero. That is, receivers and sources are normally towed by the same boat and data are recorded when the boat sails forward. To overcome this problem, I have used re-

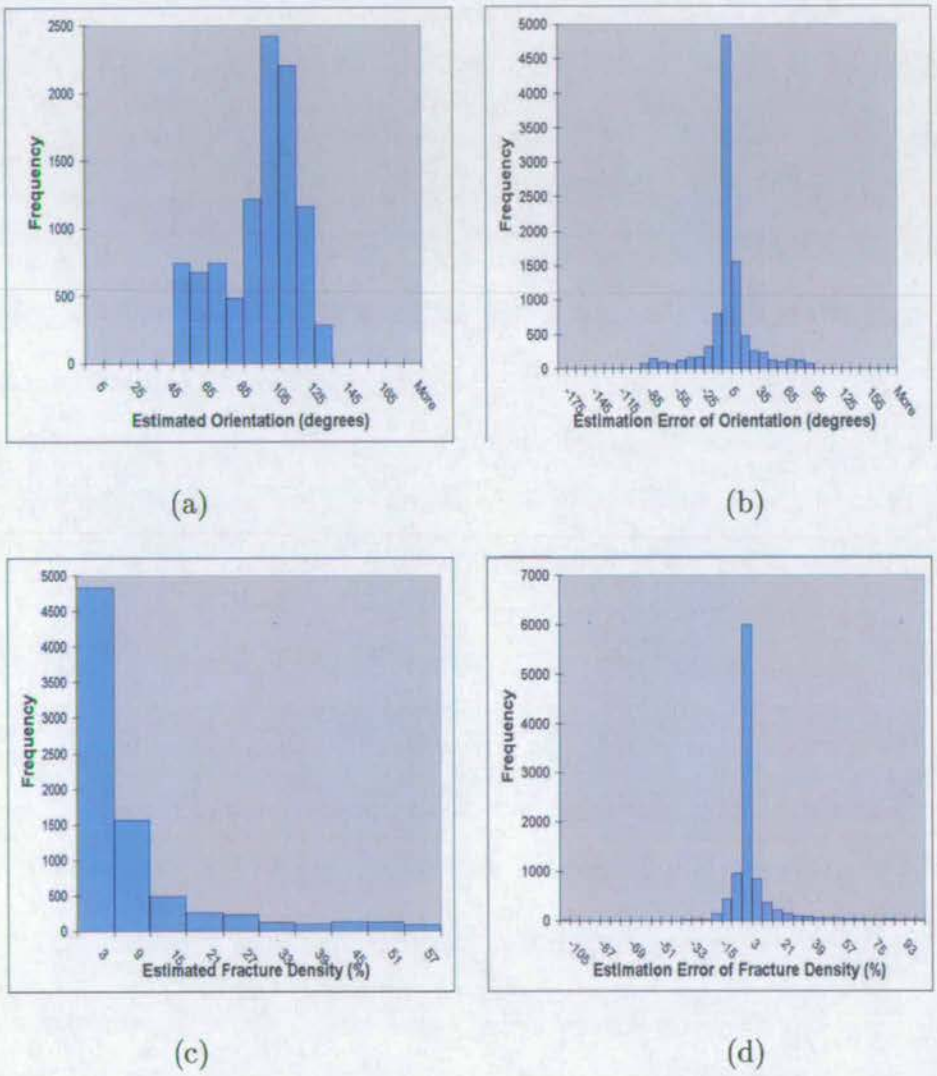

Figure 7.31: a) and b) are respectively the histograms of fracture orientation and orientation prediction error. c) and d) are respectively the histograms of fracture density and density prediction error.

peated 2D and 3D surveys of different vintages. In Chapter 6, I developed the use of 2D orthogonal lines, but these results are limited in space coverage to a single point. In this chapter, I incorporate a multi-streamer 3D survey with crossed 2D lines to improve spatial coverage. As a result, the number of intersecting points with multi-azimuthal coverage increased significantly. However, as shown in Figure 7.13, the azimuthal coverage decreases sharply as offset increases. The key question that needs to be asked is whether sufficient azimuthal variations in P-wave attributes can be observed to permit a reliable analysis. For this purpose, I have focused on azimuthal AVO analysis since azimuthal velocity and moveout analysis often require full offset coverage. Also I have focused only on those CMP positions which located on 2D lines and intersecting with the 3D surveys, since only these points have a chance to meet the requirement of a minimum of three azimuths. This is aided by the presence of strong and coherent reflection events from the top and bottom of the target (Figure 7.14).

I conclude from my study that it is possible to use repeated 2D and 3D marine streamer surveys for estimating the fracture orientation and intensity. A careful processing procedure is required to match acquisition geometry and to compensate for variations in time shifts and source signatures. For this purpose, I have proposed a three-matching scheme: geometry matching, CMP bin matching and data matching. The results from this study are very encouraging, and reveal good potential for further applications to modern 3D marine surveys with wider-azimuthal coverage and improved data quality, as demonstrated in Hall et al. (2002)

Chapter 8

Fracture Detection Using 3D Land Data

Abstract

In this chapter, I present a case study from China to demonstrate the application of the techniques described in Chapters 3, 4 and 5 for evaluating overburden anisotropy and estimating fracture information. A major aspect of this study is the comparison of the different techniques on a common dataset. My aim is to understand the merit of these different techniques, and to establish some basic guidelines for fracture detection using P-wave azimuthal anisotropy. The results from this dataset show that the commonly-used narrow-azimuth method may enhance the acquisition footprint, and should be avoided if possible. Instead, a surface fitting method is generally preferred. Furthermore, in this dataset, the amplitude is not very reliable. However the final fracture orientation and intensity maps estimated from traveltime attributes compare reasonably well with the fault and fracture patterns in the area.

8.1 Introduction

In the previous two chapters, I show how repeated 2D and 3D surveys of different vintages can be used to extend the azimuthal coverage of marine seismic data for analyzing P-wave azimuthal anisotropy for fracture detection. In this chapter, I focus on various issues related to 3D wide-azimuth data. Given such a dataset, what can we really obtain? How reliable are the results? What attributes and processing flow should we choose?

For 3D data acquired with wide azimuthal coverage, all four types of attributes, traveltime, amplitude, velocity and AVO gradient, may be used to study azimuthal anisotropy for fracture estimation. Two approaches may also be used for data processing. One is called the narrow-azimuth stacking approach. This entails sorting the data into narrow azimuthal bins, then performing azimuthal bin-stack to reduce the number of azimuths to a few selected azimuths. The other approach is called surface fitting, which is to fit surfaces of $\cos 2(\varphi - \Phi)$ and $\cos 4(\varphi - \Phi)$ variations to all offsets and azimuths simultaneously using a least-squares method.

At a field site in the Yellow River Delta in east China, a multi-azimuth, multi-offset 3D compressional wave seismic dataset was acquired and processed using azimuth-dependent processing. The purpose of this survey is to analyze a naturally fractured mud-rock reservoir in the Yellow River Delta area in East China, and to identify zones of high fracture density that are residual-oil charged for future well planning. The field site has been in production for over 10 years; however, virgin pressure wells are still being drilled. The target formation consists of mainly sands and mudrocks. The data quality is reasonable compared with similar datasets from other areas.

In my test analysis, I compare the surface fitting method with the narrow-azimuth stacking method. To perform narrow-azimuth bin stack, the data are

divided into six narrow-azimuth volumes with 30° (−15° to 15°) azimuthal bins. Corresponding to these two methods, I select four seismic attributes, including velocity, traveltime/interval traveltime, amplitude, and AVO gradient.

8.2 The study area and data description

The study area is located in the Yellow River delta in east China. The field was discovered in the early 1970s and is now the second largest oil producing province in China. The area is bounded to the west by the Yellow River plain and to the east by the Yellow Sea. Most of the area is known to be heavily faulted (Figure 8.1) and the target is fractured mud-rock located at a depth of about 3000m. Oil production in the area mainly relies on knowing fracture information.

A total of 60 km^2 of 3D data was acquired in mid-2000 and, in this study, I have only carried out test processing and analysis of part of the 3D seismic data (about 10km^2). Figure 8.2 shows the acquisition geometry and fold coverage. The data were shot with a dynamite source across the receiver line to maximize azimuthal coverage. Figure 8.3 shows a super CMP gather with 150x150m bin size. Super bins are required to perform narrow-azimuth stacking. As we can see from Figure 8.3, the data are of reasonable quality, and events are clear and continuous. The data also have good azimuthal-offset coverage (Figure 8.4), and thus can be used for fracture analysis with confidence. Two target horizons have been selected. The first one is the known sandstone (Target 1, Figure 7), located at about 2s (top) and 2.2s (bottom) at an existing borehole. The second one is the known mudstone (Target 2), located at about 2.2s (top) and 2.5 (bottom). In this study, we shall concentrate on Target 1.

The analysis is carried out in two stages: (1) data inspection and pre-processing including three key steps - surface-consistent static correction, surface-consistent

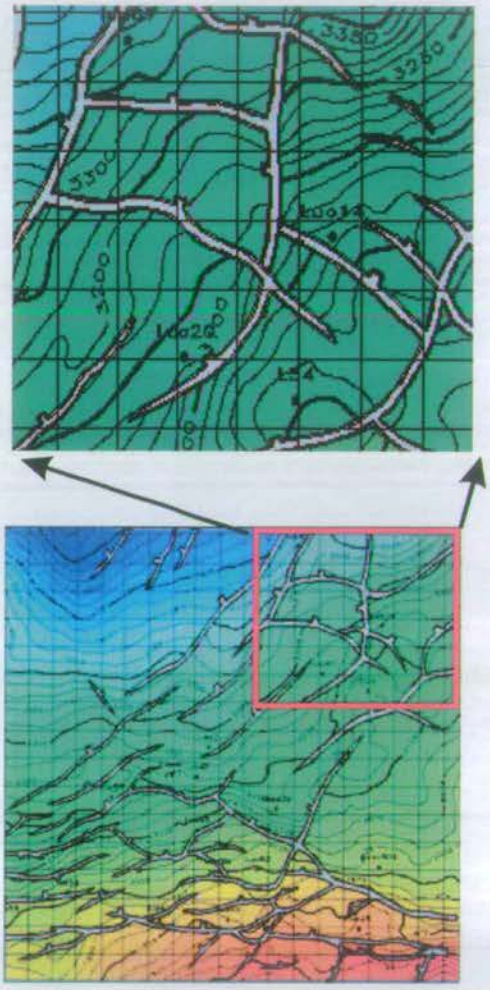

Figure 8.1: Distribution of faults/fractures in the study area (the Yellow River delta).

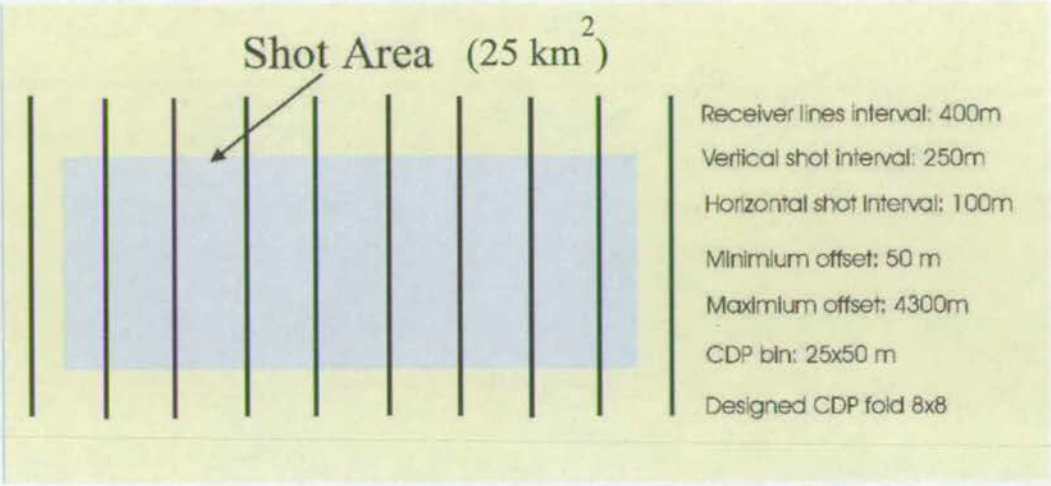

Figure 8.2: Wide-azimuthal patch-shooting geometry.

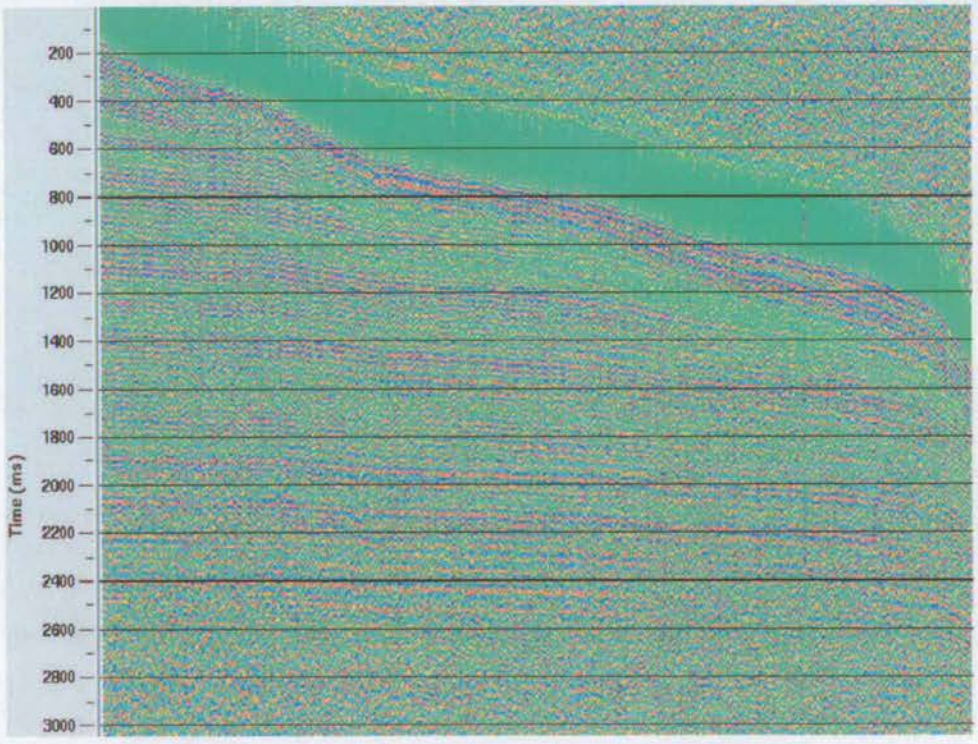

Figure 8.3: A super CMP gather with bin-size of 150mx150m.

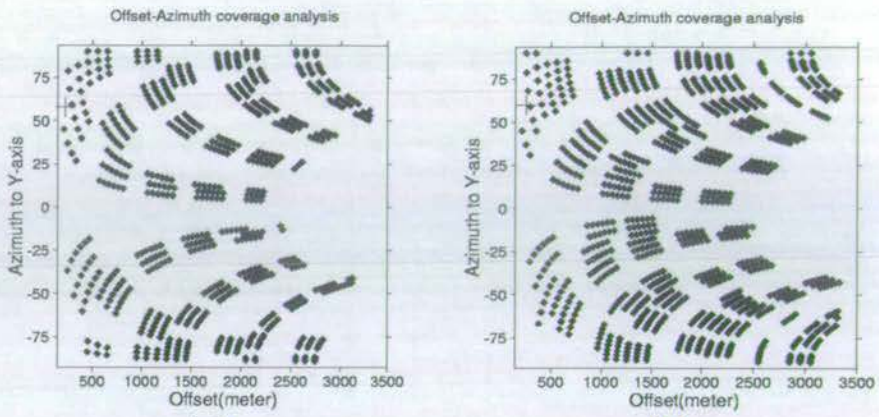

Figure 8.4: Analysis of offset-azimuthal coverage. (a) minimum coverage. (b) maximum coverage.

amplitude corrections and noise attenuation, and (2) anisotropic analysis by 3As, as described in Chapter 3, including both narrow-azimuth stacking and full-azimuth surface fitting. Here I present mainly the comparison of the different attributes and processing techniques. Full details of data inspection and processing, together with a complete listing of results, are enclosed in Appendix A for reference.

8.3 Narrow azimuth stack

In order to reveal any azimuthal variations in P-wave attributes, I divide the data into six azimuthal bins with 30° bin size, and then perform narrow-azimuth velocity analysis and stacking. This gives rise to six narrow-azimuth data volumes (-60°, -30°, 0°, 30°, 60° and 90°). 0° indicates north (N), negative angles are measured counter-clockwise from north (north-to-west, NW) and positive angles are measured clockwise from north (north-to-east, NE). This definition is used for all the processing.

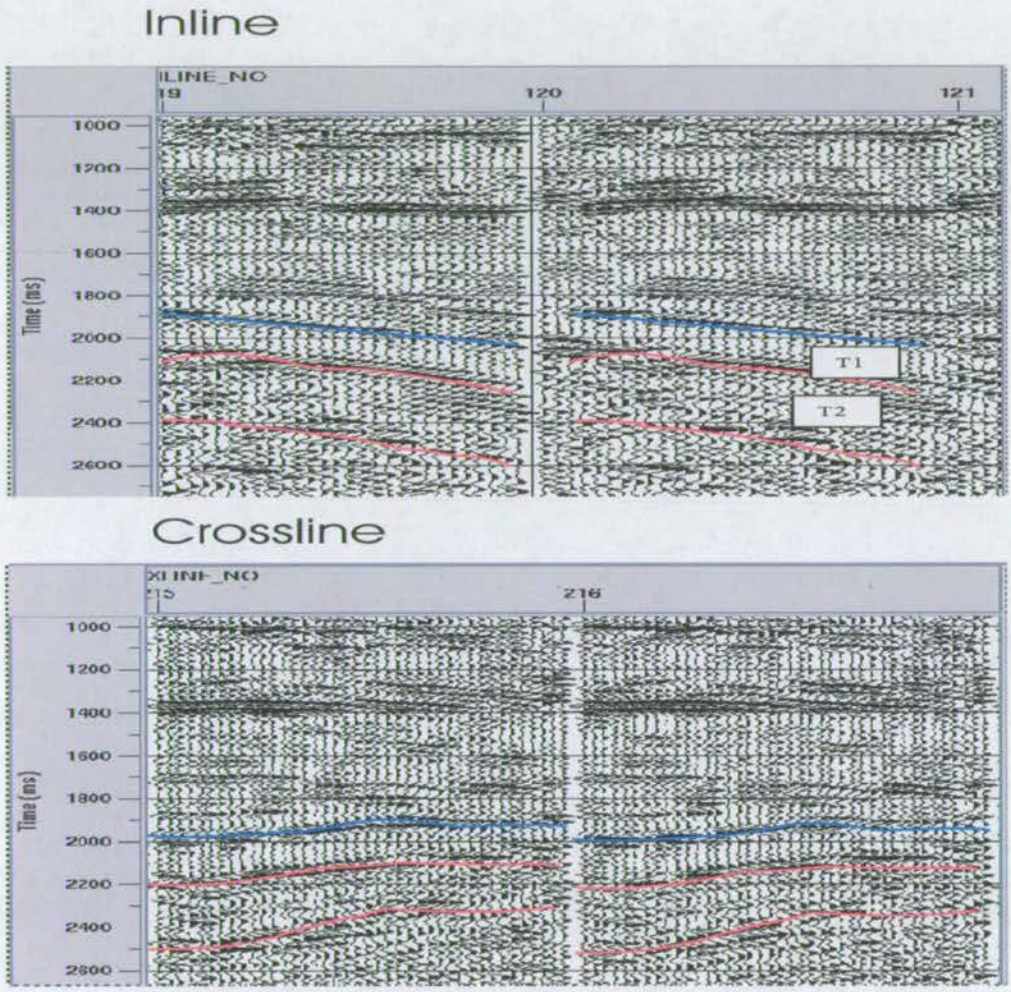

Figure 8.5: Examples of image processing results for an inline and crossline profile. Two target horizons have been identified (labelled T1 and T2. Note that the top of T2 is the same as the bottom of T1).

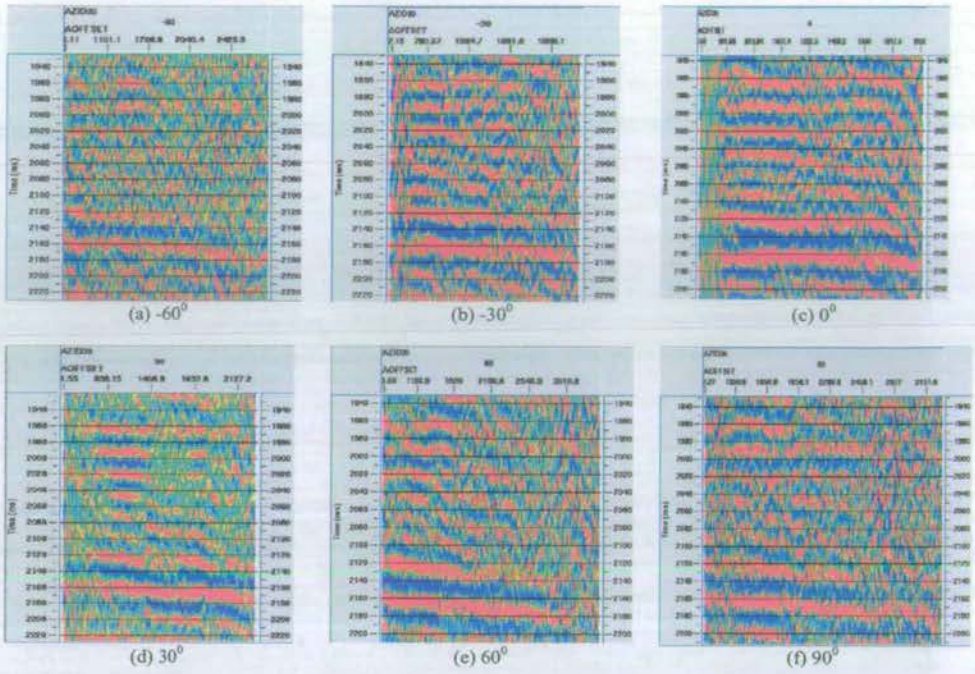

Figure 8.6: Azimuthal traveltime variation. The same NMO velocity has been applied to all six azimuthal gathers extracted from the super CMP gather.

Figure 8.6 shows the azimuthal traveltime variation at a selected Super CMP gather, focusing on the bottom of T1 (2180ms). The same velocity function is applied to all the six azimuthal gathers during NMO correction. Azimuthal variations in the residual moveout are clear. Figure 8.7 shows the corresponding velocity spectra for this CMP. Now all six gathers are flattened by different stacking velocities. The corresponding amplitude variation is shown in Figure 8.8 for the top of T1 (2000ms), and one can see that the amplitude variation with offset is very scattered, and it is very difficult to see a consistent trend. From Figures 12, I may conclude that any attribute analysis based on amplitude information in these data will not be very reliable because of the detected fracture density did not show up a good distribution (Figure 8.18-b). This is confirmed in Figures 10 and 8.20; the estimated average fracture intensity is too high (more than 30%) and the results are clearly

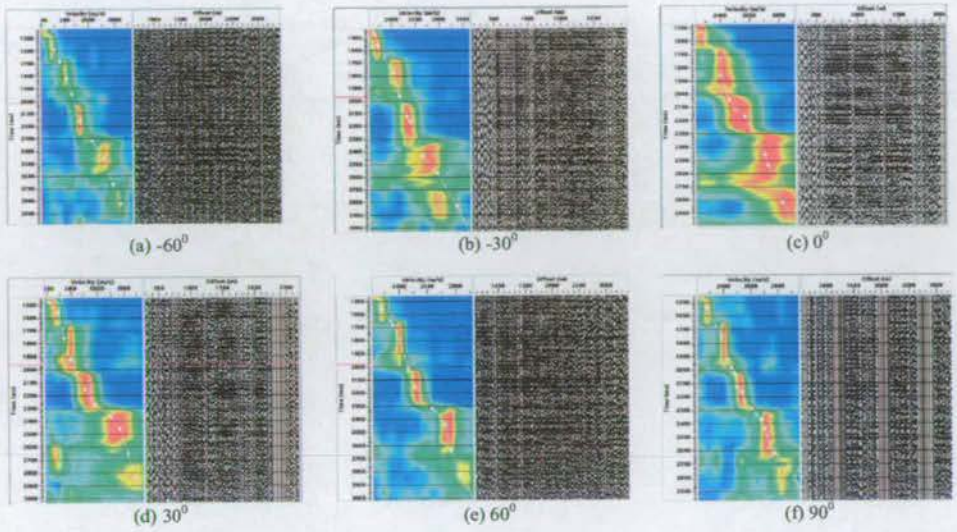

(a) -60^0 (b) -30^0 (c) 0^0

(d) 30^0 (e) 60^0 (f) 90^0

Figure 8.7: Azimuthal stacking velocity variations. Different stacking velocities are required to flatten the events.

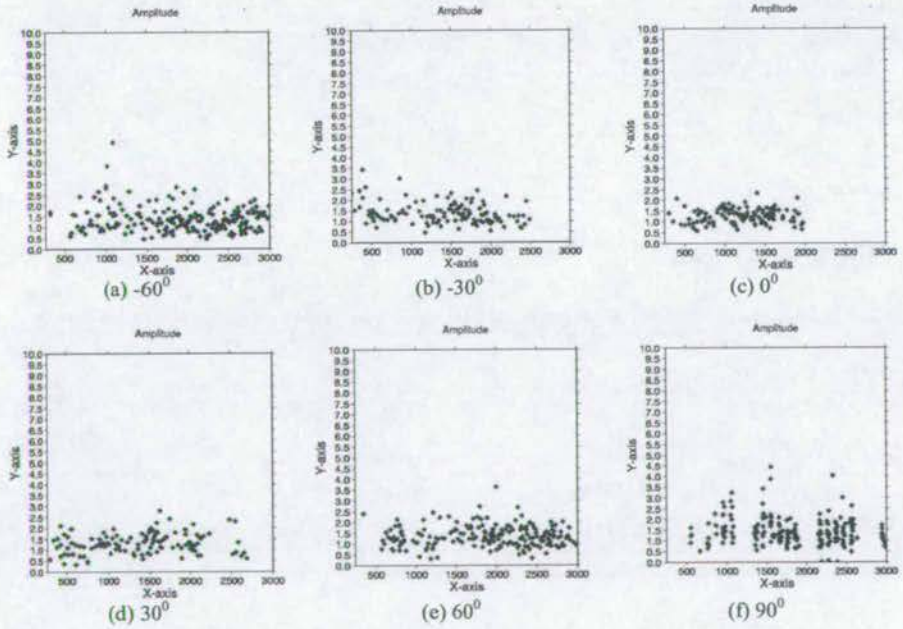

(a) -60^0 (b) -30^0 (c) 0^0

(d) 30^0 (e) 60^0 (f) 90^0

Figure 8.8: Azimuthal amplitude variation from the top of the target horizon T1 (see Figure 9) for all six azimuths.

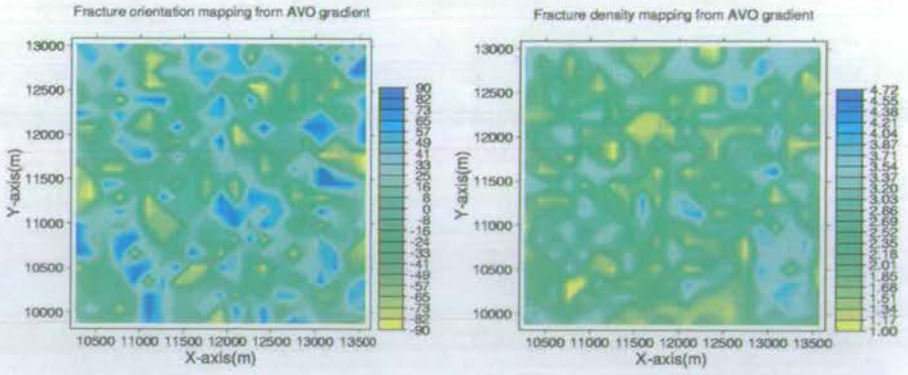

(a) Orientation (b) Intensity

Figure 8.9: Narrow-azimuth method: AVO gradient inversion from the top of the target T1. (a) Fracture orientation map. (b) Fracture intensity map.

not reliable.

I suggest that further investigation is required and care must be taken in analysing other land-based data to check the suitability of AVO analysis using amplitude information (Figures 10 and 8.19).

The fracture intensity estimated from inverted stacking velocities is within the range of 4-10% and seems reasonable (Figure 10),

but the inferred fracture orientation is mainly along east-west or north-south (Figures 10b and 8.11),

which corresponds to the source and receive line azimuth and appears to be dominated by the acquisition footprint.

8.4 Surface fitting results (full-azimuth and full-offset)

An elliptical surface is fit through all the available azimuths and offsets for a given CMP super gather. The main feature of this technique lies in the picking of traveltimes and amplitudes of the top and bottom of the target horizons. Manual picking is impossible due to the work load, and also the pick errors can be very large (up to

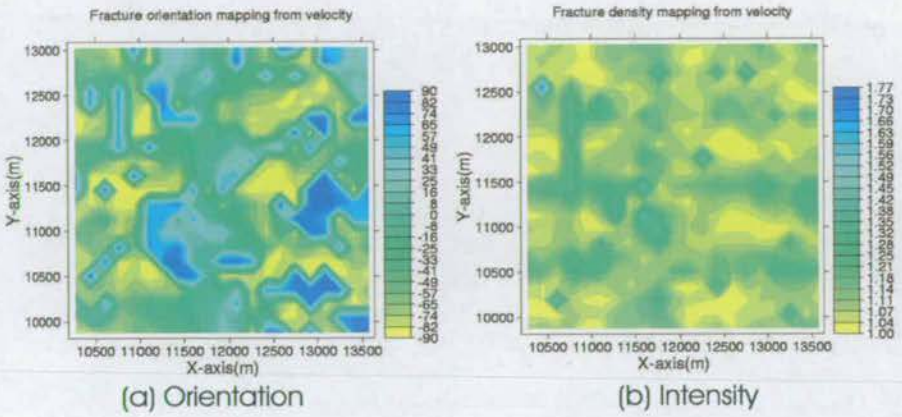

(a) Orientation (b) Intensity

Figure 8.10: Narrow-azimuth method: Stacking velocity inversion from the bottom of the target T1. (a) Fracture orientation map. (b) Fracture intensity map.

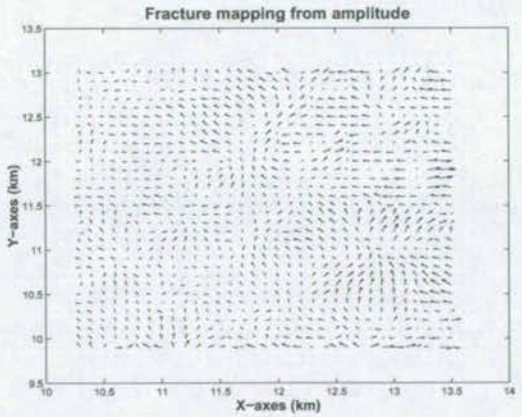

Figure 8.11: The inferred fracture pattern orientation as a function of locations from velocity using the narrow azimuth method. In the map, the direction of the short line stands for the fracture strike and the its length stands for the fracture intensity.

3% to 5% depending on a processor's experience). Thus, an automatic picker is usually employed. To ensure reliable velocity and amplitude picking, the horizons are first manually picked from the post-stack volumes and then used to control points for pre-stack automatic picking. All amplitudes and traveltime attribute are picked in this way.

After the picking, a least-squares inversion method including all azimuths and offsets is applied to the picked attributes. The advantage of this technique is that it is robust and easily handles the anisotropy effects in the overburden. More importantly, it can handle irregular offset-azimuthal coverage.

For comparison, two estimated results (Figures 8.12 and 8.13) are obtained , respectively, from applying surface fitting to two attributes of Target 1 (sandstone): top amplitude and interval time. The least-squares inversion scheme is used for the fitting. The average intensities from the two attributes are 232% and 110%, respectively. These reveal that this area is heavily fractured. If taking the fact into account that the overburden anisotropy may distort the underlying amplitude azimuthal variations significantly but has weaker effects on underlying interval time azimuthal variations, I think that the results from interval time analysis are more reliable (Figure 8.13).

In contrast, the results of interval traveltime appear to be reasonable (Figure 8.13):

two main sets of fractures are shown at N40°E indicated by the light blue colour, and at N150°E indicated by the green colour, and the average anisotropy is about 7%, giving rise to a reasonable result. Further more, the effects of acquisition footprint on the estimated orientation are small as shown in Figure (8.14).

From the above comparison, one can see that the traveltime and velocity attributes are more reliable than the amplitude attribute in this datasets. The narrow azimuth method enhances the acquisition footprint and should be avoided. Surface-

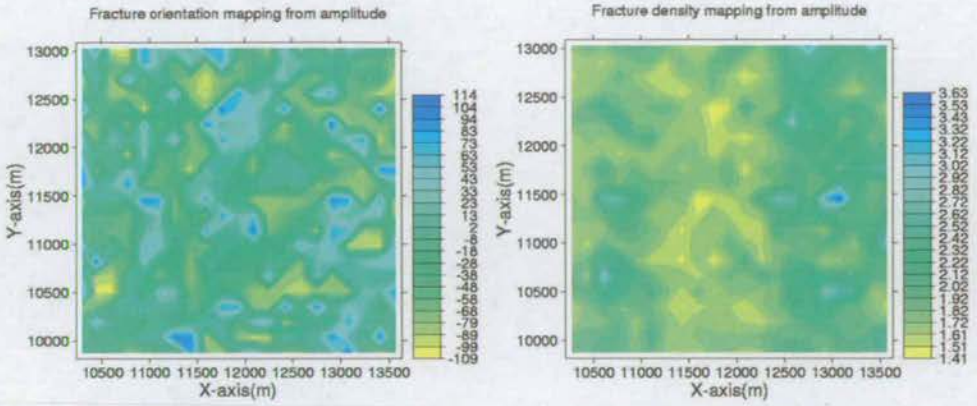

Figure 8.12: Full-azimuth and full-offset inversion: Amplitude inversion from the top of the target T1. (a) Fracture orientation map. (b) Fracture intensity map. The intensity number in the map stands for the amplitude ratio of the maximum and the minimum.

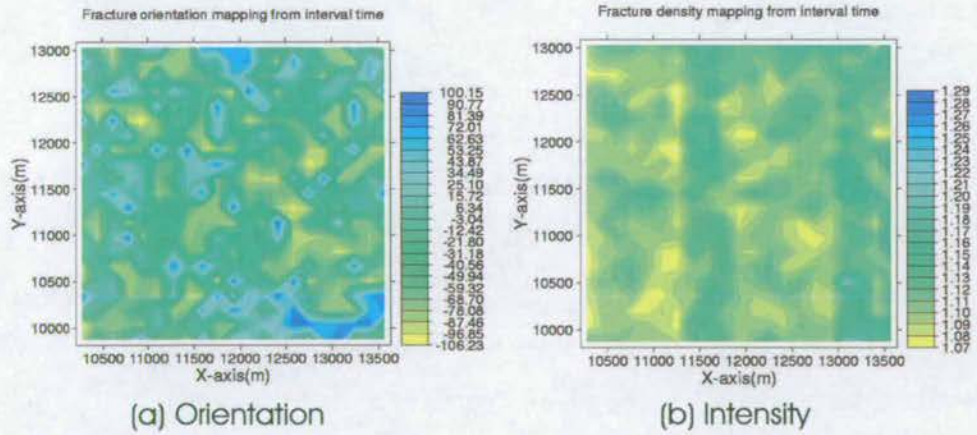

Figure 8.13: Full-azimuth and full-offset inversion: Interval traveltime inversion from the target T1. (a) Fracture orientation map. (b) Fracture intensity map. The intensity number in the map stands for the interval time ratio of the maximum and the minimum.

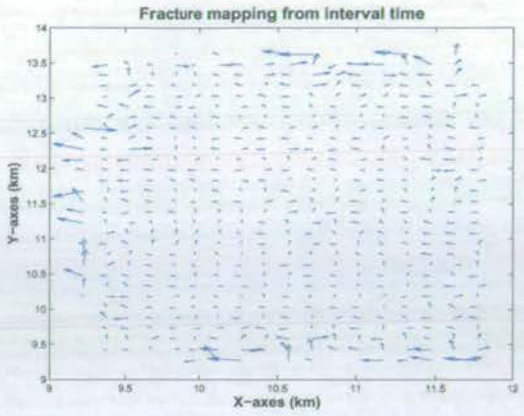

Figure 8.14: The inferred fracture pattern from interval time using the surface fitting method. In the map, the direction of the short line stands for the fracture strike and the its length stands for the fracture intensity.

fitting of interval traveltime yields the most plausible results, and is the preferred choice for fracture analysis.

Also note that interval traveltime is independent of overburden anisotropy. However, if the layer is dipping coupled with faulting, the accuracy of automatic picking will be questionable, and this will affect the results significantly. A good horizon map supplied by an interpreter will be useful to ensure the success of this technique.

8.5 Effects of structure and overburden anisotropy

This is to further assess the reliability of the results obtained from the interval traveltime. Structural influence is always of the first order on seismic data, and the subtle effect of seismic anisotropy is of the second order. Therefore, it is necessary to be able to identify and to remove the effects of any structures in the data. This problem has been tackled by Kühnel and Li (1996, 1998). He found that if the dip is less than 10°, the fracture orientation, i.e. estimated from the long axis of the ellipse in the seismic attributes, will not be affected. However, the origin of this ellipse will be shifted and the ellipse becomes elongated with the relative ratio between long

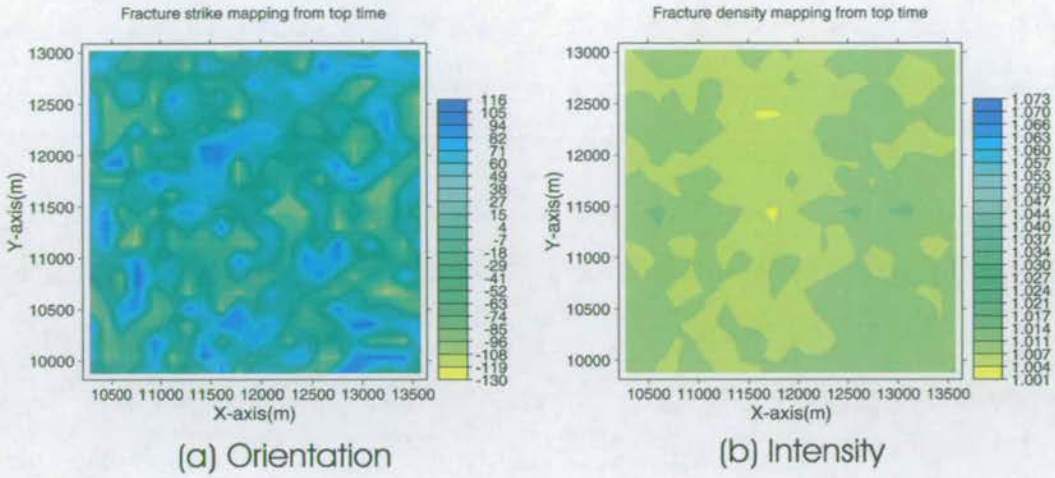

Figure 8.15: Analysis of overburden anisotropy using full-azimuth and full-offset inversion: traveltime inversion from the top of the target T1. (a) Fracture orientation map. (b) Fracture intensity map.

and short axes (i.e. the fracture intensity) significantly altered. In my study area, the dip is believed to be less than 7° and is typically around 3°, so I can therefore confidently say that the fracture parameters estimated from the interval traveltime are thought to be reliable.

To examine overburden anisotropy, surface fitting is applied to the traveltime from the top-horizon of Target 1 (sandstone), and the results are shown in Figure 8.15. The orientation appears quite random and the anisotropy is very weak, less than 1%. This confirms that the overburden is more or less isotropic with gentle dips, which increases the reliability of the results. Even in the presence of anisotropy in the overburden, the use of the interval traveltime will compensate for such effects, as shown in Chapter 4.

8.6 Results for Target 2

The above testing shows that surface-fitting of interval traveltimes is reliable whilst narrow-azimuth stacking velocity is more affected by the acquisition footprint. We

further evaluate these two attributes for Target 2 (mudstone). The results are shown in Figures 15 and 16 in the form of fracture attribute maps. Again, we notice that the narrow-azimuth velocity attributes are dominated by the acquisition footprint (15b). Final fracture map of Target 2 is made from the interval travel time, and the patterns compare reasonably well with the fault patterns in the study area shown in Figure 16. We can also see that along the faults the fracture intensity seems to increase. The dominant fracture orientation is N40° and there is a near-orthogonal direction at N30°W or N150°E, which may be interpreted as the secondary fracture set. These are consistent with the regional stress field.

8.7 Statistic evaluation

Similar to Chapter 7, all the estimated fracture density and orientation are used in statistical analysis for the evaluation of the estimated results. Figures 8.18, 8.19, 8.20 and 8.21 are the histograms and error histograms obtained from the analysis of GVAZ, VVAZ, AVAZ and TVAZ. In this section I will further to evaluate the detected fracture parameters.

8.7.1 Density distribution

After comparing the four density histograms from GVAZ (Figure 8.18b), VVAZ (Figure 8.19b), AVAZ (Figure 8.20b) and TVAZ (Figure 8.21b), I found that the peak density in the last three histograms (Figures 8.19-8.21b) has similar distribution pattern but Figure 8.18b has a very different pattern. In general, the larger the peak density, the larger the azimuthal variation and the more sensitive the method to the attribute's variation. I found that the densities from GVAZ and AVAZ analyses are in the same oder of quantity. So do the densities from VVAZ and TVAZ analyses. Furthermore, the density from AVAZ is as 5 ~10 times strong as that from TVAZ

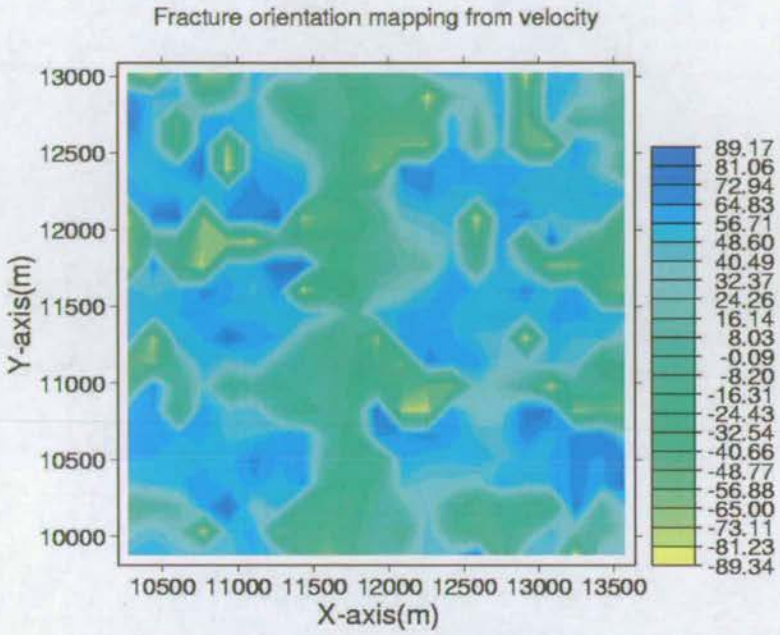

(a) Orientation

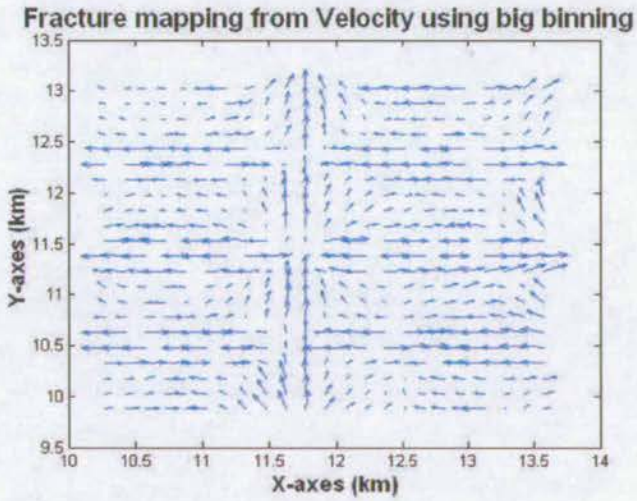

(b) Fracture map

Figure 8.16: Narrow-azimuth method: Stacking velocity inversion from the bottom of the target T2. (a) Fracture orientation map. (b) Interpreted fracture map.

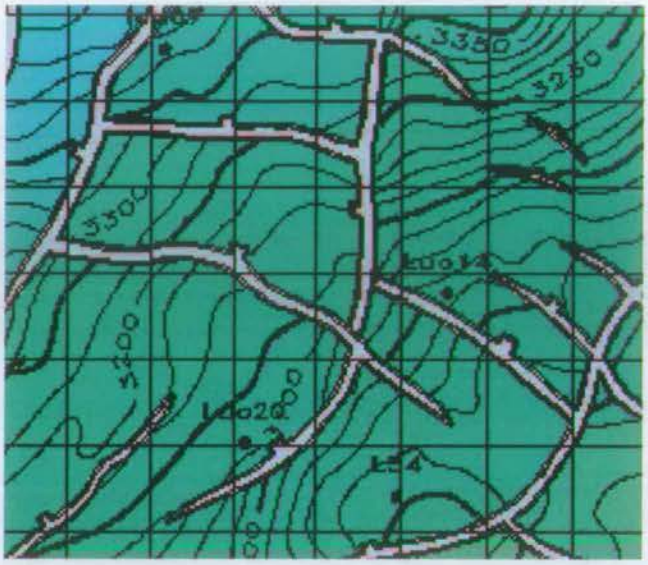

(a) Fault map

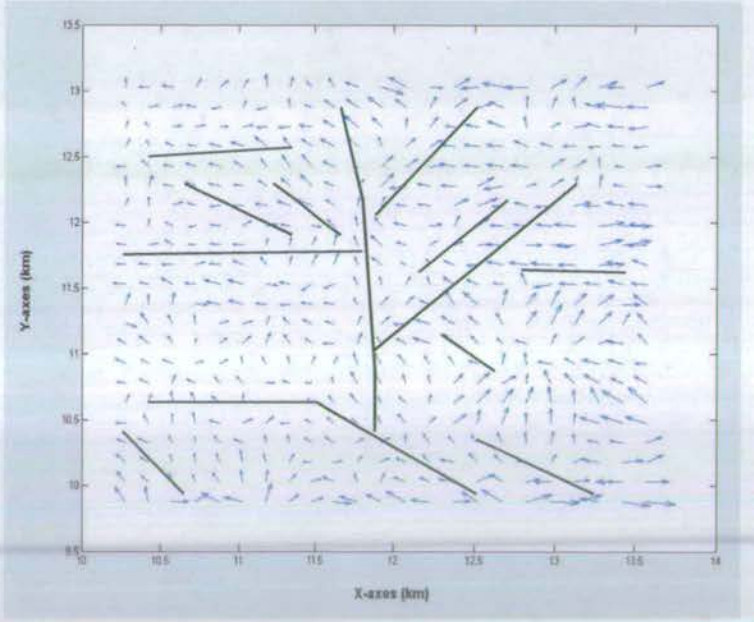

(b) Fracture map

Figure 8.17: (a) Fault map, and (b) results of surface fitting of interval traveltimes for Target T2.

analysis. For this case study, the abnormal density distribution from GVAZ implies that the amplitude based analysis is not very reliable, otherwise, a very similar histogram from both GVAZ and AVAZ should be observed.

8.7.2 Orientation distribution

The orientation histogram is commonly used in fracture interpretation. It is expected to tell us what the major fracture orientations are in the study area. Theoretically, both fracture orientation and density should be the same from a common dataset by using different seismic attribute. But practically, they are different due to two reasons. Firstly, GVAZ and AVAZ technologies are based on the reflectivity equation but seismic amplitude is always used as a replacement to reflectivity in which the X-Y-T dependent scaling of wavelets is imposed on the reflectivity (Chapter 5). The TVAZ and VVAZ technologies did not have this artificial effect. Secondly, the accumulated anisotropic overburden has different effects for different technologies. Among these technologies, the interval time based technology is the only one accounting for overburden (Chapter 4). The comparison of the four orientation histograms shows that different orientation distribution patterns (Figures 8.18a and 8.20a) between GVAZ and AVAZ analyses are observed but similar patterns (8.19a and 8.21a) are observed from VVAZ and TVAZ analyses. From Figures 8.20a) and d), the error rnges for orientation and density from AVAZ analysis can be read as $\pm 35^o$ and $\pm 20\%$, respectively. These values can be also read respectively as $\pm 15^o$ and $\pm 3.5\%$ From TVAZ Figures 8.21a) and d). These analyses show that the VVAZ and TVA Z technologies are better than amplitude based technologies in this case study. However the similarity between the statistical peak orientations from VVAZ and the acquisition system leaves us more spaces for investigation. Based on the statistic analysis on different orientation volumes, I conclude that TVAZ is most

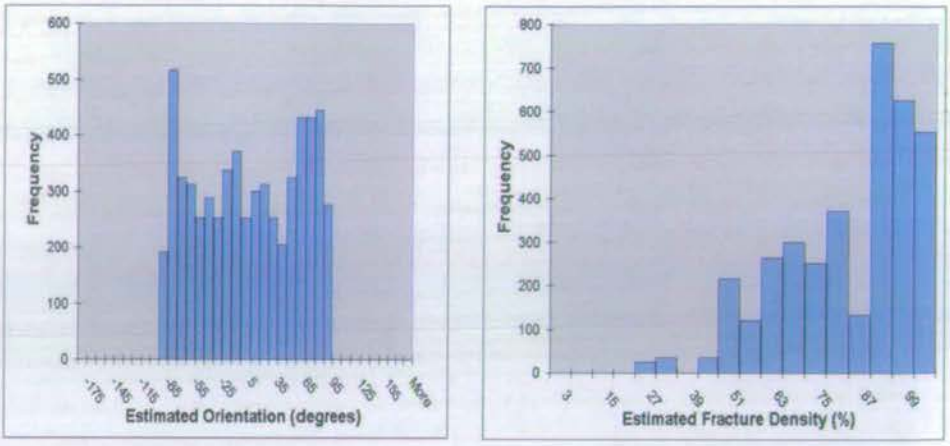

(a) (b)

Figure 8.18: a) and b) are respectively the histograms of fracture orientation and density from GVAZ analysis.

suitable for this case study.

8.7.3 Estimation errors

The standard deviation of prediction is commonly used as a tool for quality control. To better evaluate the merits of different seismic attribute, I present two sets of error histograms of orientation and density (Figures 8.20c & d and 8.21c & d) by respectively using AVAZ and TVAZ analysis results. All the four histograms are showing an approximately normal distribution.

8.8 Discussions

This section presents some of the discussions about the application of the AAA technologies to real data.

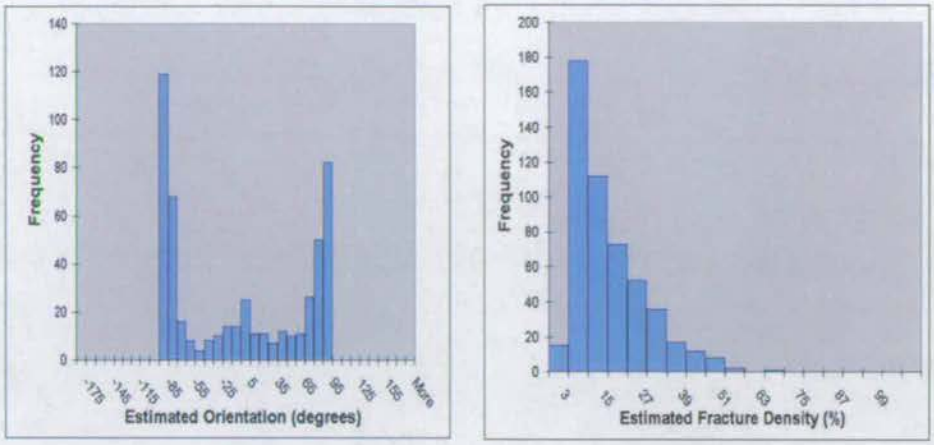

(a) (b)

Figure 8.19: a) and b) are respectively the histograms of fracture orientation and density from VVAZ analysis.

Global fitting

A question is whether a "global fitting" can be applied to the determination of fracture strike and intensity from AVO gradient and NMO velocity analysis rather than inverting fracture orientation and density for each azimuth separately. In theory, the Global fitting should generate a more accurate and robust estimation. But in practice, its requiring full-azimuth coverage may limit its application.

Pre-conditioning options

The CDP gathers after NMO correction or DMO correction or prestack time migration (preSTM) can be used for applying the P-wave azimuthal attribute techniques. Each processing has its own advantage and disadvantage. Among the three processing, NMO is a single trace processing. If an isotropic velocity is used, it has the least side effects on fracture analysis. DMO and preSTM processings perform some azimuthal but not anisotropic mixture calculation between different traces and are found to be very helpful in isotropic AVO analysis. However, in the presence

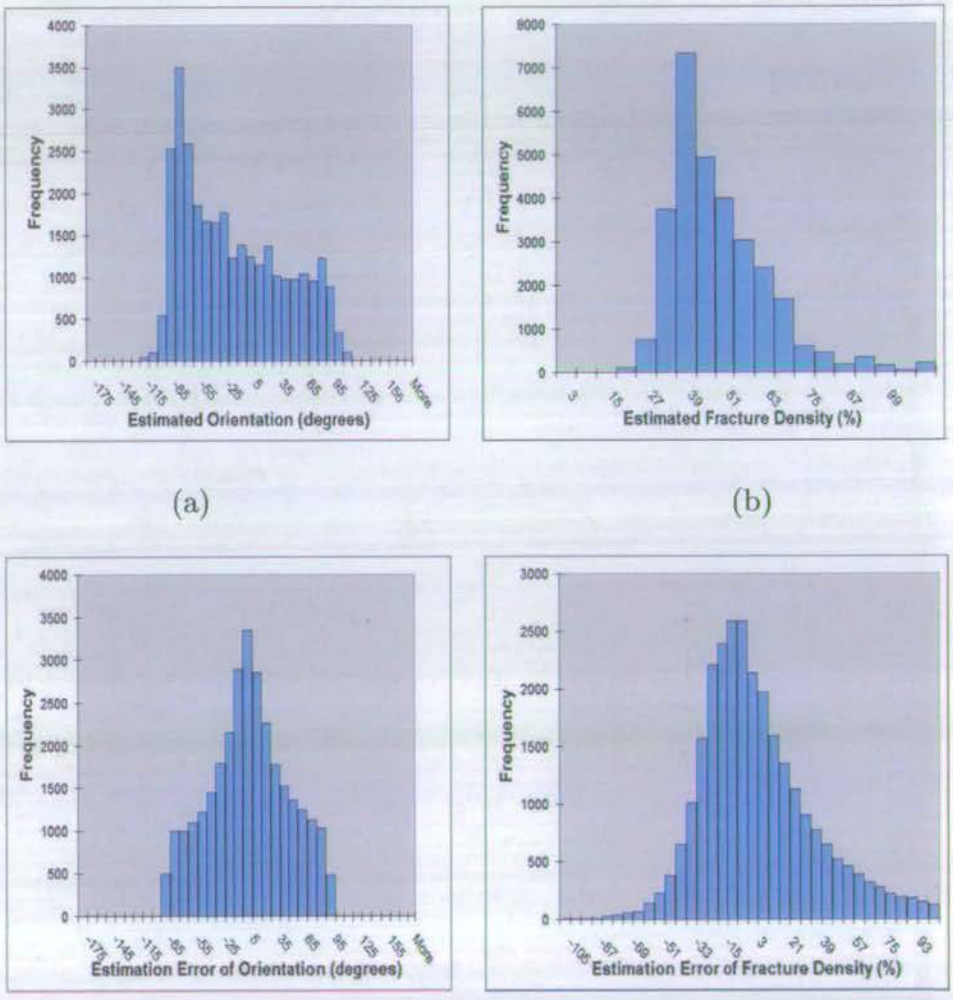

Figure 8.20: a) and c) are respectively the histograms of fracture orientation and orientation prediction error from AVAZ analysis. b) and d) are respectively their histograms of fracture density and density prediction error.

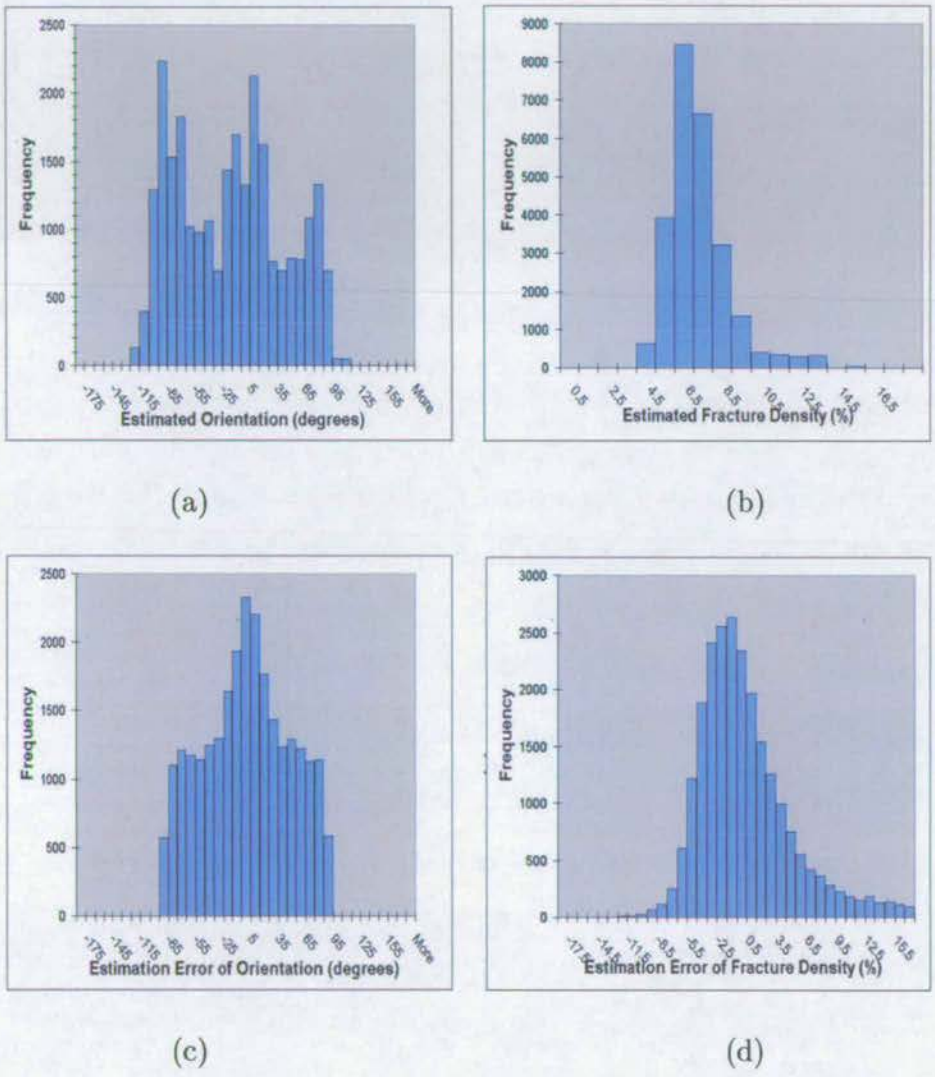

Figure 8.21: a) and c) are respectively the histograms of fracture orientation and orientation prediction error from TVAZ analysis. b) and d) are respectively their histograms of fracture density and density prediction error.

	Advantage	Disadvantage
NMO gather	economic, preserving azimuthal variation	not suitable for dipping layer
DMO gather	good for dipping layer, relatively economic	may damage azimuthal variations if not used properly expensive than NMO cheaper than preSTM
preSTM gather	precisely for structure imaging	very expensive may damage azimuthal variations if not used properly

Table 8.1: Advantages and disadvantages of using gathers of NMO, DMO and preSTM (prestack migration) for P-wave fracture technologies application.

of anisotropically azimuthal variations, if an isotropic velocity is used, DMO and preSTM will damage the relative anisotropic variations of seismic attributes with azimuth. I list the advantages and disadvantages of the three processings (Table 8.1). To obtain a most accurate pre-stack gathers for azimuthally anisotropic analysis, I suggest a three-step procedure is used in practical processing, but this is very expensive. The steps are azimuthal binning on pre-stack CDP gather that will produce a few coned 3D data, azimuthal velocity analysis that will generate a few 3D velocity field and individual processing (DMO or preSTM) using the coned velocity and 3D data from the same azimuth bin. The advantage of this procedure is that we can use our existing conventional isotropic processing system perform anisotropic processing.

Effects of thin-layering and wavelet

In Chapter 5 I discussed the effects of thin-layering on AVO and AVOZ analysis. In reality the thin-layering and wavelet are the two sides of the band-limited seismic amplitude problem. Here I will discuss the effects of wavelet on the evaluation

of fracture orientation and density. To estimate fracture parameters from AVO, reflection coefficients are assumed to be used but routinely seismic amplitudes are used which are affected in two aspects by wavelet. The limited-band of wavelet will cause the so-called thin-layering problem. The X-Y-T dependent variations of wavelet will arise a new problem: unequal scaling on the reflectivity which may seriously damage the relative variations of reflectivity and therefore seriously distort the relative variations of inverted fracture parameters. This is a serious issue in fracture detection. But based on my experiences, fracture orientation is not affected by wavelet.

Stretch effects

3A technologies (Chapter 3) can be applied on original CDP gather, NMO gather and preSTM gather. The stretches of NMO or preSTM, due to the combination of ray theory with a band-limited wavelet, will have some effects on the amplitude attributes and these effects may be more profound when thin layers exist.

If we have even-distributed and full azimuth and offset seismic data, the fracture estimation may be improved by using narrow-azimuth 3D migration but may be diluted by the migration using the whole 3D data as an input. In respect to this, the NMO correction is a single trace processing and the NMO stretch will not degrade the accuracy of orientation estimation and can preserve the relative variation of density estimation, but will affect the values of fracture density.

VTI overburden effects

As discussed in Chapter 3, one of the condition applying 3A technologies is isotropic overburden. However, if there is an VTI anisotropic layer overlying a vertical fractured layer, how about the validity of these technologies to detect the underlain vertical fractures? The key point for this question is whether VTI overburden will

bring in extra azimuthal variations to the seismic attributes used for fracture characterization. Let me take AVAZ analysis as an example to discuss. AVAZ is based on azimuthal variations of reflection reflectivity, which completely depends on the azimuthal variations of the rock property difference between the overburden VTI layer and underlying HTI layer. It is known that the azimuthal variations of rock property happens in HTI medium but certainly not in VTI medium. Therefore the azimuthal variation of seismic amplitude must be caused by the underlying HTI medium. Thus the AVAZ technology is still effective to detect the underlying HTI medium in the case of VTI overburden. So do TVAZ, VVAZ and GVAZ technologies. The assumption of isotropic overburden layer for the 3A technologies can be relaxed as non-azimuthal overburden lay.

Effects of superbinning size

Most of the conventional 3D data is designed as a bin size of 25mx25m with 60 CDP fold. Azimuthal analysis requires that we have not only full-offset seismic traces but also even-distributed full-azimuth seismic traces. Superbinning (say increasing the bin size to 150mx150m) is a normal routine to obtain such a full-azimuth and full-offset data from the conventional seismic data. The Superbinning will smooth the azimuthal variation. In general, if the azimuth and offset coverage is big enough and no superbinning is needed for fracture analysis, fracture imaging will have similar resolution as structure imaging, Fresnel zone, because both of the images are affected by the same band-limited wavelet. When a superbinning is applied, the Fresnel zone for fracture imaging will be increased to the superbinning size.

Which attribute is better?

For geological structure imaging, three seismic attributes, velocity, travel-time and amplitude, are used jointly. Seismic amplitude is also widely used for rock properties

	Advantage	Disadvantage
Amplitude	Suitable for relative short offset-coverage. Suitable for thin layering condition	Need very careful processing. The orientation has ambiguity. The density interpretation is sensitive to the wavelet assumption. Difficult to take overburden into account.
AVO gradient	The same as above	The same as above, and need full offset coverage
Traveltime	Can approximately take overburden into account Cheap processing. Not affected by wavelet assumption. Identical orientation result. Possible to give layer property. Can be used for small offset coverage but with large offsets.	Need far offset traces
Velocity	The same as above	The same as above, and need full offset coverage My be easily affected by acquisition footprints.

Table 8.2: Advantage and disadvantage of different seismic attribute for fracture estimation.

characterization. For fracture estimation, I found that any one of these seismic attributes: amplitude, velocity, AVO gradient, travel time, can be used independently or jointly to invert fracture parameters. However, different attribute has different applying conditions. Based on my previous analysis and discussion, here I briefly table the advantage and disadvantage of each seismic attribute for fracture estimation (Table 8.2). Therefore, which seismic attribute to be selected for fracture analysis in a 3D area will be decided by its acquisition parameters and the data quality.

8.9 Conclusions

I have carried out a detailed and robust analysis of the azimuthal variation in *P*-wave attributes from a 10km^2 3D land seismic dataset from the Yellow River Delta, China. Two methods (full-azimuth/full-offset and narrow-azimuth/full-offset) have been used and four seismic attributes analysed for fracture parameter estimation. Azimuthal differences in seismic attributes have been presented in the form of fracture orientation and fracture intensity maps. Analysis of narrow-azimuth stacking data reveals significant traveltime and amplitude variation in the azimuthal directions. Surface fitting of interval traveltime is recommended. More detailed guidelines related to the use of P-wave azimuthal anisotropy for fracture detection can be found in Appendix A.

Chapter 9

Summary

P-wave AVD technology for fracture detection is gradually gaining acceptance by the industry. As an emerging technology, there are some gaps between the current technology and the enhancement of the reliability of the predicted results. These include: (a) the marine environment, (b) practical procedures and guidelines for data acquisition and processing and (c) complications due to overburden anisotropy and thin-layering. To fill some of these gaps, I have developed specific techniques for extending the AVD technology to the marine environment using repeated 2D and 3D surveys of different vintages, I have carried out a series of case studies from repeated 2D surveys to 3D data with full azimuthal and offset coverage, and I have developed new techniques to handle the complications due to overburden anisotropy and thin-layering. This chapter summarizes the main results and also gives recommendations for further work in this subject.

9.1 Major conclusions from this thesis

9.1.1 Azimuthal variations of P-wave attributes

Fractures play an important role in the economic production of naturally fractured, low-permeability hydrocarbon reservoirs. These fractures tend to be aligned due to stress and induce azimuthal anisotropy for seismic wave propagation, which causes variation of P-wave amplitude, traveltime, AVO gradient and slowness with azimuth. This forms the basis of the P-wave AVD technology for fracture detection.

In fracture-induced anisotropic media, the azimuthal variation of P-wave amplitude and traveltime can be expressed as

$$F(\phi, x) = A(x) + B(x)\cos 2(\varphi - \Phi) + C(x)\cos 4(\varphi - \Phi),$$

with respect to the survey-line azimuth φ and the fracture-strike azimuth Φ, both measured from north. $A(x)$, $B(x)$ and $C(x)$ are functions of offset. For near-to-mid offsets, the $C(x)$ term is often sufficiently small and may be neglected. This gives rise to an elliptical variation of P-wave attributes in polar coordinates for near-to-mid offsets. In contrast, the azimuthal variations of AVO gradient and squared slowness (inverse of velocity squared) is only a function of $\cos 2(\varphi - \Phi)$,

$$F(\phi) = A + B\cos 2(\varphi - \Phi),$$

where A and B are constants.

Consequently, different acquisition systems may be used to quantify the azimuthal variations for estimating fracture strike and intensity. Numerical modelling confirms that Hudson's model may be used for fracture estimation (Chapters 2 and 3).

9.1.2 Basic requirements and the choice of attributes

Generally speaking, the use of traveltime and amplitude for the study of azimuthal anisotropy for fracture detection requires a minimum of four azimuths, and the use of AVO gradient and velocity requires only three azimuths with an even distribution. If the higher order term for large offsets in the traveltime and amplitude attributes are ignored, three azimuthal observations may also be sufficient for these two attributes. Since the azimuthal variation increases with offset, there should be traces with sufficiently large offset/depth ratio to quantify the azimuthal variations. Generally, the offset-depth ratio should be greater than 0.6.

For the use of traveltime and velocity attributes for studying azimuthal anisotropy for fracture detection, the layer should be sufficiently thick to enable the identification of its top and bottom. For the use of amplitudes or AVO gradient, it is sufficient to use only the attributes from the top interface of the target. Therefore, the amplitude and AVO gradient may generate more reliable results than other methods in the presence of thin layers. Particularly, if the signal to noise of the traces is high, P-wave amplitude may be expected to give an accurate result (Chapters 3, 5 and 6).

9.1.3 Considerations for the marine environment

There is a lack of azimuthal coverage in marine streamer data. Improving azimuthal coverage is the key to extend the P-wave AVD technology to the marine environment. This can be achieved either by employing a different acquisition system such as OBC (ocean-bottom cable) acquisition, which is beyond the scope of this thesis, or by the use of repeated 2D and 3D surveys of different vintages, as studied in this thesis.

Repeated 2D orthogonal surveys are quite common in marine surveys. In the case of a special orthogonal configuration, the attribute difference between two orthogonal

lines is only a function of $\cos 2(\varphi - \Phi)$ due to the canceling of the $\cos 4(\varphi - \Phi)$ term. Thus, the fracture-strike azimuth may be accurately determined from two pairs of orthogonal lines by cross-plotting the attribute difference of one pair against the difference of the other pair. This cross-plotting procedure is very robust, and particularly suited for repeated 2D surveys in the marine environment, as demonstrated in the case study in Chapter 6. However, this configuration only yields fracture information at the intersecting point, and the spatial coverage is very limited.

Joint 2D and 3D marine surveys may be employed to generate more intersecting points for larger area fracture evaluation. However, the azimuthal traces are distributed in near- to mid-offsets and the number of azimuths is often limited to three for most intersecting points. For this reason, amplitude is usually used to quantify the azimuthal anisotropy. Due to the variations in acquisition parameters in repeated surveys, application of the AVD technique to repeated surveys requires careful and special processing workflows for geometry matching and data conditioning. These workflows include CMP matching, line matching, corrections for the source and receiver responses, noise reduction, etc. A dataset consisting of ten crossed 2D lines and a 3D survey have been examined in Chapter 7 to illustrate these ideas.

9.1.4 Considerations for wide-azimuth 3D data

Wide-azimuth 3D data are ideally suited for studying azimuthal anisotropy for fracture detection. In this case, all four types of attributes (Amplitude, traveltime, AVO gradient and velocity) can be used for fracture analysis. There are often two approaches for processing such data. One is called the narrow-azimuth stacking approach, which is fitting the surface of $\cos 2(\varphi - \Phi)$ on the binned azimuths. This is to sort the data into narrow azimuthal bins, then perform azimuthal bin-stack

to reduce the number of azimuth to a few selected azimuths (usually 4, or 6, or 9). The other approach is called surface fitting which is to fit surfaces of $\cos 2(\varphi - \Phi)$ and $\cos 4(\varphi - \Phi)$ variations to all offsets and azimuths using a least squared method. Using the 3D data from Shen-Li, as shown in Chapter 8, I have evaluated the reliability and limitations of all the different attributes for both approaches. I find that the narrow azimuth method may enhance the data acquisition footprint, and the surface fitting method is generally preferred. Among the different attributes, I find that, for the data studied, the amplitude and velocity attributes are all not very reliable. The most reliable results are given by surface fitting of interval travel times, for which I am using a least-squares inversion scheme to fit the azimuthal variation equations.

9.1.5 Effects of overburden anisotropy and thin layering

Apart from the case studies, I have also studied the effects of overburden anisotropy and thin layering (Chapters 4 and 5). I developed a new layer-stripping procedure for handling overburden anisotropy. The procedure is based on the P-wave traveltime difference between two orthogonal seismic survey lines, and this difference is referred to as the P-wave azimuthal moveout response (AMR). In the case of a weakly fractured overburden (less than 3% azimuthal anisotropy) underlain by a heavily fractured target, layer stripping can be achieved through the alignment of the top-target event by performing NMO-correction separately for all survey lines. The interval AMR of the target layer may then be calculated from the residual moveout of the bottom-target event. Full-wave modelling is used to verify and illustrate the procedures (Chapter 4).

Thin-layering is another complicated but common problem. Using the picked amplitude as the effective reflection coefficient, I examine the AVD responses as a

function of layer thickness (Chapter 5). I obtained the following results.

1. The variations of the amplitude differences between two azimuthally orthogonal directions, referred to as the azimuthal amplitude response (AMR) are stable over thicknesses larger than $\lambda/2$, where λ is the wave length.

2. For noise-free data and using the AVO gradient attributes, the fracture strike can be correctly estimated for a layer as thin as one metre and correct intensity can be estimated if the thin-layer thickness is larger than $\lambda/8$.

3. For noisy datasets, if the thin-layer thickness is greater than $\lambda/4$ and the offset-depth ratio greater than 0.5, the orientation and density can be estimated correctly.

4. In the case of a fracture thin-layer being embedded in a sequence of isotropic layers, it is possible to create an effective target layer by combining the thin-layer with the surrounding isotropic layers. This procedure can be used to provide reliable information about fracture orientations and density even if the thickness of fractured reservoirs is as low as $\lambda/8$.

9.1.6 Results of the case studies

There are three case studies performed for implementing and testing the algorithms developed in this thesis. They are:

1. fracture estimation using marine 2D orthogonal lines (four lines)

2. fracture estimation using marine 2D and 3D (ten 2D lines and over 250 Km^2 of streamer 3D data)

3. fracture estimation using land 3D data: (60 Km^2 processed but only the centre 10 Km^2 is used)

The three case studies represent three typical practical problems encountered in the oil industry. For the case of the 2D orthogonal lines, all four attributes are used to examine the fracture strike. The results agree with each other, and are consistent with the fault trend in the study area (Chapter 6). In the case of repeated 2D and 3D surveys, the AVD gradient method is used for estimating the fracture information. Due to the lack of azimuthal coverage, the number of intersecting points is very few, and the obtained lateral variation in the fracture information is not very reliable (Chapter 7). However, the developed methodology and software are very useful for further applications to other similar types of datasets. In the wide-azimuthal 3D data, geological meaningful results are possible to be obtained by surface fitting of interval traveltimes (Chapter 8) if correct interpretation information about the target layer can be provided.

9.2 Future developments

9.2.1 Effects of acquisition footprint

Ideally, a multiple azimuthal dataset (general 3D) should be acquired in a regular midpoint, offset and azimuth grid. However, owing to various practical considerations such as cost and surface obstacles, only a very small subset of this space is sampled, giving rise to irregular offset and azimuth patterns. The outcome of these irregularities is that the footprint of the acquisition pattern can be sometimes observed on the 3D seismic data, which distorts the amplitude and phase of the P-wave reflections. This can lead to incorrect interpretation of fracture information. To further develop the AVD technology, the effects of the acquisition footprint and how it manifests itself in the AVD results merit further study.

9.2.2 Effects of dipping layers and complex overburden

When there are structural variations in the overburden, the AVD response in the target layer will be affected. Kühnel (1998) studied the effects of dipping layers, and he showed that when the dip is less than 15^o, the effects on the AVD response are small and negligible. Therefore the algorithms developed in this thesis can still be applied. For larger dips, the effects of dip can not be neglected. It is thus important to develop techniques to compensate for the effects of dip, and to examine the effects of migration and DMO-related processing on the AVD response.

9.2.3 The use of OBC data

Recently, marine acquisition using ocean-bottom cable (OBC) has been growing in popularity. This type of multi-component acquisition is characterized by the geophones and hydrophones being placed on the ocean-bottom, and the vessel with a source moves over the sea surface. The data recorded in this way have many advantages over conventional marine acquisition, where streamers of hydrophones are towed behind a boat. On one hand, it is possible to acquire data with a wide-azimuthal coverage, and the OBC data can then be directly used for fracture estimation (Hall and Kendall, 1997; Hall et al., 2000; Hall and Kendall, 2001; Hall et al., 2002). On the other hand, good quality converted shear waves can be recorded in the OBC data that are more sensitive to anisotropy than P-waves from which it is possible to obtain more reliable fracture features.

9.2.4 Joint P- and shear-wave analysis for fracture detection

If converted shear-wave or pure shear-wave data are available, converted-wave or shear-wave splitting (birefringence) can be used to study the azimuthal anisotropy. The shear-wave results may then be used to calibrate the P-wave results for im-

proving the accuracy and reliability of the detection. However, how the results of shear-wave splitting are correlated to the results of P-wave AVD is still not fully understood. It is thus worthwhile to examine this correlation in more detail, paving the way for an integrated approach for fracture detection.

Appendix

Appendix A

Processing report of the 3D data in Chapter 8

In this appendix, I enclose the details of the data processing procedure, the full results and some general guidelines learned from the dataset in Chapter 8.

.1 Data inspection and pre-processing

Once data have been received, the first step is normally to inspect data quality, to check geometry, and to evaluate data characteristics. As my aim is to obtain fracture details from 3D seismic data, data quality is more important than is normally required for the purpose of structural imaging. Thus this first step becomes essential to ensure that the data can be utilised for my purpose. [The acquisition geometry and data quality are discussed in Chapter 8, and Figure 1 shows the fold coverage.]

.1.1 Pre-processing

Figure 2 shows the flowchart of the pre-processing steps. The pre-processing includes: static correction, noise attenuation and surface-consistent amplitude correction, as well as conventional image processing. The first three steps are to improve data quality and prepare the data for azimuthal analysis. The static and amplitude corrections are necessary as they affect the data quality and the accuracy of the au-

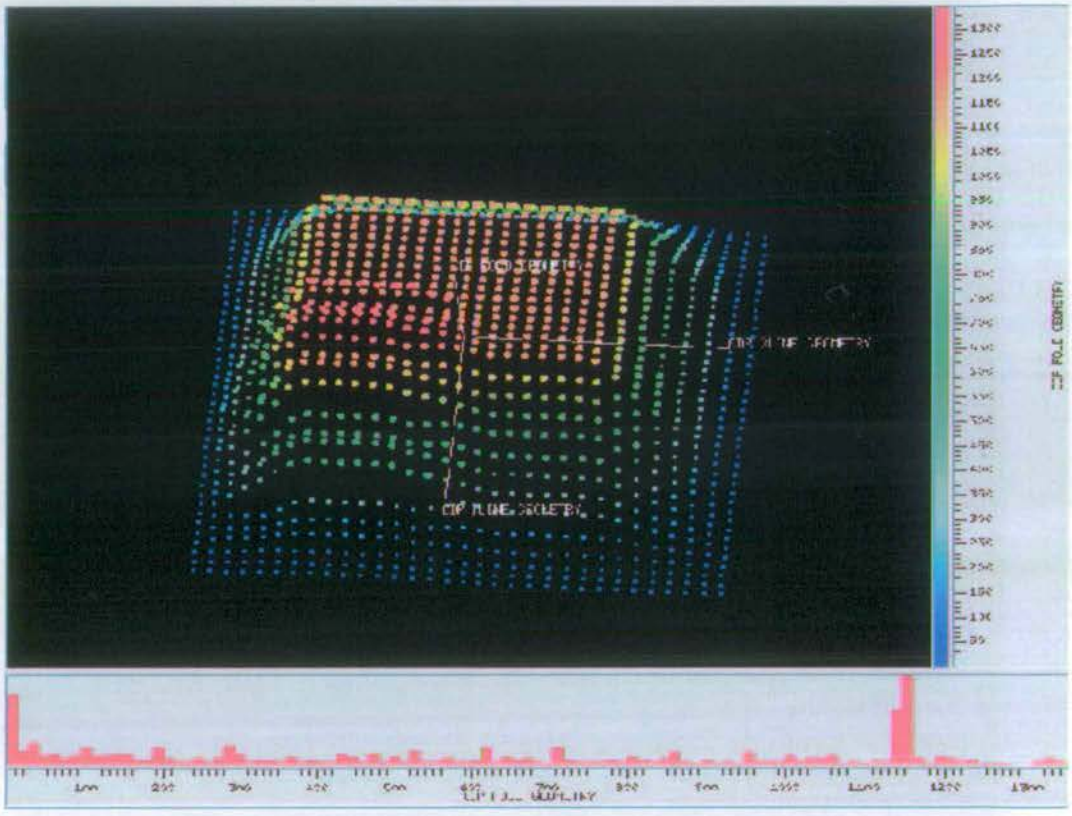

Figure 1: Fold coverage for the test data with bin size (150mx150m).

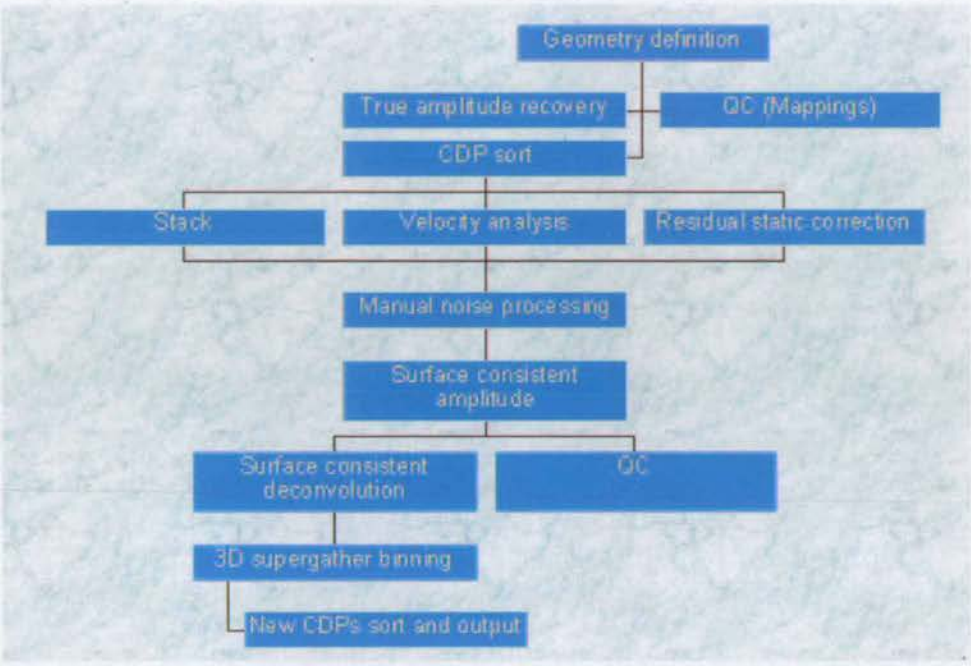

Figure 2: Processing flowchart: data preparation.

tomatic picking of events, and noise attenuation is essential for AVO analysis. Care should be taken during processing to maintain the relative amplitude and phase information among different azimuths. Image processing steps include deconvolution, NMO correction, velocity analysis, and trace stacking to produce the initial image volumes for identifying the target horizons. The target horizon time from the stack volume will be used to control the automatic horizon picking that is applied to the pre-stacked data, and NMO corrected data for picking traveltimes and amplitudes.

Figure 4 shows an example of the comparison of the data before and after surface consistent static correction. After the correction, the events are continuous and the phases are consistent in contrast to the data before the static correction. Figure 5 shows that the source energy varies significantly from location to location (or from shot to shot). This apparent amplitude variation must be eliminated before the 3A technique is applied. Figure 6 shows the comparison of the data before and after

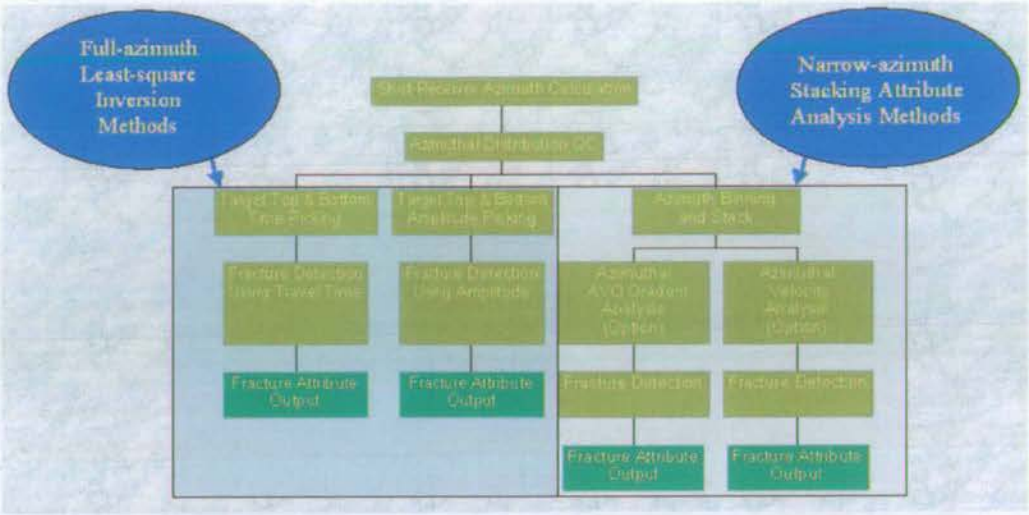

Figure 3: Processing flowchart for P-wave azimuthal attribute analysis.

surface-consistent amplitude correction. It is clearly seen that after the correction, the reflected events become clearer than before the correction. Like any other land-based seismic data, random noise is a big problem. There are many studies that have been devoted to this problem, and in this chapter, I apply a noise reduction technique to the data. There is a significant improvement in the data quality after the random noise is effectively removed and S/N ratio is enhanced (Figure 6).

After these three key pre-processing steps, and the data quality has been improved, and the data are ready for conventional imaging and anisotropic processing. Figure 7 shows an example of the selected inline and crossline sections after the imaging processing. The target horizons are marked in the map. The top of T2 (mudstone) is the bottom of the T1 (sandstone). The target horizons are hand picked from the imaging volume and are used as control points for pre-stack analysis.

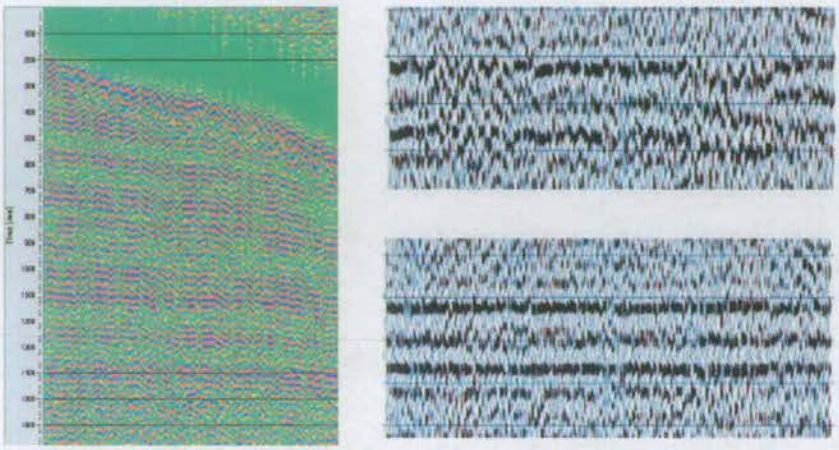

(a) (b)

Figure 4: Surface consistent residual statics correction. (a) input data. (b) stacked results with (upper panel) and without (lower panel) statics correction.

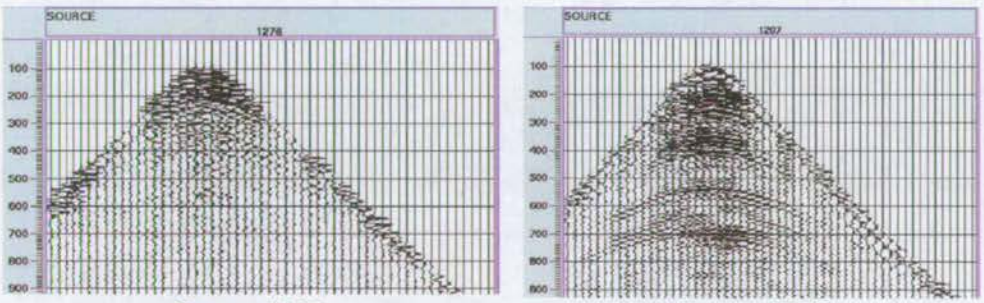

Source 1276 Source 1207

Figure 5: Two original shot gathers showing the variation of amplitudes from shot to shot.

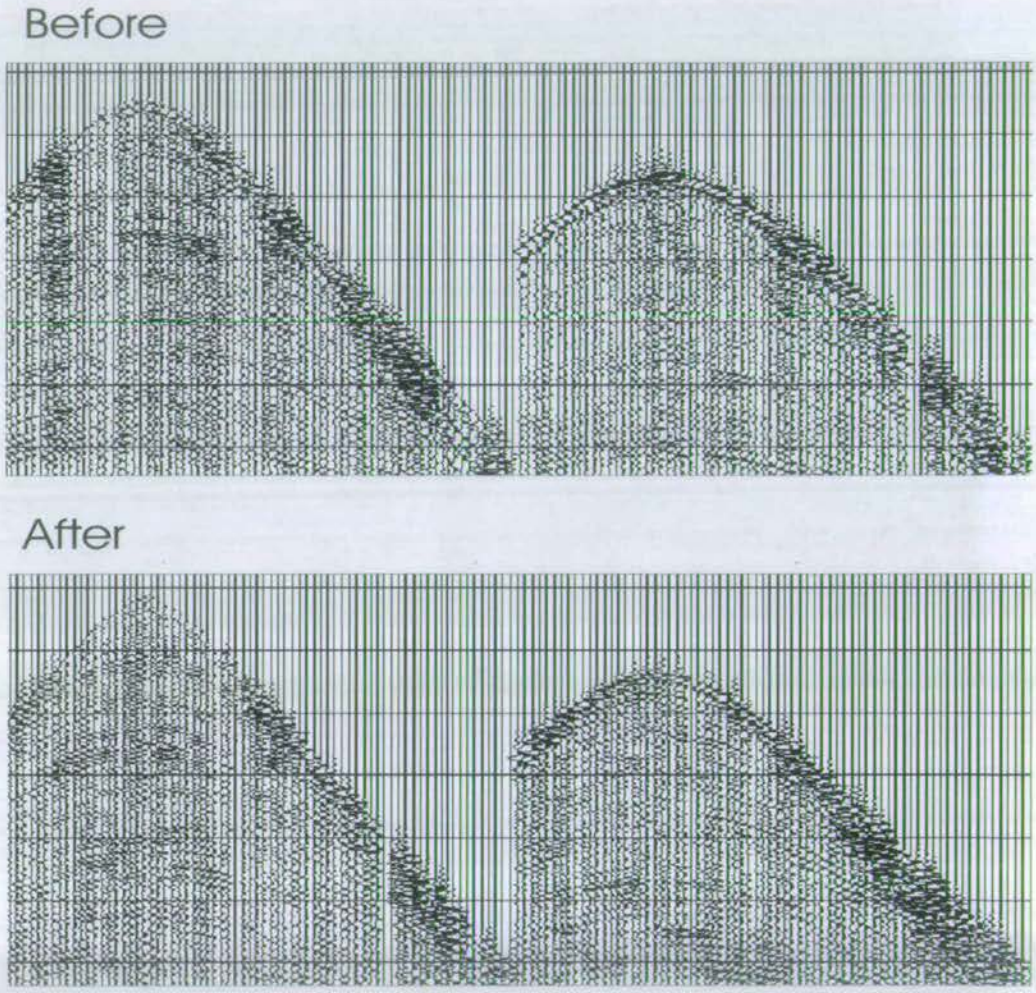

Figure 6: An example of the seismic sections before and after random noise is attenuated and surface-consistent amplitude correction is applied.

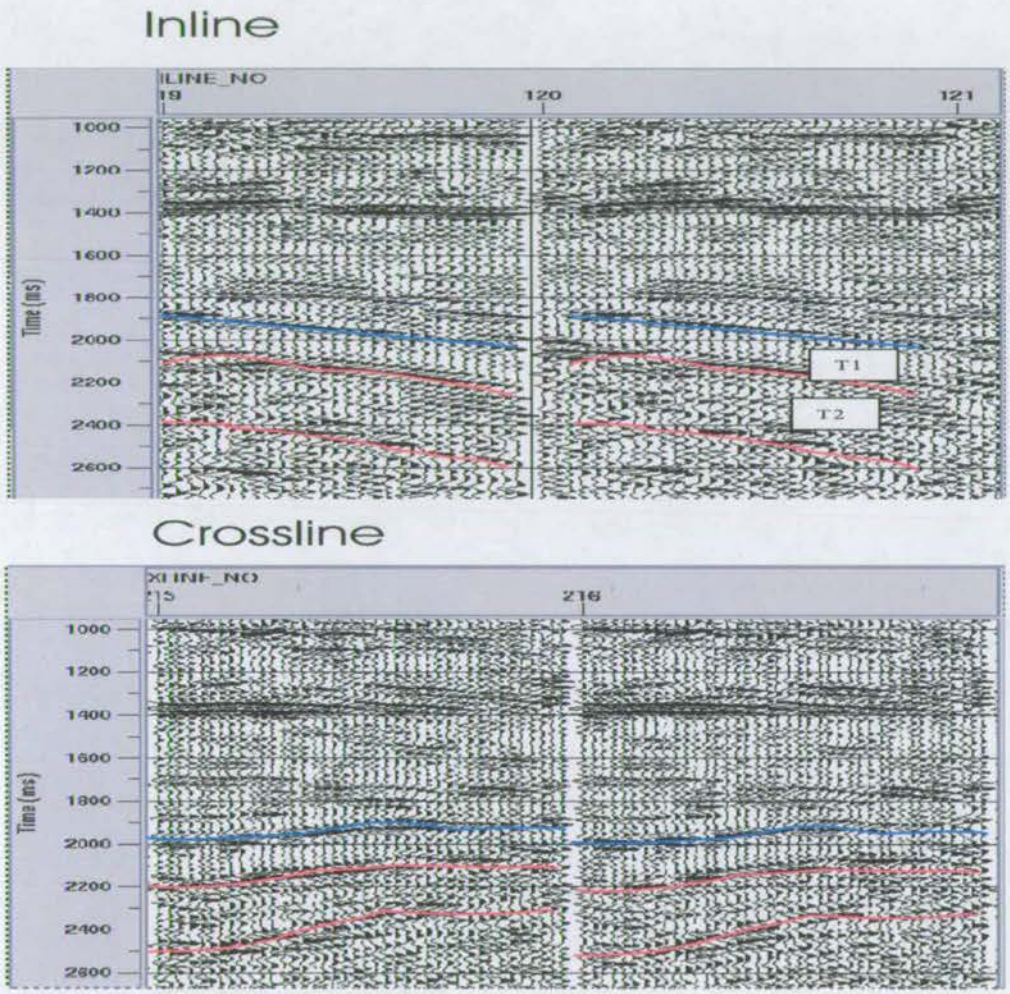

Figure 7: Examples of image processing results for an inline and crossline profiles. Two target horizons have been identified (labelled T1 and T2. Note that the top of T2 is the same as the bottom of T1).

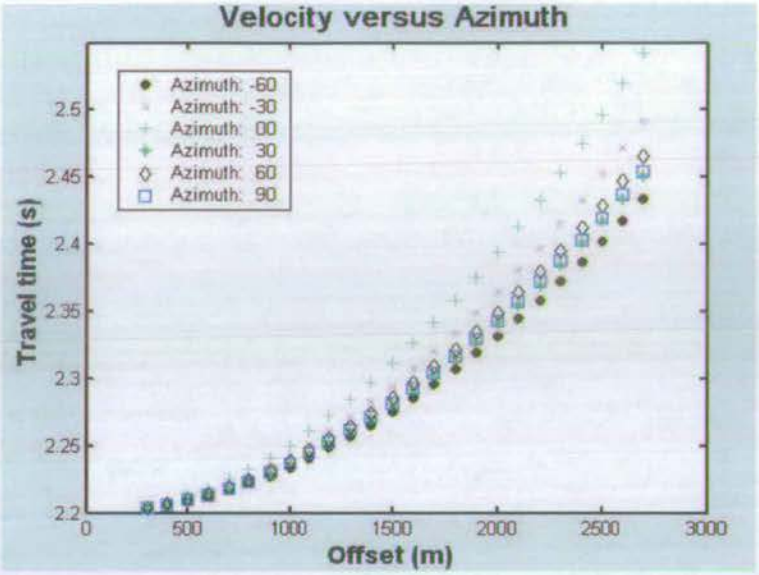

Figure 8: Least square inversion of stacking velocities from the traveltime curves for different azimuths.

.1.2 Velocity analysis and amplitude re-normalisation

Note that two procedures are critical for 3A analysis. Firstly velocity picking. It usually has an error up to 3% to 5% and therefore directly picked velocity is often not suitable for azimuthal analysis. To overcome this problem and to improve the picking accuracy, I apply a least-square traveltime inversion technique to obtain accurate stacking velocity (Figure 8). Secondly, the amplitude normalisation, which is required for AVO analysis. P-wave should in theory have the same amplitudes for all different azimuths at zero offset. This is often not the case in real data as shown in Figure 9a, and a normalisation is then necessary (Figure 9b), which also makes the amplitude less robust. Examples of amplitude normalisation are also given in Lynn *et al.* (1996). Therefore normalisation is regarded as a standard procedure.

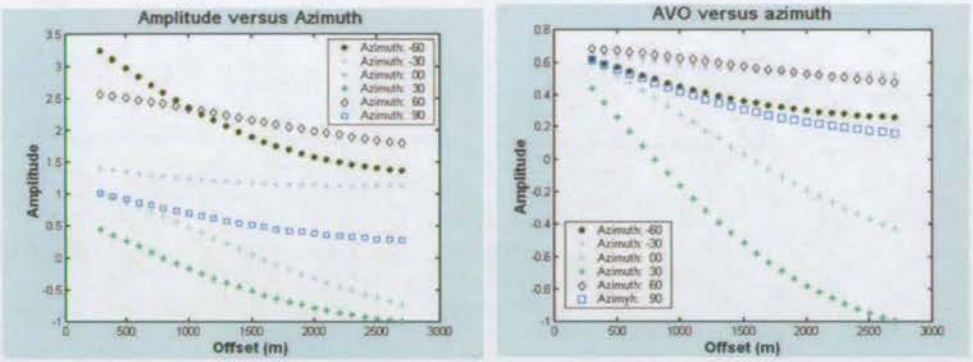

Figure 9: Comparison of azimuthal amplitude variations before and after the normalisation.

.2 Descriptions of results

For these analyses, the choice of the bin size is critical. For the surface-fitting method, a relatively small bin-size is allowed (75mx75m), while for narrow-azimuth stacking, similar to AVO analysis, a relatively large bin size is required. Here I use (150mx150m) to ensure sufficient offset and azimuthal coverage. Note that I could have used a smaller bin size (say 25mx25m), however this will increase the data volume by several times and for this test purpose I felt that this was not necessary. It is certainly necessary for detailed study, for example, if the aim is to provide a map for well planning or for production drilling.

.2.1 Surface fitting results

The surface fitting results have been fully described in the main Chapter, and are not repeated here.

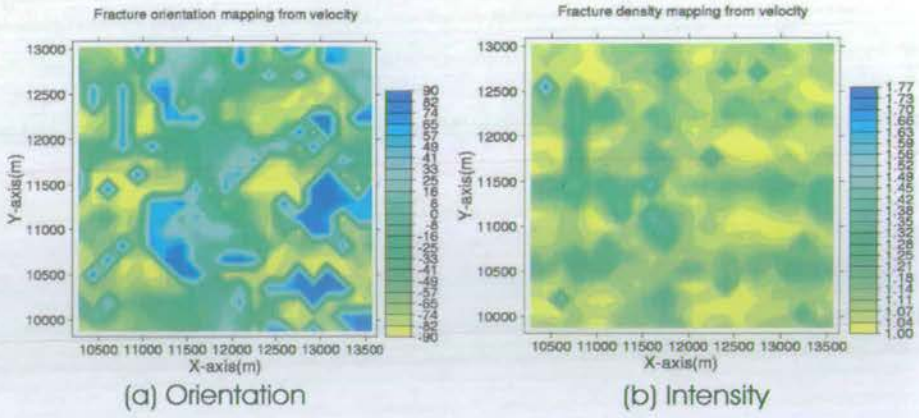

Figure 10: Narrow-azimuth method: Stacking velocity inversion from the bottom of the target T1. (a) Fracture orientation map. (b) Fracture intensity map.

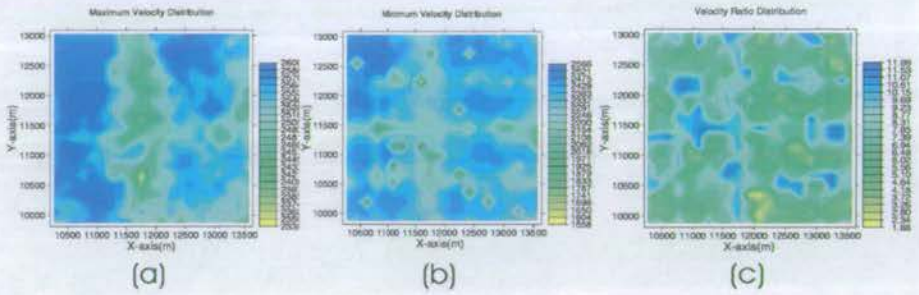

Figure 11: Analysis of the azimuthal variation of stacking velocities from the bottom of the target T1. (a) Maximum. (b) Minimum. (c) Percentage variation.

.2.2 Narrow-azimuth stacking attributes analysis

The initial analyses of the narrow-azimuth stacking data are shown in Figures 10 to 14. As a normal QC procedure, velocity picking for every CMP in all six volumes is carried out, followed by NMO correction and automatic picking of traveltimes and amplitudes. Inverse NMO is then applied and a least-square traveltime inversion method is used to obtain the stacking velocity. Each CMP has six velocities corresponding to the six azimuths. An elliptical fitting technique is applied.

Figure 10 shows the fracture maps from azimuthal analysis of velocity variation. Figure 11 shows, respectively, the maximum, minimum, and percentage variations

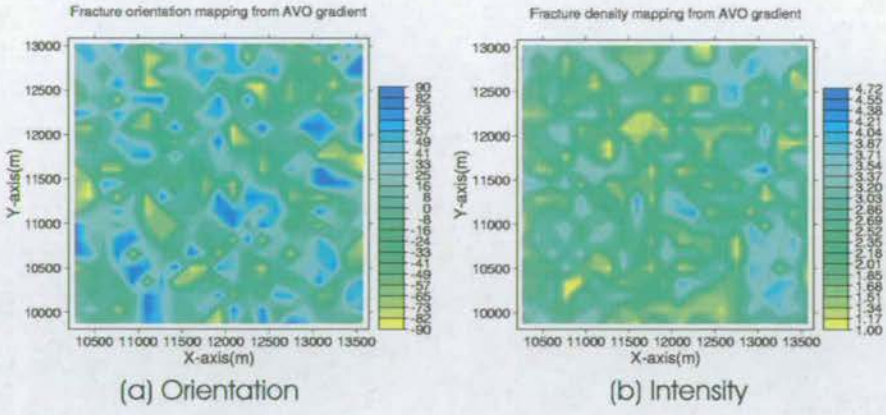

Figure 12: Narrow-azimuth method: AVO gradient inversion from the top of the target T1. (a) Fracture orientation map. (b) Fracture intensity map.

of the stacking velocity in the areas. The result appears to be very informative, and more detailed variations can be observed. Figures 12 and 13 show the corresponding results of azimuthal analysis of AVO gradient.

.2.3 All results for Target 2

There are three results in total: surface-fitting of interval traveltimes and azimuthal analysis of narrow-azimuth stacking velocity. The results are shown in Figures 14, 15, and 16 in the form of fracture attribute maps.

An independent analysis has been done in SINOPEC on the same dataset using the azimuthal variation of acoustic impedance which are inverted from stacked sections, and their results generally agree with mine

.3 General Guidelines

The observed seismic attributes (velocity, AVO gradient, traveltimes, amplitudes) are the results of all of the geological properties along the raypath, including lithology (e.g. sand or shale), stress/strain state (e.g. fractures), and pore content (gas, oil or

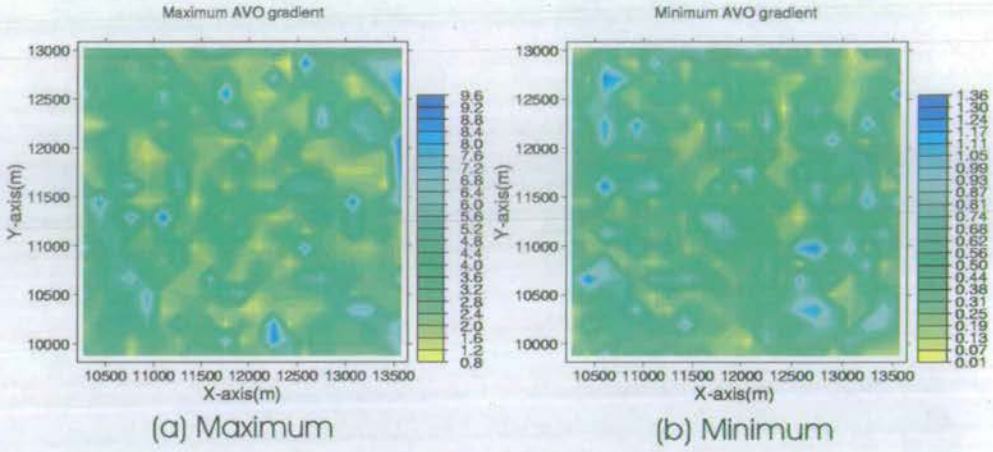

Figure 13: Analysis of the azimuthal variation of AVO gradient from the top of the target T1. (a) Maximum gradient distribution. (b) Minimum gradient distribution.

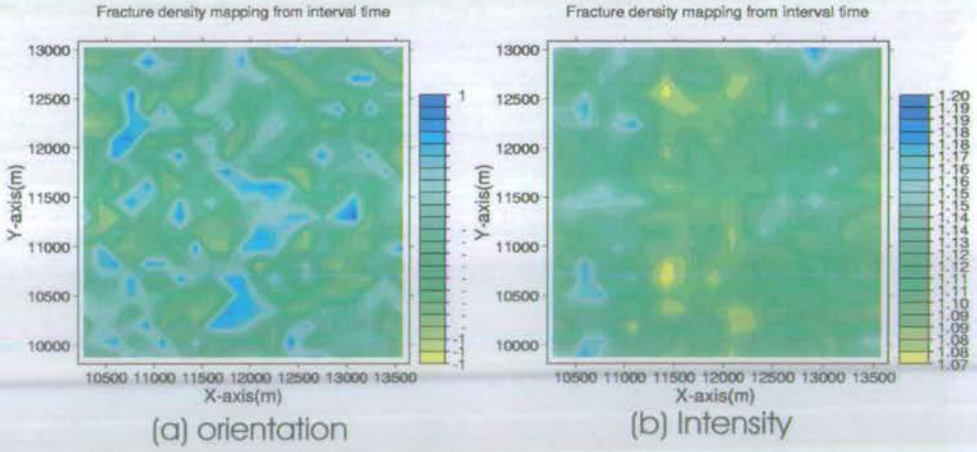

Figure 14: Full-azimuth and full-offset inversion: Interval traveltime inversion from the target T2. (a) Fracture orientation map. (b) Fracture intensity map.

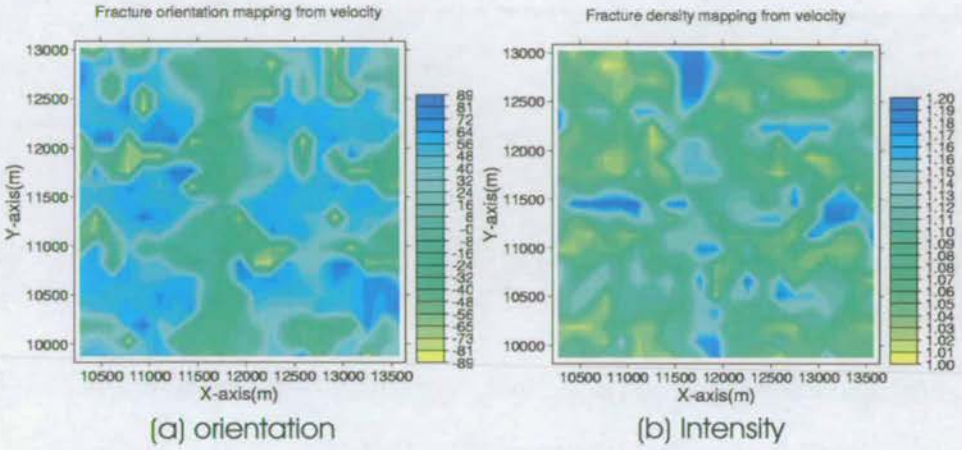

Figure 15: Narrow-azimuth method: Stacking velocity inversion from the bottom of the target T2. (a) Fracture orientation map. (b) Fracture intensity map.A super CMP gather with bin-size of 150mx150m.

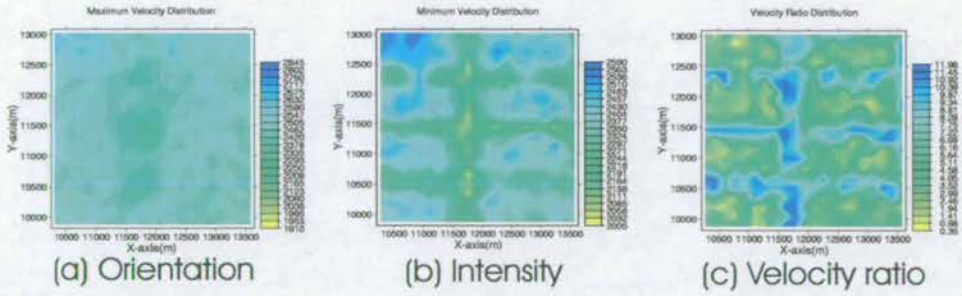

Figure 16: Analysis of the azimuthal variation in stacking velocity from the bottom of the target T2. (a) Maximum velocity distribution. (b) Minimum velocity distribution. (c) Percentage variation.

water). The effect of fractures on the dominant fracture-strike direction is minimal, so that the attributes are sensitive mostly to variations in lithology and pore content. Fracture-normal direction will contain information from both fractures and primary lithology. Azimuthal-difference or ratio attributes remove the background effects of lithology and pore content, and indicate the presence of fractures. This makes the results using relative measurements more reliable than the absolute measurements.

Based on this study, some general guidelines related to the use of P-wave azimuthal anisotropy for fracture detection can be drawn up as follows:

(1) It is in general very useful to gather sufficient reconnaissance data (geological, well log, core, etc.) to determine the general nature of fractures in the study area.

(2) It is essential to acquire 3D *P*-wave data with maximum offsets greater than or equal to the target depth in all azimuths, using azimuthally isotropic sources and receiver arrays. Every effort should be made to acquire uniform maximum offsets and fold in all azimuths specifically to avoid interpretation problems caused by acquisition 'footprints'. Cost will dictate the maximum fold; however, 'normal' fold must be maintained in each azimuth bin.

(3) It is necessary to perform narrow-azimuthal analysis for the purpose of quality control (QC) before the full-analysis of the data. But it is recommended that final results should be generated using full-azimuthal and full-offset surface fitting method.

(4) It is also necessary to compare the sensitivity and robustness of various attributes before final processing. In this dataset, I found out that the amplitude attribute is very noisy and the results are not desirable. The velocities attribute obtained narrow-azimuth bin stack is contaminated by the acquisition foot print. In contrast, the results from interval traveltime obtained by surface fitting seem to be most reliable.

Finally, in the future, I suggest the performing of a 2D converted-wave bire-

fringence analysis. The birefringence results can be used to calibrate the P-wave results as, like pure shear-waves, converted-waves are very sensitive to anisotropy. Ultimately, these results should be interpreted in terms of physical and fluid flow properties of the rock using the theories developed by Hudson (1981); Liu *et al.* (2000); Pointer *et al.* (2000); Thomsen (1995).

Reference List

Aki, K., and Richards, P. G., 1980, Quantitative seismology: Theory and methods: W.N. Freeman and Co., New York.

Al-Dajani, A., and Alkhalifah, T., 1997, Reflection moveout inversion in azimuthally anisotropic media: 67th Ann. Internat. Mtg: Soc. Expl. Geophys., Expanded Abstracts, pages 1230–1233.

Al-Dajani, A., Tsvankin, I., and Toksoz, M. N., 1998, Nonhyperbolic reflection moveout for azimuthally anisotropic media: 68th Ann. Internat. Mtg: Soc. Expl. Geophys., Expanded Abstracts, pages 1479–1482.

Alford, R. M., 2000, Shear data in the presence of azimuthal anisotropy: 70th Ann. Internat. Mtg: Soc. Expl. Geophys., Expanded Abstracts, pages 372–374.

Alkhalifah, T., Tsvankin, I., Larner, K., and Toldi, J., 1996, Velocity analysis and imaging in transversely isotropic media: Methodology and a case study: The Leading Edge, **15**, 371–378.

Alkhalifah, T. A., 1996, Velocity analysis using nonhyperbolic moveout in transversely isotropic media: 66th Ann. Internat. Mtg: Soc. Expl. Geophys., Expanded Abstracts, pages 1499–1502.

Becker, D., and Perelberg, A. I., 1986, Seismic detection of subsurface fractures: 56th Ann. Internat. Mtg: Soc. Expl. Geophys., Expanded Abstracts, page Session:S9.2.

Booth, D. C., and Crampin, S., 1983, The anisotropic reflectivity technique: anomalous reflected arrival from an anisotropic upper mantle: Geophys. J. Roy. Astr. Soc., **72**, 767–782.

Brown, R., and Korringa, J., 1975, On the dependence of the elastic properties of a porous rock on the compressibility of the pore fluid: Geophysics, **40**, 608–616.

Carnes, P. S., 1966, Effects of natural fractures on directional permeability in water flooding: Seventh Biennial Secondary Recovery Symposium, Soc.Pet. Eng. of Am. Inst. Min. Eng., North Tex. Sect. Wichita Falls, Tex.

Chapman, M., Maultzsch, S., Liu, E., and Li, X.-Y., 2003, The effect of fluid saturation in an anisotropic, multi-scale equant porosity model: Geophysical Prospecting, page in press.

Chapman, M., 2003, Frequency dependent anisotropy due to meso-scale fractures in the presence of equant porosity: Journal of Applied Geophysics, page in press.

Chen, W., 1995, AVO in azimuthally anisotropic media: fracture detection using P-wave data and a seismic study of naturally fractured tight gas reservoirs: PhD Thesis, The University of Stanford, pages 1–143.

Corrigan, D., Withers, R., Darnall, J., and Skopinski, T., 1997, Fracture mapping from azimuthal velocity analysis using 3D surface seismic data: 67th Ann. Internat. Mtg: Soc. Expl. Geophys., Expanded Abstracts, pages 1834–1837.

Crampin, S., and Booth, D., 1985, Shear-wave polarizations near the North Anatolian fault II, Interpretation in terms of crack induced anisotropy: Geophys. J. Roy. Astr. Soc., **83**, 75–92.

Crampin, S., McGonigle, R., and Bamford, D., 1980, Estimating crack parameters from observations of P-wave velocity anisotropy: Geophysics, **46**, 345–360.

Crampin, S., Evans, R., and Atkinson, B. K., 1984, Earthquake prediction: A new physical basis: Geophys. J. Roy. Astr. Soc., **76**, 147–156.

Crampin, S., 1977, A review of effects of anisotropic layering on the propagation of surface waves: Geophys. J. Roy. Astr. Soc., **49**, 9–27.

Crampin, S., 1978, Seismic wave propagation through a cracked solid: Polarization as a possible dilatancy diagnostic: Geophys. J. Roy. Astr. Soc., **53**, 467–496.

Crampin, S., 1981, A review of wave motion in anisotropic and cracked elastic-media: Wave Motion, **3**, 343–391.

Crampin, S., 1984a, Anisotropy in exploration seismics: First Break, **02**, 19–21.

——— 1984b, Effective anisotropic elastic constants for wave propagation through cracked solids: Geophys. J. Roy. Astr. Soc., **76**, 135–145.

——— 1984c, An introduction to wave propagation in anisotropic media: Geophysics, **50**, 12–28.

Crampin, S., 1985, Evaluation of anisotropy by shear-wave splitting: Geophysics, **50**, 142–152.

Crampin, S., 1987, Geological and industrial implications of extensive-dilatancy anisotropy: Nature, **328**, 491–496.

Dai, H., and Li, X.-Y., 1998, Interpreting the residual wavefield for polarization change in 4-c shear-wave data: 68th Ann. Internat. Mtg: Soc. Expl. Geophys., Expanded Abstracts, pages 726–729.

de Voogd, N., and den Rooijen, H., 1983, Thin-layer response and spectral bandwidth: Geophysics, **48**, 12–18.

Doe, T. W., Long, J., Endo, H., and Wilson, C., 1982, Approaches to evaluating the permeability and permeability of fractured rock masses: 23rd Symposium on rock mechnics, University of California Berkeley.

Dong, W., 1999, AVO detectability against tuning and stretching artifacts: Geophysics, **64**, 494–503.

Ellefsen, K. J., Hsieh, P. A., and Shapiro, A. M., 1999, Relation between seismic velocity and hydraulic conductivity at the USGS Fractured Rock Research Site: U.S. Geological Survey Toxic Substances Hydrology Program, **3**.

Floridia, C., and Teles, T. N., 1998, Effects of anisotropy in the AVO analysis: 68th Ann. Internat. Mtg: Soc. Expl. Geophys., Expanded Abstracts, pages 212–215.

Fryer, G. J., and Frazer, L., 1987, Seismic waves in stratified anisotropic media - II. Elastodynamic eigensolutions for some anistropic systems: Geophys. J. Roy. Astr. Soc., **91**, 73–101.

Gajewski, D., and Psencik, I., 1995, ANRAY(Version 4.0): Software Manual.

Gajewski, D., and Psencik, I., 1996, QP wave phase velocities in weakly anisotropic media - Perturbation approach: 66th Ann. Internat. Mtg: Soc. Expl. Geophys., Expanded Abstracts, pages 1507–1510.

Grechka, V., and Tsvankin, I., 1997, 3-D description of normal moveout in anisotropic media: 67th Ann. Internat. Mtg: Soc. Expl. Geophys., Expanded Abstracts, pages 1487–1491.

Grechka, V., and Tsvankin, I., 1998a, Inversion of azimuthally dependent NMO velocity in transversely isotropic media with a tilted axis of symmetry: 68th Ann. Internat. Mtg: Soc. Expl. Geophys., Expanded Abstracts, pages 1483–1486.

——— 1998b, 3-D moveout inversion in azimuthally anisotropic media with lateral velocity variation: Theory and a case study: 68th Ann. Internat. Mtg: Soc. Expl. Geophys., Expanded Abstracts, pages 1653–1657.

Grechka, V., 1998, AVO analysis in finely layered azimuthally anisotropic media: 68th Ann. Internat. Mtg: Soc. Expl. Geophys., Expanded Abstracts, **II**, 1649–1652.

Hall, S. A., and Kendall, J. M., 1997, Converted phase avoa effects over multiple fracture sets: Application to ocean bottom surveys: 67th Ann. Internat. Mtg: Soc. Expl. Geophys., Expanded Abstracts, pages 1195–1198.

Hall, S. A., and Kendall, J.-M., 2001, Constraining the interpretation of AVOA for fracture characterization: Anisotropy 2000: Fractures, Converted Waves, and Case Studies, Soc. of Expl. Geophys., pages 107–144.

Hall, S. A., Kendall, J. M., Barkved, O., and Mueller, M., 2000, Fracture characterization using p-wave avoa in 3-d obs data: 70th Ann. Internat. Mtg: Soc. Expl. Geophys., Expanded Abstracts, pages 1409–1412.

Hall, S. A., Kendall, J. M., and Barkved, O. I., 2002, Fractured reservoir characterization using P-wave AVOA analysis of 3D OBC data: The Leading Edge, **22**, 777–781.

Helbig, K., 1994, Foundations of anisotropy for exploration seismics: Handbook of Geophysical Exploration Section I. Seismic Exploration, **22**, 1–485.

Helbig, K., 1998, A formalism for the consistent description of non-linear elasticity of anisotropic media: The 8th International Workshop on Seismic Anisotropy, pages 89–90.

Hilterman, F. J., Sherwood, J. W. C., Schellhorn, R., Bankhead, B., and DeVault, B. C., 1996, Detection of hydrocarbons with lithostratigraphy: 66th Ann. Internat. Mtg: Soc. Expl. Geophys., Expanded Abstracts, **I**, 1751–1754.

Hudson, J., and Knopoff, L., 1989, Predicting overall the properties of composite materials with small-scale inclusions or cracks: Geophysics, **131**, 551–576.

Hudson, J., Liu, E., and Crampin, S., 1996, The mechanical properties of materials with interconnected cracks and pores: Geophys. J. Int., **124**, 105–112.

Hudson, J., 1981, Wave speeds and attenuation of elastic waves in material containing cracks: Geophys. J. Roy. Astr. Soc., **64**, 133–150.

Hudson, J., 1990, Overall elastic properties of isotropic materials with arbitrary distribution of circular cracks: Geophys. J. Int., **102**, 465–469.

Johnston, D., 1986, VSP detection of fracture-induced velocity anisotropy: 56th Ann. Internat. Mtg: Soc. Expl. Geophys., Expanded Abstracts, page Session:S9.1.

Juhlin, C., and Young, R., 1993, Implications of thin layers for amplitude variation with offset (AVO) studies: Geophysics, **58**, 1200–1204.

Kendall, J.-M., and Thomson, C., 1989, A comment on the form of the geometrical spreading equations, with some numerical examples of seismic ray tracing in inhomogeneous, anisotropic media: Geophys. J. Int., **99**, 401–413.

Kendall, R., Hall, S. A., Kendall, J.-M., and Sondergeld, C., 1998, Analysis of anisotropic velocities in a fractured, vuggy carbonate and AVOA: 68th Ann. Internat. Mtg: Soc. Expl. Geophys., Expanded Abstracts, pages 1057–1059.

Krasovec, M. L., Rodi, W., and Toksöz, M. N., 1998, Sensitivity analysis of amplitude variation with offset (AVO) in fractured media: 68th Ann. Internat. Mtg: Soc. Expl. Geophys., Expanded Abstracts, pages 201–203.

Kühnel, T., and Li, X., 1996, Anisotropy versus dip - a separation approach: 66th Ann. Internat. Mtg: Soc. Expl. Geophys., Expanded Abstracts, pages 1866–1869.

Kühnel, T., 1998, The influence of structure on seismic parameter estimation in anisotropic media: PhD Thesis, The University of Edinburgh, pages 1–145.

Leary, P. C., Crampin, S., and McEvilly, T. V., 1990, Seismic fracture anisotropy in the earth's crust: An overview: J. Geophys. Res., **95**, 11105–11114.

Lefeuvre, F., 1994, Fracture related anisotropy detection and analysis:'and if the P-waves were enough?': 64th Ann. Internat. Mtg: Soc. Expl. Geophys., Expanded Abstracts, **I**, 942–945.

Leon, T., 2002, Amplitude-versus-offset measurement errors in a finely layered medium: EAGE DISC course, Understanding seismic anisotropy in exploration and exploitation.

Li, X.-Y., and Crampin, S., 1993, Approximation of shear-wave velocity and moveout equations in anisotropic media: Geophysical Prospecting, **41**, 833–857.

Li, X.-Y., Kühnel, T., and MacBeth, C., 1996, Mixed mode AVO response in fractured media: 66th Ann. Internat. Mtg: Soc. Expl. Geophys., Expanded Abstracts, pages 1822–1825.

Li, X.-Y., 1997, Viability of azimuthal variation in P-wave moveout for fracture detection: 67th Ann. Internat. Mtg: Soc. Expl. Geophys., Expanded Abstracts, **II**, 1555–1558.

Li, X.-Y., 1998, Fracture detection using P-P and P-S wave in multicomponent sea-floor data: 68th Ann. Internat. Mtg: Soc. Expl. Geophys., Expanded Abstracts, pages 2056–2059.

Li, X.-Y., 1999, Fracture detection using azimuthal variation of P-wave moveout from orthogonal seismic survey lines: Geophysics, **64, No.4**, 1193–1201.

Liu, E., and Li, X. Y., 2000, Seismic detection of fluid saturation in aligned fractures: 70th Ann. Internat. Mtg: Soc. Expl. Geophys., Expanded Abstracts, pages 2373–2375.

Liu, E., Hudson, J., and Pointer, T., 2000, Equivalent medium representation of fractured rock: J. Geophys. Res., **105**, 2981–3000.

Ludwig, R. J., Iturrino, G. J., and Rona, P. A., 1998, Seismic velocity porosity relationship of sulfide, sulfate, and basalt samples from the TAG hydrothermal mound: Proceedings of the Ocean Drilling Program, Scientific Results, **158**.

Lynn, H., and Beckham, W., 1998, P-wave azimuthal variations in attenuation, amplitude and velocity in 3-D field data: Implications for mapping horizontial permeability anisotropy: 68th Ann. Internat. Mtg: Soc. Expl. Geophys., Expanded Abstracts, pages 193–196.

Lynn, H. B., Simon, K. M., Bates, C. R., and Dok, R. V., 1996, Naturally fractured gas reservoir's seismic characterization: 66th Ann. Internat. Mtg: Soc. Expl. Geophys., Expanded Abstracts, **II**, 1360–1363.

MacBeth, C., and Li, X.-Y., 1999, AVD-An emerging new marine technology for reservoir characterization: Acquisition and application: Geophysics, **64**, 1153–1159.

MacBeth, C., Li, X.-Y., Crampin, S., and Mueller, M., 1992, Detecting lateral viability in crack parameters from surface data: 62nd Ann. Internat. Mtg: Soc. Expl. Geophys., Expanded Abstracts, pages 816–819.

Mallick, S., Craft, K. L. J., Meister, L. J., and Chambers, R. E., 1996, Computation of principal directions of azimuthal anisotropy from P-wave seismic data: 66th Ann. Internat. Mtg: Soc. Expl. Geophys., Expanded Abstracts, pages 1862–1865.

Mandal, B., and Toksöz, M. N., 1990, Computation of complete waveforms in general anisotropic media-results from an explosion source in an anisotropic medium: Geophys. J. Int., **103**, 33–45.

Maultzsch, S., Chapman, M., Liu, E., and Li, X.-Y., 2003, The potential of measuring fracture sizes with frequency-dependent shear-wave splitting: First Break, page in press.

Mueller, M., 1991, Prediction of lateral variability in fracture intensity using multicomponent shear wave surface seismic as a precursor to horizontal drilling: Geophys. J. Int., **107**, 409–415.

Pérez, M. A., Gibson, R., and Toksöz, M., 1999, Detection of fracture orientation using azimuthal variation of P-wave AVO responses: Geophysics, **64**, 1253–1265.

Pointer, T., Liu, E., and Hudson, J., 2000, Seismic wave propagation in cracked porous media: Geophysical Journal International, **142**, 199–231.

Rüger, A., 1996a, Variation of P-wave reflectivity with offset and azimuth in anisotropic media: 66th Ann. Internat. Mtg: Soc. Expl. Geophys., Expanded Abstracts, pages 1810–1813.

——— 1996b, Analytic insight into shear-wave AVO for fractured reservoirs: 66th Ann. Internat. Mtg: Soc. Expl. Geophys., Expanded Abstracts, pages 1801–1804.

——— 1996c, Variations of P-wave reflectivity with offset and azimuth in anisotropic media: 66th Ann. Internat. Mtg: Soc. Expl. Geophys., Expanded Abstracts, pages 1810–1813.

Rüger, A., 1998, Variation of P-wave reflectivity with offset and azimuth in anisotropic media: Geophysics, **63**, 935–947.

Sayers, C. M., and Ebrom, D. A., 1997, Seismic traveltime analysis for azimuthally anisotropic media: Theory and experiment: Geophysics, **62**, 1570–1582.

Sayers, C. M., and Kachanov, M., 1995, Microcrack-induced elastic wave anisotropy of brittla rocks: J. Geophys. Res., **100**, 4149–4156.

Schoenberg, M., and Sayers, C. M., 1995, Seismic anisotropy of fractured rock: Geophysics, **60**, 204–211.

Schoenberg, M., Hsu, K., and Walsh, J. J., 1991, Anisotropy from polarization and moveout: Geophysics, pages 1526–1529.

Schoenberg, M. A., Dean, S., and Sayers, C. M., 1999, Azimuth-dependent turning of seismic waves reflected from fractured reservoirs: Geophysics, **64**, 1160–1171.

Schoenberg, M., 1994, Transverse isotropic media equivalent to thin isotropic layers: Geophysical Prospecting, **42**, 885–915.

Schoenberg, M. A., 1998, Acoustic characterization of underground fractures: 68th Ann. Internat. Mtg: Soc. Expl. Geophys., Expanded Abstracts, pages 1624–1627.

Sena, A. G., 1991, Seismic traveltime equations for azimuthally anisotropic and isotropic media: Estimation of interval elastic properties: Geophysics, **56**, 2090–2101.

Shuey, R. A., 1985, A simplification of the Zoeppritz equations: Geophysics, **50**, 609–614.

Slack, R. D., Ebrom, D. A., McDonald, J. A., and Tatham, R. H., 1993, Thin layers and shear-wave splitting: Geophysics, **58**, 1468–1480.

Slawinski, M. A., 1996, On elastic-wave propagation in anisotropic media: reflection/reflaction laws, raytracing, and traveltime inversion: PhD. thesis, University of Calgary, pages 1–208.

Swan, H. W., 1991, Amplitude-versus-offset measurement errors in a finely layered medium: Geophysics, **56**, 41–49.

Swan, H., 1993, Properties of direct AVO hydrocarbon indicators, Castagna, J. P. and Backus, M. M. (eds.) offset-dependent reflectivity: Theory and practice of AVO analysis: 63rd Ann. Internat. Mtg: Soc. Expl. Geophys., Expanded Abstracts, **I**, 78–92.

Taylor, D., 1990, ANISEIS manual: Applied Geophysical Software, **V 4.5**, 1.0–8.5.

Teng, L., and Mavko, G., 1996, Fracture signatures on P-wave AVOZ: 66th Ann. Internat. Mtg: Soc. Expl. Geophys., Expanded Abstracts, pages 1818–1821.

Thomsen, L., and Tsvankin, I., 1995, Layer-stripping of azimuthal anisotropy from reflection shear-wave data: 65th Ann. Internat. Mtg: Soc. Expl. Geophys., Expanded Abstracts, pages 289–292.

Thomsen, L., 1986, Weak elastic anisotropy: Geophysics, **51**, 1954–1966.

Thomsen, L., 1995, Elastic anisotropy due to aligned cracks in porous rock: Geophysical Prospecting, **43**, 805–829.

Tod, S. R., 2001, The effects on seismic waves of interconnected nearly aligned cracks: Geophys. J. Int., **146**, 249–263.

Tsvankin, I., 1995, Inversion of moveout velocity for horizontal transverse isotropy: 65th Ann. Internat. Mtg: Soc. Expl. Geophys., Expanded Abstracts, pages 735–738.

Tsvankin, I., 1997, Reflection moveout and parameter estimation for horizontal transverse isotropy: Geophysics, **62**, 614–629.

van der Kolk, C. M., Guest, W. S., and Potters, J. H. H. M., 2001, The 3d shear experiment over the Natih field in Oman: the effect of fracture-filling fluids on shear proagation: Geophysical Prospecting, **49**, 179–197.

Widess, M. B., 1973, How thin is a thin bed?: Geophysics, **38**, 1176–1180.

Willis, H., Rethford, G., and Bielanski, E., 1986, Azimuthal anisotropy: Occurrence and effects of shear-wave data quality: 56th Ann. Internat. Mtg: Soc. Expl. Geophys., Expanded Abstracts, page Session:S9.7.

Winterstein, D., and Meadows, M., 1991, Shear-wave polarization and substructure stress direction at Lost Hill field: Geophysics, **56**, 1331–1348.

Zhen, W., 1995, AVO in azimuthal anisotropy media, fracture detection using p-wave data and seismic study of naturally fractured tight gas reservoirs: PhD. thesis of University of Stanford.

Ziolkowski, A., and Fokkema, J., 1986, The progressive attenuation of high-frequency energy in seismic reflection data: Geophysical Prospecting, **34**, 981–1001.